



This is the accepted version of this paper. The version of record is available at  
<https://doi.org/10.1016/j.earscirev.2021.103801>

1  
2  
3  
4  
5  
6  
7  
8  
9  
10  
11  
12  
13  
14  
15  
16  
17  
18  
19  
20  
21  
22  
23  
24  
25  
26  
27  
28  
29  
30  
31  
32  
33  
34  
35  
36  
37  
38  
39  
40  
41  
42  
43  
44  
45  
46  
47  
48  
49  
50  
51  
52  
53  
54  
55  
56  
57  
58  
59  
60  
61  
62  
63  
64  
65

1  
2  
3  
4  
5  
6  
7  
8  
9  
10  
11  
12  
13  
14  
15  
16  
17  
18  
19  
20  
21  
22  
23  
24  
25  
26  
27  
28  
29  
30  
31  
32  
33  
34  
35  
36  
37  
38  
39  
40  
41  
42  
43  
44  
45  
46  
47  
48  
49  
50  
51  
52  
53  
54  
55  
56  
57  
58  
59  
60  
61  
62  
63  
64  
65

**Chemical Characteristics of Modern Deep-Sea Metalliferous Sediments in Closed  
versus Open Basins, with Emphasis on Rare-earth Elements and Nd Isotopes**

Timothy J. Barrett\*  
174 Maple Heights Drive,  
Gravenhurst, Ontario P1P 1R1, Canada

Ian Jarvis  
Dept. of Geography, Geology and the Environment,  
Kingston University London,  
Penrhyn Road, Kingston upon Thames KT1 2EE, UK

Mark D. Hannington  
Dept. of Earth Sciences, University of Ottawa,  
Marion Hall, Ottawa, Ontario K1N 6N5, Canada

Matthew F. Thirlwall  
Dept. of Earth Sciences,  
Royal Holloway University of London,  
Egham TW20 0EX, UK

Corresponding author: [tjbarrett27@gmail.com](mailto:tjbarrett27@gmail.com)

August 26, 2021

**Abstract**

38  
39  
40  
41 Metalliferous sediments deposited on and near spreading ridges show contrasting  
42 geochemical signatures depending on whether deposition occurred in a restricted basin filled  
43 with anoxic dense brines, or in an open ocean characterized by oxidized and well-circulated  
44 seawater. Metalliferous sediments of the Atlantis II Deep, which are precipitated from ca. 60°C  
45 dense brines, display a wide range of mineralogical and chemical facies. The most abundant  
46 facies are enriched in Fe-oxyhydroxides or Fe-silicates or metal sulphides; Mn-oxides and  
47 anhydrite are locally important. Terrigenous and biogenic components are minor. Base and  
48 precious metals are notably enriched in the sulphide-rich facies. By contrast, chemical  
49 precipitates in open-ocean settings consist of Fe-Mn-oxyhydroxides that were deposited from  
50 dilute hydrothermal plumes, commonly admixed with biogenic carbonate-rich ooze. On a  
51 carbonate-free basis, open-ocean metalliferous sediments show much less enrichment in  
52 trace metals relative to sediments in the Atlantis II Deep but have higher contents of rare-  
53 earth elements (REEs).

54  
55 The shale-normalised REE patterns of metalliferous sediments in the Atlantis II Deep show  
56 positive Eu anomalies, but lack Ce anomalies. Due to the low REE content of the precipitates,  
57 even minor aluminosilicate detritus (10%) can affect REE patterns. The 'baseline' of the REE  
58 pattern is determined mainly by the aluminosilicate component of the metalliferous sediment,  
59 with the Eu anomaly resulting from the hydrothermal component. Nd isotopic variations can  
60 be explained largely by the mixing of Nd provided by aluminosilicate detritus with lesser  
61 dissolved Nd derived from a basaltic-hydrothermal source. These two sources can also  
62 account for the Pb isotopic variations reported in previous studies. The majority of Sr is  
63 derived from evaporites that flank the brine deep, with a smaller contribution from the  
64 basalts.

65  
66 In open-ocean settings, plume particulates that formed above high-temperature vents acquire  
67 seawater-type REE patterns and Nd isotope ratios soon after discharge; these features are  
68 maintained as the plume drifts hundreds to a few thousand kilometres from the ridge axis.  
69 Departures from seawater isotopic and REE signatures can occur if detrital material (basaltic

1  
2  
3  
4  
5  
6  
7  
8  
9  
10  
11  
12  
13  
14  
15  
16  
17  
18  
19  
20  
21  
22  
23  
24  
25  
26  
27  
28  
29  
30  
31  
32  
33  
34  
35  
36  
37  
38  
39  
40  
41  
42  
43  
44  
45  
46  
47  
48  
49  
50  
51  
52  
53  
54  
55  
56  
57  
58  
59  
60  
61  
62  
63  
64  
65

70 or terrigenous) is present in the metalliferous sediment. The Sr-isotope ratios of open-ocean  
71 sediments are, like Nd, dominated by seawater Sr. For Pb, a basaltic component can be  
72 isotopically identified in metalliferous sediments up to 1000 km from the axis.

73  
74 Where low-temperature fluids discharge through biogenic sediments on ridge flanks, as at the  
75 Galapagos hydrothermal mounds, Fe-rich smectites (nontronite) are formed, together with  
76 minor Mn-oxides. The nontronites have very low contents of REEs, with seawater-type  
77 patterns, although Ce anomalies are less negative than those of deep Pacific seawater.  
78 Nontronites formed in high-temperature vent fields, and on intra-plate seamounts, display a  
79 range of REE patterns resulting from mixtures of hydrothermal fluid and normal seawater.

80  
81 In open-ocean basins, the REE patterns and Nd-Sr isotope ratios of chemical precipitates  
82 generally reflect those of ambient deep seawater. In closed (or restricted) anoxic basins  
83 subject to hydrothermal input, the precipitates can have REE patterns and Nd-Sr-Pb isotope  
84 ratios that differ considerably from those of ambient seawater. These results bear on the  
85 interpretation of geochemical data from ancient exhalative deposits.

86  
87  
88 **Keywords: Geochemistry, metalliferous sediments, REEs, Nd isotopes, Red Sea, Pacific Ocean**

## 89 1. Introduction

1  
2  
3 90 Chemical sedimentation resulting from hydrothermal activity in deep marine  
4  
5 91 environments can be considered in terms of two end-member settings: (1) closed basins  
6  
7 92 up to a few tens of kilometres across that lie on spreading axes, and contain up to 100 m  
8  
9 93 of hot (20–68°C) anoxic brines as near- bottom layers from which metal-rich sulphides,  
10  
11 94 silicates and oxyhydroxides precipitate (Degens and Ross, 1969; Bäcker and Richter, 1973;  
12  
13 95 Laurila et al., 2014a, b, 2015, and references therein); and (2) broad flanks of open–ocean  
14  
15 96 spreading ridges where bottom waters are well circulated and oxic, and where Fe-Mn-  
16  
17 97 oxyhydroxides precipitate from dilute, low-temperature plumes that can extend up to a  
18  
19 98 few thousand kilometres from the spreading axis (cf. Boström et al., 1969; Sayles and  
20  
21 99 Bischoff, 1973; Jarvis, 1985; Barrett et al., 1987; Owen and Olivarez, 1988; Feely et al.,  
22  
23 100 1994a, 1996; Resing et al., 2015; Fitzsimmons et al., 2017; Gartman and Findlay, 2020).

24  
25 101  
26 102 Fe-rich sediments may also form:

27  
28 103 (i) at distances of up to a few tens of km from spreading axes where uprising low-  
29  
30 104 temperature fluids react with biogenic sediments to form thick, nontronite-rich deposits  
31  
32 105 (Corliss et al., 1978; Hékinian et al., 1978; Dymond et al., 1980; Honnorez et al., 1981;  
33  
34 106 McMurtry et al., 1983; Moorby and Cronan, 1983; Barrett, 1983, 1992);  
35  
36 107 (ii) on seamounts as thin, nontronite-rich deposits encrusting volcanic rocks (De Carlo et  
37  
38 108 al., 1983; Alt, 1988; McMurtry et al., 1993; Dekov et al., 2007; Lubetkin et al., 2018);  
39  
40 109 (iii) directly on spreading axes, either by surface oxidation of high-temperature sulphide  
41  
42 110 deposits (Barrett, 1990; German et al., 1993; Damyanov et al., 1998; Dias et al., 2008; Pan  
43  
44 111 et al., 2018), or by precipitation from low-temperature fluids (Murnane and Clague, 1983;  
45  
46 112 Mills et al., 2001; Severmann et al., 2004; Dekov et al., 2010; Sun et al., 2012, 2018; Zeng  
47  
48 113 et al., 2012; Ta et al., 2017).

49 114  
50  
51 115 In order to assess chemical differences between the two end-member settings, we first  
52  
53 116 review the characteristics of metalliferous sediments from the brine-filled deeps of the  
54  
55 117 Red Sea versus those that formed in open-ocean settings of the eastern Pacific Ocean (Fig.  
56  
57 118 1). In the Atlantis II Deep of the Red Sea, metalliferous sediments form almost pure  
58  
59  
60  
61  
62

1 119 accumulations (5–20 m thick) of Fe oxyhydroxides, Fe-rich hydrous silicates, Fe-Cu-Zn-Pb  
2 120 sulphides, Fe-Mn carbonates and oxides, and amorphous compounds that overlie axial  
3  
4 121 basalts (e.g., Bäcker and Richter, 1973). In the eastern Pacific Ocean, metalliferous  
5  
6 122 sediments occur as laterally extensive, fine-grained Fe-Mn oxyhydroxides dispersed within  
7  
8 123 biogenic ooze-dominated sediments (up to 50 m thick) that accumulated over millions of  
9  
10 124 years as the seafloor spread away from the East Pacific Rise (Lyle, 1986). In both of these  
11  
12 125 settings, a small but chemically significant component of terrigenous detritus is also  
13  
14 126 present within the metalliferous sediments.  
15  
16 127

17  
18 128 For the Atlantis II Deep, we present previously unpublished chemical analyses of 53 samples of  
19  
20 129 metalliferous sediments from 13 cores in the western to southwestern portion of the Deep. In  
21  
22 130 addition, a subset of 14 samples has been analysed for Nd isotope ratios with the aim of  
23  
24 131 identifying the different possible sources of Nd (e.g., basalt, seawater, continental detritus),  
25  
26 132 and to assess relationships between rare earth element (REE) patterns and Nd isotope ratios.

27  
28 133 For the eastern Pacific Ocean, 40 new chemical analyses of metalliferous sediments, including  
29  
30 134 REEs, from Leg 92 of the Deep Sea Drilling Project (DSDP) are reported. We also review  
31  
32 135 published REE and Nd-Sr-Pb isotope data for metalliferous sediments from these two settings.  
33  
34 136

35 137 In addition to the end-members, REE and Nd isotopic data for Fe-silicate-rich, low-temperature  
36  
37 138 seafloor precipitates are reviewed, with emphasis on: (i) the nontronite-rich Galapagos  
38  
39 139 hydrothermal mounds on the flank of the Galapagos Rift in the eastern Pacific Ocean; and (ii)  
40  
41 140 Fe-rich sediments formed on the axes of spreading ridges, including nontronite-rich precipitates  
42  
43 141 and Fe-oxide-hydroxide-rich material derived from the oxidation of massive sulphides.  
44  
45 142

46  
47 143 The overall objective of this paper is to characterise the main chemical features of modern  
48  
49 144 metalliferous sediments deposited in contrasting ocean-floor settings, with an emphasis on the  
50  
51 145 interpretation of REE patterns and Nd isotopic compositions. This survey focuses on sediments  
52  
53 146 containing a significant hydrothermal component, and therefore does not include largely  
54  
55 147 hydrogenous metalliferous deposits such as ferromanganese nodules of the abyssal plains, or  
56  
57 148 ferromanganese crusts overlying basalts at spreading centres or on seamounts. We also briefly  
58  
59 149 discuss the REE patterns and Nd isotopic compositions of some ancient exhalative rocks on land  
60  
61  
62

150 that were originally deposited in deep-ocean settings, e.g., Palaeozoic umbers overlying  
151 massive sulphide deposits, and Precambrian banded iron formations.

152

153

### 1.1. Previous studies

154

155

156

157

158

159

160

161

162

163

164

165

166

167

168

169

170

171

172

173

174

175

176

177

178

179

180

181

182

183

184

185

186

187

188

189

190

191

192

193

194

195

196

197

198

199

200

201

202

The brine-filled deeps of the axial portion of the Red Sea (Figs. 1, 2) have been of interest to oceanographers and geologists since the first research cruises to the area in the 1960s and 1970s (Miller et al., 1966; Degens and Ross, 1969; Bäcker and Schoell, 1972). Numerous studies of the Atlantis II Deep sediments have since produced a detailed picture of their stratigraphy, mineralogy, chemistry and potential economic value (Bischoff, 1969; Bischoff and Manheim, 1969, 1972; Bäcker and Richter, 1973; Hackett and Bischoff, 1973; Delevaux and Doe, 1974; Steinkamp and Schumann, 1974; Bäcker, 1976; Bignall et al., 1976; Lupton et al., 1977; Shanks and Bischoff, 1977, 1980; Pottorf and Barnes, 1983; Mustafa et al., 1984; Zierenberg and Shanks, 1983, 1988; Karbe, 1987; Oudin, 1987; Singer and Stoffers, 1987; Cole, 1988; Dupré et al., 1988; Guney et al., 1988; Ramboz et al., 1988; Butuzova et al., 1990; Cocherie et al., 1994; Blanc et al., 1998; Pierret et al., 1998; Taitel-Goldman and Singer, 2001, 2002; Badaut et al., 2002; Taitel-Goldman and Singer, 2009; Bertram et al., 2011; Laurila et al., 2014a, b, 2015; Brueckmann et al., 2017; Quadros et al., 2018). The metalliferous sediments of the Atlantis II Deep constitute a major deposit of base and precious metals with an estimated in-situ value of US\$ 11 billion (Brueckmann et al., 2017); mining schemes have been proposed for piping the sediments to a surface ship, with primary processing carried out at sea (Mustafa and Amann, 1980; Nawan, 1984; Thiel et al., 2015; Hamer, 2017).

Detailed investigations have been made on the temperature and chemical composition of the brine layers that overlie the metalliferous sediments in the Atlantis II Deep (Ross, 1972; Schoell and Faber, 1978; Danielsson et al., 1980; Hartmann, 1985; Zierenberg and Shanks, 1986; Anschutz et al., 1995, 1998, 2000; Anschutz and Blanc, 1996; Winckler et al., 2000, 2001; Pierret et al., 2001; Swift et al., 2012; Anschutz, 2015; Schardt, 2016), and on microbial communities both in the hot brines (Eder et al., 2001; Qian et al., 2011; Wang et al., 2011, 2013), and in the underlying sediments (Siam et al., 2012). Several other brine pools along the spreading axis of the Red Sea (shown in Fig. 2) have also been studied, although in less detail than the Atlantis II

181 Deep (Bignell, 1975; Blum and Puchelt, 1991; Sholten et al., 1991; Pierret et al., 2010). Tectonic,  
182 igneous and sedimentological events during the opening of the Red Sea, which bear on the  
183 formation and seafloor setting of the brine pools, have been described by Bonatti and Seyler  
184 (1987), Bosworth et al. (2005), Ligi et al. (2012, 2015, 2018), Augustin et al. (2014, 2016, 2019),  
185 Bonatti et al. (2015), Bosworth (2015) and Bosworth and Stockli (2016).

186  
187 In the eastern Pacific Ocean, detailed chemical studies have been carried out on surficial (<9 m  
188 depth) Fe-Mn-oxyhydroxide-rich metalliferous sediments occurring on and near the crest of the  
189 East Pacific Rise (EPR; Boström et al., 1969; Bender et al., 1971; Marchig and Gundlach, 1982;  
190 Walter and Stoffers, 1985), and Fe-smectite-rich sediments within the Bauer Deep several  
191 hundred km east of the EPR (Dasch et al., 1971; Sayles and Bischoff, 1973; Sayles et al., 1975).  
192 Metalliferous sediments have also been recovered at depth in the Bauer Deep by Leg 34 of the  
193 DSDP (Fig. 1; Boström et al., 1976; Dymond et al., 1976) and in drill holes located up to 1700 km  
194 west of the EPR by Legs 85 and 92 of the DSDP (Fig. 1; Jarvis, 1985; Lyle, 1986; Ruhlin and  
195 Owen, 1986; Barrett et al., 1987). Chemical features of basal metalliferous sediments from  
196 DSDP drillholes in the eastern Pacific Ocean have been reported by Cronan (1976) and Jarvis  
197 (1985). Metalliferous sediments from drilled holes and near-axial surface locations span an age  
198 range from Middle Eocene to Pleistocene, and were derived from colloidal Fe-Mn  
199 oxyhydroxides that settled out of laterally spreading hydrothermal plumes originating at either  
200 the EPR or the earlier-active Galapagos and Mendoza Ridges (Dymond et al., 1973; Dymond et  
201 al., 1976; Leinen and Stakes, 1979; Marchig and Gundlach, 1982; Lyle, 1986; Rea and Leinen,  
202 1986; Marchig and Erzinger, 1986; Lyle et al., 1987). During sediment burial, early diagenetic  
203 reactions between Fe-Mn oxyhydroxides and biogenic silica can lead to the formation of Fe-rich  
204 smectitic silicates plus Mn micronodules, particularly in areas of slow sedimentation such as the  
205 Bauer Deep (Sayles and Bischoff, 1973; Heath and Dymond, 1977, 1981; Jarvis, 1985).

206  
207 In contrast to metalliferous sediments derived from Fe-Mn-oxyhydroxide-bearing plumes, the  
208 Galapagos hydrothermal mounds, located 20–30 km from the modern Galapagos Rift, consist  
209 mainly of Fe-rich, Al-poor (nontronitic) silicates, first recovered by dredging (Corliss et al.,  
210 1978). The mounds were investigated by rotary drilling on DSDP Leg 54 (Hékinian et al., 1978;  
211 Dymond et al., 1980; Schrader et al., 1980; Varnavas and Cronan, 1981) and in more detail

1 212 using piston coring on DSDP Leg 70 (Honnorez et al., 1981; Barrett and Friedrichsen, 1982;  
2 213 Moorby, 1983; Moorby and Cronan, 1983). Nontronite has also been recovered locally from the  
3  
4 214 flanks of seamounts in the Pacific Ocean (Singer et al., 1984; Lubetkin et al., 2018) and in the  
5  
6 215 Mediterranean Sea (Dekov et al., 2007).  
7  
8 216

## 9 10 217 1.2. Sample material and analytical methods 11 218

12  
13  
14 219 Locations of the Atlantis II Deep, the EPR Transect, and other metalliferous sediment and brine  
15  
16 220 sites discussed in this paper are shown in Fig. 1. Geographic coordinates of the sampled sites  
17  
18 221 are listed in Table 1. All cores from the Atlantis II Deep, except one, were sampled by TJB at  
19  
20 222 Preussag AG's archival storage facility in Berkhöpen, Germany. These cores were recovered on  
21  
22 223 R/V Valdivia cruises VA-01 (1971) and VA-03 (1972). One core (274 KS) was taken on R/V  
23  
24 224 Valdivia cruise VA 29 in 1980. This last core, stored at the Bureau de Recherches Géologiques et  
25  
26 225 Minières (BRGM) in Orléans, France, was sampled by TJB. All sediment samples were obtained  
27  
28 226 from intervals of homogeneous colour and texture (featureless muds, with the exception of  
29  
30 227 anhydrite layers/veins; see Section 2.1). Samples from the Atlantis II Deep were washed with  
31  
32 228 distilled water prior to analysis to remove crystallized salts.  
33 229

34  
35 230 Forty-three of the 53 Red Sea samples were analysed for major and trace elements; 10 samples  
36  
37 231 were analysed for trace elements only, due to limited amounts of sample material.

38  
39 232 Determination of major and trace elements by inductively coupled plasma (ICP)  
40  
41 233 spectrochemical techniques was based on total dissolution of 0.5–1 g of sample using a mixed-  
42  
43 234 acid digestion of nitric (HNO<sub>3</sub>), hydrochloric (HCl), perchloric (HClO<sub>4</sub>) and hydrofluoric (HF) acids  
44  
45 235 followed, if necessary, by a lithium metaborate-tetraborate (LiBO<sub>2</sub> – Li<sub>2</sub>B<sub>4</sub>O<sub>7</sub>) fusion and  
46  
47 236 dissolution of any residual material (Bouvier, 1991). Major elements and selected trace  
48  
49 237 elements were determined by ICP-based atomic emission spectrometry (ICP-AES). Other trace  
50  
51 238 elements including metals were analysed by ICP-based mass spectrometry (ICP-MS) at the  
52  
53 239 Analytical Laboratories of the Geological Survey of Canada, Ottawa  
54  
55 240 ([https://navigator.innovation.ca/en/facility/natural-resources-canada/trace-inorganic-  
56  
57 241 geochemistry-research-laboratory](https://navigator.innovation.ca/en/facility/natural-resources-canada/trace-inorganic-geochemistry-research-laboratory)). Pb was determined by atomic absorption (AA).

58  
59 242 Instrumental neutron activation analysis (INAA) of selected trace elements was carried out at  
60  
61  
62

1 243 Activation Laboratories, Ancaster, Ontario (<https://actlabs.com/>). INAA measurements were  
2 244 made on 1-g samples irradiated by thermal neutrons in a high-flux reactor, using gamma-ray  
3  
4 245 spectrometry with a solid-state detector. Total sulphur was determined by combustion  
5  
6 246 followed by infrared spectrophotometry (LECO), and loss on ignition (LOI) by gravimetry at  
7  
8 247 900°C; CO<sub>2</sub> (t) is the total carbon measured by LECO and is reported as CO<sub>2</sub>. The LECO  
9  
10 248 measurements were also made at the Geological Survey of Canada. Carbonate carbon was  
11  
12 249 determined by dissolving the sample in hot HCl, decanting the liquid, weighing the dried  
13  
14 250 residue, and calculating the carbonate fraction by difference. C (org) is the non-carbonate  
15  
16 251 carbon fraction, calculated as the difference between CO<sub>2</sub> (t) and carbonate carbon. All data for  
17  
18 252 the Red Sea sediments, excluding REEs, are given in Supplementary Data Table 2.

19 253  
20  
21 254 Sediment samples from holes drilled by DSDP Leg 92 (EPR Transect) were provided by the Deep  
22  
23 255 Sea Drilling Project. Prior to analysis, samples were washed using distilled water, dried at 110°C,  
24  
25 256 powdered in an agate mortar, subjected to a 10 % acetic acid leach to remove the calcium  
26  
27 257 carbonate component, then dried at 105°C and re-powdered (further details in Barrett et al.,  
28  
29 258 1987). Leg 92 samples were analysed for major and trace elements by the same methods as  
30  
31 259 outlined above for the Red Sea samples; REEs were determined by ICP-MS. In addition,  
32  
33 260 lanthanum, yttrium and zirconium were also determined by ICP-AES. For these three elements,  
34  
35 261 we have used the ICP-AES results as several of the Leg 92 samples could not be measured by  
36  
37 262 ICP-MS due to insufficient material. The ICP-MS results are, however, also reported in  
38  
39 263 Supplementary Data Table 2. For those samples measured by both techniques, the results  
40  
41 264 agree to within 5 % of their average value ( $r^2$  values for La-La, Y-Y and Zr-Zr as measured by the  
42  
43 265 two methods are 0.967, 0.870 and 0.975, respectively). All data for the Leg 92 sediments are  
44  
45 266 given in Supplementary Data Table 2.

46 267  
47  
48 268 Owing to the very low content of REEs in metalliferous sediments of the Atlantis II Deep, as well  
49  
50 269 as elevated Ba concentrations due to the presence of barite, a specific procedure was  
51  
52 270 developed by Jarvis et al. (1989) to ensure accurate analysis of such samples (cf. Barrett et al.,  
53  
54 271 1990). Splits (0.2–0.5 g) of sample powders were digested in open PTFE  
55  
56 272 (polytetrafluoroethylene) beakers using a HF-HClO<sub>4</sub> mixture (Totland et al., 1992; Jarvis, 2003,  
57  
58 273 p. 185), with final solutions taken up in 1 M HCl. Samples with visible residues following  
59  
60  
61  
62

1 274 digestion were filtered, the residues fused with 0.25 g LiBO<sub>2</sub> in platinum crucibles, and the melt  
2 275 dissolved in 1 M HCl. The two solutions were then combined. The REEs and Y were extracted  
3  
4 276 using a cation-separation procedure (Jarvis and Jarvis, 1985; Jarvis, 2003, p. 210), and  
5  
6 277 determined using a VG Elemental PlasmaQuad PQ2 Plus ICP-MS, at the NERC-ICP-MS Facility,  
7  
8 278 then at Royal Holloway University of London, UK. Operating conditions followed Totland et al.  
9  
10 279 (1992).

11 280  
12  
13  
14 281 The cation-exchange extraction utilized does not completely separate Ba from the REEs. The  
15  
16 282 determination of low levels of Eu (typically 2–50 ng ml<sup>-1</sup>), in the presence of up to 100 ng ml<sup>-1</sup> of  
17  
18 283 Ba, required a large correction to compensate for the overlap of refractory <sup>135</sup>Ba<sup>16</sup>O on <sup>151</sup>Eu.  
19  
20 284 Therefore, Eu was determined independently by adjusting the ICP-MS to give a maximum  
21  
22 285 amount of doubly charged M<sup>2+</sup> ions (Jarvis et al., 1989). Results obtained by the two techniques  
23  
24 286 were generally in good agreement; however, data obtained using the "doubly charged"  
25  
26 287 technique have been shown to be more precise and more accurate (Jarvis et al., 1989) and are  
27  
28 288 reported here. The precision of the REE and Y analyses is estimated to be better than ±10 %  
29  
30 289 RSD for all elements. Accuracy of the data is judged to be close to the precision (Totland et al.,  
31  
32 290 1992; Jarvis, 2003).

33 291  
34  
35 292 The Nd isotope ratios of 13 selected samples of metalliferous sediment from the Atlantis II  
36  
37 293 Deep were measured at the London University Radiogenic Isotope Facility. The method used  
38  
39 294 was that described by Thirlwall (1991). Six analyses of the laboratory Aldrich standard gave a  
40  
41 295 mean value of 0.511423 ± 5 (2 sd), slightly higher than the standard value of 0.511420, which in  
42  
43 296 turn is equivalent to the La Jolla standard value of 0.511855. Measured values are reported  
44  
45 297 relative to a CHUR value of 0.512646. The total blank for the analyses was 200–400 pg Nd,  
46  
47 298 which has an insignificant effect on the measured values.

## 48 299 49 50 51 300 **2. Metalliferous Sediments in Closed Ocean Basins – Atlantis II Deep, Red Sea**

### 52 53 54 301 2.1. Tectonic setting and stratigraphy

1 303 Locations of the Atlantis II Deep and five other deeps along the axis of the Red Sea are  
2 304 indicated in [Fig. 2a](#); the inset shows plate boundaries and spreading directions. The history of  
3  
4 305 opening of the Red Sea, and the important influence of evaporite deposits on seafloor  
5  
6 306 topography, as well as on brine generation, have been described by Cochran (2005), Ligi et al.  
7  
8 307 (2012, 2015, 2018), Augustin et al. (2014, 2016), Mitchell and Park (2014), Bonatti et al. (2015),  
9  
10 308 Bosworth (2015), Ehrhardt and Hübscher (2015), Hovland et al. (2015, 2019) and Stockli and  
11  
12 309 Bosworth (2019). Seafloor topography in the region of the Atlantis II Deep is illustrated in [Fig.](#)  
13  
14 310 [2b](#) (after Augustin et al., 2016), where the locations of the 15 cores sampled in the present  
15  
16 311 study are also shown (yellow-filled circles). [Figure 3](#) gives a schematic section across the Red  
17  
18 312 Sea, showing the brine layers, metalliferous sediments and underlying axial basalts of the  
19  
20 313 Atlantis II Deep with respect to laterally bounding Miocene evaporite and Pliocene-Pleistocene  
21  
22 314 siliciclastic sequences. The thickness of metalliferous sediment in the Atlantis II Deep generally  
23  
24 315 ranges from 10 to 25 m. Most of this sediment lies at depths of 2000 to 2200 m below sea level.  
25  
26 316 Accumulation rates during periods of heightened hydrothermal activity were in the order of  
27  
28 317 100 cm/kyr (Shanks and Bischoff, 1980), in contrast to the normal Red Sea hemipelagic  
29  
30 318 sedimentation rate of about 10 cm/kyr (Ku, 1969).  
31 319

32  
33 320 Early studies of gravity cores led to the recognition of seven main sediment facies within the  
34  
35 321 Atlantis II Deep (Bischoff, 1969; Hackett and Bischoff, 1973). These facies were named  
36  
37 322 according to the dominant minerals (detrital material, iron-montmorillonite, goethite-  
38  
39 323 amorphous, sulphide, manganosiderite, anhydrite, manganite), although each facies can  
40  
41 324 contain mineralogically contrasting layers in places. Subsequently, they were grouped into five  
42  
43 325 main lithostratigraphic units by Bäcker and Richter (1973) and Bäcker (1976): AM = amorphous  
44  
45 326 silicate zone; SU2 = upper sulphidic zone; CO = central oxide zone; SU1 = lower sulphidic zone;  
46  
47 327 DOP = detrital-oxide-pyrite zone. These units have been employed by most studies of Atlantis II  
48  
49 328 Deep sediments since then (e.g., Shanks and Bischoff, 1980; Pottorf and Barnes, 1983; Oudin et  
50  
51 329 al., 1984; Laurila, 2015). It should be noted, however, that these broad lithostratigraphic units  
52  
53 330 commonly display internal variations in the form of colour-banded layers and laminations of  
54  
55 331 contrasting mineralogy. Schematic sediment columns for the Atlantis II Deep as a whole, and  
56  
57 332 the Southwest Basin in particular, are shown in [Fig. 4](#) [after Laurila (2015), based on Bäcker and  
58  
59 333 Richter (1973)'s classification of lithological units]. In the Southwest Basin – the focus of the  
60  
61  
62

334 present study – most cores intersected only the upper three lithological units, owing to the  
335 presence of a major basalt sill that prevented core penetration to the basaltic basement.

336  
337 Blanc et al. (1998) suggested revisions to the lithological units proposed by Bäcker and Richter  
338 (1973), based on detailed study of two complete cores, one from the Southwest Basin, the  
339 other from the West Basin. Blanc et al. (1998) argued that only two main sedimentary units  
340 (Lower and Upper) can be distinguished in the Southwest Basin, whereas elsewhere in the  
341 Atlantis II Deep the vertical sequence is more complex, but broadly comparable to that  
342 suggested by Bäcker and Richter (1973), with the main difference being Blanc et al. (1998)'s  
343 subdivision of the Central Oxide (CO) zone into six subunits.

344  
345 In the Bäcker and Richter (1973) scheme, the oldest sedimentary unit, the detrital-oxide-pyrite  
346 (DOP) facies, overlies MOR-type basalts (Fig. 3). The DOP facies was deposited from 23,000 to  
347 12,000 years ago, during the time of the last glacial maximum (Anschutz, 2015). It is dominated  
348 by Fe-Mn carbonates, siliceous plankton tests, detrital clays and pyrite, but also includes Fe-  
349 oxyhydroxide layers. The DOP facies is overlain by SU1, the first sulphide facies (Figs. 3, 4). The  
350 contact between these two facies approximately corresponds to the Pleistocene–Holocene  
351 boundary (Anschutz, 2015). The SU1 facies is overlain by the central oxic (CO) zone, which is  
352 dominated by Fe- and Mn-oxides and oxyhydroxides, then by the SU2 zone containing  
353 significant sulphides, and finally by the AM zone dominated by amorphous Fe-silicates. In the  
354 classification of Blanc et al. (1998), the SU2 and AM zones are combined into one, as sulphides  
355 and amorphous silicates are present throughout both. In the Southwest Basin, this combined  
356 zone (SU2 + AM) is much thicker than elsewhere in the Atlantis II Deep, reaching at least 10 m.

357  
358 Fe-bearing phases in the Atlantis II Deep are commonly amorphous or poorly crystallized,  
359 especially in the upper 5 to 10 m of the sedimentary sequence, and include metastable Fe-  
360 OOH-Si compounds that transform to Fe-oxides and Fe-rich clays during burial diagenesis  
361 (Taitel-Goldman and Singer, 2002; Laurila et al., 2015). The silica is probably derived from both  
362 hydrothermal and biogenic sources (Anschutz and Blanc, 1995a). Local enrichments in detrital  
363 clays, authigenic carbonates and Mn oxides occur below the SU2 zone, mainly in the lowest  
364 (DOP) zone (Anschutz and Blanc, 1995b). Detailed features and distributions of the main

1 365 minerals of the Atlantis II Deep have been reported by Thisse (1982), Zierenberg and Shanks  
2 366 (1983), Cole (1988), Badaut et al. (1992), Blanc et al. (1998), Schwertmann et al. (1998), Taitel-  
3  
4 367 Goldman and Singer (2001), and Taitel-Goldman et al. (2004, 2009). The origin of the fine  
5  
6 368 layering that develops below depths of a few metres, often in the form of colour banding within  
7  
8 369 Fe-oxyhydroxide-rich sediments, has been ascribed to diagenetic processes by Laurila et al.  
9  
10 370 (2015).

11  
12 371  
13  
14 372 Chemical analyses in the 1970s and 1980s were commonly made on bulk samples over core  
15  
16 373 lengths of 100 cm, as a major objective of the coring was to determine average metal grades  
17  
18 374 and tonnages throughout the Atlantis II Deep (Guney et al., 1984, 1988). Given that many  
19  
20 375 lithological units can contain intervals with distinct mineralogical layering on a scale of  
21  
22 376 centimetres or less, bulk chemical analyses over lengths of 100 cm therefore often represent  
23  
24 377 averages of a number of layers of contrasting mineralogy and chemistry.  
25 378

26  
27 379 Detailed studies of 100 short sample intervals (< 2 cm) from nine cores in different parts of the  
28  
29 380 Atlantis II Deep were undertaken by Laurila et al. (2014a, b, 2015). These studies, which  
30  
31 381 documented variations in major elements, metal contents, REE patterns and mineralogy  
32  
33 382 throughout the Deep, have added significantly to our understanding of chemical sedimentation  
34  
35 383 in hot brine pools. Variations in sediment facies were interpreted by these authors to be the  
36  
37 384 result of changes in temperature, pH and Eh of the brines from which the sediments  
38  
39 385 precipitated, which in turn reflect variable hydrothermal input within the basin due to factors  
40  
41 386 such as distance from the source vent(s) and change in hydrothermal discharge rate. In  
42  
43 387 addition, diagenetic effects can modify the mineralogy of the primary precipitates  
44  
45 388 (Schwertmann et al., 1988; Taitel-Goldman and Singer, 2002; Laurila et al., 2015). Typical  
46  
47 389 examples of metalliferous sediments from the Atlantis II Deep are shown in [Fig. 5](#) (from Laurila  
48  
49 390 et al., 2015).

50  
51 391  
52  
53 392 Locations of the 16 cores sampled in the present study are shown in [Fig. 6](#) and listed in [Table 1](#).  
54  
55 393 Twelve cores are from the Southwest Basin, and three from the West Basin (345, 369, 436). The  
56  
57 394 main minerals present in each sample are given in [Table 2](#). Sample depths ranged from 0.3–  
58  
59 395 10.8 m below the seafloor. Samples were selected from intervals of differing colour and  
60

396 mineralogy, and included red, brown and yellow Fe-oxyhydroxide-rich layers, greenish Fe-  
397 silicate-rich layers, purplish metal sulphide-rich layers and (uncommon) whitish-grey anhydrite-  
398 rich layers. Apart from the anhydrite-rich layers, which contain coarse crystals, the sediments  
399 ranged from soft muds (greater depths) to gelatinous oozes (uppermost few metres). Some of  
400 the Fe oxyhydroxide-rich layers are colour laminated on a mm-scale due to differing  
401 proportions of phases such as goethite, limonite and lepidocrocite, and locally Fe-silicate clays  
402 and Mn-oxyhydroxides (Laurila et al., 2015). All samples but two were from the upper three  
403 sedimentary units as defined by Bäcker and Richter (1973), that is, units AM, SU2 and CO (Fig.  
404 4). In the Southwest Basin, using the classification of Blanc et al. (1998), all cores but one  
405 belong to their Upper (U) unit, which corresponds to the AM and SU2 zones of Bäcker and  
406 Richter (1973). The exception is Core 274 in the Southwest Basin, which intersected the SU1  
407 and DOP zones at, 7.5 m and 10.2 m, respectively, below the seafloor (the hole terminated at  
408 11.0 m, still in sediment). Given that the boundary between the upper Pleistocene and  
409 Holocene occurs at the top of the DOP unit (Anschutz, 2015), all analysed samples in this study,  
410 apart from the lowest sample in Core 274, are thus of Holocene age (<11.7 ka).

## 2.2. Major elements

414 Detailed chemical analyses for 43 samples of metalliferous sediment from the Atlantis II Deep  
415 are given in [Supplementary Data Table 1](#). Although the sediments were washed with distilled  
416 water prior to analysis, some salts remained, as indicated by high Na + Cl contents of 2–10 %  
417 ([Supplementary Data Table 1](#)). The main chemical features of the bulk sediments are the high  
418 contents of Fe (commonly 25–55 wt % Fe<sub>2</sub>O<sub>3</sub>t), combined with very low amounts of detritally-  
419 supplied elements such as Al (typically ≤2 % wt Al<sub>2</sub>O<sub>3</sub>). As shown in [Fig. 7](#), the Atlantis II Deep  
420 sediments have Fe/Mn ratios higher than those of metalliferous sediments on the spreading  
421 axis of the southern East Pacific Rise (SEPR) and most plume particulates from the northern  
422 East Pacific Rise (NEPR), and much higher than those of slowly accumulating, deep-sea  
423 ferromanganese nodules. A few samples from the Atlantis II Deep are notably enriched in Mg  
424 (talc-bearing), Ca (anhydrite) or Mn (Mn oxides) relative to most samples from the Deep. Our  
425 major-element results are broadly comparable to those reported by Laurila et al. (2015), who

426 analysed samples from a different set of cores, which included the Southwest Basin, East Basin  
427 and West Basin (our samples are mainly from the Southwest Basin).

428  
429 Iron in the Atlantis II Deep sediments occurs in both  $\text{Fe}^{2+}$  and  $\text{Fe}^{3+}$  states, in the form of  
430 oxyhydroxides (goethite, limonite, hematite), Fe-rich hydrous silicates, and iron sulphides. The  
431 proportions of these phases vary vertically and laterally within the Deep (Fig. 4). The  $\text{Al}_2\text{O}_3$   
432 content of the metalliferous sediments, which serves as a proxy for the siliciclastic detrital  
433 component, ranges from 0.2–4.0 wt %. Other detritally supplied elements such as Ti and Zr  
434 show positive correlations with  $\text{Al}_2\text{O}_3$  (Fig. 8a, b).

435  
436 The main source of the detrital component is wind-borne dust derived from the arid  
437 continental terranes that flank the Red Sea (Stein et al., 2007; Palchan et al., 2018). Detrital  
438 material has a strong influence on the REE content of the metalliferous sediments, as shown by  
439 a plot of  $\Sigma\text{REE}$  versus  $\text{Al}_2\text{O}_3$  (Fig. 8c), and as previously reported by Laurila et al. (2014a). Most  
440 of the metalliferous sediments contain 25–55 wt %  $\text{Fe}_2\text{O}_3$  and 15–30 wt %  $\text{SiO}_2$  (Fig. 8d). Much  
441 of this silica is probably hydrothermal in origin, although some could be supplied by dissolution  
442 of detrital quartz and biogenic silica (radiolaria, diatoms) in the sediments, based on  
443 calculations by Anschutz and Blanc (1995a). Several samples are notably enriched either in  
444 nontronite, a hydrous, low-Al,  $\text{Fe}^{+3}$ -rich silicate, or in Fe-oxyhydroxides, based on chemical  
445 trends (Fig. 8d). Nontronite is formed in the lowest brine layer of the Atlantis II Deep, as silica of  
446 mainly hydrothermal origin combines with hydrothermal Fe-oxyhydroxides (cf. Schwertmann et  
447 al., 1998; Taitel-Goldman et al., 2009; Cuadros et al., 2018).

### 448 449 2.3. Metals

450  
451 Metalliferous sediments in the Atlantis II Deep are enriched in base and precious metals, as  
452 documented by numerous studies since the 1970s (e.g., Bäcker and Richter, 1973; Shanks and  
453 Bischoff, 1977; Pottorf and Barnes, 1983; Mustafa et al., 1984; Oudin, 1987; Guney et al., 1988;  
454 Laurila et al., 2014a). Zinc, Cu and Pb contents in the Southwest Basin are up to 15 wt %, 3 wt %  
455 and 0.3 wt % respectively, while Au and Ag reach 5 ppm and 300 ppm, respectively. Sediments  
456 are enriched in most trace metals, containing up to 900 ppm As, 500 ppm Mo, 400 ppm Co, 120

1 457 ppm Ni, 200 ppm Sb, 50 ppm Tl and 7 ppm Hg (Oudin, 1987; Laurila et al., 2014a;  
2 458 [Supplementary Data Table 1](#)).

3 459  
4  
5 460 In the present sample set, Au correlates well with Cu ([Fig. 9a](#)), and also appears to correlate  
6  
7 461 with Zn, apart from samples with < 1 ppm Au ([Fig. 9b](#)). This suggests that the gold is associated  
8  
9 462 with chalcopyrite and sphalerite, although it is not necessarily hosted solely by these sulphides.  
10  
11 463 Overall, gold correlates positively with total sulphur (not shown); samples consisting mainly of  
12  
13 464 Fe oxyhydroxides contain low Au (<1 ppm) ([Fig. 9](#)). According to Laurila et al. (2014a, 2015), Au  
14  
15 465 shows a general association with Cu-Zn and Fe sulphides in vent-proximal sediments, and is also  
16  
17 466 enriched (together with As) in diagenetic pyrite in distal sediments. Silver correlates best with  
18  
19 467 Cu ([Fig. 9c](#)), whereas Cd correlates strongly with Zn ([Fig. 9d](#)).

20  
21 468  
22  
23 469 Although not shown, moderate positive correlations also exist between the following metal  
24  
25 470 pairs: Ag–Pb, Ag–Zn, Co–Cu, Sb–Cu, and U–Fe. Silver therefore is associated with all three  
26  
27 471 sulphides (Cu–Pb–Zn), whereas Sb and Co are mainly associated with Cu sulphide. Similar  
28  
29 472 correlations were found by Laurila et al. (2014a), who considered all of these metals to be  
30  
31 473 dominantly hydrothermal in origin, with the exception of U. The U–Fe correlation results mainly  
32  
33 474 from the absorption of seawater U by hydrothermal Fe-bearing oxyhydroxides, as originally  
34  
35 475 proposed by Ku (1969). According to Laurila et al. (2014a), Ni, Cr and V (not shown here) are  
36  
37 476 associated mainly with diagenetic pyrite, are largely of non-hydrothermal origin, and were  
38  
39 477 mainly sourced from, respectively, biological material, detrital siliciclastics, and seawater.

40 478  
41  
42 479 In the present sample set, the bulk-sediment ratio of Ag to Au is about 40, similar to the  
43  
44 480 average value of 50 reported by Oudin (1987), while the ratios of Zn to Cd, and Pb to Ag, are  
45  
46 481 about 330 and 10, respectively. As noted above, trace metals correlate mainly with the  
47  
48 482 proportion of Cu–Zn–Pb sulphides, which formed either as primary precipitates on the seafloor  
49  
50 483 or during early diagenesis (Oudin, 1987; Laurila et al., 2014a). Metals initially brought into the  
51  
52 484 Atlantis II Deep by hot saline fluids can be precipitated in the lower brine layer either as  
53  
54 485 sulphides, or by absorption onto Si-Fe-OOH particles. During burial, metals associated with the  
55  
56 486 Si-Fe-OOH particles are released and incorporated into diagenetic sulphides (Anschutz et al.,

2000; Laurila et al., 2014a). Possible sources of metals (basaltic crust, continental detritus, evaporites) are discussed in Sections 2.5 and 5.2, where Nd-Sr-Pb isotopic data are assessed.

#### 2.4. Rare-earth elements

The REE contents of 39 samples of metalliferous sediment from the Southwest and West basins of the Atlantis II Deep are given in Table 2. Shale-normalized REE patterns are nearly flat or slightly depleted in the light REE, and display moderate to large positive Eu anomalies (2–4 and 4–7, respectively; Figs. 10, 11); the Eu anomaly is defined as  $Eu_N/Eu_N^*$ , where  $Eu_N^* = (Sm_N * Gd_N)^{0.5}$  and N is the shale-normalized value. Total REE contents are very low, ranging from 2–20 ppm for most samples. Exceptions are three anhydrite-rich layers with < 2 ppm  $\Sigma$ REE, and three siliciclastic-bearing sediments with 24–112 ppm  $\Sigma$ REE. These results are broadly similar to those previously reported for metalliferous sediments in various parts of the Deep (Courtois and Treuil, 1977; Oudin and Cocherie, 1988; Cocherie et al., 1994; Laurila et al., 2014b). One difference, however, is the presence, in the data sets of Oudin and Cocherie (1988) and Cocherie et al. (1994), of several samples with high contents of P<sub>2</sub>O<sub>5</sub> and REEs (up to 1.8 wt % P<sub>2</sub>O<sub>5</sub> and 1000 ppm  $\Sigma$ REE). This association was ascribed to the presence of phosphatic fish debris that had scavenged REEs from hydrothermal fluids after deposition on the floor of the Deep (Oudin and Cocherie, 1988). Although our study lacks P<sub>2</sub>O<sub>5</sub> data, most of the 100 samples reported by Laurila et al. (2014b) contained only 0.1–0.5 wt % P<sub>2</sub>O<sub>5</sub> (maximum of 0.77 wt % P<sub>2</sub>O<sub>5</sub>). As shown by Laurila et al. (2014b), variations in REE abundances are instead largely due to the amount of siliciclastic material in each sample (cf. Fig. 8c), whereas variations in the Eu anomaly reflect the chemical state of the brine from which the metalliferous particulates precipitated.

Figure 10 shows shale-normalized REE patterns for samples from different depths and chemical facies in a single core (274). Also shown for comparison are data for three types of vent fluids from the Mid-Atlantic Ridge (after Bau and Dulski, 1999). Large positive Eu anomalies and low La/Yb ratios are typical of high-temperature vent fluids from various types of spreading ridges (Michard and Albarede, 1986; Mitra et al., 1994). In Fig. 10, four of the five sediment samples in Core 274 have nearly flat REE patterns with moderate positive Eu anomalies, differing only in

1 518 absolute contents of REEs. The exception is a near-surface sample (depth of 1.0 m), which has  
2 519 the highest content of REEs, and also the smallest positive Eu anomaly. These features suggest  
3  
4 520 that the shallow sample at 1.0 m depth is enriched in detrital material, given that Holocene  
5  
6 521 detritus entering the Red Sea (as aeolian dust) has a high REE content and nearly flat REE  
7  
8 522 pattern (Greaves et al., 1994; Palchan et al., 2013). The REE pattern of the sample at 1.0 m also  
9  
10 523 closely resembles that of biodetritral sediment from a Red Sea core (1016) taken outside of any  
11  
12 524 known deeps (Pierret et al., 2010). Based on the very small Eu anomaly of the sample at 1.0 m,  
13  
14 525 the hydrothermal component is minor.

15 526  
16  
17 527 The Southwest Basin is considered, on the basis of mineralogy (anhydrite, hematite) and the  
18  
19 528 presence of epigenetic veins and high-temperature fluid inclusions, to be the main site of  
20  
21 529 Holocene hydrothermal input to the Atlantis II Deep (Zierenberg and Shanks, 1983; Ramboz et  
22  
23 530 al., 1988; Laurila et al., 2014a, b). REE patterns for metalliferous sediments from the Southwest  
24  
25 531 Basin are shown in Fig. 11a–d. All patterns but one have a large positive Eu anomaly, and in  
26  
27 532 most cases, show slight depletion in light relative to heavy REEs. The exception is sample 397-4  
28  
29 533 from the eastern part of the Southwest Basin (Fig. 11d). This sample is notably enriched in total  
30  
31 534 REEs due to its high content of aluminosilicate detritus, but still displays a positive Eu anomaly,  
32  
33 535 although not as large as those of the purest metalliferous sediments (see also Fig. 11f).

34 536  
35  
36 537 Core 436 is located on the eastern side of the West Basin, some 3 km north of the Southwest  
37  
38 538 Basin (Fig. 6). If the main input of hydrothermal fluids in the Atlantis II Deep is in the southern  
39  
40 539 portion of the Southwest Basin, as suggested by metal distribution patterns (Laurila et al.,  
41  
42 540 2014a), then Core 436 would represent the most “distal” site in our sample set. Four samples  
43  
44 541 from depths of about 2.2 to 10.0 m have moderate Eu anomalies (Fig. 11e). These four samples  
45  
46 542 differ significantly in mineralogical composition, but share essentially the same REE pattern,  
47  
48 543 which is similar to the REE pattern of most sediments in the Southwest Basin. Based on Eu  
49  
50 544 anomalies, the hydrothermal signal in the West Basin is, however, weaker.

51 545  
52  
53 546 The effect of aluminosilicate detritus on the bulk REE patterns of metalliferous sediments in the  
54  
55 547 Atlantis II Deep is shown in Fig. 11f, for samples containing 0.4 to 3.9 wt % Al<sub>2</sub>O<sub>3</sub>. As the amount  
56  
57 548 of detritus increases, REE patterns are shifted to higher absolute levels, while the positive Eu  
58  
59  
60  
61  
62

549 anomalies become smaller in size. The sample having the highest detrital content shows a  
550 minor depletion in light relative to heavy REE. Similar light REE depletion is also seen in sample  
551 274-1 (Fig. 10), which contains the largest detrital component in our data set ( $\text{Al}_2\text{O}_3$  estimated  
552 as 7 wt %; see Section 2.5), and in hemipelagic (biodeutral) sediment from the central Red Sea  
553 (Pierret et al., 2010). The light REE depletion is presumably due to a small difference in the  
554 composition of the aeolian dust entering the Red Sea relative to PAAS (post-Archean Australian  
555 shale: Taylor and McLennan, 1985).

556  
557 The detrital contribution of REE to the bulk sediment can be calculated using the content of a  
558 lithophile element such as Al, Ti, Zr, Th or Sc, and an assumed end-member REE pattern for the  
559 detrital component. Laurila et al. (2014b) used the average REE pattern of their most Al-rich  
560 samples (ca. 7 wt %  $\text{Al}_2\text{O}_3$ ) as a proxy for this component, which when subtracted from the bulk  
561 sediment REE pattern should yield an estimate of the ‘residual’ hydrothermal REE pattern. The  
562 calculated hydrothermal REE patterns were generally nearly flat, with Eu anomalies being  
563 slightly more positive than those of the bulk metalliferous sediment. However, it is conceivable  
564 that the Al-rich samples used by Laurila et al. (2014b) contained a small hydrothermal  
565 component, as they were also taken from the Atlantis II Deep. In the present study, a similar  
566 approach was adopted, but differed in using the carbonate-free fraction ( $\text{Al}_2\text{O}_3 = 13.8\%$ ,  $\Sigma\text{REE} =$   
567 180 ppm, Nd = 34.4 ppm) of Holocene sediment from Core KL-23 in the northern Red Sea  
568 (Palchan et al., 2013) as a proxy for the detrital REE component. The calculated hydrothermal  
569 REE patterns (not shown) are flatter than the calculated patterns of Laurila et al. (2014b) but  
570 display the same moderate to large positive Eu anomalies. Such calculations are, however, very  
571 sensitive to the percentage of detritus in the bulk sediment, and to the REE pattern of this  
572 detritus, both of which can only be estimated. Because the metalliferous sediments have very  
573 low REE contents to begin with, removal of the estimated detrital REE component can leave  
574 residual hydrothermal values that are close to zero or even slightly negative for most of the  
575 REEs, thus producing irregular “baselines” to the patterns, although the positive Eu anomalies  
576 remain well defined.

## 577 578 2.5. Nd isotopes

579

1  
2 580 The Nd isotope ratios of oceanic sediments reflect the relative contributions from old  
3  
4 581 continental detritus (supplied by wind and rivers), young volcanic detritus (oceanic ridges and  
5  
6 582 island arcs), biogenic fallout, and hydrothermal plume-derived authigenic precipitates (mainly  
7  
8 583 Fe-Mn-oxyhydroxides). Biogenic components such as fish debris (Grandjean et al., 1987; Martin  
9  
10 584 and Haley, 2000) and foraminifera (Palmer and Elderfield, 1985) normally carry the Nd isotopic  
11  
12 585 signatures of ambient seawater, and also concentrate Nd relative to its very low levels in  
13  
14 586 ambient seawater. Metalliferous sediments deposited from plumes more than 10 km from  
15  
16 587 ridge-axial vents carry a seawater Nd isotopic signature due to efficient scavenging of REEs  
17  
18 588 from seawater (Halliday et al., 1992). Sediments deposited within 10 kilometres of the vents  
19  
20 589 can, however, contain a small component of basaltic-hydrothermal Nd (German et al., 1993;  
21  
22 590 Chavagnac et al., 2006; Sun et al., 2018).

591

23  
24  
25 592 Potential sources of Nd in the metalliferous sediments of the Atlantis II Deep include underlying  
26  
27 593 basaltic oceanic crust, flanking Miocene siliciclastic rocks and evaporites, and Pliocene–  
28  
29 594 Pleistocene hemipelagic sediments that overlie the Miocene sequence (Fig. 3). Literature data  
30  
31 595 on the Nd isotopic ratios and Nd contents of various potential source rocks and hydrothermal  
32  
33 596 fluids are presented and discussed in more detail, together with analogous data for Sr and Pb,  
34  
35 597 in Section 5.2, below). The brine layers within the Atlantis II Deep from which the chemical  
36  
37 598 sediments precipitated exhibit rather low and stable temperatures (currently 44°C to 68°C;  
38  
39 599 Anschutz, 2015). However, the fluids that brought metals and Nd into the basin may have  
40  
41 600 reached temperatures of 300°C, based on fluid inclusion data for veins that cut the  
42  
43 601 metalliferous sediments of the Southwest Basin (Ramboz et al., 1988).

602

44  
45  
46 603 As a first approximation, we assume that the Nd in the metalliferous sediments is derived from  
47  
48 604 mixtures of leached radiogenic basalt on the one hand, and unradiogenic terrigenous material  
49  
50 605 and/or seawater on the other. Given that high-temperature fluids venting at spreading ridges  
51  
52 606 have essentially the same  $\epsilon_{Nd}$  values as underlying basalts (Hegner and Tatsumoto, 1987;  
53  
54 607 Hinkley and Tatsumoto, 1987), we use an  $\epsilon_{Nd}$  value of +9.7 for our hydrothermal end-member,  
55  
56 608 based on the average value for two basalts from the Atlantis II Deep at 21.4°N (Volker et al.,  
57  
58 609 1993). For comparison, seven basalts from the axis of the central to northern Red Sea

610 (18.15°N–25.55°N) have an average  $\epsilon\text{Nd}$  value of +8.4, and a layer of basaltic glass in a  
611 sediment core from the Shaban Deep in the northern Red Sea (26°N; Fig. 2a) has a value of +8.5  
612 (Cocherie et al., 1994). The  $\epsilon\text{Nd}$  value of +9.7 is preferred here for the hydrothermal end-  
613 member as it leads to a more conservative estimate of the proportion of basaltic Nd in the  
614 Atlantis II metalliferous sediments.

615  
616 Unradiogenic Nd could, in theory, be contributed to the metalliferous sediments of the Atlantis  
617 II Deep by the hemipelagic sediment that slowly accumulates throughout the Red Sea. This  
618 hemipelagic sediment includes both fine-grained terrigenous material (aeolian dust) and  
619 biogenic grains such as planktonic tests and fish teeth (Arz et al., 2003; Coulibaly et al., 2006).  
620 Biogenic material initially concentrates Nd relative to seawater levels but maintains the Nd  
621 isotopic composition of seawater. In the Shaban Deep of the northern Red Sea (Fig. 2a), five  
622 samples from a “biodeutral” sediment core have an average  $\epsilon\text{Nd}$  value of  $-4.9 \pm 0.2$  which is  
623 thought to be representative of average seawater in that region (Cocherie et al., 1994).  
624 Terrigenous dust settling into northern Red Sea sediments over the last 10 kyr has a similar Nd  
625 isotopic composition, with an average  $\epsilon\text{Nd}$  value of -5.8 (Palchan et al., 2013). We have  
626 therefore used an intermediate  $\epsilon\text{Nd}$  value of -5.3 as the unradiogenic end-member for the  
627 Atlantis II Deep mixing model. The  $\epsilon\text{Nd}$  value of normal Red Sea water has not been measured  
628 directly, but eastern Mediterranean seawater at various depths has  $\epsilon\text{Nd}$  values of -7 to -6 (Frost  
629 et al., 1986; Tachikawa et al., 2004). The use of an  $\epsilon\text{Nd}$  value of -5.3 for the unradiogenic end-  
630 member, rather than a more negative number, leads to more conservative estimates of the  
631 percentage of basaltic Nd in the metalliferous sediments in the mixing model discussed below.

632  
633 In the present study, 14 samples of metalliferous sediment from the Atlantis II Deep have  $\epsilon\text{Nd}$   
634 values of -2.7 to +0.1 (Table 3). Ten of these samples show a restricted range of values from -  
635 2.24 to -1.48. Based on a simple two-phase mixing model between basaltic-hydrothermal and  
636 terrigenous/seawater end-members, the metalliferous sediments contain 17–36 % basaltic-  
637 hydrothermal Nd (Table 3). The remaining 64–83 % Nd is probably contributed mainly by  
638 terrigenous material (as the Nd content of normal seawater is orders of magnitude lower).  
639 Assuming that the 0.5–1.0 wt %  $\text{Al}_2\text{O}_3$  content of the purest metalliferous sediments is due  
640 entirely to a component of siliciclastic detritus containing 13.8 %  $\text{Al}_2\text{O}_3$  and 36 ppm Nd (5–6 ka

1 641 dust: Palchan et al., 2013), this component could contribute about 1.3 to 2.6 ppm Nd to the  
2 642 bulk sediment, or 40–100 % of the total Nd (based on Nd data from the present study; and  
3 643 Laurila, 2015). Thus, even a small terrigenous (dust) component within the metalliferous  
4 644 sediments can adequately account for the appreciable unradiogenic component implied by the  
5 645  $\epsilon$ Nd mixing model.

10 646  
11 647 The terrigenous component must mix with a low-Nd hydrothermal component having  $\epsilon$ Nd  
12 648 values in the -2 to +2 range in order to produce the  $\epsilon$ Nd values and Nd concentrations observed  
13 649 in the bulk metalliferous sediments. The low-Nd hydrothermal component could be produced  
14 650 by mixing between high-temperature fluid having a basaltic  $\epsilon$ Nd value (e.g., +9) and much  
15 651 lower-temperature seawater or brine having an  $\epsilon$ Nd value of about -5. Unfortunately, there are  
16 652 no data on the Nd contents of hydrothermal fluids or brines in the Atlantis II Deep, although  
17 653 even high-temperature fluids at vent sites on open-ocean ridges have very low Nd contents of  
18 654 <0.01 ppm (lower-temperature fluids would contain even less Nd). Thus, the metalliferous  
19 655 precipitates must concentrate Nd by a few orders of magnitude relative to the source  
20 656 hydrothermal fluid (which itself contains both basaltic and seawater Nd). In theory, absorption  
21 657 of Nd by precipitates could occur either in the brine pool or shortly after their deposition on the  
22 658 seafloor. Mixing of a small component of terrigenous dust with the precipitates then produces  
23 659 an  $\epsilon$ Nd trend towards the terrigenous dust. Although unmodified seawater in theory could  
24 660 contribute some Nd to the metalliferous precipitates, seawater Nd would have an  $\epsilon$ Nd value  
25 661 similar to that of detritus entering the Red Sea, and therefore would not be isotopically  
26 662 distinguishable from the Nd contributed by the detritus.

27 663  
28 664 The ten samples of metalliferous sediment having  $\epsilon$ Nd values of -2.24 to -1.48 all show  
29 665 moderate to large, positive Eu anomalies (Fig. 12), even though they contain only 20–25 %  
30 666 basaltic Nd according to the simple mixing model. The ten samples represent various chemical  
31 667 facies of metalliferous sediment (given in Table 3). Three samples from depths of 1.0 to 9.5 m in  
32 668 Core 274 (Southwest Basin) have  $\epsilon$ Nd values of -2.48 to -1.76 (Fig. 13a, Table 3), with the  
33 669 shallowest sample having the most negative  $\epsilon$ Nd value. This sample appears to have the  
34 670 highest terrigenous content in the entire data set (ca. 7 wt %  $\text{Al}_2\text{O}_3$ , and based on Zr and Th  
35 671 contents and their positive correlations with  $\text{Al}_2\text{O}_3$  in the overall data set; Supplementary Data

672 [Table 1](#)). Nonetheless, this sample still contains 19 % basaltic-hydrothermal Nd based on our  
1  
2 673 simple mixing model.

3  
4 674  
5  
6 675 The two highest  $\epsilon\text{Nd}$  values in the data set (+0.12 and -0.68) are for mineralogically distinct  
7  
8 676 samples dominated by anhydrite and talc, respectively ([Fig. 13b](#); [Table 3](#)). Based on the mixing  
9  
10 677 model, these two samples contain the highest proportion of basaltic-hydrothermal Nd (31–36  
11  
12 678 %). The increased basaltic-hydrothermal component conceivably could be caused by a later  
13  
14 679 phase of much hotter fluid passing through the sediment. Anhydrite and talc occur sporadically  
15  
16 680 within the Southwest Basin as veins and as replacements within the metalliferous sediments  
17  
18 681 and are inferred to have formed from high-temperature fluids (Zierenberg and Shanks, 1983;  
19  
20 682 Oudin et al., 1984; Ramboz et al., 1988).

21 683  
22  
23 684 The magnitude of the positive Eu anomaly in the metalliferous sediments generally increases as  
24  
25 685 the inferred component of basaltic-hydrothermal Nd increases ([Fig. 14](#)). However, several  
26  
27 686 samples show little correlation. A strict correlation is not expected, as the height of the Eu  
28  
29 687 anomaly also depends on the level of the flanking REEs – an increase in the proportion of  
30  
31 688 siliciclastic detritus in the bulk sediment will raise the “background” REE values, and thus  
32  
33 689 decrease the relative height of the Eu anomaly. This effect, however, is probably minor in most  
34  
35 690 of the metalliferous sediments, as their contents of detritus are uniformly low (<2 wt %  $\text{Al}_2\text{O}_3$ ).

36  
37 691  
38  
39 692 Two biodetrital-rich samples, one from outside the Atlantis II Deep, have Eu anomalies close to  
40  
41 693 that of seawater (small blue-filled squares in [Fig. 14](#)), but contain about 15 % basaltic Nd,  
42  
43 694 presumably due to a small metalliferous component. One of these samples (KS-01: 604 cm) is  
44  
45 695 from the Shaban Deep and contains goethite, whereas the other (198: 745–750 cm) is from the  
46  
47 696 detrital-oxide-pyrite facies of the Atlantis II Deep (Cocherie et al., 1994). The lack of positive Eu  
48  
49 697 anomalies in these two samples suggests that the metalliferous component precipitated from  
50  
51 698 relatively oxidizing brines, consistent with their overall mineralogy.

52 699  
53  
54 700 Two samples from the Atlantis II Deep with high contents of phosphatic fish debris (Cocherie et  
55  
56 701 al., 1994) plot well to the right of the general metalliferous sediment trend in [Fig. 14](#). Oudin and  
57  
58 702 Cocherie (1988) and Cocherie et al. (1994) have shown that where phosphatic fish debris is  
59  
60

703 present in the sediments, it can preferentially scavenge REEs from hydrothermal fluids in  
704 porewaters or overlying brine, leading to an increase in the proportion of basaltic Nd within the  
705 sediments (this process eliminates the original seawater Nd signature of the fish debris).

706  
707 In Fig. 15, calculated proportions of basaltic Nd in each metalliferous sediment sample are  
708 plotted on a map of the Atlantis II Deep, together with calculated Eu anomalies. Percentages of  
709 basaltic Nd are represented by bubble size, and values of Eu anomalies by red numbers (data in  
710 Table 3). The samples come from a range of depths (1.0–9.7 m) and represent a variety of ages,  
711 although all are younger than 12 ka, apart from one sample from the DOP facies (Core 71). No  
712 spatial trend within the basin is obvious in either  $\epsilon\text{Nd}$  or Eu anomaly, probably because the  
713 samples represent different stratigraphic levels and therefore likely formed under differing  
714 conditions of temperature, Eh and basin chemistry. However, it is worth noting that the two  
715 samples with the largest basaltic Nd component are from the southern and northern margins of  
716 the Southwest Basin (Cores 64 and 367, respectively). A higher proportion of basaltic Nd could  
717 conceivably be the result of proximity to a site of hydrothermal discharge. Higher-temperature  
718 phases such as talc and hematite have been found in cores from, respectively, the northern and  
719 southern margins of the Southwest Basin (Zierenberg and Shanks, 1983), although these phases  
720 are not present in the samples mentioned above. The sample with the smallest proportion of  
721 basaltic Nd in our data set (Fig. 15) is from the middle of the West Basin (sample 436-6).

## 2.6. Other anoxic basins

725 Anoxic, brine-filled basins are common on the continental slopes of passive margins, for  
726 example the Orca Basin in the northern Gulf of Mexico (Fig. 1), where up to 180 m of low-T (ca.  
727 6°C), very saline brine is present at seafloor depths of >2200 m (Shokes et al., 1977; Trabant  
728 and Presley, 1978; Sheu and Presley, 1986; Sheu, 1990; Pilcher and Blumstein, 2007; Schijf,  
729 2007). Sediments in the Orca Basin consist of laminated carbonaceous muds and siltstones,  
730 which contain iron sulphides (Hurtgen et al., 1999; Tribovillard et al., 2008). Brines are anoxic  
731 and enriched in Fe and Mn relative to normal bottom waters (Trefry et al., 1984). Where the  
732 top of the brine layer intersects the basin margin, additional reddish, Fe-oxide-bearing layers  
733 are deposited. As part of the present study, we obtained REE data for three 1-cm-long samples

1 734 from the top 7 cm of Core 87-G-2 from the margin of the Orca Basin. The samples consisted of  
2 735 dark muds with faint laminations. REE patterns are very close to that of average shale (PAAS),  
3  
4 736 with no Ce or Eu anomalies (data in [Table 3](#)). Thus, there is no obvious normal-seawater or  
5  
6 737 volcanic-hydrothermal contribution to the REE signature, which appears to result instead from  
7  
8 738 fine-grained terrigenous detritus (minor organic material is also present), at least in the upper  
9  
10 739 several centimetres of the core.

11 740  
12  
13  
14 741 Several seafloor deeps in the Mediterranean Sea contain strongly saline, anoxic bottom brines,  
15  
16 742 some of which, e.g the Bannock, Tyro and Urania Basins, contain significant amounts of H<sub>2</sub>S and  
17  
18 743 thus are euxinic brines (Luther et al., 1990; De Lange et al., 1990; Cita, 1991; Vengosh et al.,  
19  
20 744 1999). In the Bannock Basin ([Fig. 1](#)), the brine layer is some 450 m thick and has a temperature  
21  
22 745 of 14–15°C. There is no evidence of volcanism in the region. Normal seawater above the  
23  
24 746 Bannock brine layer shows a large negative Ce anomaly, as expected, but the brine itself carries  
25  
26 747 a positive Ce anomaly (Schijf et al., 1995). Interestingly, the brine, although reduced, lacks a  
27  
28 748 positive Eu anomaly (which is also the case for the Orca Basin brine). This suggests that even in  
29  
30 749 euxinic brines, a positive Eu anomaly is not generated unless there has been some input of a  
31  
32 750 hydrothermal fluid that previously reacted with volcanic basement – as for example in the  
33  
34 751 Atlantis II Deep. To our knowledge, no REE data have been reported as yet for the sediments of  
35  
36 752 the Bannock, Tyro and Urania Basins.

37 753  
38  
39 754 In the Thetis Deep of the Red Sea (location in [Fig. 1a](#)), the upper 1 m of metalliferous  
40  
41 755 sediments, which consist mainly of Fe-oxyhydroxides, have strong positive Eu anomalies  
42  
43 756 (Butuzova and Lyapunov, 1995; Pierret et al., 2010). However, there is no brine within this  
44  
45 757 deep, only normal seawater. The chemical precipitates (and the positive Eu anomalies) of the  
46  
47 758 Thetis Deep are interpreted to result from the rapid cooling of hydrothermal fluids that  
48  
49 759 discharged into a topographic low and mixed with seawater (Pierret et al., 2010). In the Kebrit  
50  
51 760 Deep of the Red Sea ([Fig. 1a](#)), small massive sulphide chimneys with common bituminous  
52  
53 761 impregnations have been recovered by dredging; these lie within a low-temperature, H<sub>2</sub>S-  
54  
55 762 bearing brine layer (Blum and Puchelt, 1991). Occasional limonite-rich sediment layers are also  
56  
57 763 present within cored, near-surface hemipelagic sediments of this deep (Botz et al., 2007). No  
58  
59 764 REE data, or Nd-Sr-Pb isotopic data, have been reported from the Kebrit Deep.

765

### 3. Metalliferous Sediments in Open Ocean Basins – East Pacific Rise DSDP Leg 92 Transect

#### 3.1. Tectonic setting and stratigraphy

DSDP Leg 92 drilled at four main locations to the west of the EPR (Figs. 1, 16; Sites 597 – 602). At these sites, Fe-Mn-oxyhydroxide-bearing, nannofossil oozes up to 50 m thick lie on basaltic crust ranging in age from 28 Ma to 3 Ma (Rea and Leinen, 1986). The metalliferous component of the sediments consists of fine particulates supplied by dilute hydrothermal plumes that drift westwards from the EPR for up to a few thousand kilometres (Lupton and Craig, 1981; Baker et al. 1995; Resling et al., 2015; Fitzsimmons et al., 2017). As the metalliferous sediments are buried, the Fe-Mn-oxyhydroxides are diagenetically transformed to goethite and minor clay minerals (Kastner, 1986; Poulton and Canfield, 2006). There is no evidence for diagenetic loss of Mn (or P) from the sediments with burial (Lyle, 1986; Poulton and Canfield, 2006). Simplified stratigraphic columns for the four Leg 92 holes are shown in Fig. 17, together with locations of the samples analysed in the present study. Detailed stratigraphic and sedimentological features of the Leg 92 drill cores are given in Leinen, Rea et al. (1986). Colour photographs of all cores are available at <http://deepseadrilling.org/cores/leg092/>.

Although the sampled Leg 92 metalliferous sediments range in age from about 27 Ma to 0–2 Ma, each sample was initially deposited at surface. The deepest samples in each hole were deposited closest to the axis of the EPR, with the shallowest samples deposited farthest from the axis. The age of the lowest sediment in each of the sampled holes corresponds to, or is slightly younger than the time at which the underlying basaltic crust was generated at the EPR axis. Upward changes in chemical composition in each hole reflect continuous plate motion away from the East Pacific Rise (Rea and Leinen, 1986; Lyle, 1986). With increasing distance from the axis, the proportion of laterally drifting hydrothermal precipitates that settle into the sediment will change, as will the proportion of biogenic tests, the latter varying according to surface productivity as well as depth of the seafloor relative to the lysocline. One of the major chemical changes that occurs upsection in Leg 92 metalliferous sediment (i.e., with increasing

794 palaeo-distance from the ridge axis) is an increase in the Fe/Mn ratio at about 200–300 km  
795 from the axis; this is attributed to a relative decrease in Mn as a result of chemical and  
796 sedimentation processes in the more ridge-proximal part of the plume (Lyle, 1986; Marchig and  
797 Erzinger, 1986).

798  
799 Major- and trace-element data for Leg 92 sediments are presented in [Supplementary Data](#)  
800 [Table 2](#); REE data are listed in [Table 4](#). Due to the large component of biogenic carbonate in  
801 these sediments (78–97%, Barrett et al., 1987), all analyses are reported here on a carbonate-  
802 free basis. Although this carbonate-free residue is mainly composed of metalliferous sediment  
803 (Fe-Mn oxyhydroxides), a minor terrigenous component is also present in the form of aeolian  
804 dust derived from South America (Rea and Leinen, 1986).

805  
806 Previous chemical studies of the Leg 92 sediments, including REEs, have been carried out by  
807 Lyle (1986), Marchig and Erzinger (1986), Ruhlin and Owen (1986), and Barrett and Jarvis  
808 (1988). The REE analyses in [Table 4 of the present paper](#) are for a different set of samples than  
809 those reported by Barrett and Jarvis (1988), but cover the same range of lithologies. Nd-  
810 isotopic data for the Leg 92 sediments have been reported by Halliday et al. (1992), while Pb-Sr-  
811 compositions were determined by Barrett et al. (1986, 1987); results are discussed in Sections  
812 3.4 and 5.2, respectively.

813  
814 The compositional range of the carbonate-free fraction of the Leg 92 metalliferous sediments,  
815 in terms of molar proportions of Fe, Mn and Al normalized to 100 %, is shown [Fig. 18](#). Many of  
816 the Leg 92 samples cluster around the average value of surface metalliferous sediments on the  
817 southern EPR (SEPR: Marchig and Erzinger, 1986). These latter sediments, which come from  
818 within 50 km of the spreading axis, can be considered a compositional end-member for  
819 precipitates that settle from low-temperature hydrothermal plumes in open oxidized oceans. It  
820 is of interest that both the Leg 92 and SEPR metalliferous sediments contain a higher  
821 proportion of Mn than sediments derived from the SEPR axial plume, which are dominated by  
822 Fe-rich particulates. The “additional” Mn was presumably either adsorbed onto initial Fe-rich  
823 particulates within the plume as it drifted westwards, or adsorbed from seawater after the  
824 particulates settled to the seafloor.

825  
1  
2 826 Plume particulates along the axis of the northern EPR (NEPR) show a compositional trend  
3  
4 827 extending from an Fe-dominated, SEPR plume-type end-member towards on-axis water column  
5  
6 828 particulates (Fig. 18), the latter representing re-suspended bottom sediments (Sherrell et al.,  
7  
8 829 1999). The on-axis particulates themselves appear to contain a component of normal pelagic  
9  
10 830 clay. All but five of the Leg 92 metalliferous sediments are enriched in Mn relative to the NEPR  
11  
12 831 plume particulate trend. Metalliferous sediments from Leg 92 are also enriched in Mn relative  
13  
14 832 to most metalliferous sediments in the Atlantis II Deep (compare Figs. 18 and 7).  
15  
16 833

### 17 834 3.2. Major- and trace-elements

19 835  
20  
21 836 On a carbonate-free basis, most Leg 92 metalliferous sediments contain 30–50 wt %  $\text{Fe}_2\text{O}_3(\text{t})$ ,  
22  
23 837 10–18 wt %  $\text{MnO}$ , and  $<2.0$  wt %  $\text{Al}_2\text{O}_3$  (Supplementary data Table 2). Similar abundance levels  
24  
25 838 were reported by Marchig and Erzinger (1986) for the “lower” portions of the Leg 92 holes, and  
26  
27 839 also for a transect of surficial metalliferous sediments up to 50 km from the crest of the EPR at  
28  
29 840 about  $18.5^\circ\text{S}$  (GEOMETEP cores: see also Marchig and Gundlach, 1982). Plots of  $\text{Fe}_2\text{O}_3(\text{t})$  vs  
30  
31 841  $\text{MnO}$ , and  $\text{Al}_2\text{O}_3$  vs.  $\text{Fe}_2\text{O}_3(\text{t})$  are shown in Fig. 19a and b, respectively. There is no obvious  
32  
33 842 correlation between Fe and Mn, or between Fe and Al. Two subsets of samples plot away from  
34  
35 843 the main group: (1) several near-surface, sub-lysocline sediments that are low in MnO (5.5–7.5  
36  
37 844 wt %) but high in  $\text{Al}_2\text{O}_3$  (3.2–7.4 wt %); the latter feature is attributed to an increased  
38  
39 845 proportion of terrigenous detritus; and (2) several near-basement sediments from Site 597 with  
40  
41 846 elevated  $\text{Al}_2\text{O}_3$  contents (3–4 wt %) that are mainly due to a component of intermixed basaltic  
42  
43 847 detritus (as recorded in shipboard logs). Most Leg 92 metalliferous sediments contain only 5–10  
44  
45 848 wt %  $\text{SiO}_2$  on a carbonate-free basis, with the exception of a few near-surface samples and the  
46  
47 849 Site 597 near-basement samples mentioned above. This indicates that phases such as Fe  
48  
49 850 smectites and biogenic silica must be only minor components of the metalliferous sediment.  
50  
51 851

52  
53 852 The contribution of detrital material to the composition of Leg 92 metalliferous sediments can  
54  
55 853 be examined using cross-plots of selected elements versus  $\text{Al}_2\text{O}_3$ . A  $\text{TiO}_2$ – $\text{Al}_2\text{O}_3$  plot (Fig. 19c)  
56  
57 854 suggests that the metalliferous sediments contain both basaltic and terrigenous detrital  
58  
59 855 components, based on the  $\text{TiO}_2/\text{Al}_2\text{O}_3$  ratio of Leg 92 basalt (Erzinger, 1986) and the average  
60  
61  
62

1 856  $\text{TiO}_2/\text{Al}_2\text{O}_3$  ratio of pelagic clay (Li and Schoonmaker, 2003). Fe-smectite-bearing metalliferous  
2 857 sediment from the Bauer Basin, shown by the two squares, clearly contains a significant  
3  
4 858 component of terrigenous detritus. In a plot of  $\text{SiO}_2$  versus  $\text{Al}_2\text{O}_3$  (Fig. 19d), by contrast, only  
5  
6 859 one main detrital trend is obvious; departures from this trend are probably due to the presence  
7  
8 860 of 'excess' biogenic silica and/or aeolian quartz.

9  
10 861  
11  
12 862 The total REE contents of carbonate-free Leg 92 metalliferous sediments (<2.0 wt %  $\text{Al}_2\text{O}_3$ )  
13  
14 863 range from about 100 to 350 ppm, excluding 3 near-surface sediments (Table 4). Similar levels  
15  
16 864 of REE were reported for a different set of samples by Ruhlin and Owen (1986). Total REEs  
17  
18 865 show no obvious correlation with  $\text{P}_2\text{O}_5$  (Fig. 20a), or  $\text{Fe}_2\text{O}_3(\text{t})$  (Fig. 20b). Based on a strong  
19  
20 866 positive correlation with Ca (not shown), P mainly resides in apatite, which in deep-sea  
21  
22 867 sediments is derived chiefly from fish debris (although P can also be adsorbed from seawater by  
23  
24 868 Fe-rich plume particulates: Feely et al., 1998). Biogenic apatite can also absorb large amounts  
25  
26 869 of REEs from bottom waters after settling on the seafloor, especially if sedimentation rates are  
27  
28 870 low (Dubinin and Sval'nov, 2001). However, the lack of correlation between total REEs and  $\text{P}_2\text{O}_5$   
29  
30 871 in the metalliferous sediments (apart from three samples discussed below) suggests that the  
31  
32 872 abundance of biogenic apatite does not control the final REE content of the sediment. It may be  
33  
34 873 that the length of time during which the apatite was in contact with REE-bearing porewaters is  
35  
36 874 a more important control. The abundance of  $\text{Fe}_2\text{O}_3(\text{t})$  also does not seem to determine the  
37  
38 875 total REE content of the metalliferous sediment (Fig. 20b). This suggests that detrital material is  
39  
40 876 the main source of REEs in the metalliferous sediments. As discussed in Section 3.3, seawater  
41  
42 877 has also contributed some REEs to the metalliferous component of the sediment.

43 878  
44  
45 879 Three near-surface sediments from Leg 92 (Fig. 20) with notably higher REE contents than the  
46  
47 880 main metalliferous group (800–1300 ppm vs. 100–350 ppm) also contain a larger detrital  
48  
49 881 component (4.7–7.4 wt %  $\text{Al}_2\text{O}_3$ ) and a larger phosphatic component (3.0–3.2 wt %  $\text{P}_2\text{O}_5$ ).  
50  
51 882 These three samples, which are from depths of 0.7 to 5.2 m at Site 598, accumulated slowly as  
52  
53 883 a result of being deposited at or below the lysocline (Rea and Leinen, 1986). This allowed more  
54  
55 884 time for detrital aluminosilicates, authigenic phosphate and fish debris to accumulate. These  
56  
57 885 three samples are also elevated in Zr (250–470 ppm) relative to the main group of metalliferous  
58  
59 886 sediments (40–90 ppm), and relative to terrigenous material as represented by average shale

1 887 (which could supply up to 100 ppm Zr in the highest-Al sample). The excess Zr in these three  
2 888 samples could conceivably be due to post-depositional absorption of Zr from porewaters by the  
3  
4 889 phosphatic component of the sediment (cf. Tlig et al., 1987; Oudin and Cocherie, 1988).  
5

6 890  
7  
8 891 On a carbonate-free basis, most of the Leg 92 metalliferous sediments have much lower  
9  
10 892 contents of metals (Cu = 1000–2000 ppm, Zn = 500–1500 ppm, Pb = 50–150 ppm, As = 300–500  
11  
12 893 ppm, Au = 5–50 ppb, Ag = 2–50 ppm) than those of the Atlantis II Deep ([Supplementary Data](#)  
13  
14 894 [Tables 1 and 2](#)). Exceptions are: (i) Mo, which is enriched in most of the Leg 92 sediments  
15  
16 895 relative to typical pelagic sediments; and (ii) Ba, Co and Ni, which are enriched in near-surface  
17  
18 896 sediments deposited at or below the lysocline.

19 897  
20  
21 898 Binary plots involving elements such as Al, Mo, Ba and Co ([Fig. 21](#)) can be used to help  
22  
23 899 recognize contributions from detrital, hydrothermal and hydrogenous sources. Leg 92  
24  
25 900 metalliferous sediments contain 50–600 ppm Mo ([Fig. 21a](#)), with the four highest values  
26  
27 901 occurring in sediments just above basement basalts at Site 597 ([Fig. 21b](#)). These latter Mo  
28  
29 902 values (500–600 ppm) are notably higher than the average of 134 ppm Mo for ridge-proximal  
30  
31 903 metalliferous sediments on the EPR (Marchig and Gundlach, 1982; large red-filled circle in [Fig.](#)  
32  
33 904 [21a](#)). Some of the Mo in the four near-basement samples could be contributed by hydrogenous  
34  
35 905 Fe-Mn micronodules, which in pure form can contain 300–600 ppm Mo (filled circle with N in  
36  
37 906 [Fig. 21a](#); Dubinin and Sval'nov, 2001; Li and Schoonmaker, 2003). However, Mn micronodules  
38  
39 907 are rare in Leg 92 sediments (Marchig and Erzinger, 1986). The detrital component in these four  
40  
41 908 samples (3–4 % wt Al<sub>2</sub>O<sub>3</sub>) cannot add more than a few ppm Mo to the sediment, as the Mo  
42  
43 909 contents of pelagic clay and seafloor basalt are ca. 27 ppm and <1 ppm, respectively (Sun and  
44  
45 910 McDonough, 1989; Li and Schoonmaker, 2003). Although Mo can also be enriched in seafloor  
46  
47 911 sediments where porewaters are euxinic and FeS precipitation occurs (Scott and Lyons, 2012),  
48  
49 912 the basal Leg 92 sediments are characterized by oxidized mineral assemblages with low  
50  
51 913 contents of organic carbon (see Site Reports in Leinen, Rea et al., 1986). Thus some input of  
52  
53 914 hydrothermal Mo is required. The five sub-lysocline samples, in contrast to the main group of  
54  
55 915 metalliferous sediments, outline a trend extending from low-Mo pelagic clay towards the ideal  
56  
57 916 Fe-Mn micronodule line ([Fig. 21a](#)). The intersection of the two trends suggests that the  
58  
59 917 maximum hydrogenous Mo contribution to the metalliferous sediments is about 250 ppm.  
60  
61  
62

918

919 The vertical distribution of Mo in two of the drillholes (Sites 597 and 599) that reached basaltic  
920 basement on Leg 92 is shown in Fig. 21b. Downhole trends in the two holes are similar: high Mo  
921 contents (300–600 ppm) in the lowest few metres of sediment above basement, a central  
922 interval about 20 m thick with lower Mo values (60–120 ppm), and an upper interval (1–8 m  
923 below surface) of moderate Mo values (180–360 ppm). We suggest that the near-basement Mo  
924 enrichment results from scavenging of hydrothermal and seawater Mo by Fe-Mn-rich  
925 oxyhydroxides that precipitated from a hydrothermal plume close to an axial vent, with the  
926 lower Mo values in the central interval of the two holes reflecting deposition from a distal,  
927 diluted plume as the sites moved away from the EPR. The moderate Mo values observed in  
928 near-surface samples (1–8 m below the seafloor) could be the result of increased amounts of  
929 hydrogenous plus detrital material (cf. Fig. 21a), as might be expected when seafloor descends  
930 below the lysocline and bulk sedimentation rates become much slower.

931

932 Sub-lysocline sediments are enriched in Ba (0.7–1.1 wt % in 4 of 5 samples) and Co (250–410  
933 ppm in 4 of 5 samples) relative to the underlying metalliferous sediments (Fig. 21c). The  
934 enrichment in Ba would seem to require the presence of either minor authigenic barite, or Ba  
935 substitution in biogenic apatite, although neither phase was specifically reported in the Leg 92  
936 shipboard studies (Leinen, Rea et al., 1986). The Co enrichment could be due to the presence of  
937 hydrogenous Fe-Mn micronodules (cf. Dubinin and Sval'nov, 2001).

938

939 A plot of  $\Sigma\text{REE}$  versus  $\text{Al}_2\text{O}_3$  (Fig. 21d) suggests that that REE enrichment in the sub-lysocline  
940 sediments is partly due to detrital material. This detrital material is of aeolian derivation (Rea  
941 and Leinen, 1986). However, shale and pelagic clay contain only 200–250 ppm  $\Sigma\text{REE}$  (Li and  
942 Schoonmaker, 2003) and therefore a 50 % detrital component (7.5 %  $\text{Al}_2\text{O}_3$ ) should only  
943 contribute about 100–125 ppm REE to the sediment. Therefore another source of REE must be  
944 present in the sub-lysocline sediments, for example biogenic apatite or authigenic Fe-Mn  
945 micronodules, which can respectively contain in the order of 5000 and 1000 ppm  $\Sigma\text{REE}$  (Dubinin  
946 and Sval'nov, 2001).

947

948 3.3. Rare-earth element patterns

949  
1  
2 950 REE data for Leg 92 sediments have been reported by Barrett et al. (1986), Ruhlin and Owen  
3  
4 951 (1986) and Owen and Olivarez (1988). The new REE analyses discussed below are for a different  
5  
6 952 set of samples than those reported by Barrett et al. (1986). Shale-normalized REE patterns for  
7  
8 953 the carbonate-free fraction of metalliferous sediments from Sites 599 and 598 are shown in Fig.  
9  
10 954 22a and b, respectively. Sediments from Site 599 range in age from  $\approx$  1–8 Ma, whereas those  
11  
12 955 from Site 598 (excluding the three samples from Core 1) range in age from  $\approx$  11–16 Ma. The Leg  
13  
14 956 92 REE patterns are closely comparable to those of Eocene – Oligocene metalliferous sediments  
15  
16 957 cored at Sites 573 and 574 of Leg 85 in the central equatorial Pacific (Jarvis, 1985).

17 958  
18  
19  
20 959 Almost all of the Leg 92 metalliferous sediments, regardless of age, share the same basic REE  
21  
22 960 pattern (Fig. 22). This pattern is similar to that of deep Pacific seawater, but with a flatter slope  
23  
24 961 from the middle to heavy REE, especially in the older sediments (compare the ca. 10–17 Ma  
25  
26 962 patterns from Site 598 with the 3.7–8.6 Ma patterns from Site 599). The minor flattening of REE  
27  
28 963 patterns in sediments older than ca. 10 Ma has been ascribed to diagenetic reactions during  
29  
30 964 transformation of Fe-Mn-oxyhydroxides to goethite plus minor Fe-rich smectite and apatite  
31  
32 965 (Barrett and Jarvis, 1988).

33 966  
34  
35 967 Leg 92 metalliferous sediments show a general uphole increase in  $\Sigma$ REE, with near-surface,  
36  
37 968 slowly accumulating sediments in the most axial-distal holes containing the highest abundances  
38  
39 969 of REEs (Ruhlin and Owen, 1986; Owen and Olivarez, 1988). This general upwards trend is the  
40  
41 970 result of two processes affecting surface sediments on the westward-moving plate: (1) as the  
42  
43 971 hydrothermal plume drifts hundreds of kilometres or more from the palaeo-axis, Fe-rich  
44  
45 972 oxyhydroxides within the plume scavenge progressively more REE from seawater before  
46  
47 973 settling to the seafloor; and (2) as the seafloor eventually descends below the lysocline and  
48  
49 974 towards the carbonate compensation depth (CCD), as at Sites 597 and 598, sedimentation rates  
50  
51 975 decrease (Rea and Leinen, 1986); as a result, Fe-oxyhydroxides and biogenic apatite in near-  
52  
53 976 surface sediments are able to more effectively scavenge REEs from seawater and porewaters.

54 977  
55  
56  
57 978 At Site 598, near-surface, sub-lysocline near-surface sediments contain higher proportions of  
58  
59 979 detrital aluminosilicates than underlying metalliferous sediments, which may be the cause of

1 980 the slightly flatter REE patterns of the former (the same effect is seen at the top of Site 597:  
2 981 Barrett et al., 1986). Sub-lysocline (and sub-CCD) pelagic sediments, which accumulate very  
3  
4 982 slowly, can also be enriched in phases such as biogenic apatite, authigenic Fe-Mn micronodules  
5  
6 983 and phillipsite (Dubinin and Sval'nov, 2001). Biogenic apatite probably contributes to the  
7  
8 984 elevated REE pattern of the Leg 92 sub-lysocline sediments, as the REE content of this phase  
9  
10 985 can become very high due to post-depositional scavenging of seawater REE (cf. Kon et al., 2014;  
11  
12 986 Liao et al., 2019). The contribution of Fe-Mn micronodules must be minor, as the sediments still  
13  
14 987 retain negative Ce anomalies, whereas micronodules carry positive Ce anomalies (Dubinin and  
15  
16 988 Sval'nov, 2001). Phillipsite, an authigenic Al-silicate, contains low levels of REE (Dubinin, 2000)  
17  
18 989 and therefore cannot be the cause of the REE enrichment in sub-lysocline sediments.

19 990  
20  
21 991 The relationships between Fe, P and REE metalliferous sediments in the eastern South Pacific  
22  
23 992 Ocean have been examined by Kashiwabara et al. (2018), who concluded that after an initial  
24  
25 993 period of scavenging of REEs from seawater by hydrothermal Fe-Mn oxyhydroxides, the REEs  
26  
27 994 were transferred to authigenic apatite during early diagenesis under oxic conditions. These  
28  
29 995 authors also found that biogenic apatite in the form of fish debris is the main host of REE in  
30  
31 996 slowly accumulating, sub-CCD sediments (e.g., those of the central North Pacific Ocean).

### 34 997 35 998 3.4. Nd isotopes 36 999

37  
38  
39 1000 The Nd isotopic composition of metalliferous sediments from Site 598 was determined by  
40  
41 1001 Halliday et al. (1992), who analysed six samples initially deposited at distances ranging from  
42  
43 1002 about 10 to 1000 km from the spreading axis. These samples had near-uniform  $\epsilon_{Nd}$  values of -  
44  
45 1003 5.2 to -4.2, reflecting derivation of essentially all of the Nd from Pacific seawater, with no  
46  
47 1004 evidence of a basaltic-hydrothermal contribution. This finding is consistent with the seawater-  
48  
49 1005 like REE patterns for Site 598 discussed in Section 3.3. Halliday et al. (1992) concluded that any  
50  
51 1006 basaltic Nd contained within discharging vent fluids at a spreading axis must be deposited very  
52  
53 1007 close to the vents themselves (<10 km from the palaeo-axis for Site 598).

54 1008  
55  
56 1009 In a study of sediments 2–15 km from a vent site on the Juan de Fuca Ridge, Sun et al. (2018)  
57  
58 1010 found that the Fe-Mn oxide fraction, which represents 5–7 % of the bulk sediment, and which  
59

1 1011 they interpreted as plume-derived, contained 10–20 % of basaltic-hydrothermal Nd, based on  
2 1012  $\epsilon\text{Nd}$  values of -1.6 to -1.0, i.e., somewhat higher than the range of North Pacific Deep Seawater  
3  
4 1013 (-4 to -2). In support of the restriction of dissolved basaltic Nd to the immediate environment of  
5  
6 1014 the ridge axis is Stichel et al.'s (2018) observation that the neutrally buoyant plume above the  
7  
8 1015 TAG hydrothermal field on the Mid-Atlantic Ridge shows only a small increase in  $\epsilon\text{Nd}$  (+0.7  
9  
10 1016 units) relative to background deep seawater.

#### 14 1018 **4. Metalliferous Sediments Near and On Open-Ocean Spreading Axes**

##### 18 1019 **4.1. Near-Axial Locations**

19 1020  
20  
21 1021 Metalliferous sediments can also form in near-axial locations where uprising low-temperature  
22  
23 1022 hydrothermal fluids pass through a thin blanket of pelagic sediment. The best-known example  
24  
25 1023 is the Galapagos hydrothermal mounds field, which overlies young oceanic crust (<600 ka) in  
26  
27 1024 the eastern equatorial Pacific, 18–32 km south of the Galapagos Rift spreading centre (Figs. 1,  
28  
29 1025 23a). In this area, semi-continuous chains of mounds occur above ridge-parallel basement  
30  
31 1026 faults, with individual mounds protruding up to several metres above the sediment cover  
32  
33 1027 (Williams et al., 1979). Piston-core drilling on DSDP Leg 70 determined that the mounds consist  
34  
35 1028 of 10–20 m of nontronite, an  $\text{Fe}^{3+}$ -rich, Al-poor smectite, interbedded with biogenic ooze,  
36  
37 1029 overlain by a thin surface layer of Mn-oxide-rich crusts and mud (Fig. 23b; Honnorez et al.,  
38  
39 1030 1981). The nontronite commonly occurs as intervals of dark green, unconsolidated granules;  
40  
41 1031 these are separated from cream-coloured biogenic ooze by transitional layers of fine-grained  
42  
43 1032 compact nontronite. Chemical analyses of various types of mounds sediments are given in  
44  
45 1033 Schrader et al. (1980), Barrett and Friedrichsen (1982), Moorby and Cronan (1983), Honnorez et  
46  
47 1034 al. (1983) and McMurtry et al. (1983). Temperatures of nontronite formation are mainly in the  
48  
49 1035 10–40°C range (Barrett and Friedrichsen, 1982; McMurtry et al., 1983). Stratigraphic and  
50  
51 1036 sedimentological descriptions of all Leg 70 drill cores are given by Honnorez, Von Herzen et al.  
52  
53 1037 (1983), with colour photographs available at <http://www.deepseadrilling.org/cores/leg070/>.

54 1038  
55  
56 1039 The near-axial nontronite of the Galapagos mounds field is formed as upwelling,  $\text{Fe}^{2+}$ -bearing  
57  
58 1040 fluids pass through and dissolve much of the biogenic ooze; the dissolved Fe is oxidized and  
59

1041 combines with silica of biogenic and hydrothermal derivation to form an Fe-rich, Al-poor,  
1042 hydrous silicate (Honnorez et al., 1981). Although the nontronite is largely authigenic, it is  
1043 interlayered with normal pelagic ooze and traditionally has been referred to as a low-  
1044 temperature hydrothermal sediment (cf. Honnorez et al., 1981; McMurtry et al., 1983). Locally,  
1045 nontronite is exposed on the surface of hydrothermal mounds (Corliss et al., 1978). The general  
1046 formula for nontronite can be written as  $(\text{Na,K},0.5\text{Ca})_{0.33}\text{Fe}^{3+}_2(\text{Si}_{3.67},\text{Al}_{0.33})_4\text{O}_{10}(\text{OH}_2)_n\text{H}_2\text{O}$ ,  
1047 although its composition varies in different seafloor hydrothermal settings (e.g., McMurtry et  
1048 al., 1983; Murnane and Clague, 1983; Stoffers et al., 1985; Alt, 1988; Severmann et al., 2004;  
1049 Sun et al., 2012; Ta et al., 2017).

1050  
1051 Nontronitic sediments and Fe-Mn oxide mud from the Galapagos hydrothermal mounds share  
1052 similar REE patterns (Fig. 24; Barrett et al., 1988), but differ from normal seawater (Fig. 22a) in  
1053 having flatter slopes from the middle to heavy REE, and notably less negative Ce anomalies. In  
1054 the nontronitic sediments, the absolute contents of REE vary considerably. This results from  
1055 mass changes in major elements that accompany nontronite growth (cf. Barrett, 1992). Initially,  
1056 as biogenic ooze is dissolved by low-temperature fluids, REEs associated with minor detrital  
1057 clays (incipient nontronite) are residually concentrated, together with immobile elements such  
1058 as Al and Ti, forming dm-thick intervals of transitional nontronite (arrow 1 in Fig. 24). As fluids  
1059 continue to pass through the sediment and precipitation of Fe and Si occurs, m-thick intervals  
1060 of granular nontronite form; these have very low REE contents owing to the diluting effect of  
1061 the added Fe and Si (arrow 2 in Fig. 24). Simultaneously, Al and Ti are also diluted by the added  
1062 Fe and Si (Barrett, 1992).

1063  
1064 Based on general correlations between total REE, Al and Ti, much of the REE content of the  
1065 nontronitic sediments is inherited from the minor component of detrital aluminosilicates  
1066 contained within the original biogenic ooze, which provides a shale-like 'baseline' to the REE  
1067 patterns. The hydrothermal component of the nontronitic sediment appears to carry a  
1068 seawater-like REE signature. The combined components produce a bulk sediment REE pattern  
1069 (Fig. 24) having a small negative Ce anomaly, and a somewhat steeper slope from Pr to Lu,  
1070 relative to shale. The lack of a positive Eu anomaly suggests that the upwelling fluids that  
1071 entered the Galapagos mounds had not previously reacted with basalts at high temperatures.

1072 However, low-temperature interaction likely occurred, as Pb-isotope data indicate that the  
1 nontronite contains variable proportions of basaltic and seawater Pb (Barrett, 1983; Barrett et  
2 1073 al., 1988). The Sr-isotopic composition of the nontronites demonstrates that almost all of the Sr  
3  
4 1074 is seawater-derived (Barrett, 1983).  
5  
6 1075  
7  
8 1076

9  
10 1077 Nontronite-rich sediments have also been recovered from other open-ocean settings,  
11  
12 1078 commonly seamounts, where they formed mainly at 30–80°C (De Carlo et al., 1983; Murnane  
13  
14 1079 and Clague, 1983; Singer et al., 1984; Alt, 1988; Dekov et al., 2007; Lubetkin et al., 2018). Many  
15  
16 1080 of these nontronite occurrences are found at or near the surface. In such cases, the nontronite  
17  
18 1081 appears to have precipitated directly from diffuse, low-temperature fluids (see also Section  
19  
20 1082 4.2). Nd isotopic data have not been reported for any of these nontronite occurrences, apart  
21  
22 1083 from a sample from the Eolo Seamount in the Mediterranean (Fig. 1), where an  $\epsilon_{Nd}$  value of -  
23  
24 1084 4.5 suggests it contains roughly 30 % local volcanic Nd (Dekov et al., 2007).  
25

#### 26 1085 27 1086 4.2. Axial Vent Locations 28 29 1087 30

31 1088 Nontronite is also found within Fe-oxide-rich sediments of the active TAG hydrothermal field at  
32  
33 1089 26°N on the Mid-Atlantic Ridge (Fig. 1). The nontronite is inferred to form by direct  
34  
35 1090 precipitation from relatively low-temperature fluids (81–96°C) rising through sulphide-rich  
36  
37 1091 mounds (Severmann et al., 2004). The REE patterns of nontronites from both active (TAG)  
38  
39 1092 mounds and nearby inactive (Alvin area) mounds are shown in Fig. 25. Also shown are the REE  
40  
41 1093 patterns of the 'residual' Fe-oxide component of these sediments, calculated from the  
42  
43 1094 difference between bulk sediment and nontronite REE patterns (Severmann et al., 2004).  
44

45 1095 Nontronite and residual Fe oxide from TAG mounds both carry a hydrothermal signature based  
46  
47 1096 on their large positive Eu anomalies (also a feature of diffuse vent fluids at TAG). At the inactive  
48  
49 1097 Alvin site, nontronite and residual Fe-oxides have notably smaller Eu anomalies, suggesting that  
50  
51 1098 they formed from a hydrothermal fluid that had mixed to a small degree with normal seawater.  
52  
53 1099 The Alvin Fe-oxides additionally display a small negative Ce anomaly (e.g., Fig. 25), consistent  
54  
55 1100 with an even larger seawater component in the precipitating fluid (Severmann et al., 2004).  
56

57 1101 This type of REE pattern, with a positive Eu anomaly but negative Ce anomaly, has been  
58  
59  
60  
61  
62

1102 reported from the TAG area for vent sulphides (Mills et al., 1993) and Fe-oxide-rich and Mn-  
1103 oxide-rich sediments overlying inactive sulphide mounds (Dutrieux, 2020).

1104

1105 REE patterns with positive Eu anomalies but negative Ce anomalies have also been reported  
1106 for: (i) carbonate-ooze-rich sediment 2–5 km from the Rainbow vent site at 36°N on the Mid-  
1107 Atlantic Ridge (location in Fig. 1; Chavagnac et al., 2005); (2) Fe-oxyhydroxide particulates in  
1108 neutrally buoyant plumes at both the TAG and Rainbow sites (German et al., 1990, 1993;  
1109 Chavagnac et al., 2005); and (3) low-temperature (30°C) fluids on the Juan de Fuca Ridge (Fig. 1;  
1110 Bao et al., 2008). At the TAG site, modelling suggests that sediment REE patterns with small  
1111 positive Eu anomalies, but moderately negative Ce anomalies, can be produced by mixing cold  
1112 seawater with high-temperature fluids at a ratio of about 1000:1 (German et al., 1990).

1113

1114 Sulphate minerals can also contribute a positive Eu anomaly, provided they are sufficiently  
1115 abundant (the REE content of sulphides is very low). Anhydrite with large positive Eu anomalies  
1116 is a common mineral in the TAG field on the Mid-Atlantic Ridge (Mills and Elderfield, 1995;  
1117 Humphris, 1998) and at 9–10°N on the EPR (Yao et al., 2015). Barite is generally scarce, but has  
1118 been reported from 37°N on the Mid-Atlantic Ridge (Langmuir et al., 1997; Dias et al., 2008),  
1119 and 49.7°N on the Southern Explorer Ridge in the NE Pacific Ocean (Fig. 1; Barrett et al., 1990).  
1120 The Nd isotopic composition of barite-rich sediment at 37°N on the Mid-Atlantic Ridge is close  
1121 to that of the associated basalts (Dias et al., 2008).

1122

1123 On the Southern Explorer Ridge, barite forms a component of massive sulphide-sulphate-silica  
1124 deposits at the Magic Mountain vent field (Tunnicliffe et al., 1986; Scott et al., 1990). Barite  
1125 also occurs as residual sandy material within Fe-oxyhydroxide-rich gossanous sediments  
1126 overlying inactive mounds; this barite has a large positive Eu anomaly, but no Ce anomaly  
1127 (Barrett et al., 1990). This feature is consistent with the barite originating as a high-temperature  
1128 phase that remains in the sediment as a residue after oxidative weathering has converted the  
1129 sulphides to Fe-rich oxyhydroxides. Two bulk samples of massive sulphide-sulphate-silica from  
1130 the vent field have a moderate positive Eu anomaly, but a moderate negative Ce anomaly (Fig.  
1131 26a). These two samples were interpreted by Barrett et al. (1990) to have been deposited from  
1132 a roughly 500:1 mixture of normal seawater and high-temperature vent fluid, with the positive

1 1133 Eu anomaly contributed mainly by the barite, and the negative Ce anomaly by hydrothermal  
2 1134 silica (assuming that the silica contains sufficient REEs to impart a seawater-like REE pattern).

3  
4 1135  
5  
6 1136 Other sulphide-bearing bulk samples in the Southern Explorer Ridge vent field have a negative  
7  
8 1137 Ce anomaly, with a small or no Eu anomaly (Fig. 26b), implying that the precipitating fluids  
9  
10 1138 were seawater-dominated (Barrett et al., 1990). For these samples, most of the REE content is  
11  
12 1139 probably contributed by non-sulphide phases such as sulphates and silica (the REE content of  
13  
14 1140 base-metal sulphides is very low). The REE patterns in Fig. 26 differ from that of normal deep  
15  
16 1141 seawater, which displays a much steeper slope from Dy to Lu (Fig. 26a). Mixing of hot vent  
17  
18 1142 fluids (REE patterns shown in Fig. 10) with normal seawater should act to decrease this slope,  
19  
20 1143 while also imparting a positive Eu anomaly to the resulting fluid.

## 21 22 1144 23 24 1145 **5. Discussion**

### 25 26 27 28 1146 5.1. Compositional features

29  
30 1147  
31 1148 The contrasting seafloor settings, REE patterns and Nd-Pb-Sr isotopic ratios of the main types of  
32  
33 1149 metalliferous sediment discussed in this paper are summarized in Table 5. Small, closed basins  
34  
35 1150 located on a young spreading axis, such as the Red Sea deeps, can become filled with stable,  
36  
37 1151 but chemically unusual, brines that undergo little interaction with overlying seawater. As a  
38  
39 1152 result, metals delivered by uprising hydrothermal fluids remain within the brines, eventually  
40  
41 1153 precipitating to form a variety of metalliferous facies depending upon the prevailing chemical  
42  
43 1154 features of the brine. The Atlantis II Deep precipitates are dominated overall by mixtures of Fe-  
44  
45 1155 oxyhydroxides, Fe-Si silicates, amorphous compounds, metal sulphides and Ca sulphates. The  
46  
47 1156 anoxic nature of the lower brine layer allows metals such as Zn, Cu and Pb to be distributed up  
48  
49 1157 to several km from probable vent sites. Where the content of dissolved reduced sulphur in the  
50  
51 1158 brine is high, metal sulphides precipitate; if the reduced sulphur content is low, metals carried  
52  
53 1159 as chloride complexes may be transported farther from the vent sites, and adsorbed onto  
54  
55 1160 precipitating Fe-Si-bearing oxyhydroxides (Laurila et al., 2014a). The reduced sulphur is  
56  
57 1161 provided dominantly by the hydrothermal brines that enter the Deep; in-situ reduction of

1 1162 seawater sulphate can only be a minor source of sulphur (Shanks and Bischoff, 1980;  
2 1163 Zierenberg and Shanks, 1986). Although hemipelagic biogenic sedimentation takes place  
3  
4 1164 throughout the Red Sea, almost no biogenic material (e.g. calcareous and siliceous microfossils)  
5  
6 1165 accumulates within the Atlantis II Deep above the lowest DOP facies, and detrital input (aeolian  
7  
8 1166 dust) is limited owing to the geographic and climatic features of the central Red Sea and its  
9  
10 1167 flanking landmasses.

11 1168  
12 1168  
13  
14 1169 The Atlantis II Deep deposit is of considerable economic interest as it contains a number of  
15  
16 1170 base- and precious-metal-rich intervals, has broad lateral extent, and comprises unlithified  
17  
18 1171 sediments that could be recovered from the seafloor relatively easily. Based on data from some  
19  
20 1172 600 Preussag AG drill cores, the Atlantis II Deep was estimated by Barbery et al. (1981) to  
21  
22 1173 contain an inferred resource of 89.5 Mt grading 2.06 wt % Zn, 0.44 wt % Cu and 38.4 ppm Ag on  
23  
24 1174 a dry, salt-free basis. In a more recent evaluation, the deposit was estimated to contain 3.27–  
25  
26 1175 3.75 Mt Zn, 0.74–0.81 Mt Cu, and 6500–7100 t Ag (Bertram, 2011). The gold content has been  
27  
28 1176 estimated as 47 tons Au at an average grade of 0.5 g/t Au (Mustafa et al., 1984). At 2016 prices,  
29  
30 1177 the in-situ resource had a value of about US\$11 billion (Brueckmann et al., 2017). The deposit  
31  
32 1178 also contains significant amounts of other metals. For the five chemical facies identified by  
33  
34 1179 Laurila et al. (2014a), minimum and maximum average contents of these metals are: Pb (182–  
35  
36 1180 1220 ppm), Cd (24–234 ppm), Sb (10–49 ppm), Mo (76–155 ppm) and Hg (484–3700 ppb).

37 1181  
38  
39 1182 In the Atlantis II Deep, total REE contents of the ‘purest’ metalliferous sediments (< 2 wt %  
40  
41 1183 Al<sub>2</sub>O<sub>3</sub>) are very low, mostly <25 ppm (Laurila et al., 2014b; this study). In sediments with a  
42  
43 1184 substantial detrital component (Al<sub>2</sub>O<sub>3</sub> up to 7 wt %), ΣREE can reach 60 ppm. Metalliferous  
44  
45 1185 sediments enriched in P<sub>2</sub>O<sub>5</sub> (1–2 wt %) can have ΣREE contents as high as 800–3900 ppm  
46  
47 1186 (Oudin and Cocherie, 1988). Such P-rich samples appear to be uncommon, however. The high  
48  
49 1187 REE contents of the P-rich sediments have been interpreted to be the result of absorption of  
50  
51 1188 REEs from hydrothermally influenced porewaters onto biogenic phosphate (fish teeth)  
52  
53 1189 following deposition and burial of the phosphate (Cocherie et al., 1994).

54  
55 1190  
56  
57 1191 Deep-sea pelagic sediments accumulating in open oceans on the broad flanks of spreading  
58  
59 1192 ridges typically consist of a dominant biogenic ooze component (carbonate and/or siliceous

1 1193 tests), with a lesser metalliferous component, and a very minor detrital fraction. The  
2  
3 1194 metalliferous component, which can be isolated by leach treatments, has: (i) high contents of  
4  
5 1195 Fe + Mn, commonly in the form of oxyhydroxides and oxides; (ii) low contents of Al, Ti and Zr,  
6  
7 1196 elements typically associated with detrital material (of continental and/or seafloor basaltic  
8  
9 1197 derivation); and (iii) enrichment of trace metals and REEs relative to normal pelagic sediments.

10 1198  
11  
12 1199 As a result of the oxidized nature of bottom waters in modern open oceans, metal sulphide  
13  
14 1200 deposition is limited to the immediate vicinity of high-temperature axial vents, either as  
15  
16 1201 massive mounds and chimneys, or as sulphide particulates that settle out of the buoyant plume  
17  
18 1202 (cf. Robb, 2005; Tornos et al., 2015). Most of the precipitates in the buoyant plume are,  
19  
20 1203 however, Fe-oxyhydroxides; minor sulphate phases are also present (Feely et al., 1994b, 1996).  
21  
22 1204 The Fe-rich precipitates of the buoyant plumes contain variable proportions of basalt- and  
23  
24 1205 seawater-derived metals (see Section 5.2). As the plume becomes non-buoyant and is  
25  
26 1206 dispersed by bottom currents over lateral distances up to 4000 km from the source vents  
27  
28 1207 (Resing et al., 2015; Fitzsimmons et al., 2017), trace metals and REEs derived exclusively from  
29  
30 1208 seawater are adsorbed by the Fe-rich precipitates. As these precipitates settle to the seafloor,  
31  
32 1209 they mix with ambient biogenic fallout and siliciclastic detritus (the proportions of which will  
33  
34 1210 depend on latitude, proximity to land, and depth within the ocean basin). Following  
35  
36 1211 sedimentation, the metalliferous component continues to absorb trace metals and REEs from  
37  
38 1212 pore waters (which represent diagenetically modified seawater).

39 1213  
40  
41 1214 The sediments cored on DSDP Legs 85 and 92 in the eastern Pacific Ocean were deposited  
42  
43 1215 above the CCD and lysocline over much of their history and therefore generally contain a large  
44  
45 1216 component of calcareous ooze. Expressed on a carbonate-free basis, these sediments contain  
46  
47 1217 100–500 ppm each of Cu, Ni, Zn and  $\Sigma$ REE (Jarvis, 1985; Barrett et al., 1988). As such, they are  
48  
49 1218 not likely to be of economic interest. However, in other regions of the Pacific Ocean, especially  
50  
51 1219 those lying below the CCD, REEs and associated high-tech trace metals are sufficiently  
52  
53 1220 concentrated in Mn nodules, Fe-Mn crusts and metalliferous sediments that they are being  
54  
55 1221 considered as future economic resources. (Kato et al., 2011; Hein et al., 2013; Seo et al., 2014;  
56  
57 1222 Nakamura et al., 2015; Iijima et al., 2016; Sa et al., 2018; Takaya et al., 2018; Balaram, 2019;  
58  
59 1223 Maciag and Zawadzki, 2019; Pak et al., 2019). One of the most promising areas in the Japanese

1224 Exclusive Economic Zone, some 1900 km southeast of Tokyo, where deep-sea muds contain  
 1225 two or three intervals that are very enriched in REE over thicknesses up to 1 m ( $\Sigma$ REE contents  
 1226 reach 5000 ppm). The REE enrichment in this case is due to the presence of biogenic phosphate  
 1227 debris, which in these slowly accumulating sediments has adsorbed large amounts of REEs from  
 1228 seawater (Ohta et al., 2016; Yusakawa et al., 2019; Tanaka et al., 2020).

## 5.2. Nd-Sr-Pb isotopes

1230  
 1231  
 1232  
 1233 The Nd-Pb-Sr isotopic composition of a given sample of deep-sea sediment will depend on the  
 1234 relative amounts of Nd, Pb and Sr contributed to it by: (1) hydrothermal fluids during  
 1235 precipitation of the metalliferous phases; (2) locally derived basaltic detritus; (3) continentally  
 1236 derived clays and dust; and (4) phosphatic fish debris and biogenic tests (especially calcareous  
 1237 microfossils in the case of Sr). [Table 6](#) provides a compilation of Nd-Pb-Sr isotope ratios and  
 1238 concentrations in metalliferous sediments and potential sources for both closed-basin and  
 1239 open-ocean settings. The isotopic ratios of high-temperature fluids discharging from black  
 1240 smokers indicate that the dissolved Nd-Pb-Sr in these fluids is mainly basalt-derived. However,  
 1241 mixing of these fluids with seawater in the uprising plume changes the isotopic ratios  
 1242 dramatically owing to differences in: (i) relative concentrations of Nd-Pb-Sr in vent fluids versus  
 1243 normal deep seawater ([Table 6](#)); and (ii) rates at which various metals and REEs are adsorbed  
 1244 onto Fe-rich precipitates in the plume.

1245  
 1246 Lead isotopic data for open-ocean metalliferous sediments show that most of the Pb up to  
 1247 about 100 km from vents on active ridges has a basaltic source (Bender et al., 1971), with a  
 1248 small component of basaltic Pb recognisable as far as 1000 km from the ridge (Barrett et al.,  
 1249 1987). By contrast, the Sr and Nd isotopic compositions of open-ocean metalliferous sediments  
 1250 such as those cored on Leg 92 indicate that almost all of the Sr and Nd was derived from normal  
 1251 seawater (Barrett et al., 1987; Halliday et al., 1992); this is also the case for sediments  
 1252 deposited within a few kilometres of the spreading axis (Chavagnac et al., 2006). In the Bauer  
 1253 Basin west of the Galapagos Rise ([Fig. 1](#)), a hydrogenous-hydrothermal ferromanganese crust  
 1254 that has grown for 7 Myr contains a significant component of basalt-derived Pb that apparently

1 1255 was dispersed laterally at least 200 km from the Rise; by contrast the Nd in this crust was  
2 1256 derived from Pacific deep-ocean water (van der Flierdt et al., 2004).

3  
4 1257  
5  
6 1258 In closed basins with a restricted circulation of bottom waters, such as the Atlantis II Deep, the  
7  
8 1259 situation is different due to the lack of mixing between hydrothermal, basement-derived brines  
9  
10 1260 and overlying, isotopically normal seawater. The brine that enters the Deep from below carries  
11  
12 1261 Pb, Nd and Sr that were derived from the basaltic basement, and possibly also from “old”  
13  
14 1262 seawater trapped within the Miocene evaporitic and Pliocene-Pleistocene hemipelagic  
15  
16 1263 sediments that flank the spreading axis (Fig. 3). The basaltic component is acquired in the  
17  
18 1264 discharge part of the hydrothermal convection cycle as hot brines leach Pb, Nd and Sr from  
19  
20 1265 underlying basalts, whereas the “old” seawater component originates in the recharge part of  
21  
22 1266 the convection cycle, as a result of leaching of sediments (especially evaporites) and mixing  
23  
24 1267 with trapped porewaters by descending Red Sea water (cf. Fig. 3).

25 1268  
26  
27 1269 Figure 27 summarizes the  $\epsilon\text{Nd}$  values of metalliferous sediments from the Red Sea, the eastern  
28  
29 1270 Pacific Ocean and the Mid-Atlantic Ridge, together with comparative data from the literature  
30  
31 1271 on basalts, high-temperature vent fluids, deep seawater, and selected seafloor hydrothermal  
32  
33 1272 deposits. It is worth noting that the  $\epsilon\text{Nd}$  values of deep seawater can vary from one ocean basin  
34  
35 1273 to another, and even within basins, due to variations in the average Nd isotopic composition of  
36  
37 1274 detritus entering each basin (cf. van de Flierdt et al., 2016). This point needs to be taken into  
38  
39 1275 account when comparing open-ocean metalliferous sediments on a global scale, but it is  
40  
41 1276 unlikely to be a factor for small basins such as the Atlantis II Deep.

42  
43 1277  
44  
45 1278 In the Atlantis II Deep, Nd isotopic data for the metalliferous sediments (Cocherie et al., 1994;  
46  
47 1279 this study) suggest that 20–30 % of the Nd is derived from a basaltic source. The remainder of  
48  
49 1280 the Nd in the metalliferous sediments is attributed to Holocene terrigenous detritus (aeolian  
50  
51 1281 dust), although it is conceivable that hydrothermal leaching of the Miocene evaporites and  
52  
53 1282 younger hemipelagic sediments that flank the Deep (Fig. 3) could also introduce unradiogenic  
54  
55 1283 Nd to the brine pool. Unfortunately, the Nd isotopic composition of these flanking sediments is  
56  
57 1284 unknown, although Holocene hemipelagic sediments in the northern Red Sea have an  $\epsilon\text{Nd}$   
58  
59 1285 value of about -6 (Palchan et al., 2013). Low-temperature brine from the Shaban Deep in the

1 1286 northern Red Sea has an  $\epsilon_{\text{Nd}}$  value of -4.5 (Cocherie et al., 1994), although this does not  
2 1287 necessarily represent the composition of Miocene evaporites. Also unknown is the content of  
3  
4 1288 Nd of the hydrothermal (metalliferous) brines that enter the Atlantis II Deep. Thus, the  
5  
6 1289 proportion of Nd in the metalliferous sediments that might have been leached from flanking  
7  
8 1290 sediments (or their porewaters) cannot be determined. However, it may be minor, as the Nd  
9  
10 1291 isotopic composition of the metalliferous sediment can be reasonably accounted for by mixing  
11  
12 1292 between a detrital (aeolian) component that slowly accumulates within the Deep, and a  
13  
14 1293 basaltic-hydrothermal component that is supplied by brines that flow into the Deep. Although  
15  
16 1294 the basaltic-hydrothermal fluid itself could, in theory, contain some Nd derived from Miocene  
17  
18 1295 to Pleistocene seawater, the proportion is not possible to estimate.

19  
20 1296  
21  
22 1297 Strontium-isotope ratios of both the metalliferous sediments and their porewaters in the  
23  
24 1298 Atlantis II Deep show little variation above the DOP interval (i.e., sediments younger than about  
25  
26 1299 11 ka), and reflect a mixture of seawater-derived Sr and basaltic Sr (Anschutz et al. 1995). The  
27  
28 1300 basaltic Sr component has been estimated as 30 % of the total Sr present in the sediments, the  
29  
30 1301 remainder being derived from the Late Miocene evaporites (Zierenberg and Shanks, 1986). The  
31  
32 1302 fairly limited ranges in Nd and Sr isotopic compositions observed in the metalliferous sediments  
33  
34 1303 suggest that the main brine layer in the Atlantis II Deep has been isotopically near-  
35  
36 1304 homogeneous for much of the Holocene.

37 1305  
38  
39 1306 Lead-isotope studies of metalliferous sediments in the Red Sea have been made by Dupré et al.  
40  
41 1307 (1988), Bauman (1994) and Pierret et al. (2010). Dupré et al. (1988) concluded that most of the  
42  
43 1308 Pb was not of basaltic derivation, based on isotopic differences with local basalts, whereas  
44  
45 1309 Bauman (1994) suggested that the Pb was basaltic but represented an average of Pb extracted  
46  
47 1310 from regionally isotopically variable basalts. In the study by Pierret et al. (2010), five samples of  
48  
49 1311 metalliferous sediments from the Atlantis II Deep (21.3°N) and four from the Thetis Deep  
50  
51 1312 (22.5°N) shared similar Pb isotopic ratios that could be explained by a dominantly basaltic  
52  
53 1313 source, if the least radiogenic end-member is taken as basalt from the Nereus Deep (23.2°N;  
54  
55 1314 [Fig. 2a](#)). However, if basalt from the Atlantis II Deep is taken as the end-member (using data in  
56  
57 1315 Dupré et al., 1988 and Volker et al., 1993), the samples analysed by Pierret et al. (2010) would  
58  
59 1316 instead contain 20–40 % basaltic Pb. In this regard, it is worth noting that basalts located near

1 1317 hot spots along ridges can have more radiogenic Pb-Sr isotopic compositions than normal  
2 1318 MORBs (Dosso et al., 1999; Ferreira, 2006).

4 1319  
5  
6 1320 About 20–40 % of the Nd, Sr and Pb in the metalliferous sediments of the Atlantis II Deep  
7  
8 1321 appear to have been derived from a basaltic source. The similar proportions of basaltic  
9  
10 1322 contribution shown by these three elements is likely a coincidence, given the various  
11  
12 1323 components of the hydrothermal system (normal seawater, basalts, evolved brine) would have  
13  
14 1324 varied considerably in terms of their Nd-Sr-Pb concentrations and initial isotopic ratios  
15  
16 1325 (comparative data for different possible sources and fluids are given in Table 6).

### 17 1326 18 19 20 1327 5.3. Detrital effects 21 1328

22  
23 1329 For metalliferous sediments with low contents of REE, such as those of the Atlantic II Deep and  
24  
25 1330 the Galapagos Hydrothermal Mounds, even a minor siliciclastic component can have a notable  
26  
27 1331 effect on REE patterns and Nd-Sr-Pb isotopic ratios. In the Atlantic II Deep, a 10 % siliciclastic  
28  
29 1332 component could provide as much as three-quarters of the Nd in the bulk sediment. This effect  
30  
31 1333 would result in Nd isotope ratios lying between those of detrital and hydrothermal end-  
32  
33 1334 members, but closer to the former. For Pb, the effect of a 10 % siliciclastic component would be  
34  
35 1335 minor, because it would contribute only about 2 ppm Pb to bulk sediments that contain 10–100  
36  
37 1336 ppm Pb, and locally more (Laurila, 2014a, this study). For Sr, the effect of a 10 % siliciclastic  
38  
39 1337 component would generally be minor, as it would contribute about 30 ppm Sr to bulk  
40  
41 1338 sediments that contain 50–500 ppm Sr (Anschutz et al., 1995).

42  
43 1339  
44  
45 1340 Ideally, the REE pattern of the siliciclastic component should be subtracted from that of the  
46  
47 1341 bulk metalliferous sediment in order to obtain the true REE pattern of the hydrothermal end-  
48  
49 1342 member precipitate (cf. Laurila et al., 2014a). This is particularly important in metalliferous  
50  
51 1343 sediments where  $\sum\text{REE} < 30$  ppm, for example those of the Atlantis II Deep (in open-ocean  
52  
53 1344 settings, metalliferous sediments generally contain a few hundred ppm of REE, so the  
54  
55 1345 correction will be minor). In the Atlantis II Deep, removal of the siliciclastic component's  
56  
57 1346 estimated REE pattern can leave a "baseline" metalliferous pattern that, apart from europium,

1 1347 is close to zero or slightly negative. In such cases, the calculation must be done carefully and  
2 1348 based on accurate data.

3  
4 1349  
5  
6  
7 1350 5.4. Variations in chemical signatures  
8 1351  
9

10 1352 At spreading ridges in open, oxidized oceans, the Nd isotope ratios and REE patterns of Fe-  
11  
12 1353 oxyhydroxide precipitates should shift from a dominantly basaltic-hydrothermal signature to a  
13  
14 1354 seawater-like signature within a few kilometres or less of the vents. Relative to high-  
15  
16 1355 temperature vent fluids, the precipitates show a decrease in the proportion of light to heavy  
17  
18 1356 REE, acquisition of a negative Ce anomaly, and loss of the positive Eu anomaly. Depending on  
19  
20 1357 discharge rate and degree of mixing with seawater in the near-vent region, a wide range of  
21  
22 1358 isotopic ratios and REE patterns can be expected in the earliest plume precipitates. As these Fe-  
23  
24 1359 rich precipitates drift away from the vent region, they scavenge Nd, Pb and Sr derived from  
25  
26 1360 normal deep seawater.

27  
28 1361  
29  
30 1362 The metalliferous sediments that accumulate on the seafloor generally have Nd and Sr isotopic  
31  
32 1363 ratios typical of those of ambient seawater. Biogenic phosphate in the form of fish debris  
33  
34 1364 generally forms a component of the sediments. This phosphate has a seawater Nd-Sr isotope  
35  
36 1365 signature (Grandjean et al., 1987; Martin and Haley, 2000). By contrast, the Pb isotope  
37  
38 1366 composition of surface metalliferous sediments changes with increasing distance from a  
39  
40 1367 spreading ridge, from a mainly basaltic signature acquired at the vent site, to a mainly seawater  
41  
42 1368 signature as Fe-rich precipitates in the plume absorb seawater Pb while drifting up to >1000 km  
43  
44 1369 from the ridge (cf. Barrett et al., 1987). During early burial, metalliferous sediments may also  
45  
46 1370 continue to absorb seawater Nd, Sr and Pb present from pore fluids.

47 1371  
48  
49 1372 High-temperature vent fluids at open-ocean spreading ridges generally have a large positive Eu  
50  
51 1373 anomaly but lack a negative Ce anomaly. Fe-Mn-oxyhydroxide precipitates in the buoyant  
52  
53 1374 plumes above the ridges can, however, show a negative Ce anomaly as well as a positive Eu  
54  
55 1375 anomaly (Sherrell et al., 1999; Edmonds and German, 2004), as can metalliferous precipitates  
56  
57  
58  
59  
60  
61  
62

1376 settling out from these plumes within a few kilometres of the vents (German et al., 1993;  
 1377 Chavagnac et al., 1995).  
 1378  
 1379 Representative REE patterns for metalliferous sediments in the closed basin of the Atlantis II  
 1380 Deep are shown in Fig. 28, as well as REE patterns of possible source materials such as  
 1381 seawater, brine and aeolian dust, and  $\epsilon\text{Nd}$  values where available. This diagram emphasises the  
 1382 much higher contents of REE in Saharan dust (marine clays are similar) relative to fluids such as  
 1383 seawater, brine and even typical black smokers. Even though biogenic carbonate, like seawater,  
 1384 carries a negative Ce anomaly, biotrital sediments in the Red Sea lack a Ce anomaly as a  
 1385 result of their significant content of siliciclastic detritus, which swamps the seawater signal.  
 1386 Positive Eu anomalies are present in metalliferous sediments from the brine-filled Atlantis II  
 1387 Deep. They also characterize the upper metre of metalliferous sediment in the brine-free Thetis  
 1388 Deep (not shown; Pierret et al., 2010). Outside of the axial deeps, positive Eu anomalies are  
 1389 absent. In a similar fashion, detrital and biotrital sediments in the Red Sea have distinctly  
 1390 negative  $\epsilon\text{Nd}$  value, whereas metalliferous sediments in the Atlantis II Deep have  $\epsilon\text{Nd}$  values  
 1391 mainly in the -2 to 0 range, and in the Thetis Deep (not shown), two samples have  $\epsilon\text{Nd}$  values of  
 1392 +3.3 and +3.9.  
 1393  
 1394 Representative REE patterns for metalliferous sediments, hydrothermal plumes and seawater  
 1395 in the eastern Pacific Ocean are shown in Fig. 29. Fe-Mn-oxyhydroxide sediments from the  
 1396 flanks of the EPR, such as those cored on DSDP Leg 92, have the highest REE contents and large  
 1397 negative Ce anomalies, as well as distinctly negative  $\epsilon\text{Nd}$  values of -5.2 to -4.1. Nontronite and  
 1398 Mn oxide ooze from the near-axial Galapagos hydrothermal mounds have seawater-like REE  
 1399 patterns but Ce anomaly is less negative. Plume particles from the EPR at 10°N, which are  
 1400 mainly Fe-oxyhydroxides, also have a seawater-like REE pattern with a moderately negative Ce  
 1401 anomaly, whereas plume particles from the MAR at 36°N have an additional positive Eu  
 1402 anomaly. This combination of a negative Ce anomaly and positive Eu anomaly is also shown by  
 1403 Fe oxides deposited in the Alvin zone, about 2 km from the TAG vent field on the MAR at 26°N.  
 1404  
 1405 [Figure 30 schematically](#) outlines the variations in Nd and Sr isotopic composition and REE  
 1406 patterns of sediments deposited in a range of settings, from open-ocean pelagic (siliciclastic-

1 1407 dominated Nd-Sr; at top of diagram) to hydrothermally dominated on the axes of spreading  
2 1408 ridges (basalt-influenced Nd-Sr; middle of diagram) to biogenic ooze + plume fallout dominated  
3  
4 1409 on the flanks of spreading ridges (seawater-influenced Nd-Sr; base of diagram). The Nd and Sr  
5  
6 1410 isotopic compositions of various possible source materials are given below the respective  
7  
8 1411 horizontal axes of Fig. 30. Metalliferous sediments deposited on the flanks of the East Pacific  
9  
10 1412 Rise, under oxic conditions, are shown by short, light blue bars, whereas those deposited in the  
11  
12 1413 Atlantis II Deep, under anoxic conditions, are shown by inclined red lines.

13  
14 1414  
15  
16 1415 5.5. Some comments on ancient chemical sediments

17  
18 1416  
19  
20 1417 The combination of ‘opposing’ Ce and Eu anomalies is also found in some Palaeozoic Fe-Si-rich  
21  
22 1418 hydrothermal exhalites associated with volcanogenic massive sulphide (VMS) deposits, for  
23  
24 1419 example, in the Cambrian of Newfoundland (Lode et al., 2016), the Ordovician of Norway  
25  
26 1420 (Grenne and Slack, 2005, 2019) and the Ordovician of New Brunswick (Peter and Goodfellow,  
27  
28 1421 1996). By analogy with modern buoyant plumes, ‘opposing’ Ce and Eu anomalies in ancient  
29  
30 1422 chemical sediments would imply proximity (less than a few km) to high-temperature vents and  
31  
32 1423 possible massive sulphide deposits, which could be used as an exploration tool. However, other  
33  
34 1424 chemical sediments associated with VMS deposits lack such ‘opposing’ anomalies, instead  
35  
36 1425 having seawater-like patterns, e.g. the Fe-rich umbers that overlie Cretaceous ophiolites in  
37  
38 1426 Japan (Kato, 2005) and Cyprus (Robertson and Fleet, 1976; Josso, 2017). These umbers  
39  
40 1427 presumably were deposited after high-temperature vent fluids had mixed with sufficient cold  
41  
42 1428 seawater to remove any hydrothermal REE signature. In such cases, the Pb isotopic  
43  
44 1429 composition of Fe-rich sediments overlying ophiolites provides a separate means of assessing  
45  
46 1430 the degree of basaltic-hydrothermal input (Barrett, 1980; Gale et al., 1981), and can potentially  
47  
48 1431 be used as an exploration guide to massive sulphide deposits.

49 1432  
50  
51 1433 Fe-Si-rich sediments form a major component of Precambrian banded iron formations (BIFs).  
52  
53 1434 The origin of these BIFs, some of which formed during extensive periods of mafic volcanism,  
54  
55 1435 particularly in the 3.0 –1.8 Ga period (Isley and Abbott, 1999), has been much debated over the  
56  
57 1436 last half century, and many questions remain concerning the degree of oxidation of the oceans

1 1437 and the nature of the BIF-precipitating mechanisms during this period (Bekker et al., 2010;  
2 1438 Little et al., 2021). The REE patterns of Archean and Palaeoproterozoic BIFs commonly show  
3  
4 1439 positive Eu anomalies, but these anomalies are difficult to interpret in terms of distance from a  
5  
6 1440 submarine vent source because ocean basins prior to about 1.8 Ga likely were anoxic over  
7  
8 1441 much of the water column, and therefore positive Eu anomalies generally would be expected in  
9  
10 1442 chemical sediments deposited across the basins (Kato et al., 1998).

11  
12 1443  
13  
14 1444 The Nd isotope composition of BIFs prior to about 1.8 Ga is likewise difficult to relate to specific  
15  
16 1445 vent areas, as oceans at that time generally contained a significant component of dissolved  
17  
18 1446 basaltic Nd due to long-term hydrothermal activity. Thus, the  $\epsilon\text{Nd}$  values of Fe-rich precipitates  
19  
20 1447 in general were elevated relative to those of modern open oceans, reaching values of 0 to +2  
21  
22 1448 (Jacobsen and Pimentel-Klose, 1988; Derry and Jacobsen, 1990; Bau et al., 1997). In the early  
23  
24 1449 Palaeoproterozoic, some parts of the deep ocean may have experienced mild oxidation (Little  
25  
26 1450 et al., 2021), and by the Late Palaeoproterozoic, oceans may have been characterized by both  
27  
28 1451 deeper anoxic water and shallower oxic water (Poulton et al., 2011; Konhauser et al., 2017).  
29  
30 1452 Different facies of BIF therefore would be expected to show a range of Eu anomalies (slightly to  
31  
32 1453 strongly positive) and Ce anomalies (positive to negative), as discussed by Plavansky et al.  
33  
34 1454 (2010). The possibility that coeval basins in different palaeogeographic settings (back-arc, rifted  
35  
36 1455 margin, open ocean) had different redox profiles further complicates interpretation of REE  
37  
38 1456 data. These factors need to be considered when using Eu anomalies in Precambrian iron  
39  
40 1457 formations as an exploration guide for locating high-temperature seafloor vents and associated  
41  
42 1458 massive sulphide deposits.

## 43 1459 44 45 1460 **6. Conclusions**

46  
47 1461  
48  
49 1462 Metalliferous deep-sea sediments show a number of chemical features that reflect the nature  
50  
51 1463 of the depositional basin (open oxidized oceans versus small, closed, anoxic basins) and the  
52  
53 1464 distance from source hydrothermal vents at which chemical precipitates settle to the seafloor.  
54  
55 1465 Open-ocean metalliferous sediments related to hydrothermal plumes at a spreading ridge, such  
56  
57 1466 as those in the eastern central Pacific, take the form of Fe-Mn-rich oxyhydroxides, whereas

1 1467 small anoxic basins such as the Red Sea Atlantis II Deep contain a variety of chemical facies that  
2 1468 are enriched in either Fe-oxyhydroxides, Fe-Si clays, base-metal sulphides, Mn  
3  
4 1469 oxides/carbonates, or sulphates. Nd-Sr-Pb isotopic signatures also differ, with closed-basin  
5  
6 1470 sediments preserving a modest but distinct contribution of basaltic Nd, Sr and Pb, whereas  
7  
8 1471 open-ocean sediments show normal seawater Nd and Sr isotopic signatures, although they can  
9  
10 1472 commonly contain a component of basaltic Pb, even at distances of a thousand kilometres from  
11  
12 1473 the hydrothermal source.

13  
14 1474  
15  
16 1475 The REE patterns of metalliferous sediments in closed basins should retain the positive Eu  
17  
18 1476 anomalies of the high-temperature fluids that enter the basin, owing to the anoxic state of the  
19  
20 1477 pooled brines, which allows Eu to remain in the reduced state and be dispersed laterally. By  
21  
22 1478 contrast, the REE patterns of metalliferous precipitates deposited from non-buoyant plumes in  
23  
24 1479 modern open oceans are seawater-like, with a negative Ce anomaly with no Eu anomaly.

25  
26 1480  
27  
28 1481 Low-temperature Fe-oxyhydroxide sediments formed on and near sulphide mounds on open-  
29  
30 1482 ocean spreading axes can simultaneously show positive Eu and negative Ce anomalies, implying  
31  
32 1483 precipitation from mixtures of high-temperature vent fluid and normal seawater. Metalliferous  
33  
34 1484 sediments can also form in off-axis settings where low-temperature fluids migrate up through  
35  
36 1485 seafloor sediments and react to deposit Fe-silicates, Fe-oxyhydroxides, and locally Mn-oxides,  
37  
38 1486 e.g., the Galapagos hydrothermal mounds. These off-axis deposits display seawater-like REE  
39  
40 1487 patterns and Nd-Sr isotope signatures, but typically contain some basaltic-hydrothermal Pb.

41 1488  
42  
43 1489 Metalliferous sediments in closed anoxic basins such as the Atlantis II Deep can host significant  
44  
45 1490 quantities of base and precious metals where the basins are spatially associated with a heat  
46  
47 1491 source that produces hydrothermal activity over thousands of years. In such basins, most of the  
48  
49 1492 hydrothermally supplied metals are deposited within the confines of the basin, largely as  
50  
51 1493 sulphide-rich muds, Fe-oxyhydroxides and Fe-silicates. In open ocean settings, most of the  
52  
53 1494 metals supplied by axial vents are dispersed laterally as Fe-Mn-oxyhydroxide particulates over a  
54  
55 1495 few thousand kilometres by low-density plumes. Although these particulates absorb some  
56  
57 1496 metals and REEs from seawater during transport and early burial, the metalliferous component  
58  
59 1497 of the final sediment on the seafloor is generally minor owing to dilution by large admixtures of

1498 biogenic carbonate and/or silica. However, in those parts of the deep ocean that lie below the  
1  
21499 CCD, where accumulations rates are very slow, seawater-derived REEs in particular can become  
3  
41500 sufficiently concentrated as to represent a potential economic resource.  
5

## 6. Contributions of Authors

61501  
71502  
81503  
9  
101504  
11  
121505 TJB: project design, collection of samples from Atlantis II Deep and DSDP Leg 92; writing of bulk  
13  
141506 of paper and compilation of data. IJ: REE analysis of Atlantis II Deep sediments. MDH: chemical  
15  
161507 analysis of Leg 92 sediments. MFT: Nd isotope analysis of Atlantis II Deep sediments. IJ, MDH  
17  
181508 and MFT also contributed to writing of specific sections of the paper. IJ produced the final  
19  
201509 versions of the figures.  
21  
22

## 7. Acknowledgements

231510  
241511  
25  
26  
271512 We thank Dr Zohair Nawab and the Joint Saudi-Sudanese Commission on the Red Sea for  
28  
291513 permission to carry out this research project on core material from the Atlantis II Deep. Dr  
30  
311514 Harald Bäcker of Preussag Aktiengesellschaft provided permission to visit Preussag's marine  
32  
331515 technical facility near Hannover, Germany, where the cores were stored at the time of  
34  
351516 sampling; Dr K. Steinkamp provided technical assistance and core logs. Dr Elisabeth Oudin is  
36  
371517 thanked for providing access to an Atlantis II Deep core stored at the BRGM in Orléans, France.  
38  
391518 Dr Martha Scott of Texas A&M University kindly supplied samples of Orca Basin sediment. The  
40  
411519 Deep Sea Drilling Project is gratefully acknowledged for providing samples of Leg 92 drill cores.  
42  
431520 The acquisition of analytical data presented in this study was partly funded by an NSERC  
44  
451521 (Canada) grant to TJB. The paper benefited from insightful reviews by John Slack (USGS), two  
46  
471522 anonymous reviewers, and editor Christina Yan Wang (Guangzhou Institute of Geochemistry).  
48  
491523  
50  
51  
52  
53  
54  
55  
56  
57  
58  
59  
60  
61  
62

**8. References**

- 1524  
1  
2  
3  
4  
5 1525 Aharon, P., 2003. Meltwater flooding events in the Gulf of Mexico revisited: Implications for  
6 1526 rapid climate changes during the last deglaciation. *Paleoceanogr.* 18,  
7  
8 1527 doi:10.1029/2002PA000840, 2003.  
9  
10  
11 1528 Albarède F., Goldstein S.L., 1992. World map of Nd isotopes in sea-floor ferromanganese  
12  
13 1529 deposits. *Geology* 20, 761–763.  
14  
15 1530 Albarède F., Michard A., Minster, J.F., Michard, G., 1981.  $^{87}\text{Sr}/^{86}\text{Sr}$  ratios in hydrothermal  
16  
17 1531 waters and deposits from the East Pacific Rise at 21°N. *Earth Planet. Sci. Lett.* 55, 229–  
18  
19 1532 236.  
20  
21  
22 1533 Alt J.C., 1988. Hydrothermal oxide and nontronite deposits on seamounts in the Eastern Pacific.  
23  
24 1534 *Mar. Geol.* 81, 227–239.  
25  
26 1535 Amakawa, H., Usui, A., Iijima, K., Suzuki, K., 2017. Surface layer Nd isotopic composition of  
27  
28 1536 ferromanganese crusts collected from the Takuyo-Daigo Seamount reflects ambient  
29  
30 1537 seawater. *Geochem. J.*, 51, e1–e7.  
31  
32  
33 1538 Anschutz, P., 2015. Hydrothermal activity and paleoenvironments of the Atlantis II Deep. In:  
34  
35 1539 Rasul, N.M.A., Stewart, I.C.F. (eds.), *The Red Sea: The Formation, Morphology,*  
36 1540 *Oceanography and Environment of a Young Ocean Basin.* Springer Earth System Science  
37  
38 1541 Series, Berlin-Heidelberg, 235–249.  
39  
40  
41 1542 Anschutz, P., Blanc, G., 1995a. Geochemical dynamics of the Atlantis II Deep (Red Sea): Silica  
42  
43 1543 behavior. *Mar. Geol.* 128, 25–36.  
44  
45 1544 Anschutz, P., Blanc, G., 1995b. Diagenetic evolution of the DOP facies from the Atlantis II Deep  
46  
47 1545 (Red Sea): evidence of early hydrothermal activity. *Oceanol. Acta* 18, 105–112.  
48  
49  
50 1546 Anschutz, P., Blanc, G., 1996. Heat and salt fluxes in the Atlantis II Deep (Red Sea). *Earth Planet.*  
51  
52 1547 *Sci. Lett.* 142, 147–159.  
53  
54  
55 1548 Anschutz, P., Blanc, G., Stille, P., 1995. Origin of fluids and the evolution of the Atlantis II Deep  
56 1549 hydrothermal system, Red Sea: Strontium isotope study. *Geochim. Cosmochim. Acta* 59,  
57  
58 1550 4799–4808.  
59  
60  
61  
62  
63  
64  
65

- 1551 Anschutz, P., Turner, J.S., Blanc, G., 1998. The development of layering, fluxes through double-  
1 diffusive interfaces, and location of hydrothermal sources of brines in the Atlantis II Deep:  
21552 Red Sea. *J. Geophys. Res.* 103, 27809–27819.  
3  
41553  
5  
6  
71554 Anschutz, P., Blanc G., Monnin, C., Boulègue J., 2000. Geochemical dynamics of the Atlantis II  
81555 Deep (Red Sea). II: pore water composition of metalliferous sediments. *Geochim.*  
9  
101556 *Cosmochim. Acta* 64, 3995–4006.  
11  
12  
131557 Arz, H.W., Pätzold, J., Müller, P.J., 2003. Influence of Northern Hemisphere climate and global  
14 sea level rise on the restricted Red Sea marine environment during termination I.  
151558 *Paleoceanogr.* 18, 1053, doi:10.1029/2002PA000864.  
16  
171559  
18  
191560 Augustin, N., Devey, C.W., van der Zwan, F.M., Feldens, P., Tominaga, M., Bantan, R.A.,  
20 Kwasnitschka, T., 2014. The rifting to spreading transition in the Red Sea. *Earth Planet.*  
211561 *Sci. Lett.* 395, 217–230.  
22  
231562  
24  
25  
261563 Augustin, N., van der Zwan, F.M., Devey, C.W., Ligi, M., Kwasnitschka, T., Feldens, P., Bantan,  
271564 R.A., Basaham, A.S., 2016. Geomorphology of the central Red Sea Rift: Determining  
28 spreading processes. *Geomorph.* 274, p.162–179.  
291565  
30  
31  
321566 Augustin, N., Devey, C.W., van der Zwan, F.M., 2019. A modern view on the Red Sea Rift:  
33 Tectonics, volcanism and salt blankets. In: Rasul, N.M.A., Stewart, I.C.F. (eds.), *Geological*  
341567 *Setting, Palaeoenvironment and Archaeology of the Red Sea.* Springer Nature AG,  
351568 Switzerland, 37–52.  
36  
371569  
38  
39  
401570 Bäcker, H., 1976. Fazies und chemische Zusammensetzung rezenter Ausfällungen aus  
41 Mineralquellen im Roten Meer. *Geol. Jahrb.* D17, 151–172.  
421571  
43  
44  
451572 Bäcker, H., Richter, H., 1973. Die rezente hydrothermal-sedimentärelagerstätte Atlantis II-tier  
461573 im Roten Meer. *Geol. Rundsch.* 62, 697-740.  
47  
48  
491574 Bäcker, H., Schoell, M., 1972. New deeps with brines and metalliferous sediments in the Red  
50 Sea. *Nature* 240, 153–158.  
511575  
52  
53  
541576 Badaut, D., Decarreau, A., Besson, G., 1992. Ferroporphyrillite and related Fe<sup>3+</sup>-rich 2:1 clays in  
55 recent deposits of Atlantis II Deep, Red Sea. *Clay Min.* 27, 227–244.  
561577  
57  
58  
59  
60  
61  
62

- 1578 Baker, E.T., Urabe, T., 1996. Extensive distribution of hydrothermal plumes along the superfast  
1 spreading East Pacific Rise, 13°30'–18°40'S. *J. Geophys. Res.* 101, 27809–27819.  
2  
3  
4  
51580 Baker, E.T., German, C.R., Elderfield, H., 1995. Hydrothermal plumes over spreading-centre  
6 axes: Global distributions and geological inferences. In: *Seafloor Hydrothermal Systems:  
71581 Physical, Chemical, Biological, and Geological Interactions. Geophysical Monograph Series  
81582 91, American Geophysical Union, Washington, D.C., 47–71.*  
9  
101583  
11  
12  
131584 Balaram, V., 2019. Rare earth elements: A review of applications, occurrence, exploration,  
14 analysis, recycling, and environmental impact. *Geosci. Frontiers* 10, 1285–1303.  
151585  
16  
171586 Barbery, G., Horn, R., Lecuyer, P., Lefeuvre, E., Le Lann, F., Leveque, M.-X., Snoep, J., Thomas,  
18 D., 1981. Atlantis II Feasibility Study. Saudi-Sudanese Red Sea Joint Commission.  
191587  
20  
21  
221588 Barrett, T.J., 1980. The Pb isotopic composition of Jurassic cherts overlying ophiolites in the  
23 North Apennines. *Earth Planet. Sci. Lett.* 49, 193–204.  
241589  
25  
26  
271590 Barrett T.J., 1983. Lead and strontium isotopic composition of some metalliferous and pelagic  
28 sediments and basalts from the Galapagos Mounds area, Deep Sea Drilling Project Leg 70.  
291591 In: Honnorez, J., Von Herzen, R.P., et al., *Init. Repts. DSDP, 70: Washington, D.C. (U.S.  
301592 Govt. Printing Office), 325–332.*  
31  
321593  
33  
34  
351594 Barrett T.J., 1992. Mass changes in the Galápagos hydrothermal mounds: Near-axial sediment  
36 transformation and mineralization. *Geology* 20, 1075–1078.  
371595  
38  
391596 Barrett T.J., Friedrichsen H., 1982. Elemental and isotopic compositions of some metalliferous  
40 and pelagic sediments from the Galapagos Mounds area, DSDP Leg 70. *Chem. Geol.* 36,  
411597 275–298.  
42  
431598  
44  
45  
461599 Barrett, T.J., Jarvis, I., 1988. Rare-earth element geochemistry of metalliferous sediments from  
47 DSDP Leg 92: The East Pacific Rise Transect. *Chem. Geol.* 67, 243–259.  
481600  
49  
501601 Barrett, T.J., Taylor, P.N., Jarvis, I., Lugowski, J., 1986. Pb and Sr isotope and rare earth element  
51 composition of selected metalliferous sediments from Sites 597 to 601, Deep Sea Drilling  
521602 Project Leg 92. In: Leinen, M., Rea, D.K., et al., *Init. Repts. DSDP, 92: Washington, D.C.  
53 (U.S. Govt. Printing Office), 391–407.*  
541603  
55  
561604  
57  
58  
59  
60  
61  
62

- 1605 Barrett, T.J., Taylor, P.N., Lugowski, J., 1987. Metalliferous sediments from DSDP Leg 92: the  
1 East Pacific Rise transect. *Geochim. Cosmochim. Acta* 51, 2241–2253.  
2  
3  
4  
51607 Barrett, T.J., Jarvis, I., Longstaffe, F.J., Farquhar, R., 1988. Geochemical aspects of hydrothermal  
6 sediments in the eastern Pacific Ocean: An update. *Can. Mineral.* 26, 841–858.  
71608  
8  
91609 Barrett, T.J., Jarvis, I., Jarvis, K.E., 1990. Rare earth geochemistry of massive sulfides-sulfates  
10 and gossans on the Southern Explorer Ridge. *Geology* 18, 583–586.  
111610  
12  
13  
141611 Bau, M., Dulski, P., 1999. Comparing yttrium and rare earths in hydrothermal fluids from the  
15 Mid-Atlantic Ridge: Implications for Y and REE behaviour during near-vent mixing and for  
161612 the Y/Ho ratio of Proterozoic seawater. *Chem. Geol.* 155, 77–90.  
171613  
18  
19  
201614 Bau, M., Höndorf, A., Dulski, P., Beukes, N.J., 1997. Sources of rare-earth elements and iron in  
21 Paleoproterozoic iron-formations from the Transvaal Supergroup, South Africa: Evidence  
221615 from neodymium isotopes. *J. Geol.* 105, 121–129.  
23  
241616  
25  
26  
271617 Bekker, A., Slack, J.F., Planavsky, N., Krapež, B., Hofmann, A., Konhauser, K.O., Rouxel, O.J.,  
28 2010. Iron formation: The sedimentary product of a complex interplay among mantle,  
291618 tectonic, oceanic, and biospheric processes. *Econ. Geol.* 105, 467–508.  
301619  
31  
32  
331620 Bender, M., Broecker, W., Gornitz, V., Middel, U., Kay, R., Sun, S.S., Biscaye, P., 1971.  
34 Geochemistry of three cores from the East Pacific Rise. *Earth Planet. Sci. Lett.* 12, 425–  
351621 433.  
361622  
37  
38  
391623 Bertram, C., Krätschell, A., O’Brien, K., Brückmann, W., Proelss, A., Rehdanz, K., 2011.  
40 Metalliferous sediments in the Atlantis II Deep – Assessing the geological and economic  
411624 resource potential and legal constraints. *Res. Policy* 36, 315–329.  
421625  
43  
44  
451626 Bignell, R.D., Cronan, D.S., Tooms, J.S., 1976. Red Sea metalliferous brine precipitates. *Geol.*  
46 Ass. Canada. *Spec. Paper* 14, 147–184.  
471627  
48  
49  
501628 Bischoff, J.L., 1969. Red Sea geothermal brine deposits: Their mineralogy, chemistry and  
51 genesis. In: Degens, E.T., Ross, D.A. (eds.), *Hot Brines and Recent Heavy Metal Deposits in*  
521629 *the Red Sea*. Springer-Verlag, New York, 368–406.  
531630  
54  
55  
561631 Bischoff, J.L., 1972. A ferroan nontronite from the Red Sea geothermal system. *Clays Clay Min.*  
5720, 217–223.  
581632  
59  
60  
61  
62

- 1633 Bischoff, J.L., Manheim, F.T., 1969. Economic potential of the Red Sea heavy metal deposit. In:  
1 Degens, E.T., Ross, D.A. (eds.), *Hot Brines and Recent Heavy Metal Deposits in the Red*  
21634 Sea. Springer-Verlag, New York. 535–541.  
3  
41635  
5  
6  
71636 Bischoff, J.L., Heath, G.R., Leinen, M.L., 1979. Geochemistry of deep-sea sediments from the  
8 Pacific manganese nodule province: DOMES Sites A, B, and C. In: Bischoff, J.L., Piper, D.Z.  
81637 (eds.), *Marine Geology and Oceanography of the Pacific Manganese Nodule Province*.  
9 Plenum Press, New York. 397–436.  
101638  
11  
121639  
13  
14  
151640 Blanc, G., 1987. *Géochimie de la fosse Atlantis II (Mer Rouge). Evolution spatio-temporelle et*  
16 role de l'hydrothermalisme. Unpub. Ph.D. thesis, Univ. Pierre et Marie Curie, Paris VI.  
171641  
18  
191642 Blanc, G., Boulègue, J., Michard A., 1995. Isotope compositions of the Red Sea hydrothermal  
20 end-member. *Comp. Rend. Acad. Sci. Paris, série II* 320, 1187–1193.  
211643  
22  
23  
241644 Blanc, G., Anschutz, P., Pierret, M-C., 1998. Metalliferous sedimentation in the Atlantis II Deep:  
25 A geochemical insight. In: Purser, B.H., Bosence, D.W.J. (eds.), *Sedimentation and*  
261645 *Tectonics in Rift Basins: Red Sea–Gulf of Aden*. Springer, Dordrecht, 505–520.  
271646  
28  
29  
301647 Bao, S.-X., Zhou, H.-Y., Peng, X.-T., Ji, F.-W., Yao, H.-Q., 2008. Geochemistry of REE and yttrium  
31 in hydrothermal fluids from the Endeavour Segment, Juan de Fuca Ridge. *Geochem. J.* 42,  
321648 359–370.  
33  
341649  
35  
36  
371650 Bignell, R., 1975. Timing, distribution and origin of submarine mineralization in the Red Sea.  
38 Inst. Min. Met. Trans. B84, B1–B6.  
391651  
40  
411652 Blum, N., Puchelt, H., 1991. Sedimentary-hosted polymetallic massive sulfide deposits of the  
42 Kebrit and Shaban Deeps, Red Sea. *Mineral. Deposita* 26, 217–227.  
431653  
44  
45  
461654 Bonatti, E., Seyler, M., 1987. Crustal underplating and evolution in the Red Sea rift. *J. Geophys.*  
47 Res. 92, p.12083–12821.  
481655  
49  
501656 Bonatti, E., Cipriani, A., Lupi, L., 2015. The Red Sea: Birth of an ocean. In: Rasul, N.M.A., Stewart,  
51 I.C.F. (eds.), *The Red Sea: The Formation, Morphology, Oceanography and Environment of*  
521657 *a Young Ocean Basin*. Springer, Berlin-Heidelberg, 29–44.  
53  
541658  
55  
56  
57  
58  
59  
60  
61  
62

- 1659 Bosworth, W., 2015. Geological evolution of the Red Sea: Historical background, review, and  
1 synthesis. In: Rasul, N.M.A., Stewart, I.C.F. (eds), *The Red Sea: The Formation,  
21660 Morphology, Oceanography and Environment of a Young Ocean Basin*. Springer Earth  
3  
41661 System Sciences, Berlin, 45–78.  
5  
61662  
7  
81663 Bosworth, W., Stockli, D.F., 2016. Early magmatism in the greater Red Sea rift: Timing and  
9 significance. *Can. J. Earth Sci.* 53, 1158–1176.  
101664  
11  
12  
131665 Bosworth, W., Huchon, P., McClay, K., 2005. The Red Sea and Gulf of Aden basins. *J. Afr. Earth  
14  
151666 Sci.* 43, 334–378.  
16  
171667 Boström, K., Peterson, M.N.A., Joensuu, O., Fisher, D.E., 1969. Aluminum-poor ferromanganese  
18 sediments on active ocean ridges. *J. Geophys. Res.* 74, 3261–3270.  
191668  
20  
21  
221669 Boström, K., Joensuu, O., Valdés, S., Charm, W., Glaccum, R., 1976. Geochemistry and origin of  
23 East Pacific sediments sampled during DSDP Leg 34. In: Yeats, R.S., Hart, S.R., et al., *Init.  
241670 Repts. DSDP, 34: Washington, D.C. (U.S. Govt. Printing Office)*, 559–574.  
251671  
26  
27  
281672 Bosworth, W., 2015. Geological evolution of the Red Sea: Historical background, review, and  
29 synthesis. In: Rasul, N.M.A., Stewart, I.C.F. (eds.), *The Red Sea: The Formation,  
301673 Morphology, Oceanography and Environment of a Young Ocean Basin*. Springer Earth  
31  
321674 System Sciences, Berlin-Heidelberg, 45–78.  
331675  
34  
35  
361676 Bouvier, J.-L., 1991. Total dissolution method for rock samples. MRD/ACS, Geol. Surv. Canada,  
37 Internal Technical Report.  
381677  
39  
40  
411678 Bridgestock, L., Rehkämper, M., van de Flierdt, T., Paul, M., Milne, A., Lohan, M.C., Achterberg,  
42 E.P., 2018. The distribution of lead concentrations and isotope compositions in the  
431679 eastern tropical Atlantic Ocean. *Geochim. Cosmochim. Acta* 225, 36–51.  
441680  
45  
46  
471681 Brooks, R.R., Kaplan, I.R., Peterson, M.N.A., 1969. Trace element composition of Red Sea  
48 geothermal brine and interstitial water. In: Degens, E.T., Ross, D.A. (eds.), *Hot Brines and  
491682 Recent Heavy Metal Deposits in the Red Sea*. Springer-Verlag, Berlin, 180–203.  
501683  
51  
52  
53  
541684 Brueckmann, W., Krätschell, A., Augustin, N., 2017. Data mining the Red Sea Atlantis II Deep.  
55 Offshore Technology Conference, Houston, Texas, May 1-4, 2017. OTC-27764-MS, 10 pp.  
561685  
57  
58  
59  
60  
61  
62

- 1686 Butuzova, G.Y., Lyapunov, S.M., 1995. Rare earth elements in hydrothermal-sedimentary  
1 deposits from the Red Sea. *Lithol. Mineral Res.* 1, 13–26.  
2  
3  
4  
51688 Butuzova, G. Yu., Drits, V.A., Morozov, A.A., Gorschkov, A.I., 1990. Process of formation of iron-  
6 manganese oxyhydroxides in the Atlantis-II and Thetis Deepes of the Red Sea. *Spec. Publ.*  
71689 *Int. Assoc. Sedimentol.* 11, 57–72.  
8  
9  
10  
111691 Censi, P., Raso, M., Saiano, F., Zuddas, P., Oliveri, E., 2019. Zr/Hf ratio and REE behaviour: A  
12 coupled indication of lithogenic input in marginal basins and deep-sea brines. *Deep-Sea*  
131692 *Research Part II* 164, 216–223.  
14  
151693  
16  
171694 Chavagnac, V., German, C.R., Milton, J.A., Palmer, M.R., 2005. Source of REE in sediment cores  
18 from the Rainbow vent site (36°14'N, MAR). *Chem. Geol.* 216, 329–352.  
191695  
20  
21  
221696 Chavagnac, V., Palmer, M.R., Milton, J.A., Green, D.R.H., German, C.R., 2006. Hydrothermal  
23 sediments as a potential record of seawater Nd isotopic compositions: The Rainbow vent  
241697 site (36°14'N, MAR). *Paleoceanogr.* 21, PA3012, 1–13.  
25  
261698  
27  
281699 Chavagnac, V., Ali, H.S., Jeandel, C., Leleu, T., Destrigneville, C., Castillo, A., Cotte, L., Waeles,  
29 M., Cathalot, C., Laes-Huon A., Pelleter E., Nonnotte, P., Sarradin, P.-M., Cannat, M., 2018.  
301700 Sulfate minerals control dissolved rare earth element flux and Nd isotope signature of  
31 buoyant hydrothermal plume (EMSO-Azores, 37°N Mid-Atlantic Ridge). *Chem. Geol.* 499,  
321701 111–125.  
33  
341702  
351703  
36  
37  
381704 Chen, J.H., 1987. U, Th, and Pb isotopes in hot springs on the Juan de Fuca Ridge. *J. Geophys.*  
39 *Res. v.* 92, 11411–11415.  
401705  
41  
42  
431706 Chen, J.H., Wasserburg, G.J., von Damm K.L., Edmond, J.M., 1986. The U-Th-Pb systematics in  
44 hot springs on the East Pacific Rise at 21°N and Guaymas Basin. *Geochim. Cosmochim.*  
451707 *Acta* 50, 2467–2479.  
461708  
47  
48  
491709 Cita, M.B., 1991. Anoxic basins of the eastern Mediterranean: An overview. *Paleoceanogr.* 6,  
50 133–141.  
511710  
52  
53  
541711 Cocherie, A., Calvez, J.T., Oudin-Dunlop, E., 1994. Hydrothermal activity as recorded by Red Sea  
55 sediments: Sr–Nd isotopes and REE signatures. *Mar. Geol.* 118, 291–302.  
561712  
57  
58  
59  
60  
61  
62

- 1713 Cochran, J.R., 2005. Northern Red Sea: Nucleation of an oceanic spreading center within a  
1 continental rift. *Geochem. Geophys. Geosyst.* 6, doi.org/10.1029/2004GC000826.  
21714  
3  
4  
51715 Cole T.G., 1985. Composition, oxygen isotope geochemistry, and origin of smectite in the  
6  
71716 metalliferous sediments of the Bauer Deep, southeast Pacific. *Geochim. Cosmochim. Acta*  
8  
91717 49, 221–235.  
10  
111718 Cole T.G., 1988. The nature and origin of smectite in the Atlantis II Deep, Red Sea. *Can. Min.* 26,  
12  
131719 755–763.  
14  
15  
161720 Corliss J.B., Lyle, M., Dymond, J., 1978. The chemistry of hydrothermal mounds near the  
17  
181721 Galapagos Rift. *Earth Planet. Sci. Lett.* 40, 12–24.  
19  
201722 Coulibaly, A., Anschutz, P., Blanc, G., Malaizé, B., Pujol, C., 2006. The effect of paleo-  
21  
221723 oceanographic changes on the sedimentary recording of hydrothermal activity in the Red  
23  
241724 Sea during the last 30,000 years. *Mar. Geol.* 226, 51–64.  
25  
26  
271725 Courtois, C., Treuil, M., 1977. Distribution des terres rares et de quelques éléments en trace  
28  
291726 dans les sédiments récents des fosses de la mer rouge. *Chem. Geol.* 20, 57–72.  
30  
311727 Cronan, D.S., 1976. Basal metalliferous sediments from the eastern Pacific. *Bull. Geol. Soc. Am.*  
32  
331728 87, 928–934.  
34  
35  
361729 Cuadros, J., Šegvić, B., Dekov, V., Michalski, J.R., Bardají, D.B., 2018. Electron microscopy  
37  
381730 investigation of the genetic link between Fe oxides/oxyhydroxides and nontronite in  
39  
401731 submarine hydrothermal fields. *Mar. Geol.* 395, 247–259.  
41  
421732 Danielsson, L.G., Dyrssen, D., Graneli, A., 1980. Chemical investigations of Atlantis II and  
43  
441733 Discovery brines in the Red Sea. *Geochim. Cosmochim. Acta* 44, 2051–2065.  
45  
46  
471734 Dasch, E.J., Dymond, J., Heath, G.R., 1971. Isotopic analysis of metalliferous sediments from the  
48  
491735 East Pacific Rise. *Earth Planet. Sci. Lett.* 13, 175–180.  
50  
511736 De Baar, H.J.W., Bacon, M.P., Brewer, P.G., 1985. Rare earth elements in the Pacific and Atlantic  
52  
531737 Oceans. *Geochim. Cosmochim. Acta* 49, 1943–1959.  
54  
55  
561738 De Carlo, E.H., McMurtry, G.M., Yeh, H.-W., 1983. Geochemistry of hydrothermal deposits from  
57  
581739 Loihi submarine volcano, Hawaii. *Earth Planet. Sci. Lett.* 66, 438–449.  
59  
60  
61  
62

- 1740 Degens, E.T., Ross, D.A. (eds.), 1969. Hot Brines and Recent Heavy Metal Deposits in the Red  
1 Sea. Springer-Verlag, Berlin, 600 pp.  
21741  
3  
4  
51742 Dekov, V.M., Kamenov, G.D., Stummeyer, J., Thiry, M., Savelli, C., Shanks, W.C., Fortin, D.,  
6  
71743 Kuzmann, E., Vértes, A., 2007. Hydrothermal nontronite formation at Eolo Seamount  
8  
91744 (Aeolian volcanic arc, Tyrrhenian Sea). *Chem. Geol.* 245, 103–119.  
10  
111745 Dekov, V.M., Petersen, S., Garbe-Schonberg, C.D., Kamenov, G.D., Perner, M., Kuzmann, E.,  
12  
131746 Schmidt, M., 2010. Fe-Si-oxyhydroxide deposits at a slow-spreading centre with thickened  
14  
151747 oceanic crust: The Lilliput hydrothermal field (9°33'S, Mid-Atlantic Ridge). *Chem. Geol.*  
16  
171748 278, 186–200.  
18  
191749 De Lange, G.J., Middelburg, J.J., Van der Weijden, C.H., Catalano, G., Luther, G.W. III, Hydes,  
20  
211750 D.J., Woittiez, J.R.W., Klinkhammer, G.P., 1990. Composition of anoxic hypersaline brines  
22  
231751 in the Tyro and Bannock Basins, eastern Mediterranean. *Mar. Chem.* 31, 63–88.  
24  
25  
261752 Delevaux, M.H., Doe, B.R., 1974. Preliminary report on uranium, thorium and lead contents and  
271753 lead isotopic composition of sediment samples from the Red Sea. In: Whitmarsh, R.B.,  
28  
291754 Weser, O.E., Ross, D.A., et al., *Init. Repts. DSDP, 23*: Washington, D.C. (U.S. Govt. Printing  
30  
311755 Office), 943–946.  
32  
33  
341756 Delevaux, M.H., Doe, B.R., Brown, G.F., 1967. Preliminary lead isotope investigations of brine  
351757 from the Red Sea, galena from the Kingdom of Saudi Arabia, and galena from the United  
36  
371758 Arab Republic (Egypt). *Earth Planet. Sci. Lett.* 3, 139–144.  
38  
39  
401759 Derry, L.A., Jacobsen, S.B., 1990. The chemical evolution of Precambrian seawater: Evidence  
41  
421760 from REEs in banded iron formations. *Geochim. Cosmochim. Acta* 54, 2965–2977.  
43  
44  
451761 Deschamps, A., Tivey, M.A., Chadwick, W.W., Jr., Embley, R.W., 2013. Waning magmatic activity  
461762 along the Southern Explorer Ridge revealed through fault restoration of rift topography.  
47  
481763 *Geochem. Geophys. Geosyst.* 14, 1609–1625. doi:10.1002/ggge.20110  
49  
50  
511764 De Villiers, S., 1999. Seawater strontium and Sr/Ca variability in the Atlantic and Pacific Oceans.  
52  
531765 *Earth Planet. Sci. Lett.* 171, 623–634.  
54  
55  
56  
57  
58  
59  
60  
61  
62

- 1766 Dias, Á.S., Mills, R.A., Taylor, R.N., Ferreira, P., Barriga, F.J.A.S., 2008. Geochemistry of a  
1 sediment push-core from the Lucky Strike hydrothermal field, Mid-Atlantic Ridge. *Chem.*  
21767 *Geol.* 247, 339–351.  
3  
41768  
5  
6  
71769 Dosso, L., Bougault, H., Langmuir, C., Bollinger, C., Bonnier, O., Etoubleau, J., 1999. The age and  
8 distribution of mantle heterogeneity along the Mid-Atlantic Ridge (31–41 degrees N).  
9 *Earth Planet. Sci. Lett.* 170, 269–286.  
101771  
11  
12  
131772 Douville, E., Bienvenu, P., Charlou, J.L., Donval, J.P., Fouquet, Y., Appriou, P., Gamo, T., 1999.  
14 Yttrium and rare earth elements in fluids from various deep-sea hydrothermal systems.  
151773 *Geochim. Cosmochim. Acta* 63, 627–643.  
161774  
17  
18  
191775 Douville, E., Charlou, J.L., Oelkers, E.H., Bienvenu, P., Colon, C.F.J., Donval, J.P., Fouquet, Y.,  
20 Prieur, D., Appriou, P., 2002. The Rainbow vent fluids (36°14'N, MAR): The influence of  
211776 ultramafic rocks and phase separation on trace metal content in Mid-Atlantic Ridge  
22 hydrothermal fluids. *Chem. Geol.* 184, 37–48.  
231777  
24  
251778  
26  
271779 Dubinin, A.V., 2000. Geochemistry of rare earth elements in oceanic phillipsites. *Lithol. Min.*  
28 *Resources* 35, 101–108.  
291780  
30  
31  
321781 Dubinin, A.V., Sval'nov, V.N., 2001. Evolution of sedimentation: A study of authigenic and  
33 biogenic phases in pelagic sediments of the Southern Basin, Pacific Ocean. *Geochem. Int.*  
341782 39, 356–372.  
351783  
36  
37  
381784 Dupré, B., Blanc, G., Boulègue, J., Allègre, J., 1988. Metal remobilization at a spreading centre  
39 studied using lead isotopes. *Nature* 333, 165–167.  
401785  
41  
42  
431786 Dutrieux, A.M., 2020. Rise and fall of a hydrothermal system: A tale of metalliferous sediments  
44 (TAG hydrothermal field, MAR, 26°N). Unpub. Ph.D. thesis, University of Southampton,  
451787 U.K., 286 pp.  
461788  
47  
48  
491789 Dymond, J., Corliss, J.B., Heath, G.R., Field, C.W., Dasch, E.J., Veeh, H.H., 1973. Origin of  
50 metalliferous sediments from the Pacific Ocean. *Geol. Soc. Am. Bull.* 84, 3355–3372.  
511790  
52  
53  
541791 Dymond, J., Corliss, J.B., Stilling, R., 1976. Chemical composition and metal accumulation  
55 rates of metalliferous sediments from Sites 319, 320 and 321. In: Yeats, R. S., Hart, S. R.,  
561792 et al., *Init. Repts. DSDP, 34: Washington (U.S. Govt. Printing Office)*, 575–588.  
571793  
58  
59  
60  
61  
62

- 1794 Dymond, J., Corliss, J.B., Cobler, R., Muratli, M., Chou, C., Conard, R., 1980. Composition and  
1 origin of sediments recovered by deep drilling of sediment mounds, Galapagos Spreading  
21795 Center. In: Rosendahl, B.R., Hékinian, R. et al., Init. Repts. DSDP, 54: Washington (U.S.  
3 Govt. Printing Office), 377–385.  
41796  
5  
61797  
7  
81798 Eder, W., Jahnke, L.L., Schmidt, M., Huber, R., 2001. Microbial diversity of the brine-seawater  
9 interface of the Kebrit Deep, Red Sea, studied via 16S rRNA gene sequences and  
101799 cultivation methods. *Appl. Environ. Microbiol.* 67, 3077–3085.  
11  
121800  
13  
14  
151801 Edmond, J.M., Campbell, A.C., Palmer, M.R., German, C.R., 1990. Geochemistry of  
16 hydrothermal fluids from the Mid-Atlantic Ridge: TAG & MARK 1990. *Trans. Am. Geophys.*  
17 Union 43, 1650–1651.  
181803  
19  
20  
211804 Edmonds, H.N., German, C.R., 2004. Particle geochemistry in the Rainbow hydrothermal plume,  
22 Mid-Atlantic Ridge. *Geochim. Cosmochim. Acta* 68, 759–772.  
231805  
24  
25  
261806 Ehrhardt, A. Hübscher, C., 2015. The northern Red Sea in transition from rifting to drifting –  
27 lessons learned from ocean deeps. In: Rasul, N.M.A., Stewart, I.C.F. (eds.), *The Red Sea:  
28 The Formation, Morphology, Oceanography and Environment of a Young Ocean Basin.*  
291808 Springer Earth System Sciences, Berlin-Heidelberg, 99–121.  
30  
311809  
32  
33  
341810 Eissen, J.-P., Juteau, T., Joron, J.-J., Dupré, B., Humler, E., Al’Mukhamedov, A., 1989. Petrology  
35 and geochemistry of basalts from the Red Sea axial rift at 18°N. *J. Petrol.* 30, 791–839.  
361811  
37  
381812 Encyclopædia Britannica, 2011. Red Sea media images. [https://www.britannica.com/place/Red-  
39 Sea/images-videos](https://www.britannica.com/place/Red-Sea/images-videos). Accessed 5th May 2020.  
401813  
41  
42  
431814 Erzinger, J., 1986. Basement geochemistry, Leg 92. In: In: Leinen, M., Rea, D.K., et al., Init.  
44 Repts. DSDP, 92: Washington, D.C. (U.S. Govt. Printing Office), 471–480.  
451815  
46  
47  
481816 Feely, R.A., Gendron, J.F., Baker, E.T., Lebon, G.T., 1994a. Hydrothermal plumes along the East  
49 Pacific Rise, 8°40’ to 11°50’N: Particle distribution and composition. *Earth Planet. Sci. Lett.*  
50 128, 19–36.  
511818  
52  
53  
54  
55  
56  
57  
58  
59  
60  
61  
62

- 1819 Feely, R.A., Massoth, G.J., Trefry, J.H., Baker, E.T., Paulson, A.J., Lebon, G.T., 1994b.  
1  
21820 Composition and sedimentation of hydrothermal plume particles from North Cleft  
3  
41821 segment, Juan de Fuca Ridge. *J. Geophys. Res.* 99, 4985–5006. [https://doi.](https://doi.org/10.1029/93JB02509)  
5  
61822 [org/10.1029/93JB02509](https://doi.org/10.1029/93JB02509)  
7  
81823 Feely, R.A., Baker, E.T., Marumo, K., Urabe, T., Ishibashi, J., Gendron, J., Lebon, G. T., Okamura,  
9  
101824 K., 1996. Hydrothermal plume particles and dissolved phosphate over the superfast-  
11  
121825 spreading southern East Pacific Rise. *Geochim. Cosmochim. Acta* 60, 2297–2323.  
13  
14  
151826 Feely, R.A., Trefry, J.H., Lebon, G.T., German, C.R., 1998. The relationship between P/Fe and  
16  
171827 V/Fe ratios in hydrothermal precipitates and dissolved phosphate in seawater. *Geophys.*  
181828 *Res. Lett.* 25, 2253–2256.  
19  
20  
211829 Ferreira, P.L., 2006. Melt supply and magmatic evolution at a large central MOR volcano located  
22  
231830 in the Lucky Strike segment, 37° N on the Mid-Atlantic Ridge, Azores region. Unpub. Ph.D.  
24  
251831 thesis, University of Southampton, Southampton, U.K., 386 pp.  
26  
271832 Fitzsimmons, J.N., John, S.G., Marsay, C.M., Hoffman, C.L., Nicholas, S.L., Toner, B.M., German,  
28  
291833 C.R., Sherrell, R.M., 2015. Iron persistence in a distal hydrothermal plume supported by  
30  
311834 dissolved–particulate exchange. *Nature Geosci.* 10, 195–201.  
32  
33  
341835 Frost, C.D., O'Nions, R.K., Goldstein, S.L., 1986. Mass balance for Nd in the Mediterranean Sea.  
35  
361836 *Chem. Geol.* 55, 45–50.  
37  
381837 Gale, N.H., Spooner, E.T.C., Potts, P.J., 1981. The lead and strontium isotope geochemistry of  
39  
401838 metalliferous sediments associated with Upper Cretaceous ophiolitic rocks in Cyprus,  
41  
421839 Syria and the Sultanate of Oman, **Can. J. Earth Sci.** 18, 1290–302.  
43  
44  
451840 Gartman, A., Findlay, A.J., 2020. Impacts of hydrothermal plume processes on oceanic metal  
46  
471841 cycles and transport. *Nature Geosci.* 13, 396–402.  
48  
491842 GEBCO Compilation Group, 2020. General bathymetric chart of the oceans, GEBCO 2020 Grid.  
50  
511843 Data accessed 11 June 2020, [doi:10.5285/a29c5465-b138-234d-e053-6c86abc040b9](https://doi.org/10.5285/a29c5465-b138-234d-e053-6c86abc040b9).  
52  
53  
541844 German, C.R., Klinkhammer, G.P., Edmond, J.M., Mitra, A., Elderfield, H., 1990. Hydrothermal  
55  
561845 scavenging of rare-earth elements in the ocean. *Nature* 345, 516–518.  
57  
58  
59  
60  
61  
62

- 1846 German, C.R., Higgs, N.C., Thomson, J., Mills, R., Elderfield, H., Blusztajn, J., Fler, A.P., Bacon,  
1 M.P., 1993. A geochemical study of metalliferous sediment from the TAG hydrothermal  
21847 mound, 26°08'N, Mid-Atlantic Ridge. *J. Geophys. Res.* 98 (B6), 9683–9692.  
3  
41848  
5  
6  
71849 Godfrey, L.V., Mills, R., Elderfield, H., Gurvich, E., 1994. Lead behaviour at the TAG hydrothermal  
81850 vent field, 26°N, Mid-Atlantic Ridge. *Mar. Chem.* 46, 237–254.  
9  
10  
111851 Grandjean, P., Cappetta, H., Michard, A., Albarède, F., 1987. The assessment of REE patterns  
12 and  $^{143}\text{Nd}/^{144}\text{Nd}$  ratios in fish remains. *Earth Planet. Sci. Lett.* 84, 181–196.  
131852  
14  
15  
161853 Grasse, P., Stichel, T., Stumpf, R., Stramma, L., Frank, M., 2012. The distribution of neodymium  
171854 isotopes and concentrations in the Eastern Equatorial Pacific: Water mass advection  
18 versus particle exchange. *Earth Planet. Sci. Lett.* 353–354, 198–207.  
191855  
20  
21  
221856 Greaves, M.J., Elderfield, H., Sholkovitz, E.R., 1994. Aeolian sources of rare earth elements to  
23 the Western Pacific Ocean. *Mar. Chem.* 68, 31–37.  
241857  
25  
26  
271858 Grenne, T., Slack, J.F., 2005. Geochemistry of jasper beds from the Ordovician Løkken ophiolite,  
281859 Norway: Origin of proximal and distal siliceous exhalites. *Econ. Geol.* 100, 1511–1527.  
29  
30  
311860 Grenne, T., Slack, J.F., 2019. Mineralogy and geochemistry of silicate, sulfide, and oxide iron  
32 formations in Norway: Evidence for fluctuating redox states of early Paleozoic marine  
331861 basins. *Min. Deposita* 54, 829–848.  
34  
351862  
36  
37  
381863 Guney, M., Al-Marhoun, M.A., Nawab, Z.A., 1988. Metalliferous sub-marine sediments of the  
391864 Atlantis-II-Deep, Red Sea. *Can. Inst. Min. Metal. Bull.* 81, 33–39.  
40  
41  
421865 Hackett, J., Bischoff, J.L., 1973. New data on the stratigraphy, extent, and geologic history of the  
43 Red Sea geothermal deposits. *Econ. Geol.* 68, 553–564.  
441866  
45  
46  
471867 Halliday, A.N., Davidson, J.P., Holden, P., Owen, R.M., Olivarez, A.M., 1992. Metalliferous  
481868 sediments and the scavenging residence time of Nd near hydrothermal vents. *Geophys.*  
49 Res. Lett. 19, 761–764.  
501869  
51  
52  
531870 Hamer, R.D., 2017. Mineral resources from the seabed: Current status and planning for the  
54 development of the Atlantis II Deep deposit, Red Sea. SIMFE Conference, Khartoum,  
551871 Sudan, March 27-29, 2017 (Powerpoint presentation).  
561872  
57  
58  
59  
60  
61  
62

- 1873 Hannington, M.D., Gorton, M.P., 1991. Analysis of sulfides for gold and associated trace metals  
1 by direct neutron activation with a low-flux reactor. *Geostand. Newslett.* 15, 145–154.  
21874  
3  
4  
51875 Harder, H., 1976. Nontronite synthesis at low temperatures. *Chem. Geol.* 18, 169–180.  
6  
7  
81876 Hartmann, M., 1985. Atlantis II Deep geothermal brine system. Chemical processes between  
9 hydrothermal brines and Red Sea deep water. *Mar. Geol.* 64, 157–177.  
10  
11  
121878 Haase, K.M., Mühe, R., Stoffers, P., 2000. Magmatism during extension of the lithosphere:  
13 Geochemical constraints from lavas of the Shaban Deep, northern Red Sea. *Chem. Geol.*  
141879 166, 225–239.  
15  
161880  
17  
18  
191881 Heath, G.R., Dymond, J., 1977. Genesis and transformation of metalliferous sediments from the  
20 East Pacific Rise, Bauer Deep, and northern Nazca Plate. *Geol. Soc. Am. Bull.* 88, 723–733.  
21  
22  
231883 Heath, G.R., Dymond, J., 1981. Metalliferous sediment deposition in time and space: East  
24 Pacific Rise and Bauer Basin, northern Nazca Plate. *Geol. Soc. Am. Mem.* 154, 175–197.  
251884  
26  
27  
281885 Hegner, E., Tatsumoto, M., 1987. Pb, Sr, and Nd isotopes in basalts and sulfides from the Juan  
29 de Fuca Ridge. *J. Geophys. Res.* 92, 11380–11386.  
301886  
31  
321887 Hein, J.R., Mizell, K., Koschinsky, A., Conrad, T.A., 2013. Deep-ocean mineral deposits as a  
33 source of critical metals for high- and green-technology applications: Comparison with  
341888 land-based resources. *Ore Geol. Rev.* 51, 1–14.  
35  
361889  
37  
38  
391890 Hékinian, R., Rosendahl, B.R., Cronan, D.S., Dmitriev, Y., Fodor, R.V., Goll, R.M., Hoffert, M.,  
40 Humphris, S.E., Matthey, D.P., Matland, J., Petersen, N., Roggenthen, W., Schrader, E.L.,  
411891 Srivastava, R.K., Warren, N., 1978. Hydrothermal deposits and associated basement rocks  
42 from the Galapagos Spreading Center. *Oceanolog. Acta* 1, 473–482.  
43  
441893  
45  
46  
471894 Hékinian R., Hoffert M., Larqué, P., Cheminée J. L., Stoffers P. and Bideau D., 1993.  
48 Hydrothermal Fe and Si oxyhydroxide deposits from South Pacific intraplate volcanoes  
491895 and East Pacific Rise axial and off-axial regions. *Econ. Geol.* 88, 2099–2121.  
501896  
51  
52  
531897 Hemleben, C., Meischner, D., Zahn, R., Almogi-Labin, A., Erlenkeuser, H., Hiller, B., 1996. Three  
54 hundred eighty thousand year long stable isotope and faunal records from the Red Sea:  
551898 Influence of global sea level change on hydrography. *Paleoceanogr.* 11, 147–156.  
56  
571899  
58  
59  
60  
61  
62

- 1900 Hinkley, T.K., Tatsumoto, M., 1987. Metals and isotopes in Juan de Fuca Ridge hydrothermal  
1 fluids and their associated solid materials. *J. Geophys. Res.* 92, 11400–11410.  
2  
3  
4  
51902 Höfig, T.W., Hoernle, K., Hauff, F., Frank, M., 2016. Hydrothermal versus active margin  
6 sediment supply to the eastern equatorial Pacific over the past 23 million years traced by  
71903 radiogenic Pb isotopes: Paleoceanographic and paleoclimatic implications. *Geochim.*  
81904 *Cosmochim. Acta* 190, 213–238.  
9  
101905  
11  
12  
131906 Honnorez, J., Von Herzen, R.P., Barrett, T., Becker, K., Bender, M., Borella, P., Hubberten, H.-W.,  
14  
151907 Jones, S., Karato, S., Laverne, C., Levi, S., Migdisov, A., Moorby, S.A., Schrader, E.L., 1981.  
16 Preliminary results of Deep Sea Drilling Project, Leg 70. *Geol. Soc. Am. Bull.* 92, 457–472.  
171908  
18  
191909 Honnorez, J., Karpoff, A.M., Trauth Badaut, D., 1983. Sedimentology, mineralogy and  
20 geochemistry of green clay samples from the Galapagos hydrothermal mounds, holes  
211910 506, 506C, and 507D Deep Sea Drilling Project leg 70. In: Honnorez, J., Von Herzen, R.P.,  
22 et al., *Init. Repts. DSDP, 70: Washington, D.C. (U.S. Govt. Printing Office)*, 221–224.  
231911  
241912  
25  
26  
271913 Honnorez, J., Von Herzen, R.P. et al., 1983. *Init. Repts. DSDP, 70: Washington (U.S. Govt.*  
28 *Printing Office)*.  
291914  
30  
31  
321915 Hovland, M., Rueslåtten, H., Johnsen, H.K., 2015. Red Sea salt formations—A result of  
33 hydrothermal processes. In: Rasul, N.M.A., Stewart, I.C.F. (eds.), *The Red Sea: The*  
341916 *Formation, Morphology, Oceanography and Environment of a Young Ocean Basin.*  
351917 Springer Earth System Sciences, Berlin-Heidelberg, 187–203.  
361918  
37  
38  
39  
401919 Humphris, S.E., 1998. Rare earth element composition of anhydrite: Implications for deposition  
41 and mobility within the active TAG hydrothermal mound. In: *Proc. ODP, Sci. Results, Vol.*  
421920 *158 (P.M. Herzig, S.E. Humphris, D.J. Miller, R.A. Zierenberg, eds.)*, College Station, Texas  
431921 (Ocean Drilling Program), 143–159.  
441922  
45  
46  
47  
481923 Hurtgen, M.T., Lyons, T.W., Ingall, E.D., Cruse, A.M., 1999. Anomalous enrichments of iron  
49 monosulfide in euxinic marine sediments and the role of H<sub>2</sub>S in iron sulfide  
501924 transformations: Examples from Effingham Inlet, Orca Basin, and the Black Sea. *Am. J. Sci.*  
51 299, 556–588.  
521925  
531926  
54  
55  
56  
57  
58  
59  
60  
61  
62

- 1927 Iijima, K., Yasukawa, K., Fujinaga, K., Nakamura, K., Machida, S., Takaya, Y., Ohta, J., Haraguchi,  
1  
21928 S., Nishio, T., Usui, Y., Nozaki, T., Yamazaki, T., Ichiyama, Y., Ijiri, A., Inagaki, F.,  
3  
41929 Machiyama, H., Suzuki, K., Kato, Y., 2016. Discovery of extremely REY-rich mud in the  
5  
61930 western North Pacific Ocean. *Geochem. J.* 50, 557–573.  
7  
81931 Jacobsen S.B., Pimentel-Klose M.R., 1988. Neodymium isotopic variations in Precambrian  
9  
101932 banded iron formations. *Geophys. Res. Lett.* 15, 393–396.  
11  
12  
131933 Jarvis, I., 1985. Geochemistry and origin of Eocene-Oligocene metalliferous sediments from the  
14  
151934 central equatorial Pacific: Deep Sea Drilling Project Sites 573 and 574. In: Mayer, L.,  
16  
171935 Theyer, F., et al., *Init. Repts. DSDP, 85*: Washington, D.C. (U.S. Govt. Printing Office), 781–  
181936 804.  
19  
20  
211937 Jarvis, I., 2003. Sample preparation for ICP-MS. In: *Handbook of Inductively Coupled Plasma*  
22  
231938 *Mass Spectrometry* (Jarvis, K.E., Gray, A.L., Houk, R.S., eds.), Viridian, Woking, 172–224.  
24  
25  
261939 Jarvis I., Jarvis, K.E., 1985. Rare-earth element geochemistry of standard sediments: A study  
271940 using inductively coupled plasma spectrometry. *Chem. Geol.* 53, 335–344.  
28  
29  
301941 Jarvis, K.E., Gray, A.L., McCurdy, E., 1989. Avoidance of spectral interference on europium in  
31  
321942 inductively coupled plasma-mass spectrometry by sensitive measurement of the doubly  
33  
341943 charged ion. *J. Anal. Atom. Spectr.* 4, 743–748.  
35  
36  
371944 Jeandel, C., Delattre, H., Grenier, M., Pradoux, C., Lacan, F., 2013. Rare earth element  
381945 concentrations and Nd isotopes in the southeast Pacific Ocean. *Geochem. Geophys.*  
39  
401946 *Geosyst.* 14, 328–341.  
41  
42  
431947 Josso, 2017. Investigating the potential recovery of REY from metalliferous sediments in a  
44  
451948 seafloor analogue: The Troodos ophiolite, Cyprus. Unpub. Ph.D. thesis, Southampton  
461949 University, U.K., 201 pp.  
47  
48  
491950 Karbe, L., 1987. Hot brines and the deep sea environment. In: Edwards. A.J., Head, S.M. (eds.),  
50  
511951 *Key Environment, Red Sea*. Pergamon Press, Oxford, p. 70–89.  
52  
531952 Kashiwabara, T., Toda, R., Nakamura, K., Yasukawa, K., Fujinaga, K., Kubo, S., Nozaki, T.,  
54  
551953 Takahashi, Y., Suzuki, K., Kato, Y., 2018. Synchrotron X-ray spectroscopic perspective on  
56  
571954 the formation mechanism of REY-rich muds in the Pacific Ocean. *Geochim. Cosmochim.*  
58  
591955 *Acta* 240, 274–292. <https://doi.org/10.1016/j.gca.2018.08.013>  
60  
61  
62

- 1956 Kastner, M., 1986. Mineralogy and diagenesis of sediments at Site 597: Preliminary results. In:  
1 Honnorez, J., Von Herzen, R.P., et al., Init. Repts. DSDP, 70: Washington, D.C. (U.S. Govt.  
2 Printing Office), 345–349.  
3  
41958  
5  
61959 Kato, Y., Ohta, I., Tsunematsu, T., Watanabe, Y., Isozaki, Y., Maruyama, S., Imai, N., 1998. Rare  
7 earth element variations in mid-Archean banded iron formations: Implications for the  
8 chemistry of ocean and continent and plate tectonics. *Geochim. Cosmochim. Acta* 62,  
9 3475–349.  
101961  
11  
121962  
13  
14  
151963 Kato, Y., Fujinaga, K., Suzuki, K., 2005. Major and trace element geochemistry and Os isotopic  
16 composition of metalliferous umbers from the Late Cretaceous Japanese accretionary  
17 complex. *Geochem. Geophys. Geosys.* 6, doi.org/10.1029/2005GC000920.  
181965  
19  
20  
211966 Kato, Y., Fujinaga, K., Nakamura, K., Takaya, Y., Kitamura, K., Ohta, J., Toda, R., Nakashima, T.,  
22 Iwamori, H., 2011. Deep-sea mud in the Pacific Ocean as a potential resource for rare-  
23 earth elements. *Nature Geosci.* 4, 535–539.  
24  
251968  
26  
271969 Knüttel, S., 1986. Calcareous nannofossil biostratigraphy of the central East Pacific Rise, Deep  
28 Sea Drilling Project Leg 92: Evidence for downslope transport of sediments. In: Leinen, M.,  
29 Rea, D.K., et al., Init. Repts. DSDP, 92: Washington (U.S. Govt. Printing Office), 255–290.  
30  
311971  
32  
33  
341972 Kon Y., Hoshino, M., Sanematsu, K., Morita, S., Tsunematsu, M., Okamoto, N., Yano, N., Tanaka,  
35 M., Takagi, T., 2014. Geochemical characteristics of apatite in heavy REE-rich deep-sea  
36 mud from Minami-Torishima area, southeastern Japan. *Res. Geol.* 64, 47–57.  
371974  
38  
39  
401975 Konhauser, K.O., Planavsky, N.J., Hardisty, D.S., Robbins, L.J., Warchola, T.J., Haugaard, R.,  
41 Lalonde, S.V., Partin, C.A., Oonk, P.B.H., Tsikos, H., Lyons, T.W., Bekker, A., Johnson, C.M.,  
421976 2017. Iron formations: A global record of Neoproterozoic to Palaeoproterozoic  
43 environmental history. *Earth-Sci. Rev.* 172, 140–177. [https://doi.  
441977 org/10.1016/j.earscirev.2017.06.012](https://doi.org/10.1016/j.earscirev.2017.06.012)  
451978  
46  
471979  
48  
49  
501980 Ku, T.L., Thurber, D.L., Mathieu, G.G., 1969. Radiocarbon chronology of Red Sea sediments. In:  
51 Degens, E.T., Ross, D.A. (eds.), *Hot Brines and Recent Heavy Metal Deposits in the Red  
521981 Sea*. Springer-Verlag, New York. 348–359.  
53  
541982  
55  
561983 Lacan, F., Tachikawa, K., Jeandel, C., 2012. Neodymium isotopic composition of the oceans: a  
57 compilation of seawater data. *Chem. Geol.* 300–301, 177–184.  
581984  
59  
60  
61  
62

- 1985 Langmuir, C., Humphris, S., Fornari, D., Van Dover, C., Von Damm, K., Tivey, M.K., Colodner, D.,  
1  
21986 Charlou, J.L., Desonie, D., Wilson, C., 1997. Hydrothermal vents near a mantle hot spot:  
3  
41987 The Lucky Strike vent field at 37°N on the Mid-Atlantic Ridge. *Earth Planet. Sci. Lett.* 148,  
5  
61988 69–91.  
7  
81989 Laurila, T.E., 2015. The Metalliferous Sediments of the Atlantis II Deep (Red Sea). Unpub. Ph.D.  
9  
101990 thesis, University of Ottawa, Ottawa, Canada, 642 pp.  
11  
12  
131991 Laurila, T.E., Hannington, M.D., Petersen, S., Garbe-Schönberg, D., 2014a. Trace metal  
14  
151992 distribution in the Atlantis II Deep (Red Sea) sediments. *Chem. Geol.* 386, 80–100.  
16  
17  
181993 Laurila, T.E., Hannington, M.D., Petersen, S., Garbe-Schönberg, D., 2014b. Early depositional  
191994 history of metalliferous sediments in the Atlantis II Deep of the Red Sea: Evidence from  
20  
211995 rare earth element geochemistry. *Geochim. Cosmochim. Acta* 126, 146–168.  
22  
23  
241996 Laurila, T.E., Hannington, M.D., Leybourne, M., Petersen, S., Devey, C.W., Garbe-Schönberg, D.,  
25  
261997 2015. New insights into the mineralogy of the Atlantis II Deep metalliferous sediments,  
271998 Red Sea. *Geochem. Geophys. Geosyst.* 16, 4449–4478, doi:10.1002/2015GC006010.  
28  
29  
301999 Leinen, M., Rea, D.K., et al., 1986. *Init. Repts. DSDP, 92*: Washington, D.C. (U.S. Govt. Printing  
31  
322000 Office).  
33  
34  
352001 Leinen, M., Stakes, D., 1979. Metal accumulation rates in the central equatorial Pacific during  
36  
372002 Cenozoic time. *Geol. Soc. Am. Bull.* 90, 357–375.  
38  
39  
402003 Li, Y.-H., Schoonmaker, J.H., 2003. Chemical composition and mineralogy of marine sediments.  
412004 In: *Treatise on Geochemistry*, v.7, Elsevier, Amsterdam 1–35.  
42  
43  
442005 Ligi, M., Bonatti, E., Bortoluzzi, G., Cipriani, A., Cocchi, L., Caratori Tontini, F., Carminati, E.,  
45  
462006 Ottolini, L., Schettino, A., 2012. Birth of an ocean in the Red Sea: Initial pangs. *Geochem.*  
47  
482007 *Geophys. Geosys.* 13, Q08009. <https://doi.org/10.1029/2012GC004155>.  
49  
502008 Ligi, M., Bonatti, E., Rasul, N.M.A., 2015. Seafloor spreading initiation: Geophysical and  
51  
522009 geochemical constraints from the Thetis and Nereus Deeps, central Red Sea. In: Rasul,  
53  
542010 N.M.A., Stewart, I.C.F. (eds.), *The Red Sea: The Formation, Morphology, Oceanography*  
55  
562011 *and Environment of a Young Ocean Basin*. Springer Earth System Sciences, Berlin-  
572012 Heidelberg, 79–98.  
58  
59  
60  
61  
62

- 1 2013 Ligi, M., Bonatti, E., Bosworth, W., Cai, Y., Cipriana, A., Palmiotto, C., Ronca, S., Seyler, M., 2018.  
2 2014 Birth of an ocean in the Red Sea: Oceanic-type basaltic melt intrusions precede  
3 continental rapture. *Gondwana Res.* 54, 150–160.  
4 2015  
5  
6 2016 Ling, H.-F., Jiang, S.-Y., Frank, M., Zhou, H.-Y., Zhou, F., Lu, Z.-L., Chen, X.-M., Jiang, Y.-H., Ge, C.-  
7 D., 2005. Differing controls over the Cenozoic Pb and Nd isotope evolution of deepwater  
8 in the central North Pacific Ocean. *Earth Planet. Sci. Lett.* 232, 345–361.  
9 2018  
10  
11  
12 2019 Little, C.T.S., Johannessen, K.C., Bengtson, S., Chan, C.S., Ivarsson, M., Slack, J.F., Broman, C.,  
13  
14 2020 Thorseth, I.H., Grenne, T., Rouxel, O.J., Bekker, A., 2021. A late Paleoproterozoic (1.74 Ga)  
15 deep-sea, low-temperature, iron-oxidizing microbial hydrothermal vent community from  
16 Arizona, USA. *Geobiology* 19, 228-249, doi:10.1111/gbi.12434.  
17 2021  
18  
19 2022  
20  
21 2023 Lode, S., Piercey, S.J., Squires, G.C., 2016. Role of metalliferous mudstones and detrital shales in  
22 the localization, genesis, and paleoenvironment of volcanogenic massive sulphide  
23 deposits of the Tally Pond volcanic belt, central Newfoundland, Canada. *Can. J. Earth Sci.*  
24 53, 1–29.  
25 2025  
26 2026  
27  
28  
29 2027 Lubetkin, M., Carey, S., Kelley, K.A., Robert, G., Cornell, W., Raineault, N., Balcanoff, J., Ballard,  
30 R.D., Salinas-de-León, P., 2018. Nontronite-bearing tubular hydrothermal deposits from a  
31 Galapagos seamount. *Deep Sea Res., Part II*, 150, 181–144.  
32 2029  
33  
34  
35 2030 Lupton, J.E., Craig, H., 1981. A major helium-3 source at 15°S on the East Pacific Rise. *Science*  
36 214, 13–18.  
37 2031  
38  
39 2032 Lupton, J.E., Weiss, R.F., Craig H., 1977. Mantle helium in the Red Sea brines. *Nature* 266, 244–  
40 246.  
41 2033  
42  
43  
44 2034 Luther, G.W. III, Catalano, G., de Lange G.J., Woittiez, J.R.W., 1990. Reduced sulfur in the  
45 hypersaline anoxic basins of the Mediterranean Sea. *Mar. Chem.* 31, 137–152.  
46 2035  
47  
48  
49 2036 Lyle, M.W., 1986. Major element composition of Leg 92 sediments. In: Leinen, M., Rea, D.K., et  
50 al., *Init. Repts. DSDP, 92: Washington, D.C. (U.S. Govt. Printing Office)*, 355–370.  
51 2037  
52  
53  
54 2038 Lyle, M., Leinen, M., Owen, R.M., Rea, D.K., 1987. Late Tertiary history of hydrothermal  
55 deposition at the East Pacific Rise, 19°S: Correlation to volcano-tectonic events. *Geophys.*  
56 14, 595–598.  
57 2040  
58  
59  
60  
61  
62

- 2041 Maciag, Ł., Zawadzki, D., 2019. Spatial variability and resources estimation of selected critical  
1 metals and rare earth elements in surface sediments from the Clarion-Clipperton Fracture  
22042 Zone, equatorial Pacific Ocean, Interoceanmetal claim area. In: Proceedings of the IAMG  
3  
42043 2019 – 20th Annual Conference of the International Association for Mathematical  
5  
62044 Geosciences, State College, PA, USA, IAMG: Lawrence, Kansas, USA 174–178.  
72045  
8  
9  
102046 Manheim, F.T., Siems, D.E., 1974. Chemical analyses of Red Sea sediments. In: Whitmarsh, R.B.,  
11  
122047 Weser, O.E., Ross, D.A., et al., Init. Repts. DSDP, 23: Washington, D.C. (U.S. Govt. Printing  
13  
142048 Office), 923–938.  
15  
162049 Marchig, V., Erzinger, J., 1986. Chemical composition of Pacific sediments near 20°S: Changes  
17  
182050 with increasing distance from the East Pacific Rise. In: Leinen, M., Rea, D.K., et al., Init.  
19  
202051 Rept. DSDP, 92: Washington, D.C. (U.S. Govt. Printing Office), 371–381.  
21  
22  
232052 Marchig, V., Gundlach, H., 1982. Iron-rich metalliferous sediments on the East Pacific Rise–  
24  
252053 Prototype of undifferentiated metalliferous sediments in divergent plate boundaries.  
262054 Earth Planet. Sci. Lett. 58, 361–382.  
27  
28  
292055 Marchig, V., Gundlach, H., Moller, P., Schley, R., 1982. Some geochemical indicators for  
30  
312056 discriminating between diagenetic and hydrothermal metalliferous sediments. Mar. Geol.  
32  
332057 50, 241–256.  
34  
352058 Martin, E.E., Haley, B.A., 2000. Fossil fish teeth as proxies for seawater Sr and Nd isotopes.  
36  
372059 Geochim. Cosmochim. Acta 64, 835–847.  
38  
39  
402060 McLennan, S.M., 1989. Rare earth elements in sedimentary rocks: Influence of provenance and  
41  
422061 sedimentary processes. In: Lipin, B.R., McKay, G.A. (eds.), Geochemistry and Mineralogy  
43  
442062 of Rare Earth Elements. Rev. Mineral. 21, 169–200.  
45  
462063 McMurtry, G.M., Wang, C.-H., Yeh, H.-W., 1983. Chemical and isotopic investigations into the  
47  
482064 origin of clay minerals from the Galapagos hydrothermal mound field. Geochim.  
49  
502065 Cosmochim. Acta 47, 475–489.  
51  
52  
532066 McMurtry, G.M., Sedwick, P.N., Fryer, P., VonderHaar, D.L., Yeh, H.-W., 1993. Unusual  
54  
552067 geochemistry of hydrothermal vents on submarine arc volcanoes: Kasuga Seamounts,  
562068 northern Mariana arc. Earth Planet. Sci. Lett. 114, 517–528.  
57  
58  
59  
60  
61  
62

- 2069 Michard, A., Albarède, F., 1986. The REE content of some hydrothermal fluids. *Chem. Geol.* 55,  
1 51–60.  
22070  
3  
4  
52071 Michard, G., Albarède, F., Michard, A., Minster, J.-F., Charlou, J.-L., Tan, N., 1984. Chemistry of  
6 solutions from the 13°N East Pacific Rise hydrothermal site. *Earth Planet. Sci. Lett.* 67,  
72072 297–307.  
82073  
9  
10  
112074 Miller, A.R., Densmore, C.D., Degens, E.T., Hathaway, J.C., Manheim, F.T., McFarling, P.F.,  
12 Pocklington, R., Jokela, A., 1966. Hot brines and recent iron deposits in deeps of the Red  
132075 Sea. *Geochim. Cosmochim. Acta* 30, 341–359.  
14  
152076  
16  
172077 Mills, R., Elderfield, H., Thomson, J., 1993. A dual origin for the hydrothermal component in a  
182078 metalliferous sediment core from the Mid-Atlantic Ridge. *J. Geophys. Res.* 98, 9671–9682.  
19  
20  
21  
222079 Mills, R.A., Elderfield, H., 1995. Rare earth element geochemistry of hydrothermal deposits  
23 from the active TAG Mound, 26°N Mid-Atlantic Ridge. *Geochim. Cosmochim. Acta* 95,  
242080 3511–3524.  
25  
262081  
27  
282082 Mills, R.A., Wells, D.M., Roberts, S., 2001. Genesis of ferromanganese crusts from the TAG  
29 hydrothermal field. *Chem. Geol.* 176, 283–293.  
302083  
31  
32  
332084 Mitchell, N.C., Ligi, M., Ferrante, V., Bonatti, E., Rutter, E., 2010. Submarine salt flows in the  
34 central Red Sea. *Geol. Soc. Am. Bull.* 122, 701–713.  
352085  
36  
37  
382086 Mitra, A., Elderfield, H., Greaves, M., 1994. Rare earth elements in submarine hydrothermal  
392087 fluids and plumes from the Mid-Atlantic Ridge. *Mar. Geol.* 46, 217–236.  
40  
41  
422088 Molina-Kescher, M., Frank, M., Hathorne, E., 2014. South Pacific dissolved Nd isotope  
43 compositions and rare earth element distributions: Water mass mixing versus  
442089 biogeochemical cycling. *Geochim. Cosmochim. Acta* 127, 171–189.  
45  
462090  
47  
482091 Moorby, S.A., 1983. The geochemistry of transitional sediments recovered from the Galapagos  
49 hydrothermal mounds field during DSDP Leg 70—Implications for mounds formation.  
502092 *Earth Planet. Sci. Lett.* 62, 367–376.  
51  
522093  
53  
54  
552094 Moorby, S.A., Cronan, D.S., 1983. The geochemistry of hydrothermal and pelagic sediments  
56 from the Galapagos hydrothermal mounds field, DSDP Leg 70. *Min. Mag.* 47, 291–300.  
572095  
58  
59  
60  
61  
62

- 2096 Murnane, R., Clague, R.A., 1983. Nontronite from a low-temperature hydrothermal system on  
1 the Juan de Fuca Ridge. *Earth Planet. Sci. Lett.* 65, 343–352.  
22097  
3  
4  
52098 Mustafa, H.E.Z., Nawab, Z., Horn, R., LeLann, F., 1984. Economic interest of hydrothermal  
6 deposits. The Atlantis II Project. In: *Proc. Second Int. Seminar Offshore Mineral Resources*  
72099 (GERMINAL), Brest, France, 509–538.  
82100  
9  
10  
112101 Nakamura, K., Fujinaga, K., Yasukawa, K., Takaya, Y., Ohta, J., Machida, S., Haraguchi, S., Kato,  
12 Y., 2015. REY-rich mud: A deep-sea mineral resource for rare earths and yttrium. In:  
132102 *Handbook on the Physics and Chemistry of Rare Earths*, Elsevier, Amsterdam, The  
14 Netherlands 46, 79–127.  
152103  
162104  
17  
18  
192105 Nawab, Z.A., 1984. Red Sea mining: a new era. *Deep-Sea Res.* 31A, 813–822.  
20  
21  
222106 Ohta, J., Yasukawa, K., Machida, S., Fujinaga, K., Nakamura, K., Takaya, Y., Iijima, K., Suzuki, K.,  
23 Kato, Y., 2016. Geological factors responsible for REY-rich mud in the western North  
242107 Pacific Ocean: Implications from mineralogy and grain size distributions. *Geochem. J.* 50,  
25 591–603.  
262108  
272109  
28  
29  
302110 Olivarez, A.M., R.M. Owen, 1989. REE/Fe variations in hydrothermal sediments: Implications for  
31 the REE content of seawater. *Geochim. Cosmochim. Acta* 53, 757–762.  
322111  
33  
34  
352112 O'Nions, R.K., Carter, S.R., Cohen, R.S., Evensen, N.M., Hamilton, P.J., 1978. Pb, Nd and Sr  
36 isotopes in oceanic ferromanganese deposits and ocean floor basalts. *Nature* 273, 435–  
372113 438.  
382114  
39  
40  
412115 Oudin, E., 1987. Trace element and precious metal concentrations in East Pacific Rise, Cyprus  
42 and Red Sea submarine sulfide deposits. In: Teleki, P.G., Dobson, M.R., Moore, J.R.,  
432116 Stackelberg, U. (eds.), *Marine Minerals: Advances in Research and Resource Assessment*  
44 Strategies. *Proc. NATO Advanced Research Workshop, Series C.* 194, 349–362.  
452117  
462118  
47  
48  
492119 Oudin, E., Cocherie, A., 1988. Fish debris record the hydrothermal activity in the Atlantis II Deep  
50 sediments (Red Sea). *Geochim. Cosmochim. Acta* 52, 177–184.  
512120  
52  
53  
542121 Oudin, E., Thisse, Y., Ramboz, C., 1984. Fluid inclusion and mineralogical evidence for high  
55 temperature saline hydrothermal circulation in the Red Sea metalliferous sediments:  
562122 Preliminary results. *Mar. Mining* 5, 3–31.  
572123  
58  
59  
60  
61  
62

- 2124 Owen, R.M., Olivarez, A.M., 1988. Geochemistry of rare earth elements in Pacific hydrothermal  
1  
22125 sediments. *Mar. Chem.* 25, 183–196.  
3  
4  
52126 Pak, S.J., Seo, I., Lee, K.Y., Hyeong, K., 2019. Rare earth elements and other critical metals in  
6  
72127 deep seabed mineral deposits: Composition and implications for resource potential.  
8  
92128 *Minerals* 9, 1–19.  
10  
112129 Palchan, D., Stein, M., Almogi-Labin, A., Erel, Y., Goldstein, S., 2013. Dust transport and synoptic  
12  
132130 conditions over the Sahara–Arabia deserts during the MIS6/5 and 2/1 transitions from  
14  
152131 grain-size, chemical and isotopic properties of Red Sea cores. *Earth Planet. Sci. Lett.* 382,  
16  
172132 125–139.  
18  
192133 Palchan, D., Stein, M., Goldstein, S.L., Almogi-Labin, A., Tirosh, O., Erel, Y., 2018. Synoptic  
20  
212134 conditions of fine-particle transport to the last interglacial Red Sea-Dead Sea from Nd-Sr  
22  
232135 compositions of sediment cores. *Quat. Sci. Rev.* 179, 123–136.  
24  
25  
262136 Palmer, M.R., 1985. Rare earth elements in foraminifera. *Earth Planet. Sci. Lett.* 73, 285–298.  
27  
28  
292137 Palmer, M.R., Elderfield, H., 1985. Variations in the Nd isotopic composition of foraminifera  
30  
312138 from Atlantic Ocean sediments. *Earth Planet. Sci. Lett.* 73, 299–305.  
32  
332139 Pan, A., Yang, Q., Zhou, H., Ji, F., Wang, Hu, Pancost, R.D., 2018. Geochemical impacts of  
34  
352140 hydrothermal activity on surface deposits at the Southwest Indian Ridge. *Deep Sea Res.*  
36  
372141 *Part I: Oceanog. Res. Paper* 139, 1-13.  
38  
39  
402142 Paul, S.A.L., Volz, J.B., Bau, M., Köster, M., Kasten, S., Koschinsky, A., 2019. Calcium phosphate  
41  
422143 control of REY patterns of siliceous-ooze-rich deep-sea sediments from the central  
43  
442144 equatorial Pacific. *Geochim. Cosmochim. Acta* 251, 56–72.  
45  
462145 Pedersen, R.B., Furnes, H., 2001. Nd-and Pb-isotopic variations through the upper oceanic crust  
47  
482146 in DSDP/ODP Hole 504B, Costa Rica Rift. *Earth Planet. Sci. Lett.* 189, 221–235.  
49  
50  
512147 Piepgras, D.J., Wasserburg, G.J., 1985. Strontium and neodymium isotopes in hot springs on the  
52  
532148 East Pacific Rise and Guaymas Basin. *Earth Planet. Sci. Lett.* 72, 341–356.  
54  
552149 Piepgras, D.J., Wasserburg, G.J., Dasch, E.J., 1979. The isotopic composition of Nd in different  
56  
572150 ocean masses. *Earth Planet. Sci. Lett.* 45, 223–236.  
58  
59  
60  
61  
62

- 1 2151 Pierret, M.-C., Blanc, G., Bosch, D., 1998. Sr, Pb isotopes and REE analyses of five cores of the  
2 2152 Red Sea: An insight into hydrothermal input. *Min. Mag.* 62A, 1176–1177.  
3  
4  
5 2153 Pierret, M.-C., Clauer, N., Bosch, D., Blanc, G., France-Lanord, C., 2001. Chemical and isotopic  
6 2154 ( $^{87}\text{Sr}/^{86}\text{Sr}$ ,  $\delta^{18}\text{O}$ ,  $\delta\text{D}$ ) constraints to the formation processes of Red-Sea brines. *Geochim.*  
7 2155 *Cosmochim. Acta* 65, 1259–1275.  
8  
9  
10  
11 2156 Pierret, M.C., Clauer, N., Bosch, D., Blanc, G., 2010. Formation of Thetis Deep metal-rich  
12 2157 sediments in the absence of brines, Red Sea. *J. Geochem. Explor.* 104, 12–26.  
13  
14  
15  
16 2158 Pilcher, R.S., Blumstein, R.D., 2007. Brine volume and salt dissolution rates in Orca Basin,  
17 2159 northeast Gulf of Mexico. *AAPG Bull.* 91, 823–833  
18  
19  
20 2160 Pilson, M.E.Q., 2013. *Introduction to the Chemistry of the Sea* (2<sup>nd</sup> Edn.). Cambridge University  
21 2161 Press, New York, 529 pp.  
22  
23  
24  
25 2162 Piper, D.Z., Graef, P.A., 1974. Gold and rare-earth elements in sediments from the East Pacific  
26 2163 Rise. *Mar. Geol.* 17, 287–297.  
27  
28  
29 2164 Plavansky, N., Bekker, A., Rouxel, O.J., Kamber, B., Hofmann, A., Knudsen, A., Lyons, T.W., 2010.  
30 2165 Rare earth element and yttrium compositions of Archean and Paleoproterozoic Fe  
31 2166 formations revisited: New perspectives on the significance and mechanisms of  
32 2167 deposition. *Geochim. Cosmochim. Acta* 74, 6387–6405.  
33  
34  
35  
36  
37  
38 2168 Pottorf, R.J., Barnes, H.L., 1983. Mineralogy, geochemistry, and ore genesis of hydrothermal  
39 2169 sediments from the Atlantis II Deep, Red Sea. *Econ. Geol. Monogr.* 5, 198–223.  
40  
41  
42 2170 Poulton, S.W., Canfield, D.E., 2006. Co-diagenesis of iron and phosphorus in hydrothermal  
43 2171 sediments from the southern East Pacific Rise: Implications for the evaluation of  
44 2172 paleoseawater phosphate concentrations. *Geochim. Cosmochim. Acta* 70, 5883–5898.  
45  
46  
47  
48 2173 Poulton, S.W., Fralick, P.W., Canfield, D.E., 2010. Spatial variability in oceanic redox structure  
49 2174 1.8 billion years ago. *Nature Geosci.* 3, 486–490.  
50  
51  
52  
53 2175 Qian, P.Y., Wang, Y., Lee, O.O., Lau, S.C., Yang, J., et al., 2011. Vertical stratification of microbial  
54 2176 communities in the Red Sea revealed by 16S rDNA pyrosequencing. *ISME J.* 5, 507–518.  
55  
56  
57  
58  
59  
60  
61  
62

- 2177 Ramboz, C., Oudin, E., Thisse, Y., 1988. Geyser-type discharge in Atlantis II Deep, Red Sea:  
1  
22178 Evidence of boiling from fluid inclusions in epigenetic anhydrite. *Can. Mineral.* 26, 765–  
3  
42179 786.  
5  
6  
72180 Rea, D.K., Leinen, M., 1986. Neogene controls on hydrothermal activity and paleoceanography  
82181 of the southeast Pacific Ocean. In: Leinen, M., Rea, D.K., et al., *Init. Repts. DSDP, 92:*  
9  
102182 Washington, D.C. (U.S. Govt. Printing Office), 597–617.  
11  
12  
132183 Resing, J.A., Sedwick, P.N., German, C.R., Jenkins, W.J., Moffett, J.W., Sohst, B.M., Tagliabue, A.,  
14  
152184 2015. Basin-scale transport of hydrothermal dissolved metals across the South Pacific  
162185 Ocean. *Nature* 523, 200–203.  
17  
18  
192186 Reynolds, P.H., Dasch, E., 1971. Lead isotopes in marine manganese nodules and the ore-lead  
20  
212187 growth curve: *J. Geophys. Res.* 76, 5124–5129.  
22  
23  
242188 Robb, L., 2005. *Introduction to Ore-Forming Processes*. Blackwell, Oxford, 373 p.  
25  
26  
272189 Robertson, A.H.F., Fleet, A.J., 1976. The origins of rare earths in metalliferous sediments of the  
282190 Troodos massif, Cyprus. *Earth Planet. Sci. Lett.* 28, 385–394.  
29  
30  
312191 Ross, D.A., 1972. Red Sea hot brine area—Revised. *Science* 175, 1455–1456.  
32  
33  
342192 Ruhlin, D.E., Owen, R.M., 1986. The rare earth element geochemistry of hydrothermal  
352193 sediments from the East Pacific Rise: Examination of a seawater scavenging mechanism.  
362194 *Geochim. Cosmochim. Acta* 50, 393–400.  
37  
38  
39  
402195 Sa, R., Sun, X., He, G., Xu, L., Pan, Q., Liao, J., Zhu, K., Deng, X., 2018. Enrichment of rare earth  
412196 elements in siliceous sediments under slow deposition: A case study of the central north  
422197 Pacific. *Ore Geol. Rev.* 94, 12–23.  
43  
44  
45  
46  
472198 Sayles, F.L., Bischoff, J.L., 1973. Ferromanganese sediments in the equatorial east Pacific. *Earth*  
482199 *Planet. Sci. Lett.* 19, 330–336.  
49  
50  
512200 Sayles, F.L., Ku, T.-L., Bowker, P.C., 1975. Chemistry of ferromanganoan sediment of the Bauer  
522201 Deep. *Geol. Soc. Am. Bull.*, 86, 1423–1431.  
53  
54  
55  
562202 Schardt, C., 2016. Hydrothermal fluid migration and brine pool formation in the Red Sea: The  
572203 Atlantis II Deep. *Miner. Deposita* 51, 89–111.  
58  
59  
60  
61  
62

- 2204 Scheibner, E., Moore, G.W., Drummond, K.J., Dalziel, I.W., Corvalan, Q.J., Moritani, T., Teraoka,  
1  
22205 Y., Sato, T., and Craddock, C. (compilers), 2013, Tectonic map of the circum-Pacific region,  
3  
42206 Pacific basin sheet, U.S. Geological Survey Circum-Pacific Map CP-52, pamphlet 134 p., 2  
5  
62207 sheets, scale 1:17,000,000, and GIS data, <https://pubs.usgs.gov/cp/52/>.  
7  
8  
92208 Schijf, J., 2007. Alkali elements (Na, K, Rb) and alkaline earth elements (Mg, Ca, Sr, Ba) in the  
10  
112209 anoxic brine of Orca Basin, northern Gulf of Mexico. *Chem. Geol.* 243, 255–274.  
12  
132210 Schijf, J., de Baar, H.J.W., Millero, F.J., 1995. Vertical distributions and speciations of dissolved  
14  
152211 rare earth elements in the anoxic brines of Bannock Basin, eastern Mediterranean Sea.  
16  
172212 *Geochim. Cosmochim. Acta* 59, 3285–3299.  
18  
19  
202213 Schoell, M., Faber, E., 1978. New isotopic evidence for the origin of Red Sea brines. *Nature* 275,  
21  
222214 436–438.  
23  
242215 Schrader, E.L., Rosendahl, B.R., Furbish, W.J., Matthey, D.P., 1980. Mineralogy and geochemistry  
25  
262216 of hydrothermal and pelagic sediments from the Mounds hydrothermal field, Galapagos  
27  
282217 spreading center: DSDP Leg 54. *J. Sed. Res.* 50, 917–928.  
29  
30  
312218 Schwertmann, U., Friedl, J., Stanjek, H., Murad, E., Bender Koch, C., 1998. Iron oxides and  
32  
332219 smectites in sediments from the Atlantis II Deep, Red Sea. *Eur. J. Mineral.* 10, 953–967.  
34  
352220 Scott, S.D., R.L. Chase, M.D. Hannington, P.J. Michael, T.F. McConachy, and G.T. Shea, 1990.  
36  
372221 Sulphide deposits, tectonics and petrogenesis of Southern Explorer Ridge, northeast  
38  
392222 Pacific Ocean. In: Malpas, J., Moores, E.M., Panayootou, A., C. Xenophontos, C. (eds.),  
40  
412223 Ophiolites and Oceanic Lithosphere: Proceedings of the Troodos '87 Symposium (edited  
42  
432224 by, Geological Survey of Cyprus, Nicosia, 719–733.  
44  
452225 Scrivner, A., Vance, D., Rohling, E.J., 2004. New neodymium isotope data quantify Nile  
46  
472226 involvement in Mediterranean anoxic episodes. *Geology* 32, 565–568.  
48  
49  
502227 Seo, I., Pak, S.J., Kiseong, H., Kong, G.S., Kim, J., 2014. Composition of rare earth elements in  
51  
522228 Northeast Pacific surface sediments, and their potential as rare earth elements resources.  
53  
542229 *Ocean Polar Res.* 36, 383–394.  
55  
562230 Severmann, S., Mills, R.A., Palmer, M.R., Fallick, A.E., 2004. The origin of clay minerals in active  
57  
582231 and relict hydrothermal deposits. *Geochim. Cosmochim. Acta* 68, 73–88.  
59  
60  
61  
62

- 2232 Seyfried, W.E., Seewald, J.S., Berndt, M.E., Ding, K., Foustoukos, D.I., 2003. Chemistry of  
1 hydrothermal fluids from the main Endeavour Field, northern Juan de Fuca Ridge:  
2233 hydrothermal fluids from the main Endeavour Field, northern Juan de Fuca Ridge:  
3  
42234 Geochemical controls in the aftermath of June 1999 seismic events. *J. Geophys. Res.*  
5  
62235 108(B9), 2429, doi:10.1029/2002JB001957.  
7  
82236 Shanks, W.C., Bischoff, J.L., 1977. Ore transport and deposition in the Red Sea geothermal  
9 system: A geochemical model. *Geochim. Cosmochim. Acta* 41, 1507–1519.  
102237  
11  
12  
132238 Shanks, W.C., Bischoff, J.L., 1980. Geochemistry, sulfur isotope composition and accumulation  
14 rates of Red Sea geothermal deposits. *Econ. Geol.* 75, 445–459.  
152239  
16  
172240 Sherrell, R.M., Field, M.P., Ravizza, G., 1999. Uptake and fractionation of rare earth elements on  
18 hydrothermal plume particles at 9°45'N, East Pacific Rise. *Geochim. Cosmochim. Acta* 63,  
192241 1709–1722.  
20  
212242  
22  
23  
242243 Sheu, D.-D., 1990. The anoxic Orca Basin (Gulf of Mexico): Geochemistry of brines and  
25 sediments. *Rev. Aquatic Sci.* 2, 491–507.  
262244  
27  
282245 Sheu, D.-D., Presley, B.J., 1986. Variations of calcium carbonate, organic carbon and iron  
29 sulfides in anoxic sediment from the Orca Basin, northern Gulf of Mexico. *Mar. Geol.* 70,  
302246 103–118.  
31  
322247  
33  
34  
352248 Shokes, R.F., Trabant, P.K., Presley, B.J., Reid, D.R., 1977. Anoxic, hypersaline basin in the  
36 northern Gulf of Mexico. *Science* 196, 1443–1446.  
372249  
38  
392250 Scholten, J.C., Stoffers, P., Walter, P., Plüger, W., 1991. Evidence for episodic hydrothermal  
40 activity in the Red Sea from the composition and formation of hydrothermal sediments,  
412251 Thetis Deep. *Tectonophys.* 190, 109–117.  
42  
432252  
44  
45  
462253 Siam, R., Mustafa, G.A., Sharaf, H., Moustafa, A., Ramadan, A.R., et al., 2012. Unique  
47 prokaryotic consortia in geochemically distinct sediments from Red Sea Atlantis II and  
482254 Discovery Deep brine pools. *PLoS ONE* 7, doi:10.1371/journal.pone.0042872.  
492255  
50  
51  
522256 Singer, A., Stoffers, P., 1987. Mineralogy of a hydrothermal sequence in a core from the Atlantis  
53 II Deep, Red Sea. *Clay Min.* 22, 251–267.  
542257  
55  
56  
572258 Singer, A., Stoffers, P., Heller-Kallai, L., Szafranek, D., 1984. Nontronite in a deep-sea core from  
58 the South Pacific. *Clays Clay Miner.* 32, 375–383.  
592259  
60  
61  
62

- 2260 Sionneau, T., Bout-Roumazeilles, V., Flower, B.P., Bory, A., Tribovillard, N., Kissel, C., Van Vliet-  
1 Lanoë, B., Serrano, J.C.M., 2010. Provenance of freshwater pulses in the Gulf of Mexico  
2261 during the last deglaciation. *Quat. Res.* 74, 235–245.  
3  
42262  
5  
6  
72263 Stein, M., Almogi-Labin, A., Goldstein, S.L., Hemleben, C., Starinsky, A., 2007. Late Quaternary  
82264 changes in desert dust inputs to the Red Sea and Gulf of Aden from  $^{87}\text{Sr}/^{86}\text{Sr}$  ratios in  
9 deep-sea cores. *Earth Planet. Sci. Lett.* 261, 104–119.  
102265  
11  
12  
132266 Steinkamp, K., Schumann, D., 1974. The chemical composition of sediment cores recovered  
14 during Valdivia Cruises VA01 and VA03 from the Atlantis II Deep (Red Sea). Unpub. cruise  
152267 report 1.11.1974, Series CL, Preussag, Hannover, 155 pp.  
162268  
17  
18  
192269 Steinmann, M., Bodeï, S., Buatier, M., 2012. Nd–Sr isotope and REY geochemistry of  
20 metalliferous sediments in a low-temperature off-axis hydrothermal environment (Costa  
212270 Rica margin). *Mar. Geol.* 315-318, 132–142.  
22  
232271  
24  
25  
262272 Stewart, F.H., 1963. Marine evaporites. Chapter Y, Data of Geochemistry. U.S. Geol. Survey  
272273 Prof. Paper 440-Y, 52 pp.  
28  
29  
302274 Stichel, T., Pahnke, K., Duggan, B., Goldstein, S.L., Hartman, A.E., Paffrath, R., Scher, H.D., 2018.  
31 TAG Plume: Revisiting the hydrothermal neodymium contribution to seawater. *Frontiers*  
322275 *Mar. Sci.* 5:96. doi: 10.3389/fmars.2018.00096.  
33  
342276  
35  
36  
372277 Stockli, D.F., Bosworth, W., 2019. Timing of extensional faulting along the magma-poor central  
382278 and northern Red Sea rift margin—Transition from regional extension to necking along a  
39 hyperextended rifted margin. In: Rasul, N.M.A., Stewart, I.C.F. (eds.), *Geological Setting,  
402279 Palaeoenvironment and Archaeology of the Red Sea. Earth System Science Series,*  
41 Springer Nature Switzerland AG, 81–112.  
422280  
43  
442281  
45  
462282 Stoffers, P., Lallier-Verges, E., Plüger, W., Schmitz, W., Bonnot-Courtois, C., Hoffert, M., 1985. A  
47 “fossil” hydrothermal deposit in the South Pacific. *Mar. Geol.* 62, 133–151.  
482283  
49  
50  
512284 Sun, S.-s., McDonough, W.F., 1989. Chemical and isotopic systematics of oceanic basalts:  
52 Implications for mantle composition and processes. *Geol. Soc. Lond. Spec. Publ.* 42, 313–  
532285 345.  
542286  
55  
56  
57  
58  
59  
60  
61  
62

- 2287 Sun, Z., Zhou, H., Glasby, G.P., Yang, Q., Yin, X., Li, J., Chen, Z., 2012. Formation of Fe-Mn-Si  
1 oxide and nontronite deposits in hydrothermal fields on the Valu Fa Ridge, Lau Basin. *J.*  
2288 *Asian Earth Sci.* 43, 64–76.  
3  
42289  
5  
6  
72290 Sun, Z., Cao, H., Yin, X., Zhang, X., Dong, A., Liu, L., Geng, W., 2018. Precipitation and  
8 subsequent preservation of hydrothermal Fe-Mn oxides in distal plume sediments on  
9 Juan de Fuca Ridge. *J. Mar. Syst.* 187, 128–140.  
102292  
11  
12  
132293 Swift, A., Bower, A.S., Schmitt, R., 2012. Vertical, horizontal, and temporal changes in  
14 temperature in the Atlantis II and Discovery hot brine pools, Red Sea. *Deep Sea Res. Part*  
152294 *I: Ocean. Res. Pap.* 64, 118–128.  
162295  
17  
18  
192296 Ta, K., Peng, X., Chen, S., Xu, H., Li, J., Du, M., Hao, J., Lin, Y., 2017. Hydrothermal nontronite  
20 formation associated with microbes from low-temperature diffuse hydrothermal vents at  
212297 the south Mid-Atlantic Ridge. *J. Geophys. Res. Biogeosci.* 122, 2375–2392.  
222298  
23  
24  
252299 Tachikawa, K., Roy-Barman, M., Michard, A., Thouron, D., Yeghicheyan, D., Jeandel, C., 2004.  
26 Neodymium isotopes in the Mediterranean Sea: Comparison between seawater and  
272300 sediment signals. *Geochim. Cosmochim. Acta* 68, 3095–3106.  
282301  
29  
30  
31  
322302 Tachikawa, K., Arsouze, T., Bayon, G., Colin, C., Dutay, J.-C., Frank, N., et al., 2017. The large-  
33 scale evolution of neodymium isotopic composition in the global modern and Holocene  
342303 ocean revealed from seawater and archive data. *Chem. Geol.* 457, 131–148.  
352304  
36  
37  
382305 Taitel-Goldman, N., Singer, A., 2001. High-resolution transmission electron microscopy study of  
39 newly formed sediments in the Atlantis II Deep, Red Sea. *Clays Clay Min.* 49, 174–182.  
402306  
41  
42  
432307 Taitel-Goldman, N., Singer, A., 2002, Metastable Si-Fe phases in hydrothermal sediments of  
44 Atlantis II Deep: Red Sea. *Clay Miner.* 37, 235–248.  
452308  
46  
472309 Taitel-Goldman, N., Koch, C.B. Singer A., 2004. Si-associated goethite in hydrothermal  
48 sediments of the Atlantis II and Thetis Deeps, Red Sea. *Clays Clay Miner.* 52, 115–129.  
492310  
50  
51  
522311 Taitel-Goldman, N., Ezersky, V., Mogilyanski, D., 2009. High-resolution transmission electron  
53 microscopy study of Fe-Mn oxides in the hydrothermal sediments of the Red Sea Deeps  
542312 system. *Clays Clay Min.* 57, 465–475.  
552313  
56  
57  
58  
59  
60  
61  
62

- 2314 Takaya, Y., Yasukawa, K., Kawasaki, T., Fujinaga, K., Ohta, J., Usui, Y., Nakamura, K., Kimura, J. I.,  
1 Chang, Q., Hamada, M., Dodbiba, G., Nozaki, T., Iijima, K., Morisawa, T., Kuwahara, T.,  
22315  
3 Ishida, Y., Ichimura, T., Kitazume, M., Fujita, T., Kato, Y., 2018. The tremendous potential  
42316  
5 of deep-sea mud as a source of rare-earth elements. *Scientific Reports* 8, 1–8.  
62317  
7  
82318 Tanaka, E., Nakamura, K., Yasukawa, K., Mimura, K., Fujinaga, K., Iijima, K., Nozaki, T., Kato, Y.,  
9  
102319 2020. Chemostratigraphy of deep-sea sediments in the western North Pacific Ocean:  
11  
122320 Implications for genesis of mud highly enriched in rare-earth elements and yttrium. *Ore*  
13  
142321 *Geol. Rev.* 119, doi.org/10.1016/j.oregeorev.2020.103392  
15  
162322 Taylor, S.R., McLennan, S.M., 1995. The geochemical evolution of the continental crust. *Rev.*  
17  
182323 *Geophys.* 33, 241–265.  
19  
20  
212324 Thirlwall, M.F., 1991. High-precision multicollector isotopic analysis of low levels of Nd as oxide.  
22  
232325 *Chem. Geol. (Isotope Geosci. Sect.)* 94, 13–22.  
24  
25  
262326 Thisse, Y., 1982. Sédiments métallifères de la fosse Atlantis II (mer Rouge): Contribution à  
27  
282327 l'étude de leur contexte morpho-structural et de leurs caractéristiques minéralogiques et  
29  
302328 géochimiques. Thèse Université Orleans et BRGM, France, 155 pp.  
31  
322329 Thisse, Y., Guennoc, P., Pouit, G., Nawab, Z., 1983. The Red Sea: A natural geodynamic and  
33  
342330 metallogenic laboratory. *Episodes* 3, 3–9.  
35  
36  
372331 Tlig, S., Sassi, A., Belayouni, H., Michel, D., 1987. Distribution de l'uranium, du thorium, du  
38  
392332 zirconium, du hafnium et des terres rares (TR) dans des grains de phosphates  
40  
412333 sédimentaires. *Chem. Geol.* 62, 209–221.  
42  
432334 Tornos, F., Peter, J.M., Allen, R., Cone, C., 2015. Controls on the siting and style of volcanogenic  
44  
452335 massive sulphide deposits. *Ore Geol. Rev.*, 68, 142–163.  
46  
47  
482336 Totland, M.M., Jarvis, I., Jarvis K.E., 1992. An assessment of dissolution techniques for  
49  
502337 the analysis of geological samples by plasma spectrometry. *Chem. Geol.* 95, 35–62.  
51  
522338 Trabant, P.K., Presley, B.J., 1978. Orca Basin, anoxic depression on the continental slope,  
53  
542339 northwest Gulf of Mexico. In: Bouma, A.H., Moore, G.T., Coleman, J.M. (eds.), *Framework,*  
55  
562340 *Facies, and Oil-Trapping Characteristics of the Upper Continental Margin.* AAPG Stud.  
57  
58  
59  
60  
61  
62  
63  
64  
65

- 2342 Trefry, J.H., Presley, B.J., Keeney-Kennicutt, W.L., Trocine, R.P., 1984. Distribution and chemistry  
1 of manganese, iron, and suspended particulates in Orca Basin. *Geo-Mar. Lett.* 4, 125–130.  
22343  
3  
4  
52344 Tribovillard, N., Bout-Roumazeilles, V., Algeo, T., Lyons, T.W., Sionneau, T., Montero-Serrano,  
6 J.C., Riboulleau, A., Baudin, F., 2008. Paleodepositional conditions in the Orca Basin as  
72345 inferred from organic matter and trace metal contents. *Mar. Geol.* 254, 62–72.  
82346  
9  
10  
112347 Tunnicliffe, V., Botros, M., Deburgh, M.E., Dinet, A., Johnson, H.P., Juniper, S.K., McDuff, R.E.,  
12 1986. Hydrothermal vents of the Explorer Region, Northeast Pacific. *Deep Sea Res.* 33,  
132348 401–412.  
14  
152349  
16  
172350 van Andel, T.H., Heath, G.R., Malfait, B.T., Heinrichs, D.F., Ewing, J.I., 1971. Tectonics of the  
18 Panama Basin, eastern equatorial Pacific. *Geol. Soc. Am. Bull.* 82, 1489–1508.  
192351  
20  
21  
222352 Van der Flierdt, T., Frank, M., Halliday, A.N., Hein, J.R., Hattendorf, B., Günther, D., Kubik, P.W.,  
23 2004. Tracing the history of submarine hydrothermal inputs and the significance of  
242353 hydrothermal hafnium for the seawater budget—A combined Pb-Hf-Nd isotope approach.  
252354 *Earth Planet. Sci. Lett.* 222, 259–273.  
26  
272355  
28  
29  
302356 Van der Flierdt, T., Griffiths, A.M., Lambelet, M., Little, S.H., Stichel, T., Wilson, D.J., 2016.  
31 Neodymium in the oceans: A global database, a regional comparison and implications for  
322357 palaeoceanographic research. *Phil. Trans. Royal Soc. A* 374,  
33 doi.org/10.1098/rsta.2015.0293.  
342358  
352359  
36  
37  
382360 Varnavas, S.P., Cronan, D.S., 1981. Partition geochemistry of sediments from DSDP 424 in the  
39 Galapagos hydrothermal mounds field. *Min. Mag.* 44, 325–331.  
402361  
41  
42  
432362 Vengosh, A., De Lange, G.J., Starinsky, A., 1998. Boron isotope and geochemical evidence for  
44 the origin of Urania and Bannock brines at the eastern Mediterranean: Effect of water-  
452363 rock interactions. *Geochim. Cosmochim. Acta* 62, 3221–3228.  
462364  
47  
48  
492365 Volker, F., McCulloch, M.T., Altherr, R., 1993. Submarine basalts from the Red Sea: New Pb, Sr  
50 and Nd isotopic data. *Geophys. Res. Lett.* 20, 927–930.  
512366  
52  
53  
542367 Von Damm, K. 1990. Seafloor hydrothermal activity: Black smoker chemistry and chimneys.  
55 *Ann. Rev. Earth Planet. Sci.* 18, 173–204.  
562368  
57  
58  
59  
60  
61  
62

- 2369 Walter, P., Stoffers, P., 1985. Chemical characteristics of metalliferous sediments from eight  
1  
22370 areas on the Galapagos Rift and East Pacific Rise between 2°N and 42°S. *Mar. Geol.* 65,  
3  
42371 271–287.  
5
- 6  
72372 Wang, Y., Yang, J., Lee O.O., Dash, S., Lau, S.C., et al., 2011. Hydrothermally generated aromatic  
8  
92373 compounds are consumed by bacteria colonizing in Atlantis II Deep of the Red Sea. *ISME*  
10  
102374 *J.* 5, 1652–1659.  
11
- 12  
132375 Wang, Y., Cao, H., Zhang, G., Bougouffa, S., Lee, O.O., Al-Suwailem, A., Qian, P.-Y., 2013.  
14  
152376 Autotrophic microbe metagenomes and metabolic pathways differentiate adjacent Red  
16  
172377 Sea brine pools. *Sci. Rep.* 3, article 1748, doi:10.1038/srep01748.  
18
- 192378 White, W.M., Hofman, A.W., Puchelt, H., 1987. Isotope geochemistry of Pacific mid-ocean ridge  
20  
212379 basalt. *J. Geophys. Res.* 92, 4881–4893.  
22
- 23  
242380 Williams, D. L., Green, K., van Andel, Tj. H., Von Herzen, R. P., Dymond, J. R., Crane, K., 1979.  
25  
262381 The hydrothermal mounds of the Galapagos Rift: Observations with DS R/V Alvin and  
27  
282382 detailed heat flow studies. *J. Geophys. Res.* 84 (B13), 7467–7484.  
29
- 302383 Winckler G., Kipfer, R., Aeschbach-Hertig, W., Botz, R., Schmidt, M., Schuler, S., Bayer, R., 2000.  
31  
322384 Sub sea floor boiling of Red Sea Brine –New indication from noble gas data. *Geochim.*  
33  
342385 *Cosmochim. Acta* 64, 1567–1575.  
35
- 36  
372386 Winckler, G., Aeschbach-Hertig, W., Kipfer, R., Botz, R., Rübel, A.P., Bayer, R., Stoffers, P., 2001.  
38  
392387 Constraints on origin and evolution of Red Sea brines from helium and argon isotopes.  
40  
402388 *Earth Planet. Sci. Lett.* 184, 671–683.  
41
- 42  
432389 Yao, H., Zhou, H., Peng, X., He, G., 2015. Sr isotopes and REEs geochemistry of anhydrites from L  
44  
452390 vent black smoker chimney, East Pacific Rise, 9°N–10°N. *J. Earth Sci.* 26, 920–928.  
46
- 47  
482391 Yasukawa, K., Ohta, J., Miyazaki, T., Vaglarov, B.S., Chang, Q., Ueki, K., Toyama, C., Kimura, J.-I.,  
49  
502392 Tanaka, E., Nakamura, K., Fujinaga, K., Iijima, K., Iwamori, H., Kato, Y., 2019. Statistic and  
51  
522393 isotopic characterization of deep-sea sediments in the western North Pacific Ocean:  
53  
532394 Implications for genesis of the sediment extremely enriched in rare-earth elements.  
54  
552395 *Geochem. Geophys. Geosyst.* 20, 3402–3430.  
56

2396 Zeng, Z., Ouyang, H., Yin, X., Chen, S., Wang, X., Wu, L., 2012. Formation of Fe-Si-Mn  
1 oxyhydroxides at the PACMANUS hydrothermal field, eastern Manus Basin: Mineralogical  
22397 and geochemical evidence. *J. Asian Earth Sci.* 60, 130–146.  
3  
42398  
5  
6  
72399 Zheng, X.Y., Plancherel, Y., Saito, M.A., Scott, P.M., Henderson, G.M., 2016. Rare earth elements  
82400 (REEs) in the tropical South Atlantic and quantitative deconvolution of their non-  
9 conservative behavior. *Geochim. Cosmochim. Acta* 177, 217–237.  
102401  
11  
12  
132402 Zierenberg, R.A., Shanks, W.C., 1983. Mineralogy and geochemistry of epigenetic features in  
14 metalliferous sediments, Atlantis II Deep, Red Sea. *Econ. Geol.* 78, 57– 72.  
152403  
16  
172404 Zierenberg, R.A., Shanks, W.C., 1986. Isotopic constraints on the origin of the Atlantis II, Suakin  
18 and Valdivia brines, Red Sea. *Geochim. Cosmochim. Acta* 50, 2205–2214.  
192405  
20  
21  
222406 Zierenberg, R.A., Shanks, W.C., 1988. Isotopic studies of epigenetic features in metalliferous  
23 sediment, Atlantis II Deep, Red Sea. *Can. Miner.* 26, 737–753.  
242407  
25  
262408  
27  
28  
29  
30  
31  
32  
33  
34  
35  
36  
37  
38  
39  
40  
41  
42  
43  
44  
45  
46  
47  
48  
49  
50  
51  
52  
53  
54  
55  
56  
57  
58  
59  
60  
61  
62  
63  
64  
65

2409 **Tables in Paper**

- 1<sup>2</sup>2410  
2  
32411 Table 1. Locations of analyzed samples from Atlantis II Deep, East Pacific Rise transect,  
4  
5<sup>4</sup>2412 Galapagos hydrothermal mounds, and Southern Explorer Ridge  
6  
7<sup>2</sup>2413 Table 2. Rare-earth element composition of metalliferous sediments from Atlantis II Deep  
8  
9<sup>2</sup>2414 (Red Sea) and hemipelagic sediments from Orca Basin (Gulf of Mexico)  
10  
11<sup>2</sup>2415 Table 3. Nd isotope data for metalliferous sediments from Atlantis II Deep, Red Sea  
12  
13  
14<sup>2</sup>2416 Table 4. Rare-earth element composition of metalliferous sediments from East Pacific  
15  
16<sup>2</sup>2417 Rise transect (DSDP Leg 92)  
17  
18<sup>2</sup>2418 Table 5. Summary of REE and Nd-Pb-Sr isotopic features of metalliferous sediment types  
19  
20<sup>2</sup>2419 discussed in present paper  
21  
22<sup>2</sup>2420 Table 6. Compilation of Nd, Pb and Sr isotopic and concentration data for oceanic  
23  
24<sup>2</sup>2421 metalliferous sediments, deep seawater, Atlantis II Deep brine, MOR  
25  
26<sup>2</sup>2422 hydrothermal vent fluids, and MOR basalt  
27

28<sup>2</sup>2423  
29  
30<sup>2</sup>2424 **Supplementary Data Tables**

- 31<sup>2</sup>2425  
32  
33<sup>2</sup>2426 Supplementary Data Table 1. Chemical analyses of metalliferous sediments from Atlantis II  
34  
35<sup>2</sup>2427 Deep, Red Sea  
36  
37<sup>2</sup>2428 Supplementary Data Table 2. Chemical analyses of metalliferous sediments from East Pacific  
38  
39<sup>2</sup>2429 Rise transect (DSDP Leg 92) on carbonate-free basis  
40

41<sup>2</sup>2430  
42  
43  
44  
45  
46  
47  
48  
49  
50  
51  
52  
53  
54  
55  
56  
57  
58  
59  
60  
61  
62

2431

1  
2432**Figure captions**

32433

4  
52434

**Fig. 1.** Location of study sites. Red-filled circles are main study localities; yellow-filled circles are other key sites providing comparative literature data. NEPR is northern East Pacific Rise, SEPR is southern East Pacific Rise, TAG is Trans-Atlantic Geotraverse hydrothermal field on Mid-Atlantic Ridge. Base map from GEBCO (2020).

62435

7  
824369  
102437

112438

12  
132439

**Fig. 2.** Location and bathymetry of the Red Sea Atlantis II Deep. (a) Map indicating positions of major deeps along spreading axis of the Red Sea; inset shows bounding tectonic plates and opening directions (modified from Encyclopædia Britannica, 2011). The Atlantis II Deep is marked by the yellow arrow. (b) Bathymetric map of central Red Sea showing Atlantis II Deep and nearby Chain Deep and Discovery Deep (modified from Augustin et al., 2016); yellow-filled circles locate sediment cores sampled in present study (Table 1); colour codes give depth below sea-level in metres.

142440

15  
16244117  
182442

192443

20  
212444

222445

23  
242446

**Fig. 3.** Schematic cross-section of Atlantis II Deep showing brine layers and geological setting. Note basalt below Deep, flanking Miocene evaporites, and Pliocene–Pleistocene hemipelagic sediments. Compiled from Bäcker (1973), Laurila et al. (2014a) and Schardt (2016). Brine temperatures after Swift et al. (2012).

252447

26  
27244828  
292449

302450

31  
322451

**Fig. 4.** Schematic summary of metalliferous sediment facies in Atlantis II Deep showing generalized column on left side and Southwest Basin column on right side (modified from Laurila (2015), based on Bäcker and Richter (1973)'s classification of lithological units). Core lengths are typically 10–15 m, rarely reaching 20 m. The base of unit SU1 in the general column has an age of ca. 12 ka, yielding high sedimentation rates of >1 m/kyr for overlying sediment units. Most samples in present study are from units CO, SU2 and SAM in the Southwest Basin.

332452

34  
35245336  
372454

382455

39  
40245641  
42245743  
44245845  
462459

**Fig. 5.** Core photographs of metalliferous sediments from the Atlantis II Deep. A selection of units and facies (Fig. 4) are illustrated (core photographs from Laurila et al., 2015). (A) Unit COS: top part mainly green clays; lower part mainly Fe oxyhydroxides. (B) Unit CO: Si-Fe-oxyhydroxides with layers of hydrothermal carbonate and Mn-oxyhydroxide; white layer (arrowed) consists of detrital silicates + biogenic calcite. (C) Unit OAN: red Fe-oxyhydroxide, and grey anhydrite-rich layers and subvertical veins (arrowed). (D) Unit AM with diffuse lamination (unit SU2 occurs below arrowed orange band). Scale bars = 2 cm.

47  
48246149  
50246251  
52246353  
54246455  
56246657  
58246759  
602468

61

62

63

64

65

**Fig. 6.** Bathymetric map and basins of Atlantis II Deep and nearby deeps, showing locations of cores sampled in present study (red-filled circles with core numbers). Contours show depths below sea-level in metres. 2000 m isobath corresponds to top of present-day brine-filled deep. Modified from Anschultz (2015).

**Fig. 7.** Composition of metalliferous sediments from Atlantis II Deep plotted as molar proportions of Fe–Mn–Al. Shown for comparison are compositions of axial southern EPR (SEPR) metalliferous sediment (Marchig and Erzinger, 1986), Fe-rich SEPR plume particulates (Feely et al., 1996), plume particulates from the northern EPR (NEPR; Feely et al., 1994a, Sherrell et al., 1999), Fe-Mn nodules (Hein et al., 2013), and average Pacific pelagic clay (Cronan, 1976). Geographic locations of data sets are shown in Fig. 1. Note the tight clustering of Atlantis II Deep samples towards the Fe apex, close to composition of SEPR modern plume particulates.

**Fig. 8.** Composition of metalliferous sediments from the Atlantis II Deep. (a) – (c) Elements associated principally with the siliciclastic fraction: TiO<sub>2</sub>, Zr, and  $\Sigma$ REE vs. Al<sub>2</sub>O<sub>3</sub>. (d) Hydrothermally supplied elements: SiO<sub>2</sub> vs. Fe<sub>2</sub>O<sub>3</sub>. Major elements reported as oxides; total Fe expressed as Fe<sub>2</sub>O<sub>3</sub>(t). Compositions of nontronite from Galapagos hydrothermal mounds (Barrett and Friedrichsen, 1982) and ideal hematite are shown for comparison.

**Fig. 9.** Composition of metalliferous sediments from the Atlantis II Deep (dashed lines are estimated trends). Gold is associated with Cu (a), with Zn in many samples (b), and with total S (not shown). Samples with low contents of gold (<0.7 ppm), Zn (< 0.5 wt %), and Cu (<0.2 wt %) are rich in Fe-oxyhydroxides based on chemical data in Supplementary Data Table 1. The Cd-Zn relation in (d) reflects substitution of Cd for Zn in sphalerite.

**Fig. 10.** REE composition of metalliferous sediments from Core 274, NE margin of the SW Basin, Atlantis II Deep. Data are normalized to Post-Archean Average Australian Shale (PAAS; Taylor and McLennan, 1995). Vent fluids from the TAG area (26°N, Mid-Atlantic Ridge; Fig. 1) are shown for comparison (from Bau and Dulski, 1999). Core 274, which penetrated 11 m of metalliferous sediments, is interpreted to have passed, from top to bottom, through units AM, SU2, CO, SU1, and DOP (cf. Fig. 4; Thisse, 1982).

**Fig. 11.** REE composition of metalliferous sediments from Atlantis II Deep. (a) – (d) Samples from different parts of SW Basin, which is considered to be the main area of hydrothermal input into the Deep (Laurila et al., 2014a). (e) Samples from various depths within a ‘distal’ core from West Basin. Note smaller Eu anomaly compared to proximal cores. (f) Effect of detrital aluminosilicate content on bulk-sediment REE patterns: with increasing  $\Sigma$ REE contents, the Eu anomaly decreases. First part of each hyphenated sample number is the core number. Core locations are shown in Fig. 6. REE concentrations normalized to PAAS.

**Fig. 12.** REE composition of metalliferous sediments from Atlantis II Deep having  $\epsilon$ Nd values of -2.24 to -1.48 (i.e., most of the sample set). This  $\epsilon$ Nd range suggests these sediments contain 20–25 % basaltic-hydrothermal Nd, based on two-component mixing model; other source of Nd in mixing model is terrigenous detritus (see text). All samples have distinct positive Eu anomalies. All samples are from SW Basin, except Core 345 from West Basin (Fig. 6). REE concentrations normalized to PAAS.

**Fig. 13.** Variation in Atlantis II Deep REE patterns with respect to  $\epsilon$ Nd. (a) REE and Nd isotope variations in Core 274 near eastern margin of SW Basin (Fig. 6); sample at 1.1 m has a higher aluminosilicate content than the two deeper samples. (b) Two most radiogenic  $\epsilon$ Nd samples in present study; samples are also rich in anhydrite or talc. REE concentrations normalized to PAAS.

**Fig. 14.** Plot of calculated  $\text{Eu}/\text{Eu}^*$  versus  $\epsilon$ Nd values for metalliferous sediments from Atlantis II Deep, based on samples from this study and Cocherie et al. (1994). Orange curve shows estimated exponential trend for metalliferous sediments, excluding two samples containing fish debris, and a talc-anhydrite sample (64-3). Horizontal arrows schematically show effect of increasing dissolved basaltic Nd component versus increasing normal seawater component in precipitating fluid. Vertical arrow shows effect of increasing proportion of reduced fluid on Eu anomaly (temperature and extent of basalt-fluid reaction prior to discharge of fluid into brine pool may also play a role in Eu supply). Red-filled circles: this study; red-filled triangles: Cocherie et al. (1994). Also shown are data for two samples of metalliferous sediment containing phosphatic fish debris, and two biotrital sediments (small blue-filled squares; Cocherie et al., 1994). Blue rectangle is estimated composition of normal Red Sea seawater;  $\epsilon$ Nd range is based on five near-surface samples of biotrital sediment ( $-4.9 \pm 0.4$ ) from core KS-01 in Shaban Deep (Cocherie et al., 1994). The estimated  $\text{Eu}/\text{Eu}^*$  range for normal Red Sea seawater is based on 10 samples of biotrital

2541  
 1  
 2542  
 3  
 2543  
 4  
 52544  
 6  
 2545  
 7  
 82546  
 9  
 102547  
 112548  
 12  
 132549  
 14  
 2550  
 15  
 162551  
 17  
 182552  
 192553  
 20  
 212554  
 222555  
 23  
 242556  
 25  
 2557  
 26  
 272558  
 28  
 292559  
 302560  
 31  
 322561  
 33  
 2562  
 34  
 352563  
 36  
 372564  
 382565  
 39  
 402566  
 412567  
 42  
 432568  
 44  
 452569  
 462570  
 47  
 482571  
 492572  
 50  
 512573  
 52  
 2574  
 53  
 54  
 55  
 56  
 57  
 58  
 59  
 60  
 61  
 62  
 63  
 64  
 65

sediments from core 1016 in central Red Sea (Pierret et al., 2010), and on deep oxic seawater from eastern Mediterranean (Censi et al., 2019). Detritus entering the Red Sea (mainly windborne dust) may also affect bulk-sediment  $\epsilon\text{Nd}$  and  $\text{Eu}/\text{Eu}^*$  values. Over the last 10 kyr, this detritus (represented by grey polygon with 2 sigma error bars) has had a fairly constant  $\epsilon\text{Nd}$  value of  $-5.8 \pm 0.8$  (Palchan et al., 2013) with a negligible Eu anomaly ( $\text{Eu}/\text{Eu}^* = 1.0 - 1.3$ ; Greaves et al., 1994; Palchan et al., 2013). Labeled samples: 274-1: contains ca. 75 % siliciclastic component; 64-3: contains ca. 20 % anhydrite; 345-4: large Eu anomaly, low content of base metals, west margin of West Basin. Sample 436-6 (unlabelled, next to 274-1), from center of West Basin, is compositionally similar to 345-5 but has a much smaller Eu anomaly; this may reflect its greater distance from a discharge site along the west margin of the West Basin.

**Fig. 15.** Bathymetric map of Atlantis II Deep showing calculated basaltic-hydrothermal component (brown-filled circles) and corresponding PAAS-normalized Eu anomalies ( $\text{Eu}/\text{Eu}^*$ , red numerals) for metalliferous sediment samples from the present study. Bubble widths are proportional to basaltic-hydrothermal component (legend shows two selected values). Core numbers indicated by the black numerals. Sample depths range from 1 to 10 m. For cores 274 and 345, an average of two samples was used to obtain the values shown on the map (samples 274-1 and 274-4 at depths of 1.0 m and 3.9 m, respectively; and samples 345-4 and 345-5 at depths of 5.1 m and 5.7 m, respectively). Base map modified from Anschutz (2015).

**Fig. 16.** Map of eastern Pacific Ocean showing locations of DSDP Leg 92 Sites 597–602, East Pacific Rise transect. Also shown are locations of: (a) Leg 85 sites (573, 574) where Eocene–Oligocene basal metalliferous sediments (Fe-Mn oxyhydroxides) were intersected (Jarvis, 1985); (b) surficial metalliferous sediments (Fe-Mn-oxyhydroxides) from crest of East Pacific Rise (EPR) (Bender et al., 1971); (c) Galapagos Mounds Sites 506–508 where Fe-rich silicates (nontronite) form within pelagic sediments 20–30 km south of Galapagos Rift (Honnorez et al., 1983); and (d) Bauer Basin, where Fe-smectite and Fe-Mn-oxyhydroxides occur throughout much of the sediment column (red-filled squares: cores 11 and 14, Sayles and Bischoff, 1973; red-filled circle: DSDP Site 319, Dymond et al., 1976). Base map from GEBCO (2020) with additional annotation.

- 2575  
1  
2576  
3  
2577  
4  
52578  
6  
2579  
7  
82580  
9  
102581  
112582  
12  
132583  
14  
2584  
15  
162585  
17  
182586  
19  
2587  
20  
212588  
22  
2589  
23  
242590  
25  
2591  
26  
272592  
28  
292593  
30  
2594  
31  
322595  
33  
2596  
34  
352597  
36  
372598  
38  
2599  
39  
402600  
41  
2601  
42  
432602  
44  
2603  
45  
462604  
47  
482605  
49  
2606  
50  
512607  
52  
2608  
53  
542609  
55  
562610  
57  
2611  
58  
59  
60  
61  
62  
63  
64  
65
- Fig. 17.** Simplified stratigraphic columns for drill holes from East Pacific Rise transect (DSDP Leg 92), showing locations of samples analysed in present study. Site positions are shown in Fig. 16 and listed in Table 1. Stratigraphic columns are from Knüttel (1986). Samples range in age from late Oligocene to Pleistocene. Axis of East Pacific Rise (EPR) lies about 350 km east of Site 601.
- Fig. 18.** Composition of metalliferous sediments from East Pacific Rise transect (DSDP Leg 92) plotted as molar proportions of Fe–Mn–Al. Shown for comparison are data for axial SEPR metalliferous sediment, high-Fe SEPR plume, plume particulates from NEPR, Pacific Fe–Mn nodules, and average pelagic clay. Note clustering of Leg 92 metalliferous sediment compositions around values for modern SEPR axial sediments. Data sources as in Fig. 7.
- Fig. 19.** Major-element compositions of metalliferous sediments from East Pacific Rise transect (DSDP Leg 92) on a carbonate-free basis. (a) MnO vs. Fe<sub>2</sub>O<sub>3</sub>(t). (b) Al<sub>2</sub>O<sub>3</sub> vs. Fe<sub>2</sub>O<sub>3</sub>(t). (c) TiO<sub>2</sub> vs. Al<sub>2</sub>O<sub>3</sub>. (d) SiO<sub>2</sub> vs. Al<sub>2</sub>O<sub>3</sub>. Total Fe expressed as Fe<sub>2</sub>O<sub>3</sub>(t). Three groups of metalliferous sediments can be discerned: orange = samples deposited above lysocline (intermixed with biogenic carbonate ooze prior to chemical leaching to remove carbonate); blue = samples deposited at or below lysocline; green = samples deposited a few metres or less above basaltic basement (all five green samples in Fig. 19 are from Site 597). Comparative literature data: EPR crest, average of 20 samples from five cores on crest of East Pacific Rise (Marchig and Gundlach, 1982); Bauer Deep, open square: average of seven samples from cores 11 and 14 at depths of 0.2–8.8 m (Sayles and Bischoff, 1973; square with X: DSDP Site 319, one sample at 0.2 m depth (Boström et al., 1976).
- Fig. 20.** Total REE contents of metalliferous sediments from East Pacific Rise transect (DSDP Leg 92) on a carbonate-free basis versus (a) P<sub>2</sub>O<sub>5</sub>; and (b) Fe<sub>2</sub>O<sub>3</sub>(t). Orange symbols: typical metalliferous sediments with <2 wt % Al<sub>2</sub>O<sub>3</sub>; blue symbols: metalliferous sediments deposited at or below lysocline. Latter sediments are enriched in Al<sub>2</sub>O<sub>3</sub>, Zr and REE due to higher proportions of detrital aluminosilicates. [Note that only three of the five sub-lysocline samples shown in Figs. 19 and 21 were analysed for REE.]
- Fig. 21.** Selected trace element contents of metalliferous sediments from East Pacific Rise transect (DSDP Leg 92) on a carbonate-free basis. (a) Mo vs. Al<sub>2</sub>O<sub>3</sub>; (b) Mo vs. depth for Sites 597 and 599; (c) Ba vs. Co; (d) ΣREE vs. Al<sub>2</sub>O<sub>3</sub>. Orange symbols: metalliferous sediments with <2 wt % Al<sub>2</sub>O<sub>3</sub>; blue symbols: sediments deposited at or below

lysocline and enriched in terrigenous aluminosilicates; green dots: near-basement sediments containing basaltic detritus (Site 597). In (a), detrital trend is based on average shale composition (Taylor and McLennan, 1995); hydrothermal trend is based on (but extrapolated beyond) the maximum value of 249 ppm Mo and 1.12 % Al<sub>2</sub>O<sub>3</sub> reported by Marchig and Gundlach (1982) for carbonate-free metalliferous sediments from crest of East Pacific Rise; hydrogenous trend is based on Pacific Fe-Mn nodules (N symbol; Li and Schoonmaker, 2003). In (b), increase in Mo to values of 500–600 ppm near basaltic basement is attributed to increased hydrothermal contribution, as terrigenous detritus and basaltic debris cannot provide more than several ppm Mo to sediment. In (c), sub-lysocline sediments tend to be enriched in Ba and Co relative to metalliferous sediments due to hydrogenous and detrital components. In (d), most samples lie along a roughly linear trend that is interpreted to result from mixing between rapidly accumulating metalliferous end-member (low Al, low REE) and slowly accumulating detrital + hydrogenous end-member (high Al, high REE).

**Fig. 22.** REE composition of metalliferous sediments from Sites 599 and 598, East Pacific Rise transect (DSDP Leg 92) on a carbonate-free basis. (a) Site 599; (b) Site 598. Shown for comparison are REE patterns of deep seawater at 18°N, 108°W, 3000 m depth, in east Pacific Ocean (De Baar et al. 1985; deep waters at 26°S, 114°W are very similar: Jeandel et al., 2013), and bone debris and Fe-Mn micronodules from south-central Pacific Ocean (Dubinin and Sval'nov, 2001). Also shown are approximate age ranges (in Ma) of sampled Leg 92 metalliferous sediments. Leg 92 REE patterns shown here are very similar to those reported by Barrett et al. (1986) and Ruhlin and Owen (1986) for different sample suites from Sites 597 to 600, Leg 92. All REE concentrations normalized to PAAS.

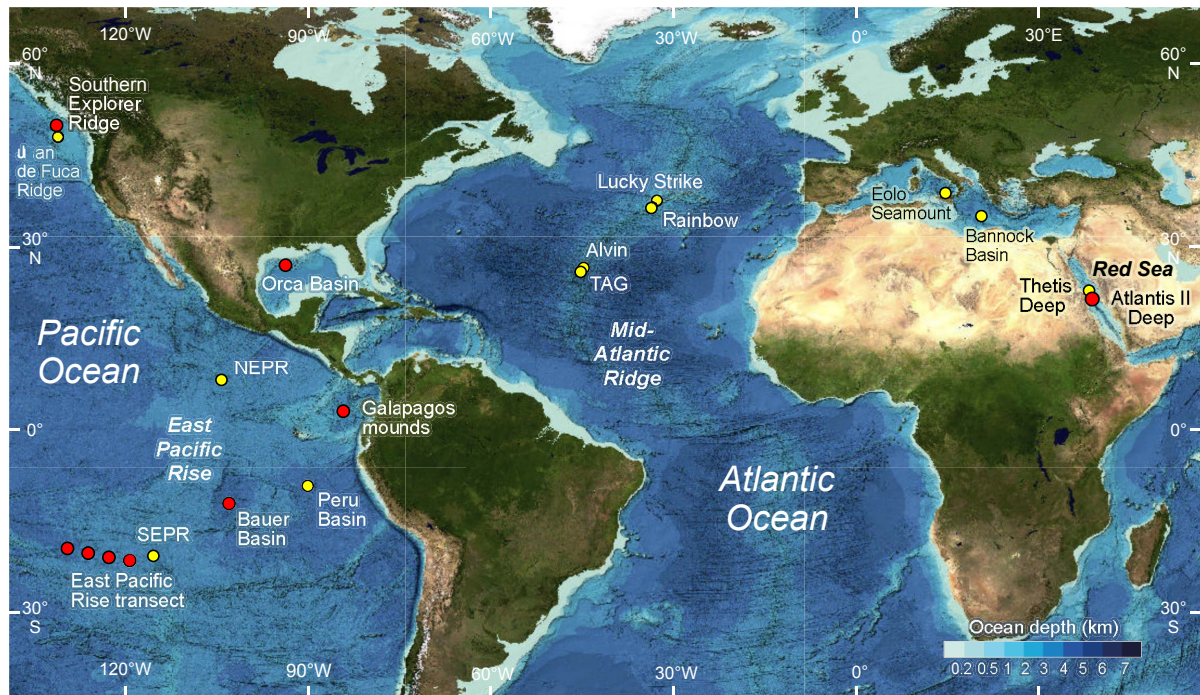
**Fig. 23.** Location and structure of Galapagos hydrothermal mounds. (a) Simplified map of eastern equatorial Pacific Ocean, showing location of Galapagos hydrothermal mounds field on southern flank of Galapagos Rift spreading ridge. Compiled from Van Andel et al. (1971), Pedersen and Furnes (2001), and Scheibner et al. (2013). Location of DSDP Leg 70 Sites 506 to 508, which sampled the Galapagos hydrothermal mounds, is indicated by yellow arrow; other Leg 70 drilling sites are shown as open circles (unlabelled). (b) Schematic cross-section of mound consisting of 20–30 m of interlayered nontronite-rich precipitates and normal calcareous ooze, overlain by thin surficial Mn oxide crusts. Modified from Honnorez et al. (1981).

- 2648 **Fig. 24.** REE composition of nontronite and Fe-Mn oxide sediments from Galapagos  
 1 hydrothermal mounds (Barrett et al., 1988). Arrows show effects of (1) net mass loss  
 2 during formation of transitional nontronite; and (2) net mass gain during formation of  
 3 granular nontronite, relative to composition of “incipient nontronite” (nontronite-  
 4 bearing calcareous pelagic ooze from below the main nontronite interval in Hole 506).  
 5  
 6 Oxygen-isotope data suggest that nontronites formed at 20–50°C (Barrett and  
 7 Friedrichsen, 1982; McMurtry et al., 1983). REE concentrations normalized to PAAS.  
 8  
 9  
 10  
 11  
 12  
 13 **Fig. 25.** REE composition of nontronites and residual Fe-oxides from TAG and Alvin areas at  
 14 26°N, Mid-Atlantic Ridge (Severmann et al., 2004; location in Fig. 1). REE  
 15 concentrations normalized to PAAS.  
 16  
 17  
 18  
 19  
 20  
 21 **Fig. 26.** REE composition of sulphide-silica-sulphate deposits on Southern Explorer Ridge, NE  
 22 Pacific Ocean (location in Fig. 1). (a) Samples with mixed hydrothermal-seawater REE  
 23 signal. (b) Samples with mainly seawater REE signal. Data for Southern Explorer Ridge  
 24 from Barrett et al. (1990). Shown for comparison are REE patterns for deep seawater  
 25 at 2975 m in eastern Pacific (Jeandel et al., 2013), and Fe-Mn oxide mud from a low-  
 26 temperature hydrothermal mound near Galapagos Spreading Centre (Barrett et al.,  
 27 1988). REE concentrations normalized to PAAS.  
 28  
 29  
 30  
 31  
 32 **Fig. 27.** Compilation of  $\epsilon\text{Nd}$  values for oceanic metalliferous sediments, biotrital sediments,  
 33 vent fluids, seawater and basalts. (a) closed-basin settings along axis of Red Sea; (b)  
 34 and (c) open-ocean settings along spreading axes of eastern Pacific Ocean and Mid-  
 35 Atlantic Ridge, respectively. Data sources: <sup>1</sup> Scrivner et al. (2004); Tachikawa et al.  
 36 (2004); <sup>2</sup> Cocherie et al. (1994); <sup>3</sup> this study; <sup>4</sup> Pierrot et al. (2010); <sup>5</sup> Eissen et al. (1989),  
 37 Volker et al. (1993); <sup>6</sup> Grasse et al. (2012), Jeandel et al. (2013), Molina-Kescher et al.  
 38 (2014); Tachikawa et al. (2017); <sup>7</sup> O’Nions et al. (1978), Piepgras et al. (1979), Albarède  
 39 and Goldstein (1992), Ling et al. (1997), van der Fliedrt et al. (2004), Amakawa et al.  
 40 (2017); <sup>8a</sup> O’Nions et al. (1978), Piepgras et al. (1979), Sun et al. (2018); <sup>8b</sup> Halliday et al.  
 41 (1992); <sup>9</sup> Piepgras and Wasserburg (1985), Hinkley and Tatsumoto (1987); <sup>10</sup> Hegner  
 42 and Tatsumoto (1987), Hinkley and Tatsumoto (1987), White et al. (1987); <sup>11</sup> van de  
 43 Fliedrt et al. (2016), Tachikawa et al. (2017), Stichel et al. (2018); <sup>12</sup> Chavagnac et al.  
 44 (2006); <sup>13</sup> Mills et al. (1993); <sup>14</sup> Dias et al. (2008); <sup>15</sup> Chavagnac et al. (2018); <sup>16</sup> Ferreira  
 45 et al. (2006), Dosso et al. (1999).  
 46  
 47  
 48  
 49  
 50  
 51  
 52  
 53  
 54  
 55  
 56  
 57  
 58  
 59  
 60  
 61  
 62  
 63  
 64  
 65

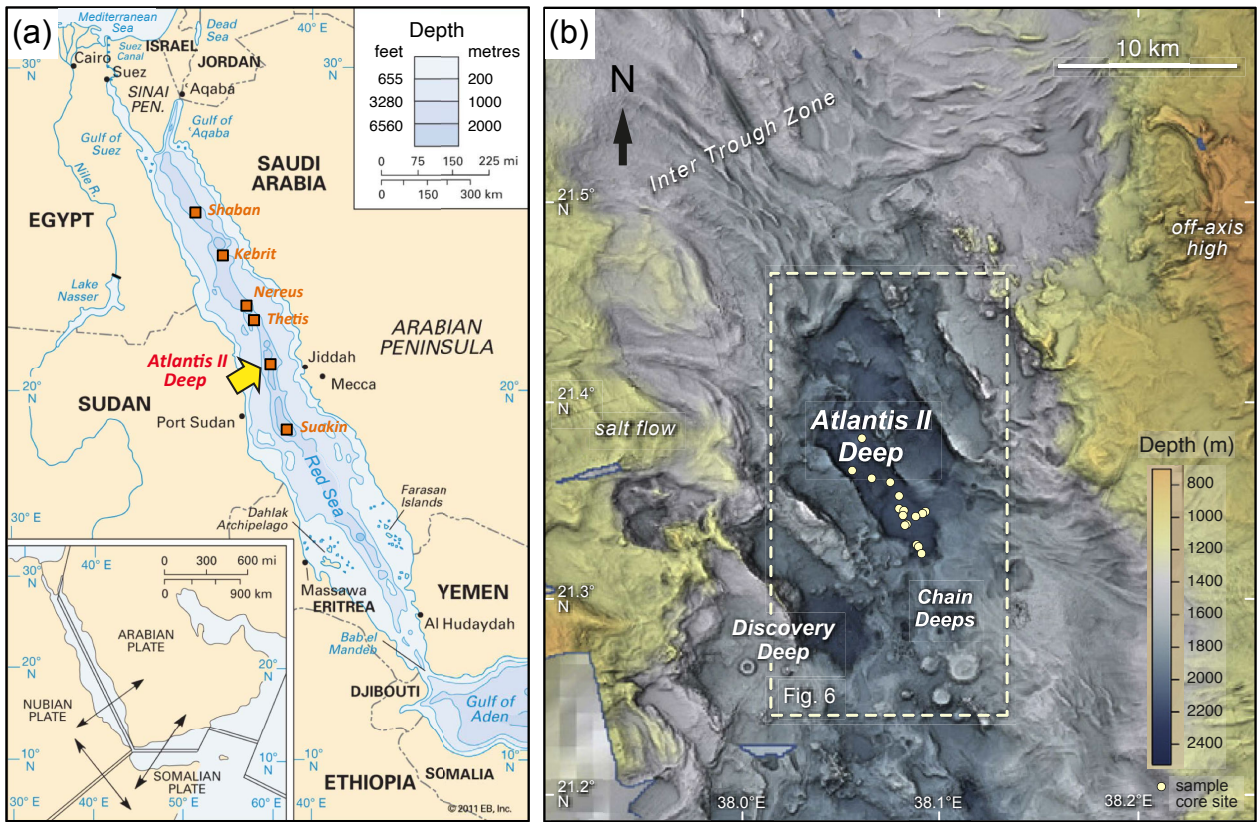
**Fig. 28.** Representative REE patterns and  $\epsilon\text{Nd}$  values for typical metalliferous sediment from the Atlantis II Deep (this study; see also Cocherie et al., 1994) and possible source materials in the Red Sea and surrounding region. Sample details, top to bottom: Saharan dust: Greaves (1994); Red Sea sediments: insoluble residue (dust) from biotrital sample PD55 (15.1 ka), core K23, northern Red Sea (Palchan et al., 2013); Red Sea sediments: biotrital sample at 15–20 cm, core 1016, central Red Sea (Pierret et al., 2010); Atlantis II Deep: metalliferous sediment 443-2, Table 2 (this paper); MAR smoker fluid: sample 2598 Ti8BS (361°C) from TAG vent field, 26°N on Mid-Atlantic Ridge (Douville et al., 1999); MAR plume particles: sample SAP09-01 from Rainbow plume, 36°N on Mid-Atlantic Ridge (Edmonds and German, 2004); Bannock brine: sample at 3730 m in lower brine (15°C) of Bannock Basin in eastern Mediterranean Sea (Schijf et al., 1995); Mediterranean seawater: sample from 860 m depth (14°C), station S-290, central Mediterranean Sea (Censi et al., 2004).

**Fig. 29.** Representative REE patterns and  $\epsilon\text{Nd}$  values for metalliferous sediments, plume particulates and deep seawater from the eastern Pacific Ocean (and plume particulates from the Mid-Atlantic Ridge, MAR). East Pacific Rise (EPR) Fe-Mn-oxyhydroxide sediments on carbonate-free basis from Leg 92, western flank of the Rise at 19°S (this study; see also Ruhlin and Owen, 1986): (1) sediments deposited above lysocline; (2) sediments deposited below lysocline. Galapagos Hydrothermal Mounds (GHM) granular nontronite and manganiferous mud from Mounds at 1°N on south flank of Galapagos Rift in east Pacific Ocean (Barrett et al., 1988); MAR Fe-oxide sediments from Alvin area, 2 km from TAG sulphide mounds at 26°N on axis of Mid-Atlantic Ridge (Severmann et al., 2004); Deep seawater from VERTEX II site (18°N, 108°W) in east-central Pacific Ocean, 3000 m depth (de Baar et al., 1985); MAR 36°N plume particles: sample SAP09-01 from Rainbow plume, 36°N on the MAR (Edmonds and German, 2004); EPR 10°N plume particles: hydrocast 4, average of two samples (Sherrell et al., 1999). Nd isotopic compositions: DSDP Leg 92 sediments from Halliday et al. (1992); eastern Pacific Ocean deep waters from Grasse et al. (2012); Lacan et al. (2012); Jeandel et al. (2013); Molina-Kescher et al. (2014).

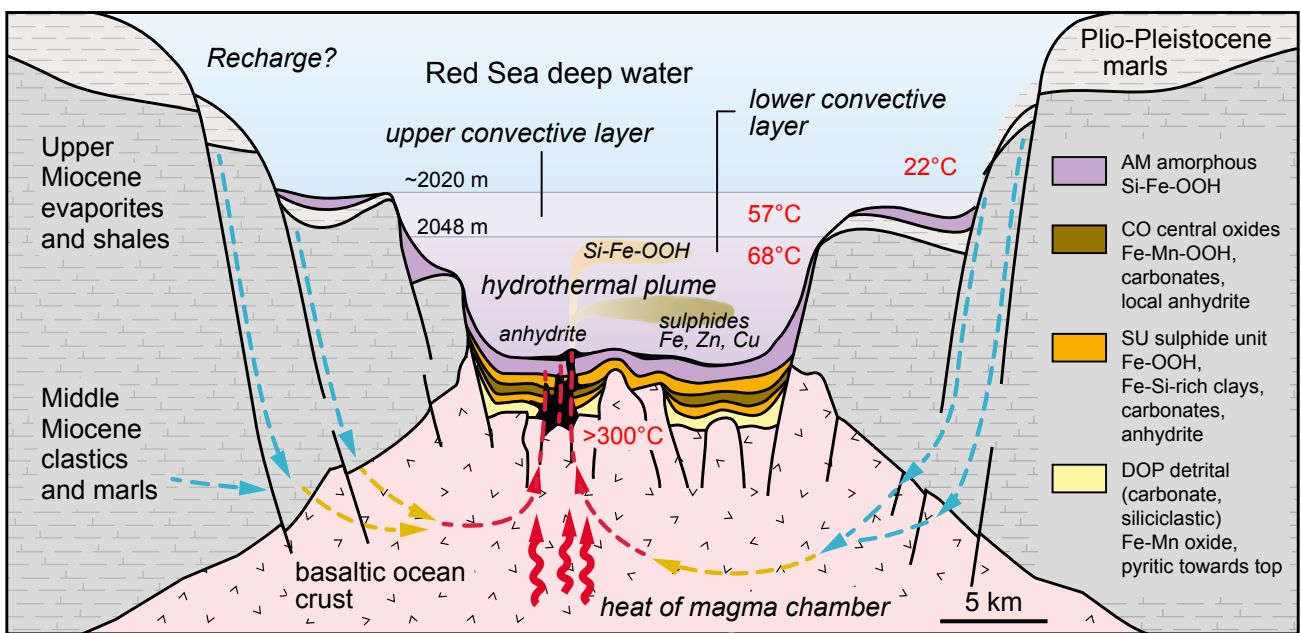
**Fig. 30.** Schematic trends in Nd and Sr isotopic compositions and REE patterns for metalliferous sediments containing different proportions of three source materials: pelagic shale (terrigenous siliciclastic component), hydrothermal fluid (leached basaltic component), and normal seawater plus biogenic debris (authigenic component). (a) Nd isotopic data for metalliferous sediments from Atlantis II Deep and East Pacific Rise transect (DSDP Leg 92) from present study and Halliday et al. (1992), respectively. (b) Schematic REE patterns, from top to bottom, represent pelagic shale, to which is added a hydrothermal component, then a normal (oxidized) seawater component. Metalliferous precipitates in anoxic closed basins would not develop lower three REE patterns unless hydrological conditions change and brine mixes with normal seawater. (c) Sr isotopic data for the Atlantis II Deep and East Pacific Rise transect (DSDP Leg 92) from Zierenberg and Shanks (1983) and Barrett et al. (1986), respectively. Typical values of potential sources of Nd and Sr to metalliferous sediments are shown on isotopic axes below the two plots. Values are selected from references listed in [Table 6](#) and are meant to be illustrative. Vent fluids, for example, can have  $\epsilon\text{Nd}$  values from +3.8 to +9.5 (Piepgras and Wasserburg, 1985; Hinkley and Tatsumoto, 1987; Chavignac et al., 2018), depending on proportion of seawater vs. basaltic Nd in hydrothermal fluid. Range for seawater  $\epsilon\text{Nd}$  is based on shallow and deep waters from eastern Mediterranean (Scrivner et al., 2004; Tachikawa et al., 2004). Biogenic range is based on biodepositional sediment from northern Red Sea (Cocherie et al., 1994). “Detrital” refers to terrigenous material supplied by airborne dust and rivers. Nd and Sr isotopic compositions of this material can vary amongst and even within major ocean basins. A-II = Atlantis II Deep.



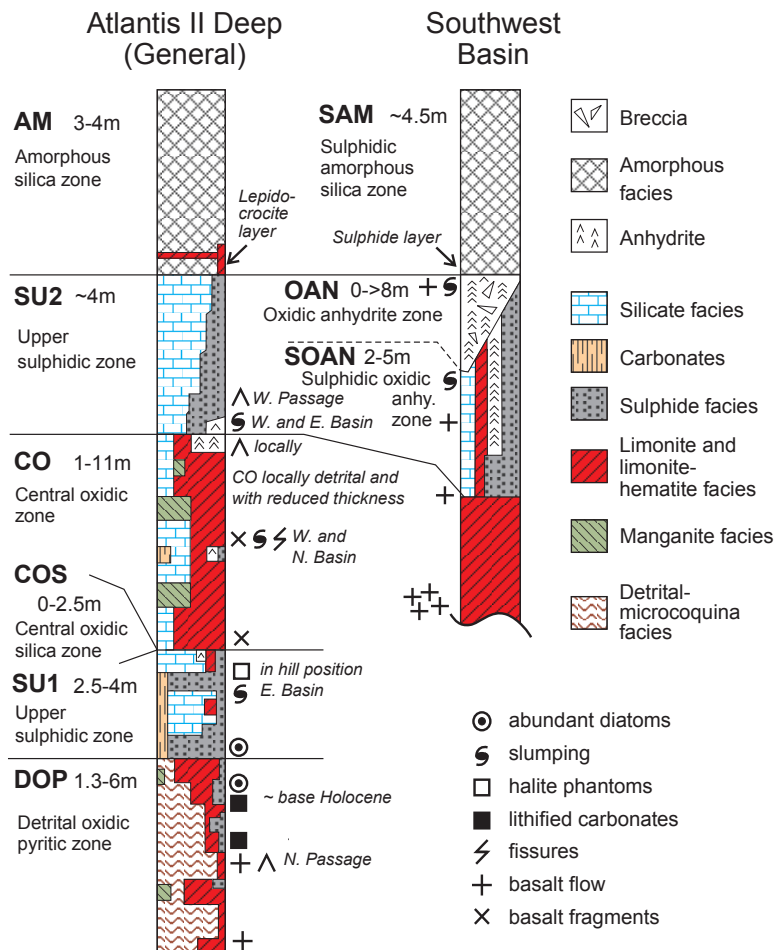
Barrett et al. Fig.1



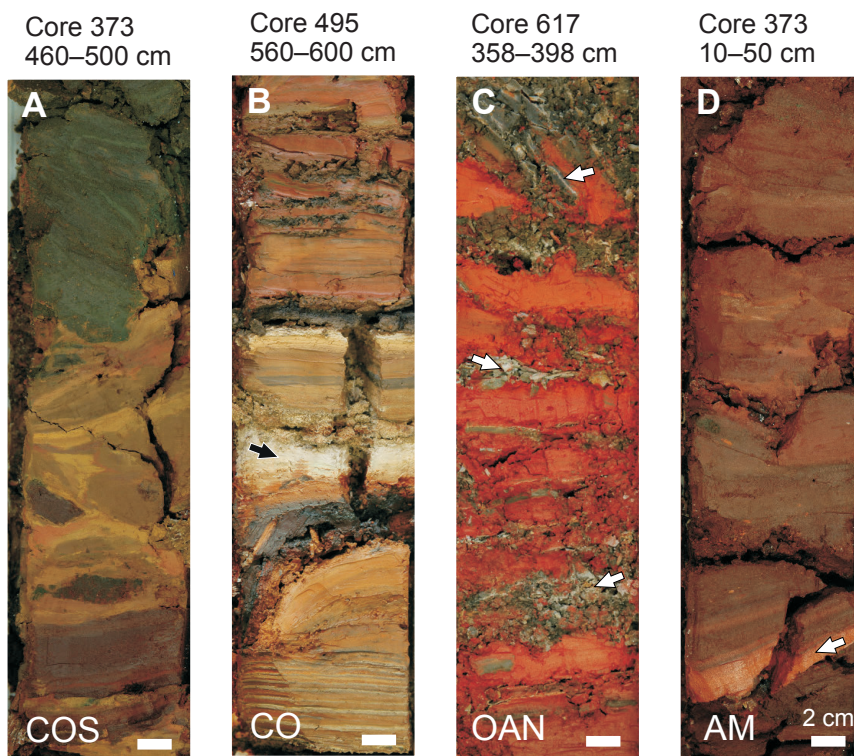
Barrett et al. Fig. 2



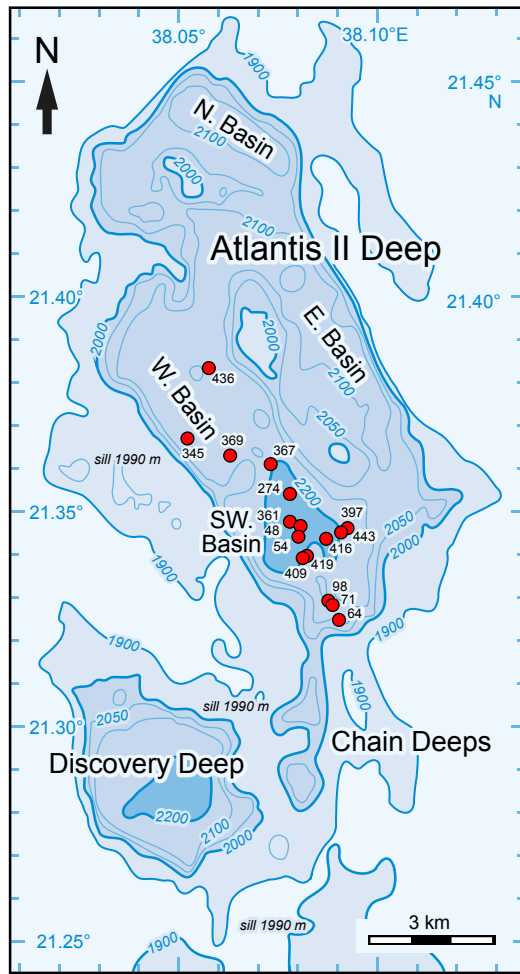
Barrett et al. Fig. 3



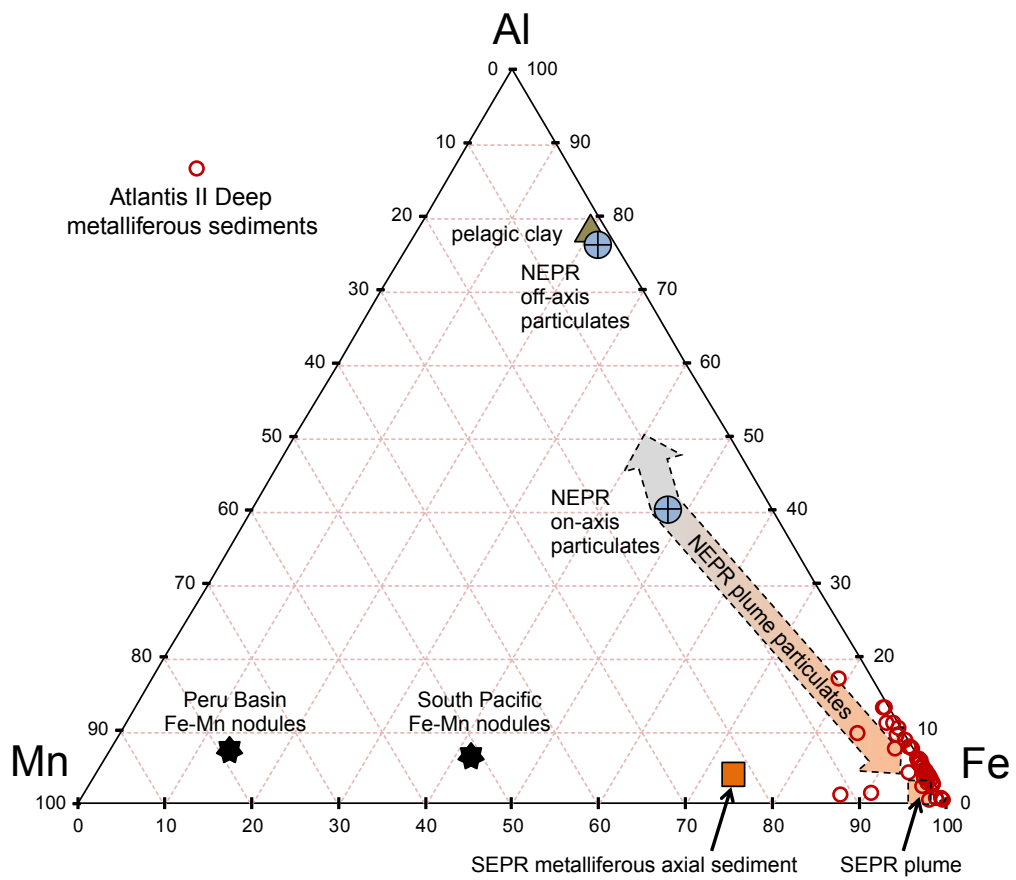
Barrett et al. Fig. 4



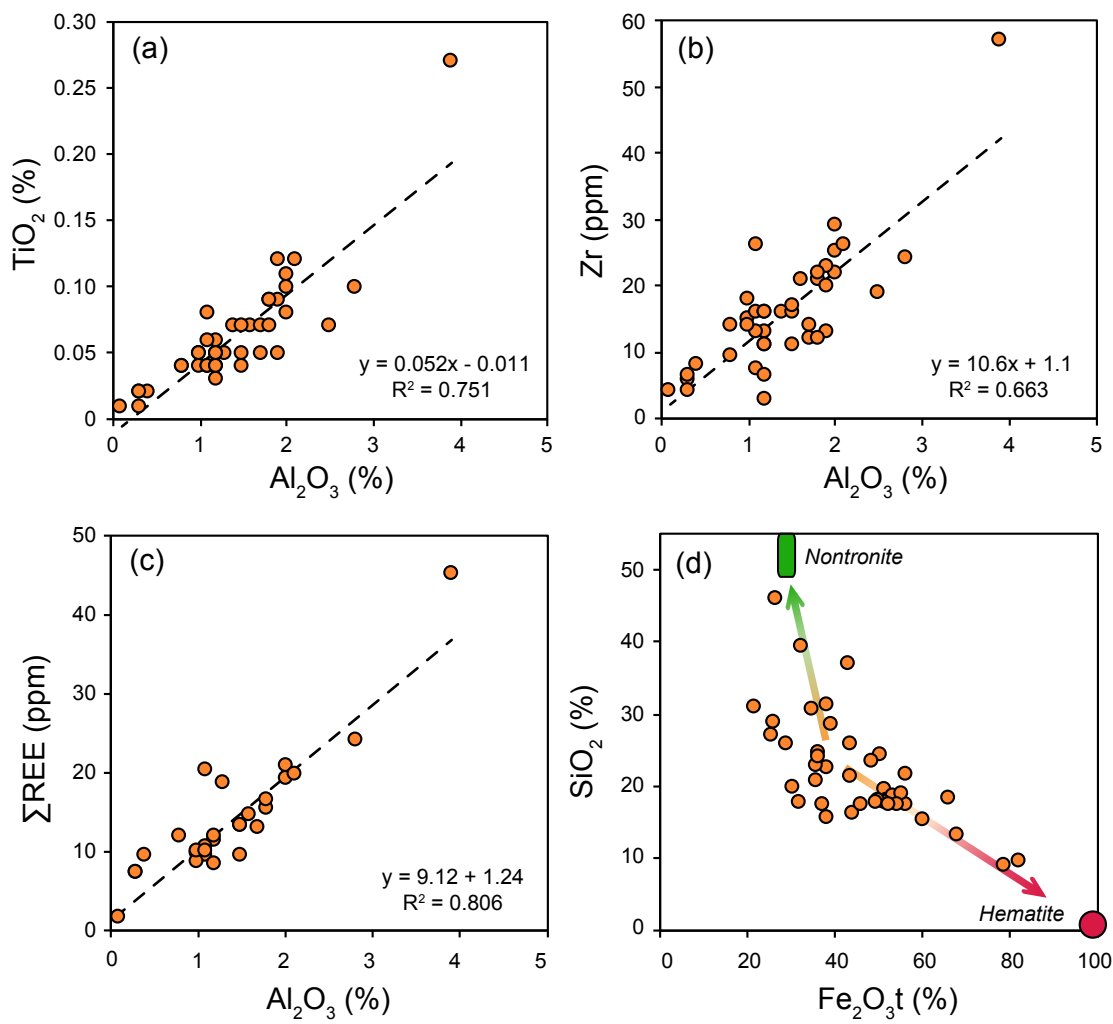
Barrett et al. Fig. 5



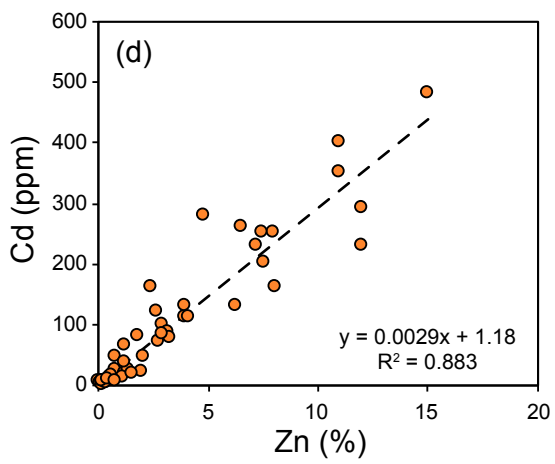
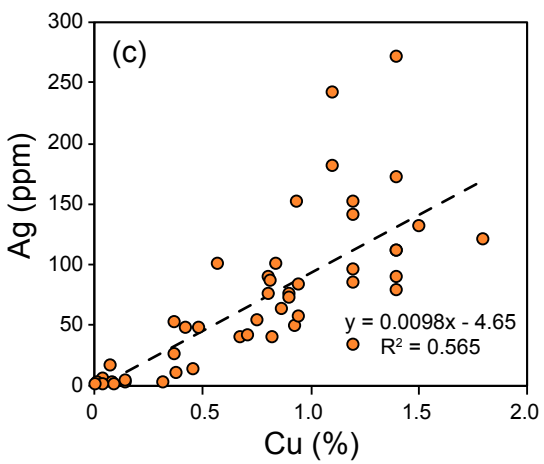
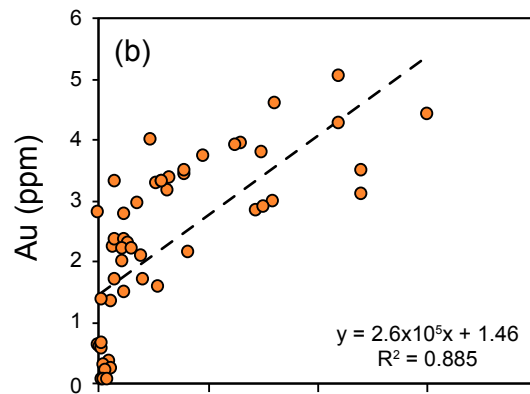
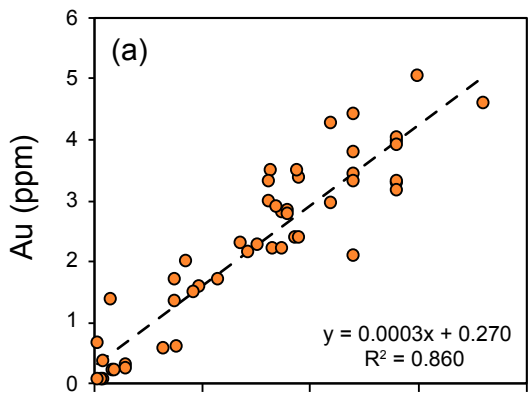
Barrett et al. Fig. 6



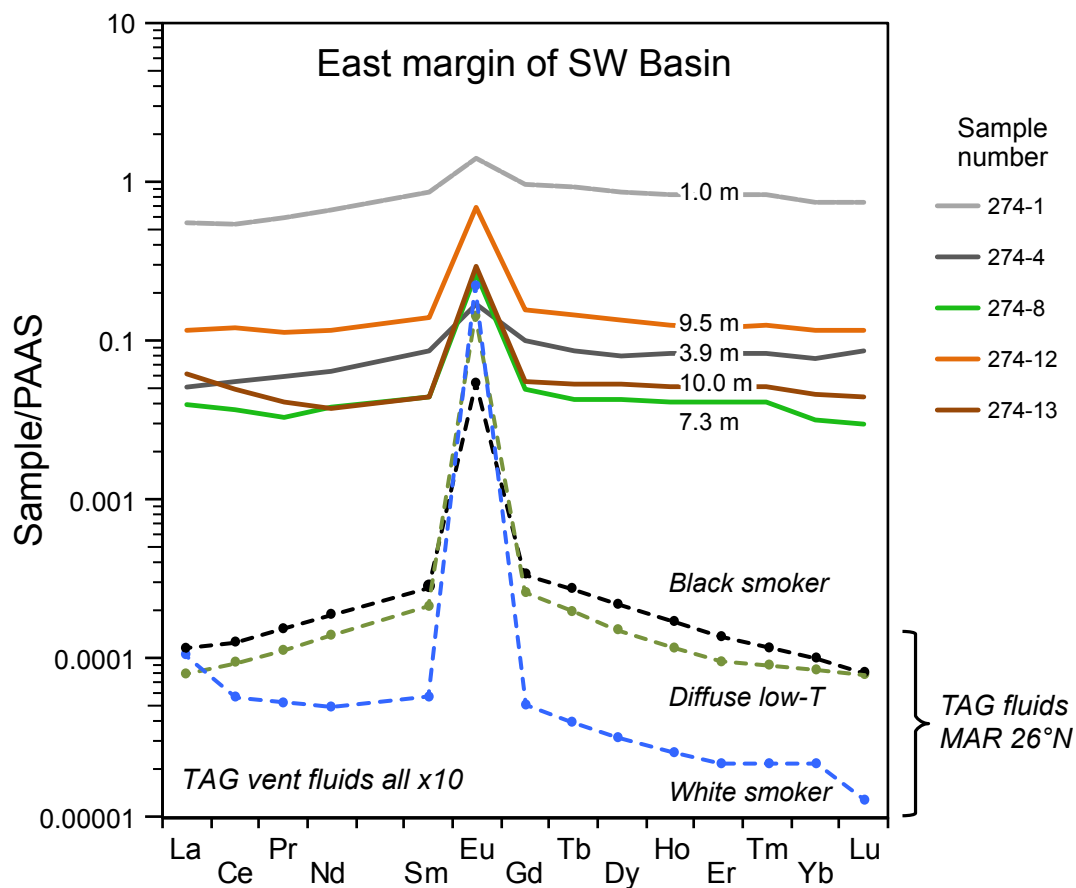
Barrett et al. Fig. 7



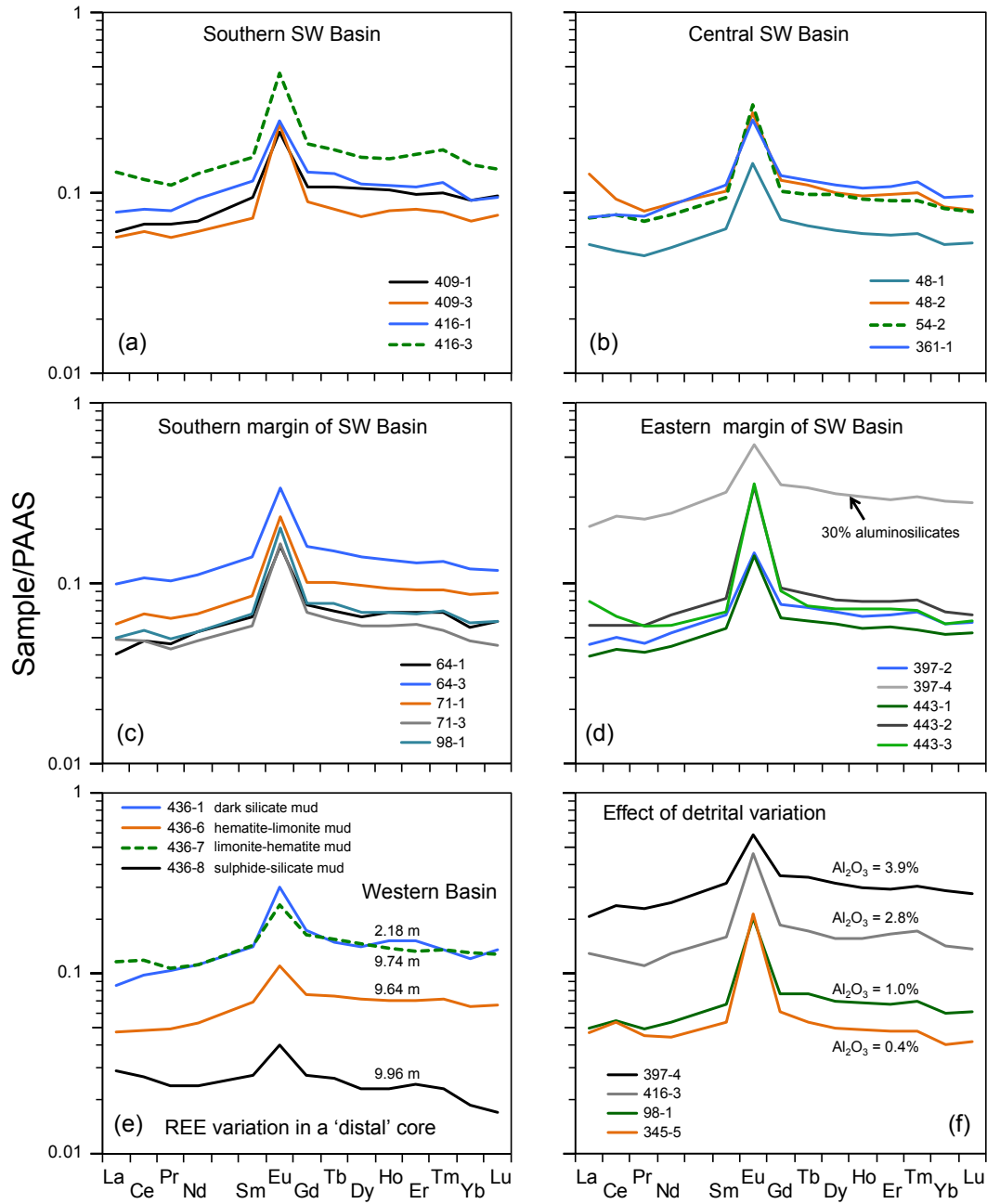
Barrett et al. Fig. 8



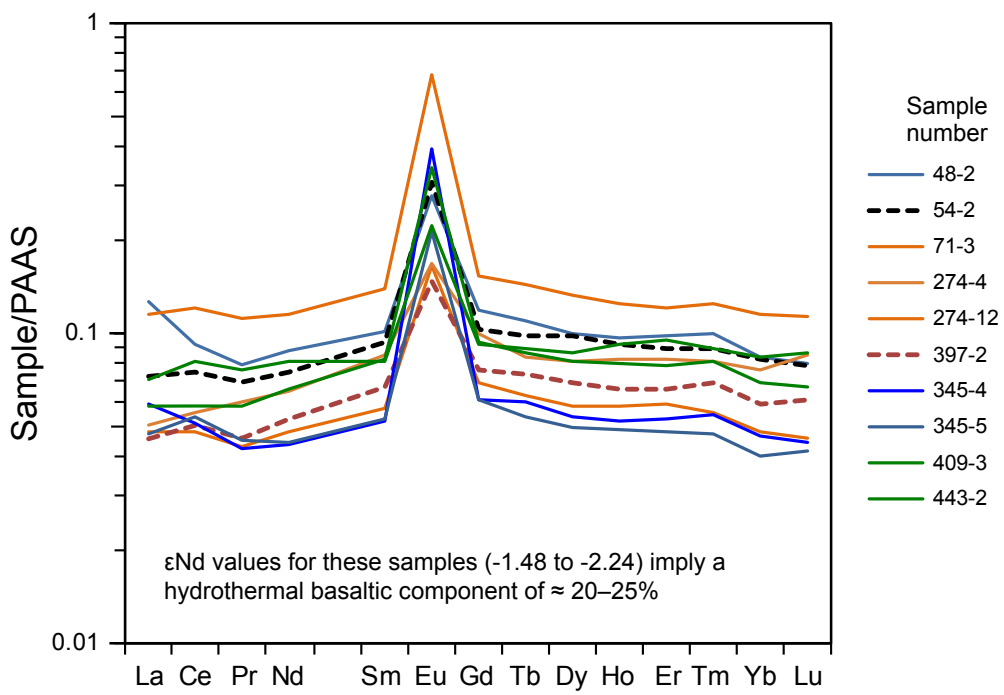
Barrett et al. Fig. 9



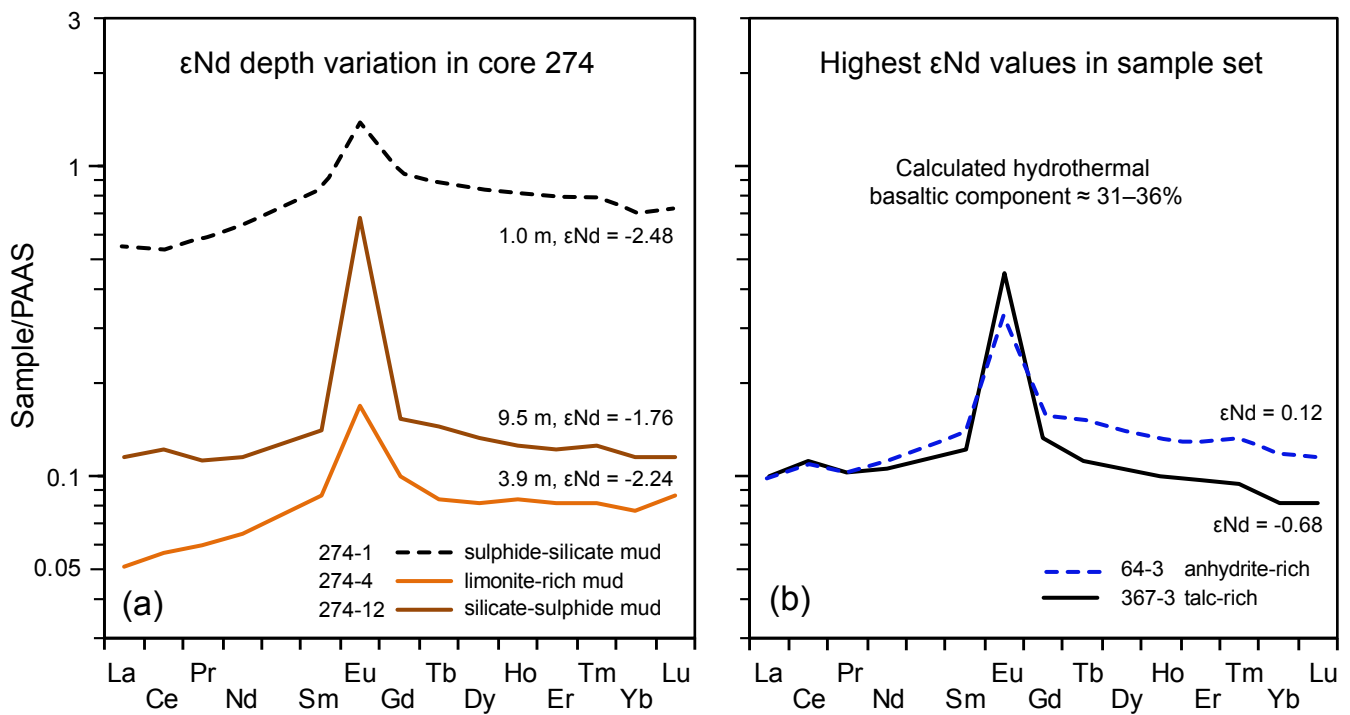
Barrett et al. Fig. 10



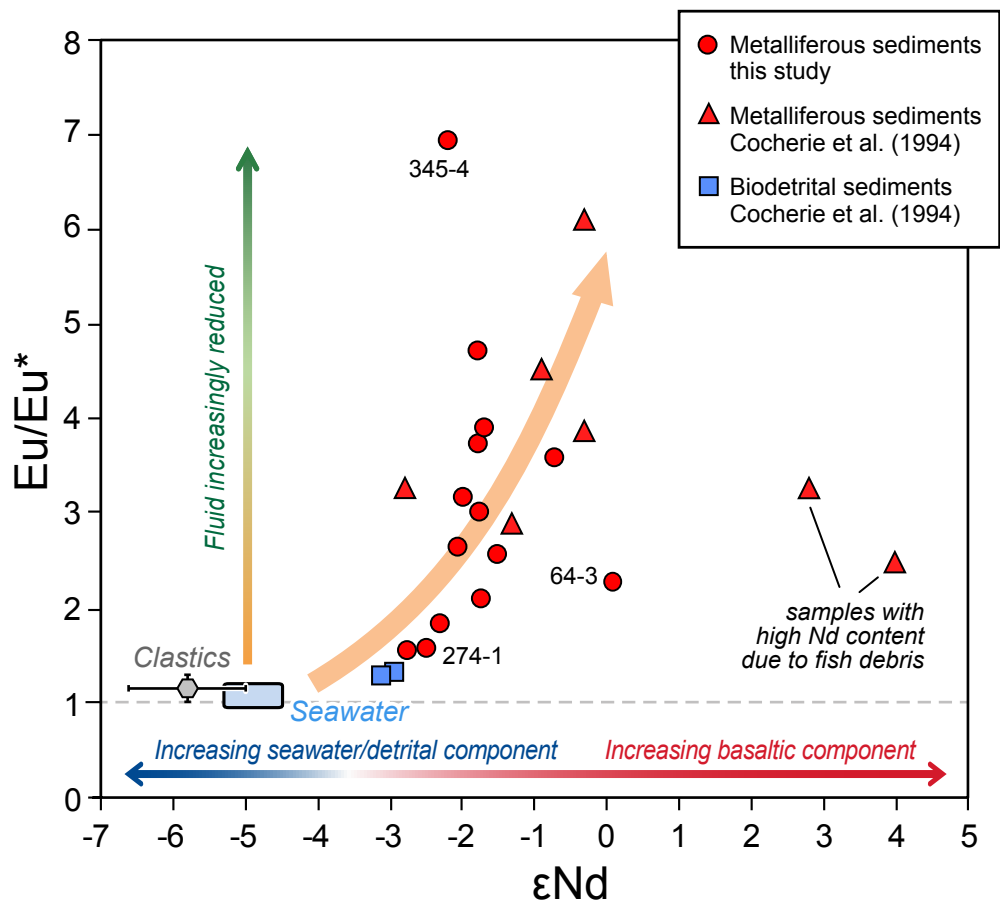
Barrett et al. Fig. 11



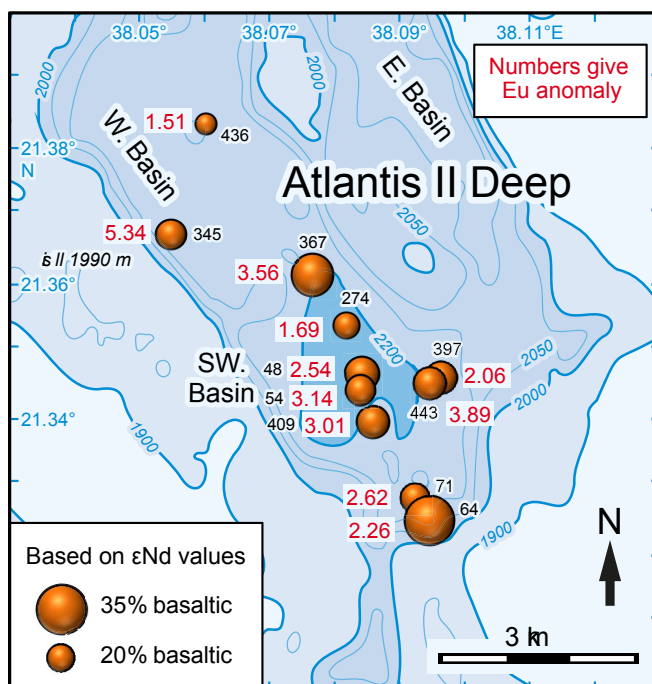
Barrett et al. Fig. 12



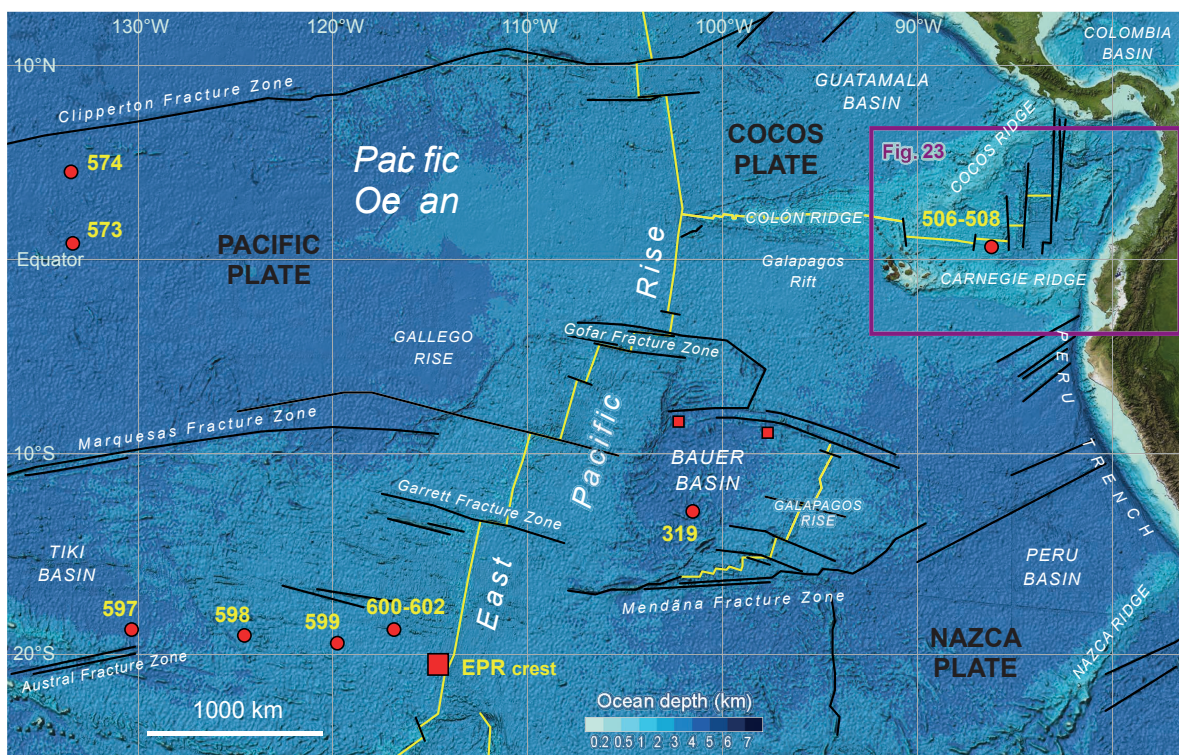
Barrett et al. Fig. 13



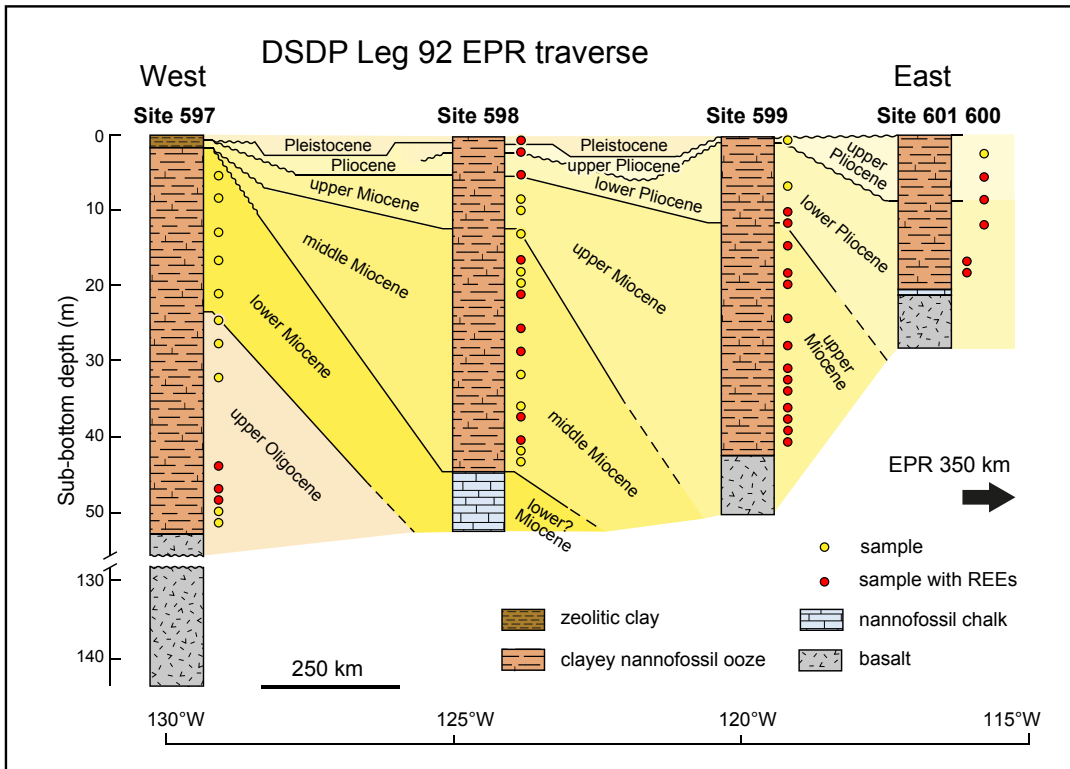
Barrett et al. Fig. 14



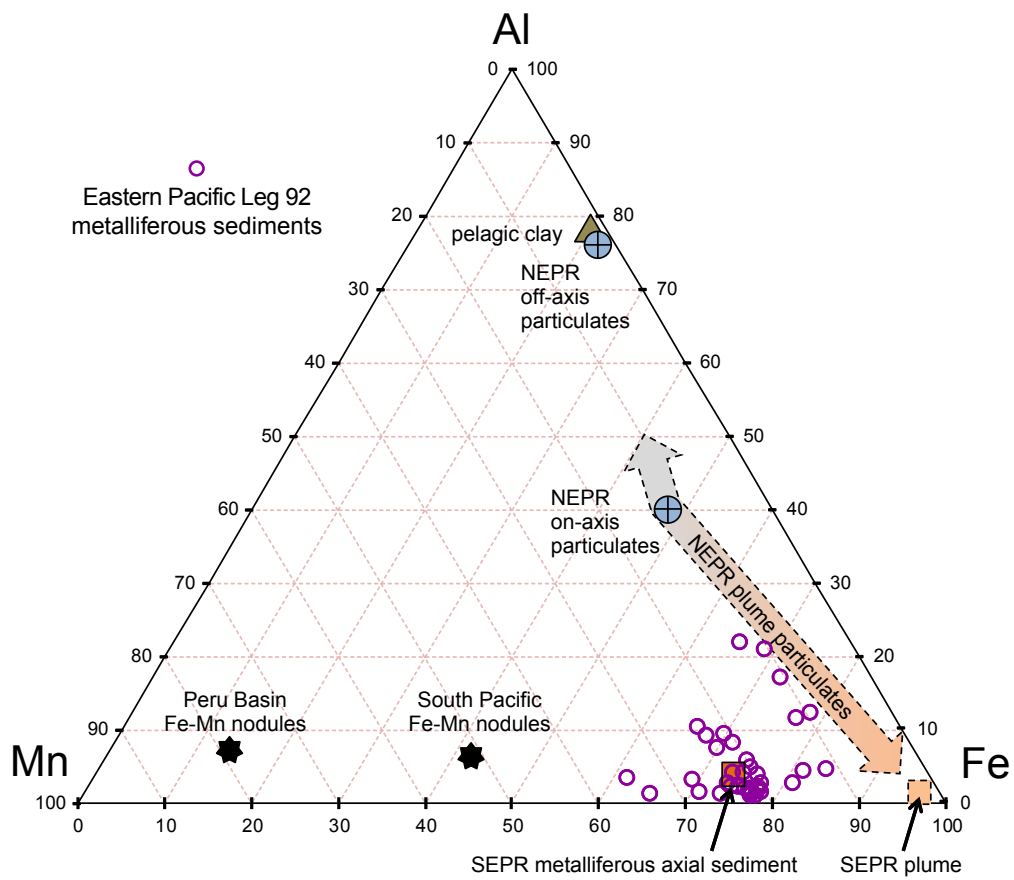
Barrett et al. Fig.15



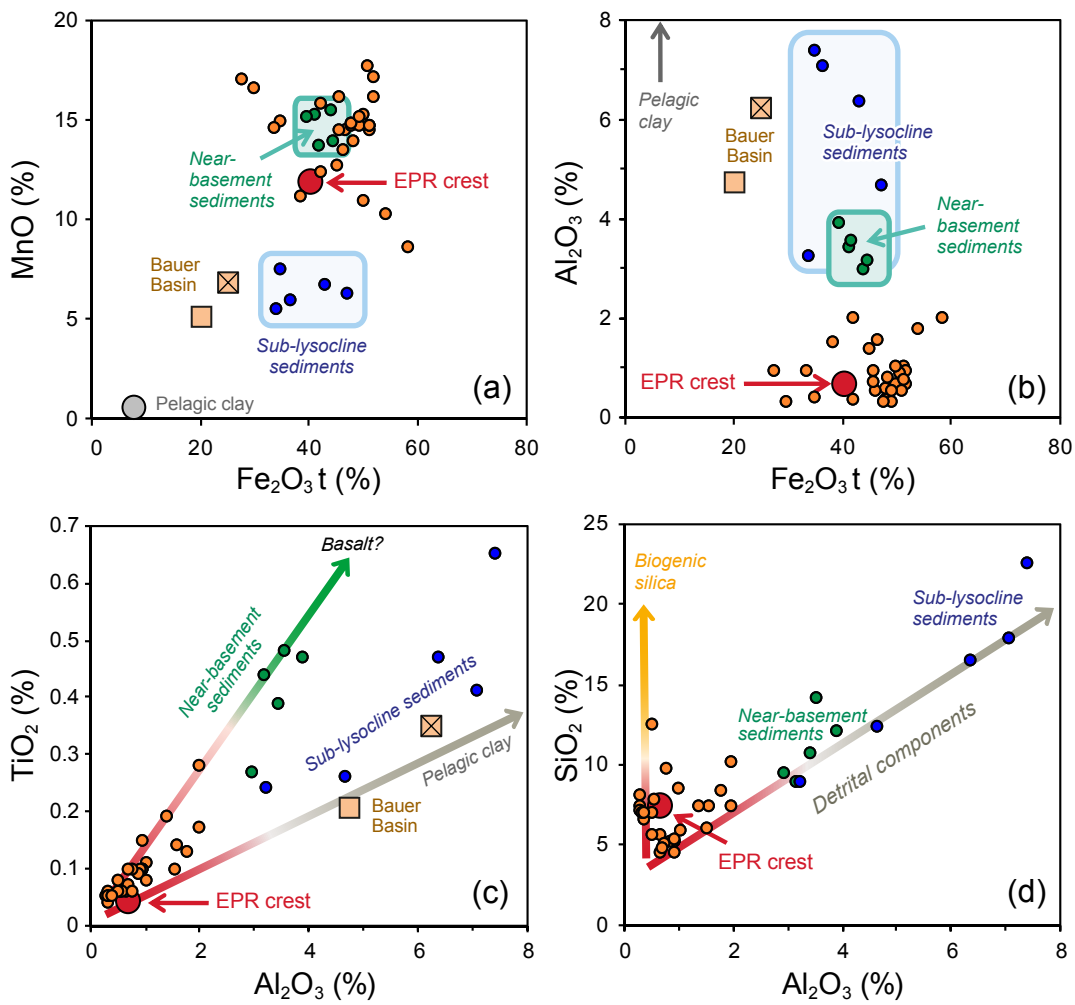
Barrett et al. Fig.16



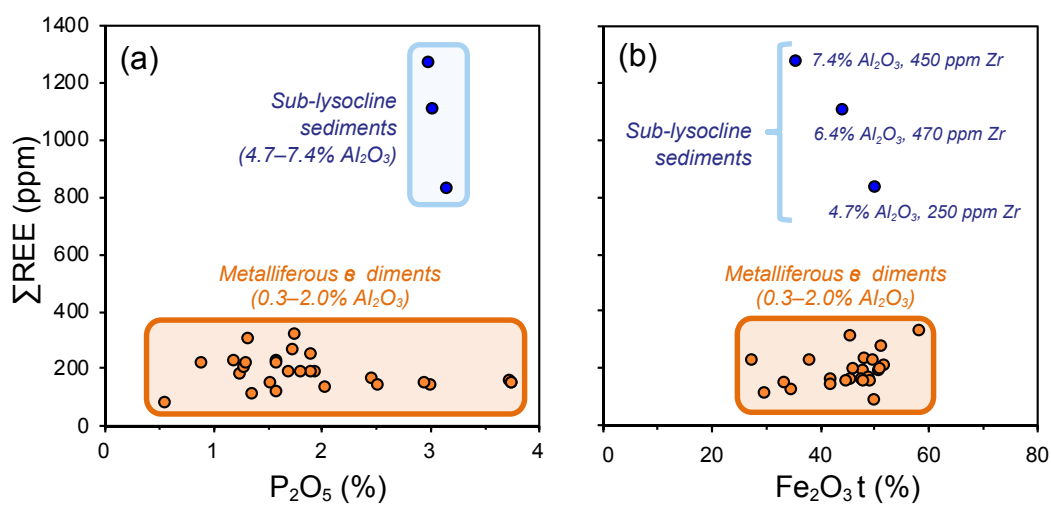
Barrett et al. Fig.17



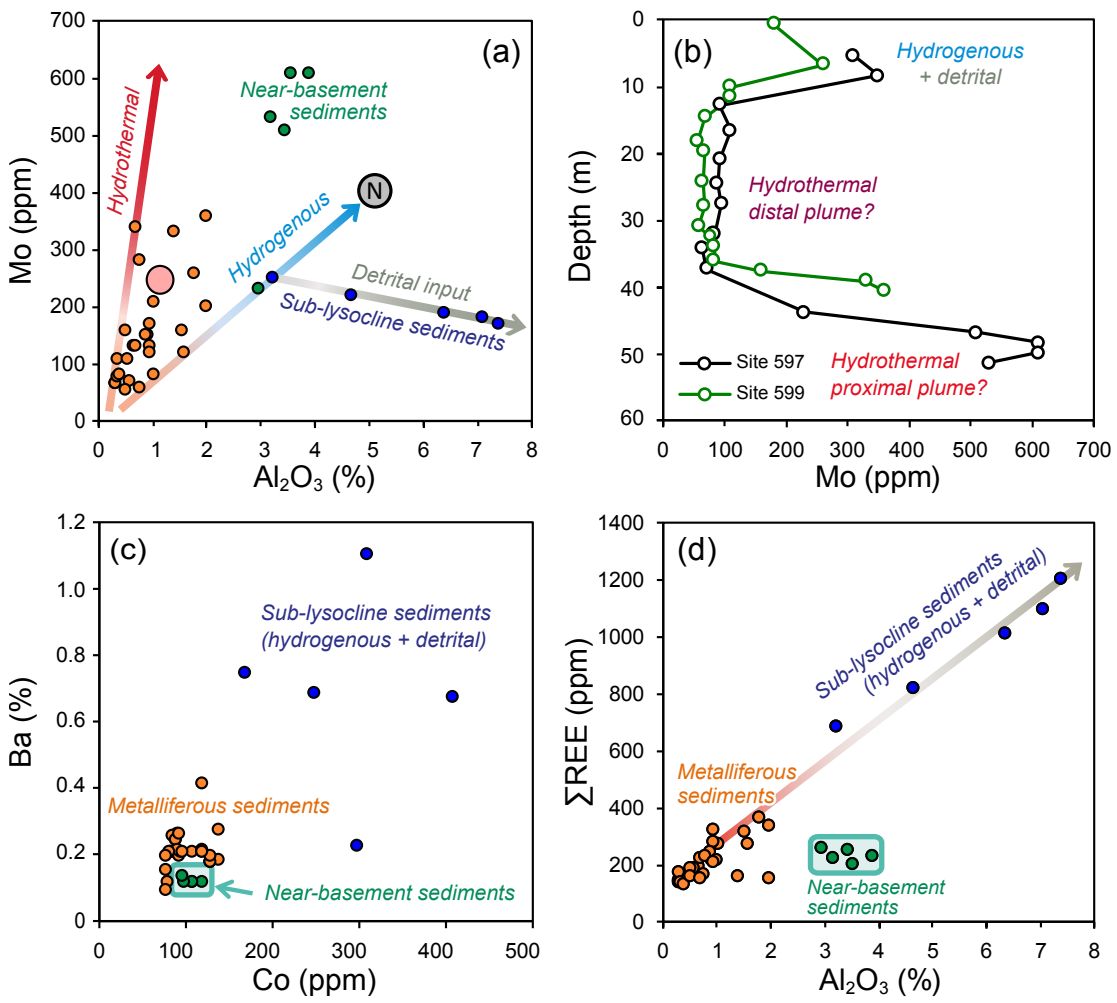
Barrett et al. Fig.18



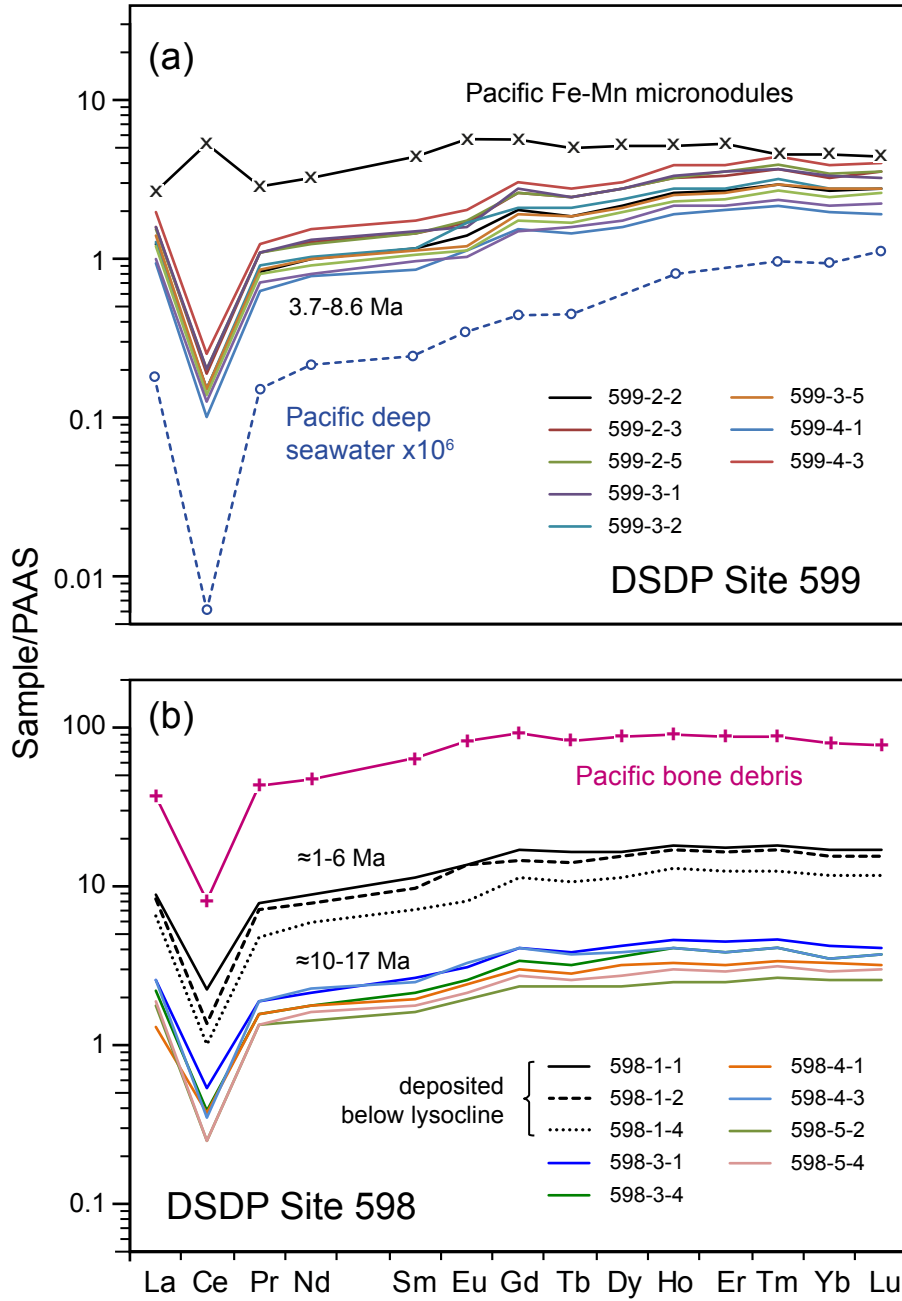
Barrett et al. Fig.19



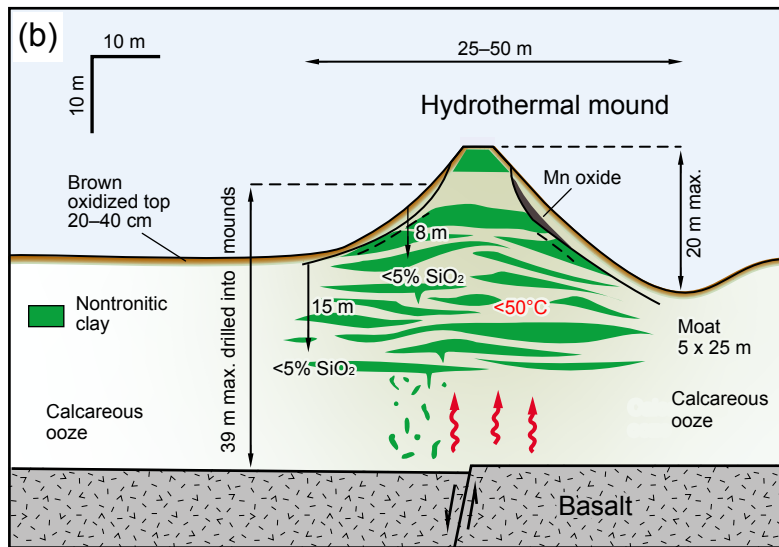
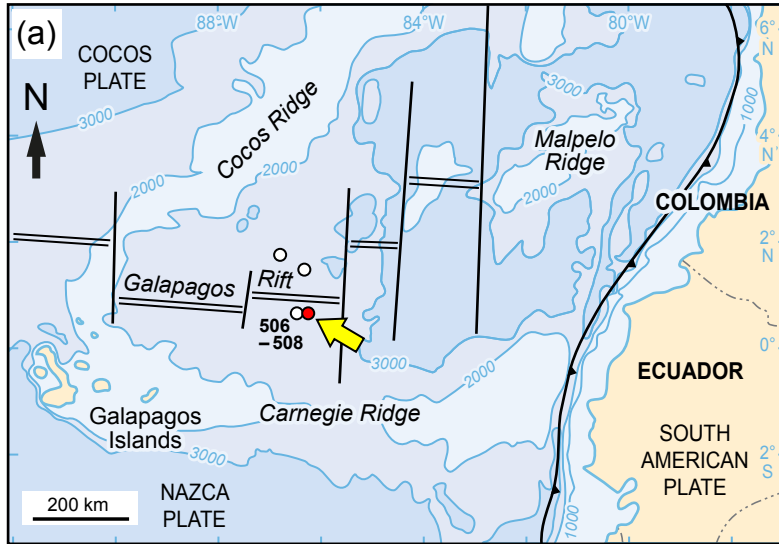
Barrett et al. Fig. 20



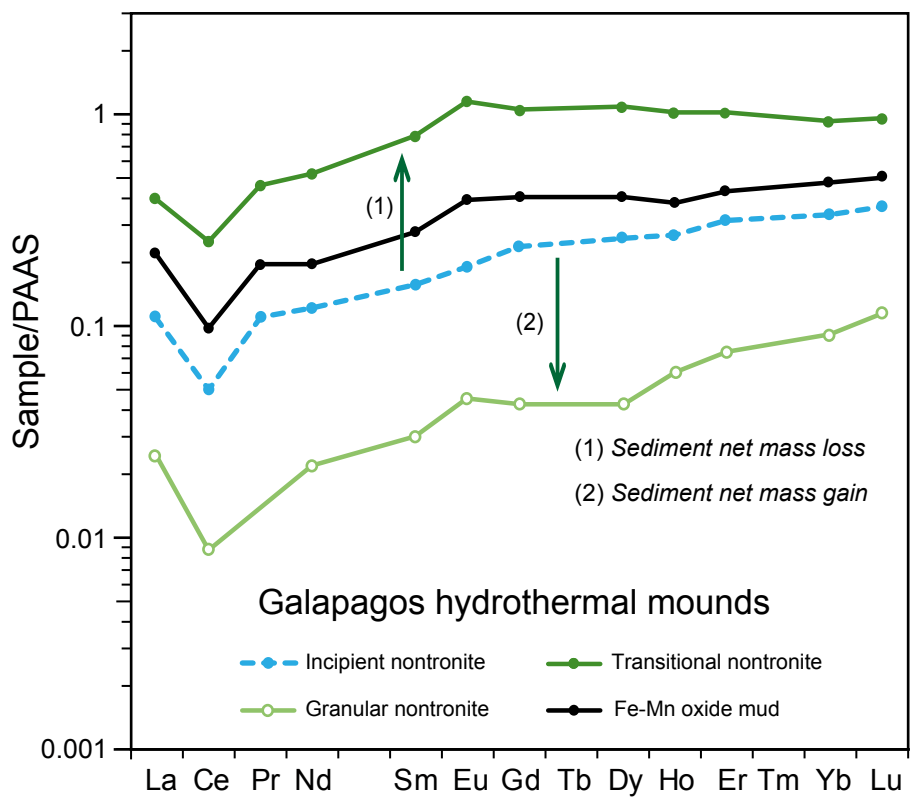
Barrett et al. Fig. 21



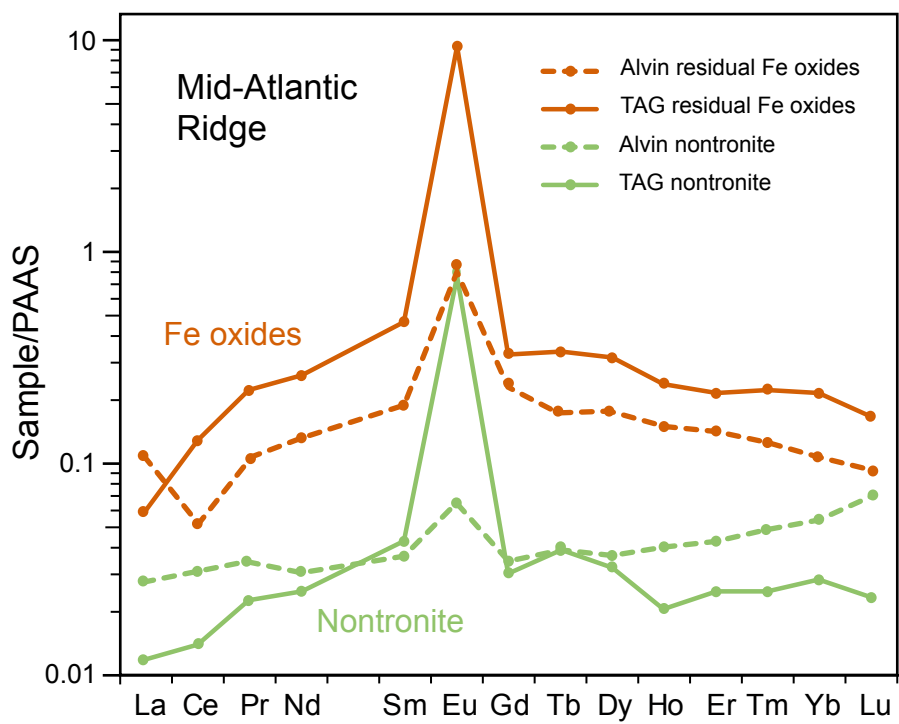
Barrett et al. Fig. 22



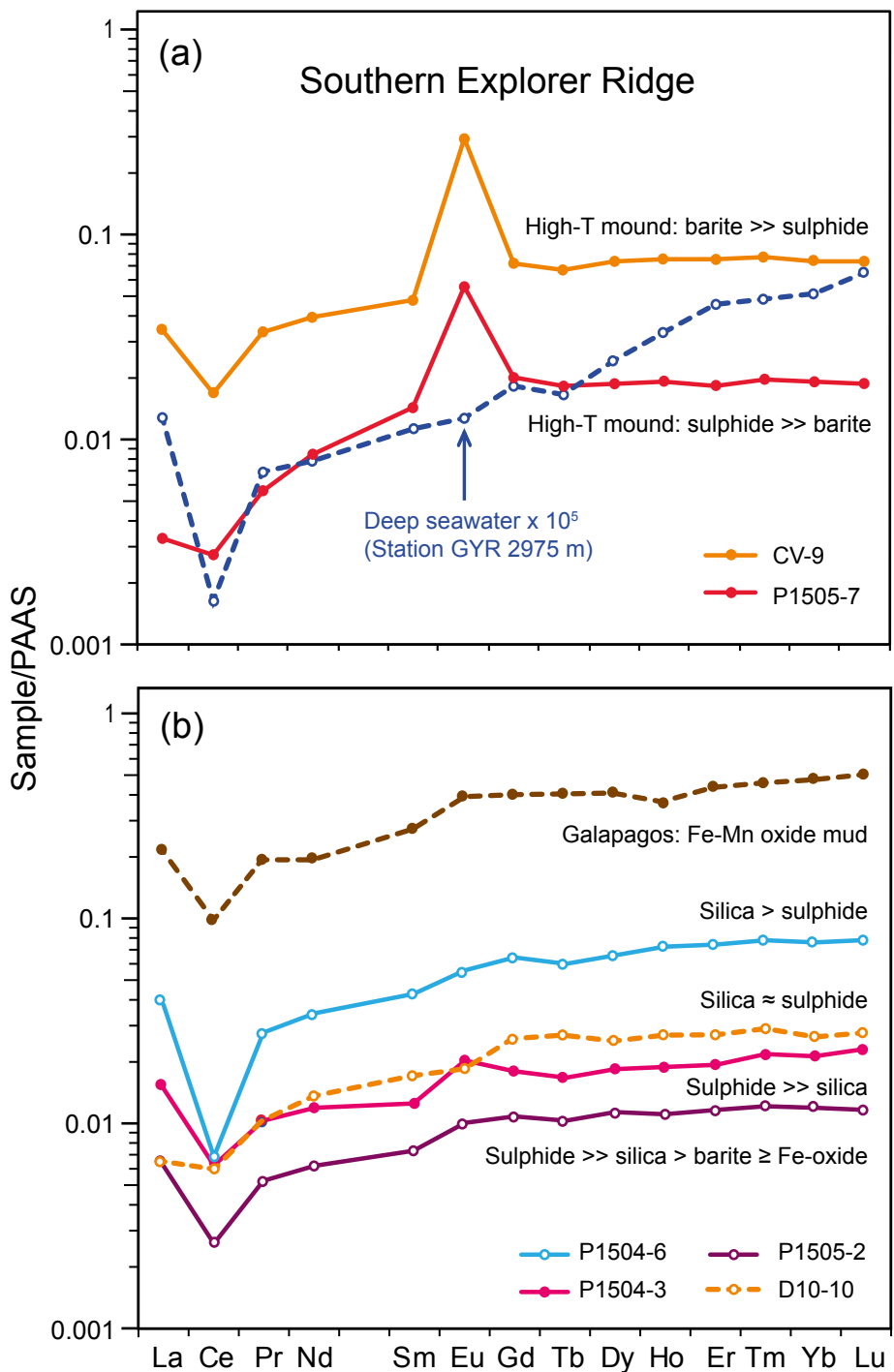
Barrett et al. Fig. 23



Barrett et al. Fig. 24

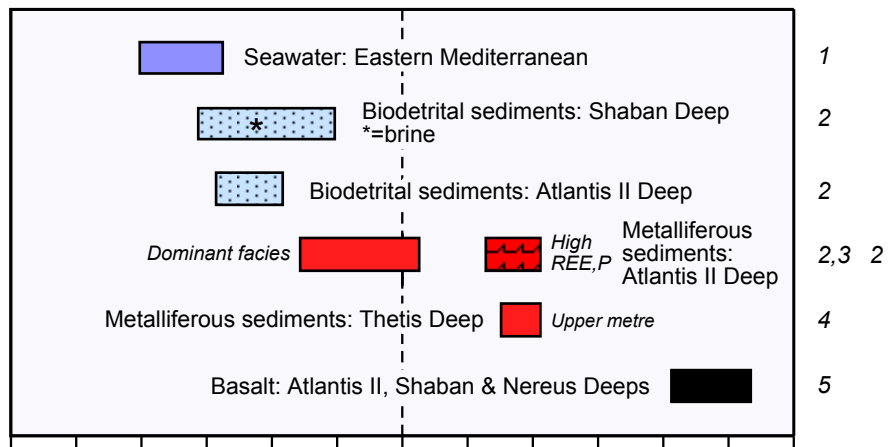


Barrett et al. Fig. 25

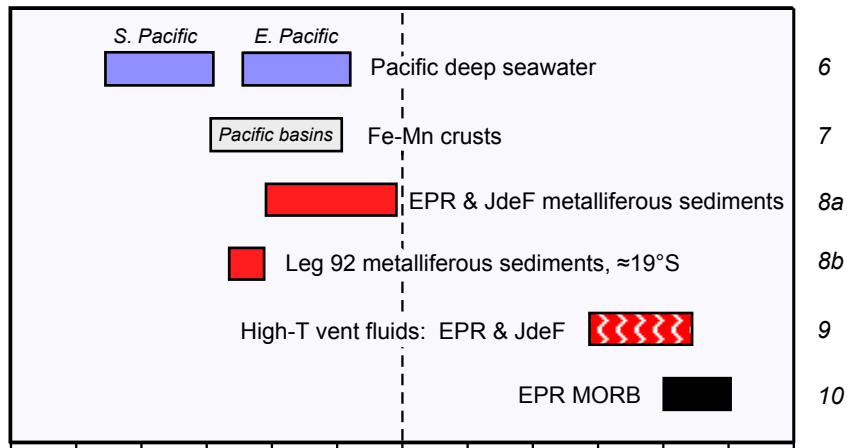


Barrett et al. Fig. 26

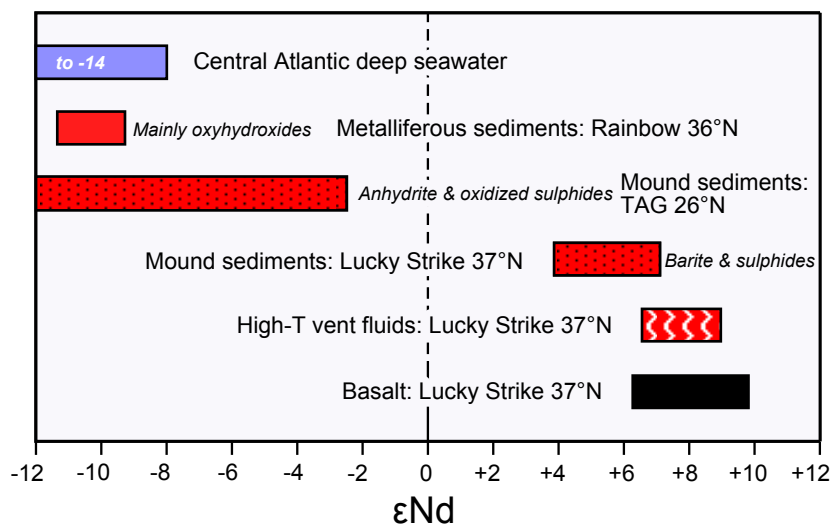
(a) Red Sea Deeps



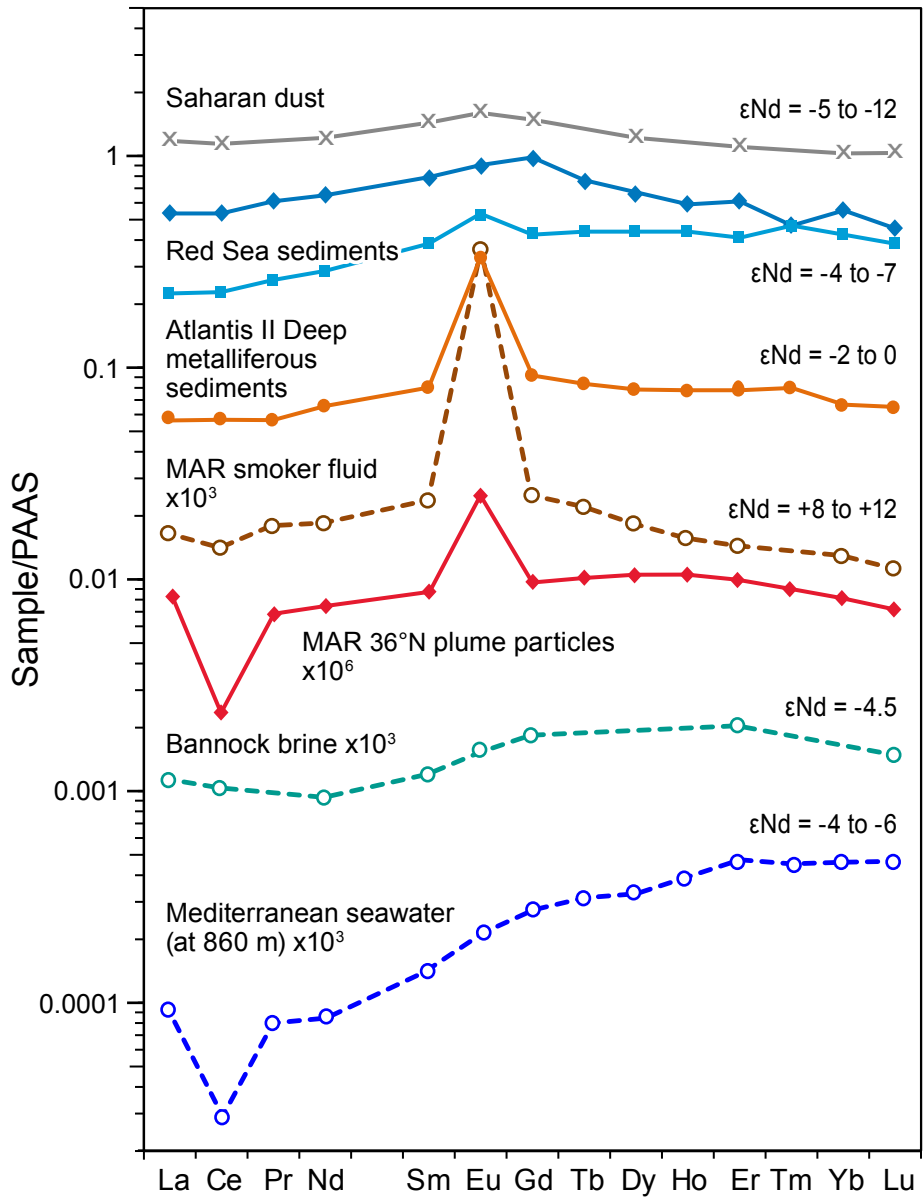
(b) Eastern Pacific Ridges



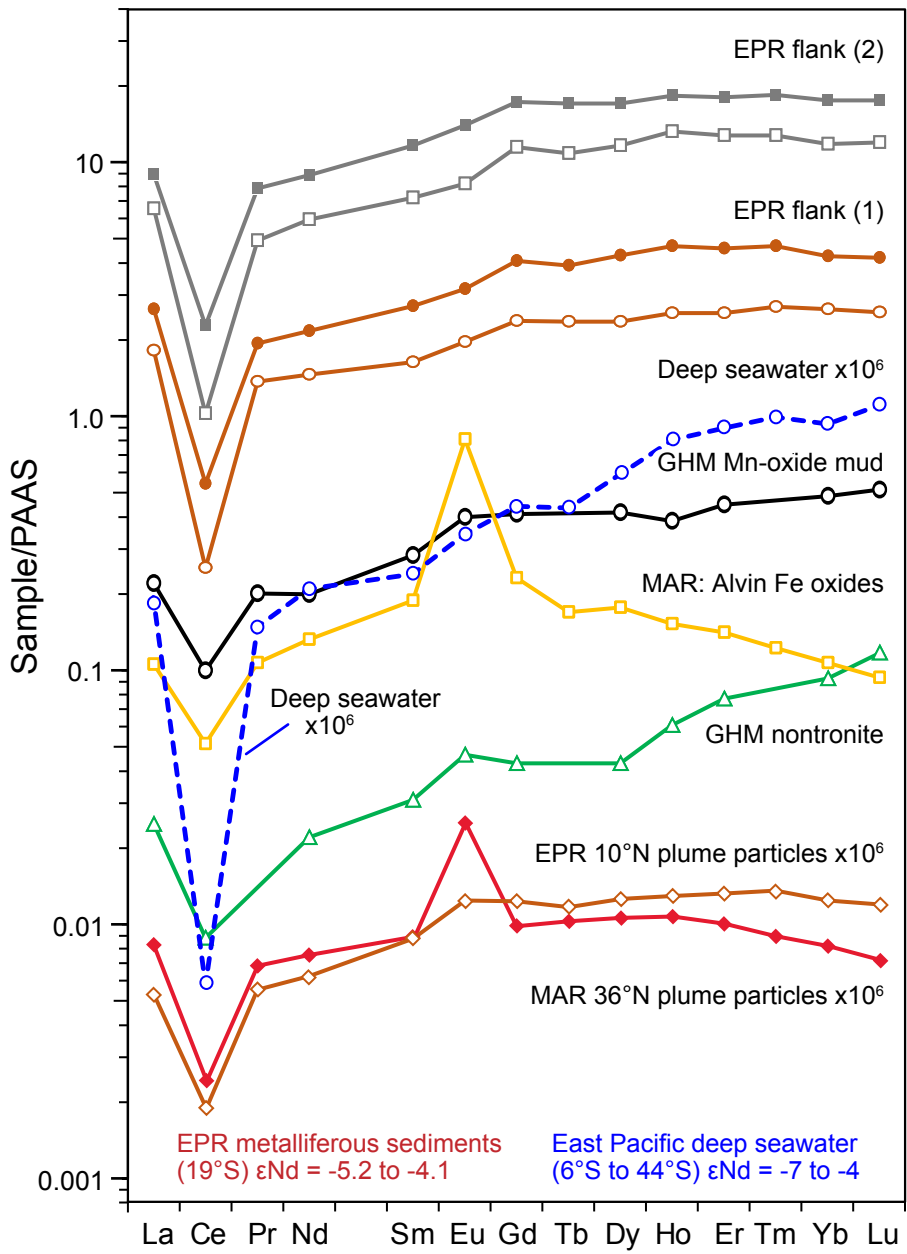
(c) Mid-Atlantic Ridge



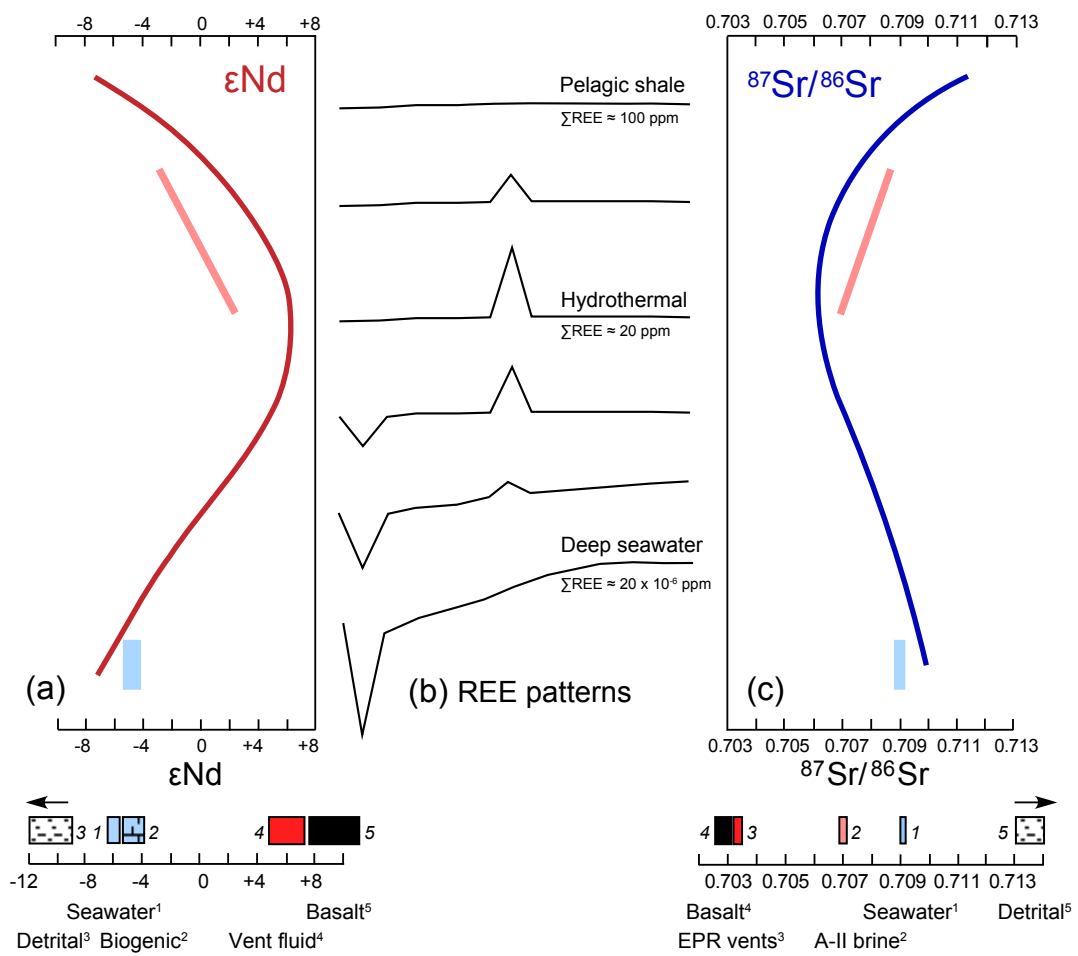
Barrett et al. Fig. 27



Barrett et al. Fig. 28



Barrett et al. Fig. 29



Barrett et al. Fig. 30

Barrett et al 2021 EarthSciRev TABLE 1 Aug 23 2021

**Table 1.** Locations of samples from the Atlantis II Deep, the East Pacific Rise transect, the Galapagos hydrothermal mounds, and the Southern Explorer Ridge

Cruise	Core no.	Latitude (°N)	Longitude (°E)	Depth (m)
Atlantis II Deep, central Red Sea (R/V Valdivia cruises)				
VA-1	48	21.3462	38.0842	2179
VA-1	54	21.3437	38.0838	2180
VA-1	64	21.3245	38.0938	2165
VA-1	71	21.3278	38.0922	2162
VA-1	98	21.3287	38.0912	2158
VA-29*	274	21.353	38.082	≈2150
VA-3	345	21.3667	38.0552	2133
VA-3	361	21.3470	38.0812	2170
VA-3	367	21.3607	38.0765	2164
VA-3	369	21.3623	38.0658	2154
VA-3	397	21.3455	38.0962	2078
VA-3	409	21.3390	38.0858	2164
VA-3	416	21.3430	38.0907	2155
VA-3	419	21.3388	38.0848	2162
VA-3	436	21.3813	38.0607	2086
VA-3	443	21.3447	38.0945	2102
East Pacific Rise transect (west of spreading axis, at ca. 19°S)				
DSDP Leg 92	597	-18.8063	-129.7705	4157
DSDP Leg 92	597A	-18.8072	-129.7703	4163
DSDP Leg 92	598	-19.0047	-124.6768	3703
DSDP Leg 92	599, 599B	-19.4515	-119.8813	3644
DSDP Leg 92	600C	-18.9283	-116.8408	3406
DSDP Leg 92	601B	-18.9203	-166.8685	3448
Galapagos Spreading Ridge: hydrothermal mounds on southern flank of ridge				
DSDP Leg 70	506	0.6098	-86.0915	2714
DSDP Leg 70	509B	0.5888	-86.1322	2702
Southern Explorer Ridge: surface samples from axis of ridge				
CASM IV (1)	P1504-3	49.761	-130.259	≈1800
CASM IV (2)	P1504-6	49.761	-130.259	≈1800
CASM IV (3)	P1505-2	49.761	-130.259	≈1800
CASM IV (4)	P1505-7	49.761	-130.259	≈1800
CASM V (5)	CV-9	49.74	-130.27	≈1850
CASM V (6)	D10-10	49.74	-130.27	≈1850

\*Location estimated from Bäcker and Richter (1973). CASM samples: (1) sulphides > silica; ≈200 m north of Magic Mountain; (2) sulphides + silica, ≈200 m north of Magic Mountain; (3) sulphides > silica, ≈300 m west of Magic Mountain; (4) sulphides > silica ≈ sulphate, west side of Magic Mountain; (5) silica > sulphate ≈ sulphides, ≈2 km SSW of Magic Mountain; (6) sulphides > silica, ≈2 km SSW of Magic Mountain. The location of the Magic Mountain sulphide deposit is estimated as 49.76°N, 130.26°W based on figure 2 in Deschamps et al. (2013). CASM IV, V = Canadian American Seamount expeditions IV and V. Sample numbers given in second column; prefixes identify the dive/dredge number.

**Table 2.** Rare-earth element composition of metalliferous sediments from Atlantis II Deep (Red Sea) and hemipelagic sediments from Orca Basin (Gulf of Mexico)

Sample number	Depth (cm)	Sediment unit: facies	Element (ppm)															
			La	Ce	Pr	Nd	Sm	Eu	Gd	Tb	Dy	Ho	Er	Tm	Yb	Lu	ΣREE	Y
Red Sea Atlantis II Deep																		
48-1	111–114	AM: silicate-sulphide	1.97	3.78	0.396	1.68	0.353	0.157	0.329	0.0509	0.289	0.0593	0.166	0.0244	0.146	0.0226	9.42	1.72
48-2	484–487	CO: hematite-silicate	4.81	7.35	0.699	2.96	0.565	0.300	0.550	0.0847	0.465	0.0951	0.280	0.0410	0.236	0.0343	18.5	2.60
54-2	394–398	CO: silicate-hematite	2.76	6.02	0.615	2.54	0.518	0.332	0.477	0.0757	0.457	0.0915	0.256	0.0368	0.231	0.0341	14.4	2.41
54-3	444–448	CO: anhydrite layer	0.112	0.199	0.0181	0.0696	0.0117	0.0112	0.0120	0.0019	0.0093	0.0018	0.0043	0.0006	0.0042	0.0006	0.456	0.03
64-1	148–152	AM: silicate-sulphide	1.55	3.81	0.406	1.84	0.358	0.174	0.354	0.0540	0.306	0.0680	0.197	0.0285	0.160	0.0264	9.32	1.65
64-2	511–514	AM/SU2: anhydrite layer	0.410	0.643	0.0634	0.228	0.0558	0.0223	0.0480	0.0074	0.0418	0.0082	0.0244	0.0029	0.0177	0.0038	1.62	0.33
64-3	567–569	SOAN: silicate-sulphide-anhydrite	3.77	8.58	0.908	3.74	0.775	0.364	0.739	0.116	0.657	0.132	0.366	0.0539	0.335	0.0502	20.6	3.42
71-1	190–194	AM: silicate-sulphide	2.27	5.42	0.562	2.29	0.471	0.252	0.469	0.0770	0.450	0.0920	0.263	0.0378	0.246	0.0378	12.9	2.02
71-3	967–970	CO: hematite-argillaceous	1.85	3.84	0.381	1.64	0.320	0.179	0.321	0.0484	0.271	0.0577	0.168	0.0226	0.135	0.0196	9.25	1.66
98-1	113–116	AM: silicate-sulphide	1.89	4.32	0.433	1.82	0.376	0.218	0.360	0.0595	0.324	0.0677	0.193	0.0287	0.170	0.0262	10.3	1.86
274-1#	ca. 100	SU2: silicate-sulphide	20.9	42.6	5.18	22.2	4.67	1.50	4.43	0.693	3.95	0.813	2.30	0.332	2.03	0.318	112	18.5
274-4#	ca. 390	CO: limonite-silicate	1.93	4.42	0.527	2.19	0.473	0.182	0.468	0.0650	0.378	0.0823	0.235	0.0333	0.216	0.0368	11.2	2.61
274-8#	ca. 730	CO: silicate-limonite	1.48	2.86	0.291	1.28	0.243	0.283	0.226	0.0328	0.197	0.0402	0.117	0.0170	0.0890	0.0127	7.18	1.05
274-12#	ca. 950	SU1: silicate-sulphide	4.42	9.57	0.986	3.87	0.774	0.737	0.715	0.110	0.617	0.122	0.342	0.0508	0.323	0.0487	22.7	2.91
274-13#	ca. 1000	SU1: silicate-sulphide	2.38	3.93	0.354	1.26	0.242	0.314	0.254	0.0403	0.248	0.0506	0.147	0.0212	0.127	0.0189	9.38	1.39
345-1	182–186	AM: silicate	2.81	4.75	0.486	1.93	0.374	0.197	0.360	0.0574	0.331	0.0694	0.194	0.0282	0.176	0.0279	11.8	1.79
345-3	451–453	CO: limonite	1.76	2.81	0.270	1.10	0.196	0.101	0.219	0.0302	0.190	0.0436	0.130	0.0173	0.108	0.0171	6.99	1.30
345-4	507–510	CO: silicate-hematite	2.24	4.08	0.375	1.49	0.291	0.425	0.286	0.0461	0.252	0.0516	0.151	0.0226	0.131	0.0190	9.85	1.37
345-5	570–574	CO: silicate-hematite-Mn	1.80	4.26	0.396	1.51	0.296	0.230	0.286	0.0413	0.233	0.0482	0.137	0.0194	0.113	0.0178	9.39	1.32
361-1	169–163	AM: silicate	2.80	5.97	0.654	2.90	0.613	0.274	0.580	0.0907	0.513	0.105	0.308	0.0471	0.264	0.0411	15.2	2.72
367-1	24–26	AM: silicate-sulphide	3.47	7.54	0.829	3.55	0.765	0.322	0.713	0.110	0.654	0.130	0.381	0.0571	0.335	0.0509	18.9	3.47
367-3	187–190	AM: silicate-limonite-hematite	3.81	8.78	0.911	3.59	0.670	0.490	0.626	0.0859	0.492	0.100	0.277	0.0384	0.230	0.0353	20.1	2.54
367-4	459–463	SU2: sulphide ooze	2.33	4.89	0.612	2.65	0.533	0.283	0.553	0.0759	0.450	0.101	0.297	0.0406	0.258	0.0434	13.1	2.78
369-1	134–137	AM: silicate	1.51	3.53	0.356	1.60	0.333	0.150	0.312	0.0492	0.297	0.0561	0.170	0.0241	0.146	0.0230	8.55	1.49
369-3	476–485	AM: anhydrite layer	0.488	0.473	0.0334	0.105	0.0270	0.078	0.038	0.0063	0.044	0.0107	0.0378	0.0067	0.0486	0.0089	1.41	0.26
397-2	244–247	AM: silicate	1.75	4.02	0.408	1.80	0.370	0.159	0.357	0.0565	0.326	0.0651	0.188	0.0283	0.167	0.0262	9.73	1.64
397-4	583–585	SU2: silicate-limonite-Mn (within SU2)	7.86	18.8	2.01	8.28	1.76	0.631	1.62	0.260	1.47	0.297	0.830	0.124	0.804	0.120	44.8	6.97
409-1	146–149	AM: silicate-sulphide	2.31	5.30	0.590	2.37	0.518	0.234	0.500	0.0822	0.497	0.102	0.276	0.0405	0.257	0.0414	13.1	2.15
409-3	572–576	CO: silicate-hematite	2.16	4.83	0.499	2.07	0.399	0.260	0.416	0.0621	0.343	0.0780	0.232	0.0319	0.196	0.0321	11.6	2.00
416-1	112–116	AM: silicate	2.97	6.46	0.705	3.15	0.643	0.270	0.607	0.0972	0.518	0.108	0.309	0.0467	0.256	0.0407	16.2	2.73
416-3	553–556	SU2: sulphide-anhydrite	4.92	9.42	0.971	4.32	0.874	0.496	0.863	0.1324	0.730	0.155	0.465	0.0704	0.399	0.0580	23.9	3.91
436-1	216–219	AM: silicate	3.28	7.82	0.908	3.80	0.776	0.325	0.800	0.114	0.661	0.151	0.433	0.0553	0.341	0.0585	19.5	3.66
436-4	760–765	CO: limonite-anhydrite	0.139	0.0749	0.0061	0.0246	0.0058	0.0017	0.0044	0.0006	0.0027	<0.001	<0.002	<0.0004	<0.002	<0.0005	0.260	<0.02
436-6	962–966	CO: hematite-limonite	1.81	3.88	0.439	1.81	0.387	0.119	0.355	0.0579	0.335	0.0695	0.201	0.0296	0.185	0.0285	9.70	1.76
436-7	973–975	CO: limonite-hematite	4.40	9.35	0.943	3.79	0.798	0.259	0.766	0.119	0.684	0.136	0.378	0.0560	0.364	0.0549	22.1	3.80
436-8	994–997	CO?: silicate-sulphide	1.10	2.12	0.212	0.806	0.151	0.0434	0.126	0.0201	0.108	0.0228	0.0697	0.0094	0.0521	0.0073	4.84	0.81
443-1	135–138	AM: silicate	1.50	3.45	0.366	1.50	0.310	0.153	0.299	0.0472	0.278	0.0560	0.162	0.0225	0.146	0.0228	8.31	1.46
443-2	261–264	AM: silicate-limonite	2.24	4.64	0.515	2.25	0.459	0.370	0.437	0.0671	0.378	0.0790	0.224	0.0334	0.194	0.0289	11.9	1.80
443-3	472–475	SU2: sulphide-silicate	3.01	5.21	0.510	1.99	0.385	0.384	0.418	0.0576	0.337	0.0718	0.205	0.0287	0.168	0.0267	12.8	2.22

**Table 1.** Rare-earth element analyses for metalliferous sediments from the Atlantis II Deep (Red Sea) and Orca Basin (Gulf of Mexico) (continued)

Sample number	Depth (cm)	Sediment unit: facies	Element (ppm)															
			La	Ce	Pr	Nd	Sm	Eu	Gd	Tb	Dy	Ho	Er	Tm	Yb	Lu	∑REE	Y
Gulf of Mexico Orca Basin																		
87-G-2	4–5 cm	Silty mud, lam. black/grey/red	11.6	23.2	2.59	10.4	1.78	0.396	1.62	0.233	1.33	0.260	0.731	0.111	0.710	0.108	55.1	nd
87-G-2	5–6 cm	Silty mud, lam. black/grey/red	14.5	30.5	3.40	13.7	2.38	0.515	2.12	0.306	1.72	0.349	1.00	0.147	0.941	0.141	71.7	nd
87-G-2	6–7 cm	Silty mud, lam. black/grey/red	11.1	22.6	2.53	10.2	1.78	0.394	1.59	0.228	1.28	0.257	0.724	0.108	0.693	0.108	53.6	nd
Reference material																		
SCo-1	This study	USGS Cody Shale	30.34	59.4	6.57	25.72	4.91	1.17	4.52	0.694	3.98	0.846	2.45	0.356	2.32	0.370	144	21.8
SCo-1	Ref 1	USGS Cody Shale	29.60	60.0	6.22	24.70	4.71	1.16	3.97	nd	3.27	0.660	1.90	nd	1.88	0.290	nd	20.3
SCo-1	Ref 2	USGS Cody Shale	29.50	62.0	6.60	26.00	5.30	1.19	4.60	0.700	4.20	0.970	2.50	0.420	2.27	0.340	nd	26.0

Depth = cm below seafloor. # Location of core 274 estimated from map provided by E. Oudin (pers. comm., 1988). Ref 1 = Jarvis and Jarvis (1985); Ref 2 = Govindarju (1989); nd = not determined; SCo-1 and other determinations include fusion of insoluble residues with lithium metaborate. Gulf of Mexico: lam. = laminated.

**Table 3.** Nd isotope composition and related data for metalliferous sediments from the Atlantis II Deep, Red Sea

Cruise	Sample number	Depth (cm)	Latitude (°N)	Longitude (°E)	Sediment unit: facies	$^{143}\text{Nd}/^{144}\text{Nd}$	$\epsilon\text{Nd}$	Basaltic Nd (%)	$\text{Eu}_\text{N}/\text{Eu}_\text{N}^*$	$\text{Fe}_2\text{O}_3\text{t}$ (wt%)	$\text{Al}_2\text{O}_3$ (wt%)	$\Sigma\text{REE}$ (ppm)
		(1)				(2)	(3)	(4)	(5)			
VA-1	48-2	484–487	21.3461	38.0842	CO: hematite-silicate	0.512570 ± 5	-1.48	25.4	2.54	51.2	1.3	18.5
VA-1	54-2	394–398	21.3436	38.0839	CO: hematite-silicate SOAN: silicate-sulphide-	0.512546 ± 5	-1.95	22.3	3.14	50.5	1.6	14.4
VA-1	64-3 §	567–569	21.3244	38.0939	anhydrite	0.512652 ± 5	+0.12	36.1	2.26	30.4	2.0	20.6
VA-1	71-3	967–970	21.3278	38.0922	DOP: hematite-argillaceous	0.512543 ± 9	-2.01	21.9	2.62	65.9	1.1	9.2
VA-3	274-1 #	ca. 100	21.3533	38.0817	SU2: silicate-sulphide	0.512519 ± 5	-2.48	18.8	1.55	nd	6.9 (6)	112
VA-3	274-4 #	ca. 390	21.3533	38.0817	CO: limonite	0.512531 ± 11	-2.24	20.4	1.82	nd	1.2	11.2
VA-3	274-12 #	ca. 950	21.3533	38.0817	SU1: silicate-sulphide	0.512556 ± 10	-1.76	23.6	4.67	nd	nd	22.7
VA-3	345-4	507–510	21.3667	38.0552	CO: silicate-hematite	0.512535 ± 6	-2.17	20.9	6.95	nd	nd	9.9
VA-3	345-5	570–574	21.3667	38.0552	CO: silicate-hematite	0.512556 ± 8	-1.76	23.6	3.73	43.8	0.4	9.4
VA-3	367-3 *	187–190	21.3607	38.0765	AM: silicate-limonite-anhydrite	0.512611 ± 8	-0.68	30.8	3.56	38.0	1.1	20.1
VA-3	397-2	244–247	21.3455	38.0962	AM: silicate	0.512559 ± 5	-1.70	24.0	2.06	48.4	1.0	9.7
VA-3	409-3	572–576	21.3390	38.0858	CO: silicate-hematite	0.512558 ± 6	-1.72	23.9	3.01	56.1	1.2	11.6
VA-3	436-6	962–966	21.3830	38.0607	CO: limonite-hematite	0.512506 ± 11	-2.73	17.1	1.51	67.8	1.1	9.7
VA-3	443-2	261–264	21.3447	38.0945	AM: silicate-limonite	0.512561 ± 11	-1.66	24.3	3.89	nd	nd	11.9

(1) Depth = cm below seafloor. (2) Error is ± 2 standard errors on the 6<sup>th</sup> decimal place. (3) Relative to CHUR value of 0.512646. (4) Calculated from estimated basaltic and seawater end-members of  $\epsilon\text{Nd} = 9.7$  and  $\epsilon\text{Nd} = -5.3$ , respectively. (5) Eu anomaly =  $\text{Eu}_\text{N}/\text{Eu}_\text{N}^*$ , where  $\text{Eu}_\text{N}^* = (\text{Sm}_\text{N}^*/\text{Gd}_\text{N})^{0.5}$  and N is the shale-normalized value (PAAS from Taylor and McLennan, 1985). # Location of core 274 estimated from map provided by E. Oudin (pers. comm., 1988). (6)  $\text{Al}_2\text{O}_3$  estimated as 6.9 % based on  $\text{Al}_2\text{O}_3$ -Zr-Th trends for entire data set (Supplementary Data Table 1). § Anhydrite-bearing sample. \* Talc-bearing sample. nd = not determined.

**Table 4.** Rare-earth element composition of metalliferous sediments from East Pacific Rise transect, DSDP Leg 92

Sample number	Depth (cm)	Depth below seafloor (m)	Element (ppm)															
			La	Ce	Pr	Nd	Sm	Eu	Gd	Tb	Dy	Ho	Er	Tm	Yb	Lu	ΣREE	Y
597-6-1	75-77	43.76	79	26	13	55	10	1.4	13	2.0	12	2.8	7.8	1.2	7.1	1.0	231	86
597-6-3	74-76	46.75	85	21	15	62	12	3.5	15	2.4	16	3.6	9.9	1.4	8.9	1.3	257	110
597-6-4	74-76	48.25	56	18	12	45	9.4	2.4	10	1.8	11	2.4	6.6	1.0	6.1	0.9	183	62
598-1-1	71-73	0.72	340	180	69	300	64	15	80	13	79	18	51	7.5	49	7.5	1273	640
598-1-2	71-73	2.22	320	110	63	270	54	15	69	11	74	17	47	7.0	44	6.7	1108	600
598-1-4	71-75	5.23	250	81	43	200	40	8.8	53	8.3	54	13	36	5.2	33	5.1	830	480
598-3-1	67-69	16.48	100	43	17	73	15	3.4	19	3.0	20	4.6	13	1.9	12	1.8	327	140
598-3-4	70-74	21.02	90	31	14	61	12	2.8	16	2.5	17	4.1	11	1.7	10	1.6	275	120
598-4-1	15-17	25.56	93	30	14	61	11	2.6	14	2.2	15	3.3	9.3	1.4	9.3	1.4	268	51
598-4-3	25-27	28.66	99	28	17	77	14	3.6	19	2.9	18	4.1	11	1.7	10	1.6	307	120
598-5-2	72-74	37.23	67	20	12	49	9.0	2.1	11	1.8	11	2.5	7.2	1.1	7.4	1.1	202	68
598-5-4	80-82	40.31	76	20	12	55	10	2.3	13	2.0	13	3.0	8.5	1.3	8.4	1.3	226	87
599-2-2	70-74	10.12	50	12	7.4	34	6.4	1.5	9.3	1.4	10	2.6	7.7	1.2	7.5	1.2	152	86
599-2-3	70-74	11.62	63	15	9.5	43	8.0	1.8	12	1.9	13	3.2	9.5	1.5	9.1	1.5	192	110
599-2-5	70-73	14.62	68	16	9.6	42	8.0	1.9	12	1.9	13	3.2	10	1.6	9.6	1.5	198	110
599-3-1	70-74	18.22	66	16	9.6	45	8.3	1.7	13	1.9	13	3.3	10	1.5	9.5	1.4	200	110
599-3-2	70-74	19.72	51	12	7.9	35	6.5	1.8	9.7	1.6	11	2.7	7.8	1.3	7.7	1.2	157	86
599-3-5	70-74	24.22	56	12	7.5	34	6.2	1.3	8.8	1.4	9.8	2.5	7.5	1.2	7.7	1.2	157	81
599-4-1	71-73	27.82	38	8.0	5.6	26	4.7	1.2	7.1	1.1	7.5	1.9	5.7	0.9	5.5	0.8	114	67
599-4-3	71-73	30.82	80	20	11	52	9.5	2.2	14	2.1	14	3.8	11	1.8	11	1.7	234	130
599-4-4	72-74	32.33	47	11	7.0	31	5.9	1.2	8.2	1.3	9.2	2.3	6.8	1.1	6.9	1.1	140	71
599-4-5	72-74	33.82	42	10	6.2	27	5.3	1.1	7.0	1.2	8.1	2.1	6.1	1.0	6.1	1.0	124	61
599B-2-3	70-74	36.02	29	8.7	4.2	20	3.7	0.77	5.3	0.8	5.7	1.5	4.2	0.7	3.8	0.6	89	53
599B-2-4	70-73	37.52	59	14	8.7	38	7.1	1.5	9.5	1.5	10	2.6	7.7	1.2	7.8	1.2	170	84
599B-2-5	74-77	39.06	52	13	7.5	34	6.7	1.9	9.3	1.5	10	2.6	7.6	1.2	7.7	1.2	156	81
599B-2-6	71-74	40.53	51	13	7.2	34	6.8	2.0	9.8	1.6	11	2.9	8.5	1.4	8.3	1.3	159	97
600C-1-4	99-104	5.52	70	19	12	52	10	<0.02	14	2.3	15	3.8	11	1.6	9.9	1.6	222	120
600C-1-6	99-104	8.52	48	10	7.0	33	6.4	1.8	9.7	1.5	10	2.6	7.8	1.2	7.7	1.2	148	94
600C-2-2#	91-96	11.84	6.9	3.9	1.2	6.2	1.3	0.42	2.1	0.4	2.4	0.6	2.0	0.3	2.0	0.3	30	20
601B-1-2	76-81	16.69	65	14	9.3	43	8.2	2.1	12	2.0	13	3.3	9.8	1.6	9.6	1.6	195	110

Note: All data are reported on a carbonate-free basis. Sample number indicates DSDP hole-core-section; depth is sampled interval (cm) in core section. # Contains basaltic material.

**Table 5.** Summary of REE and Nd-Pb-Sr isotopic features of metalliferous

<b>Basin type</b>	<b>Tectonic setting</b>	<b>Type Example</b>
Closed Basin	Spreading axis	Atlantis II Deep
Closed Basin	Continental slope	Orca Basin
Open Ocean	Spreading axis	East Pacific Rise
Open Ocean	Spreading axis	Mid-Atlantic Ridge
Open Ocean	Spreading axis flank	Galapagos mounds

; sediment types discussed in present paper

### **Local Setting of Metalliferous Sediments**

### **REE patterns**

(PAAS-normalized)

Sediments precipitated in sub-oxic to anoxic brine layers (T = 43–68°C) as Fe-oxyhydroxides, Fe-silicates, Mn oxides, metal sulfides, carbonates, sulfates and amorphous compounds.

Mainly flat; moderate to strong positive Eu anomalies; no Ce anomaly, no Y anomaly.

Sediments accumulate in brine pools (T= 5°C) are mainly detrital muds, with some authigenic Fe-Mn and biogenic input.

Mainly flat; no Eu or Ce anomaly.

Fe-Mn oxyhydroxides precipitate from plumes rising above high-T vents and absorb metals, REEs and other cations from both the plume and seawater during lateral dispersion up to a few thousand km from axis.

Patterns slightly LREE-depleted; strong negative Ce anomaly, no Eu anomaly; usually a small positive Y anomaly.

Oxidation of pre-existing sulfide mounds forms Fe-oxyhydroxide-rich sediments that remain in situ or are dispersed by bottom currents up to a few km from mounds. Locally, direct precipitation of Fe-Si-oxyhydroxides and nontronite occurs at low-T vents.

Patterns flat to slightly convex upwards, with moderate to large positive Eu anomaly; often with a small negative Ce anomaly.

Fe-silicate (nontronite)-rich precipitates form as upwelling fluids react with a cover of biogenic sediments at T= 20–50°C. Mn oxides precipitated at surface.

Patterns commonly similar to normal seawater but with a less negative Ce anomaly; some additionally have a small positive Eu anomaly.

## Nd isotopes

$\epsilon$ Nd mostly -2.7 to +0.2, suggesting 20–30 % basaltic-hydrothermal Nd; rare sediments with fish teeth have  $\epsilon$ Nd up to +4 and high  $\Sigma$ REE.

No data

$\epsilon$ Nd ranges from -5.2 to -4.1 (DSDP Leg 92 sediments), close to ambient East Pacific seawater values.

$\epsilon$ Nd ranges from -12.6 to -2.5, Lowest values are close to ambient North Atlantic seawater and pelagic sediments; higher values due to a component of sulfide detritus.

No data

## Pb isotopes

Isotope ratios range from near-pelagic-detrital-seawater values to values suggesting up to 30 % basaltic-hydrothermal Pb in sediments.

No data

Isotope ratios range from near-pelagic-detrital-seawater values to basaltic values (proportion of basaltic component depends partly on distance from paleo-ridge).

Isotope ratios range from basaltic-hydrothermal (TAG sediments) to values close to seawater and pelagic sediments (low-T Lilliput deposits).

Isotope ratios range from near-basaltic to near-seawater values.

## **Sr isotopes**

Isotope ratios mostly 0.7072 to 0.7080, suggesting 15–30 % basaltic-hydrothermal Sr, with majority of Sr derived from rift-flank Miocene evaporites (=seawater).

No data

Isotope ratios very close to seawater value of 0.7091.

Isotope ratios close to seawater value of 0.7091, but locally down to 0.7082 (due to a small basaltic-hydrothermal component in sediment).

Isotope ratios very close to seawater value of 0.7091.

**Table 6.** Compilation of Nd, Pb and Sr isotopic and concentration data for oceanic metalliferous sediments, deep seawater, Atlantis II Deep brine, MOR hydrothermal vent fluids and MOR basalt

	Axial MORB (Global and Red Sea)	High-T vent fluids (Global)	Seawater (Global and Red Sea)	Deep-sea detritus (Red Sea)	Seafloor brine pool (Atlantis II Deep)	Metalliferous sediments (Atlantis II Deep)	Metalliferous sediments (Eastern Pacific Ocean)
<b>Nd content</b>	50.6 $\mu\text{mol/kg}$ (1)	1–10 nmol/kg (9) 1–2 nmol/kg (10)	0.010–0.040 nmol/kg (16a,16b)	ca. 83 $\mu\text{mol/kg}$ (27)	No data	mostly 7–83 $\mu\text{mol/kg}$ (41,36)	290–500 $\mu\text{mol/kg}$ (44)
<b>eNd</b>	+8.0 to +9.8 (2) +6.9 to +8.2 (3) +7.5 to +12.0 (4a)	ca. +9.0 (4b) +5.9 to +7.9 (4c) +7.8 to +9.0 (10)	-9 to -2 (16a) -14 to -8 (16b) -5.0 $\pm$ 0.3 (17); -7.0 $\pm$ 0.4 (18) -4.9 $\pm$ 0.2 (42b)	-5.2 to -4.6 (28) -4.7 to -6.3 (29)	No data [Shaban Deep brine: -4.5 (32)]	-2.7 to +0.1 (present study) -1.8 to -0.3 (42a)	-5.2 to -4.1 (45) -1.0 to -1.6 (46) -0.2 to -4.2 (47) -2.8 to -3.6 (48)
<b>Sr content</b>	1.3–1.9 mmol/kg (5) 1.0 mmol/kg (1)	63–135 $\mu\text{mol/kg}$ (11) 80–312 $\mu\text{mol/kg}$ (12) 45–130 $\mu\text{mol/kg}$ (13)	122 $\mu\text{mol/kg}$ (19) 88–90 $\mu\text{mol/kg}$ (20,21)		400 $\mu\text{mol/kg}$ (33) 514 $\mu\text{mol/kg}$ (34)	228–8440 $\mu\text{mol/kg}$ (34)	4400–4900 $\mu\text{mol/kg}$ (44)
<b><sup>87</sup>Sr/<sup>86</sup>Sr</b>	0.7027–0.7031 (2,3)	0.7028–0.7046 (14)	0.70917 (19) 0.7088–0.7090 (22)	0.7075–0.7085 (30)	0.7071–0.7072 (34) 0.7071 (35)	0.7072–0.7077 (34) 0.7073–0.7079 (42a,36)	0.7090–0.7092 (46) 0.7089–0.7091 (44)
<b>Pb content</b>	483 nmol/kg (6) 1450 nmol/kg (1)	60–275 nmol/kg (11) 14–900 nmol/kg (12) 21–265 nmol/kg (13)	0.013 nmol/kg (13) 0.01–0.03 nmol/kg (23)	15–30 $\mu\text{mol/kg}$ (31)	0.48–3.48 $\mu\text{mol/kg}$ (37a) 0.1–1.1 $\mu\text{mol/kg}$ (37b) 0.68 $\mu\text{mol/kg}$ (38); 0.05 $\mu\text{mol/kg}$ (39)	mostly 10–160 $\mu\text{mol/kg}$ (43) mostly 100–11,000 $\mu\text{mol/kg}$ (41)	870–1210 $\mu\text{mol/kg}$ (44)
<b><sup>207</sup>Pb/<sup>204</sup>Pb</b>	15.44–15.54 (6,7,8)	15.48 (15a); 15.47–15.51 (15b)	15.7 (24); 15.63 (25); 15.55–15.63 (26)	15.58–15.59 (31)	ca. 15.69 (40); 15.56 (38)	15.53–15.58 (43,36)	15.48–15.58 (44)
<b><sup>206</sup>Pb/<sup>200</sup>Pb</b>	18.11–18.67 (6,7,8)	18.30 (15a); 18.44–18.50 (15b)	18.8 (24); 18.91 (25); 18.79–18.82 (26)	18.83–18.99 (31)	ca. 18.72 (40); 18.62 (38)	18.70–18.77 (43,36)	18.41–18.66 (44)

Axial Mid-Ocean Ridge Basalts

- (1) Average MORB (Sun and McDonough, 1989)  
(2) Red Sea spreading axis: 8 basalts from 6 locations, including 2 in Atlantis II Deep (Volker et al., 1993)  
(3) Red Sea: 4 basalts from spreading axis at 18°N (Eissen et al., 1989)  
(4a) East Pacific MORB (Hinkley and Tatsumoto, 1987; Hegner and Tatsumoto, 1987; White et al., 1987)  
(5) Red Sea: 21 basalts from spreading axis at 18°N (Eissen et al., 1989)  
(6) Atlantis II Deep: 2 basalt samples (Dupré et al., 1988)  
(7) Atlantis II Deep: 2 basalt samples (Volker et al., 1993)  
(8) Atlantis II Deep: 1 basalt sample from hole 226, DSDP Leg 23 (Delevaux and Doe, 1974)

Mid-Ocean Ridge high-T vent fluids

- (4b) Southern Juan de Fuca vents (Hinkley and Tatsumoto, 1987)  
(4c) EPR 21°N vents, 3 most radiogenic fluids (Piepgras and Wasserburg, 1985)  
(9) 27 samples from vents on Mid-Atlantic Ridge, East Pacific Rise, and Lau and Manus back-arc basins (Douville et al., 1999)  
(10) 4 high-T vents at 37°N on Mid-Atlantic Ridge: calculated end-member values (Chavagnac et al., 2018)  
(11) Juan de Fuca Ridge: 3 vents at 48°N with T = 347–368°C and salinities = 38–77 % of normal seawater (Seyfried et al., 2003)  
(12) Eastern Pacific Ocean: 4 vent fields with T = 224–355°C and salinities = 69–118 % of normal seawater (Von Damm, 1990)  
(13) Mid-Atlantic Ridge: 5 vent sites in basaltic settings (Douville et al., 2002)  
(14) Mid-ocean ridges in eastern Pacific Ocean and Atlantic Ocean: Albarède et al. (1981), Michaud et al. (1984), Edmond et al. (1990)  
(15a) Mid-Atlantic Ridge: vent fluids at 26°N (Godfrey et al., 1994)  
(15b) East Pacific Rise: vent fluids at 21°N (Chen et al., 1986)

Seawater

- (16a) Pacific Ocean deep seawater (>1500 m): Grasse et al. (2012), Jeandel et al. (2013); Molina-Kescher et al. (2014), Tachikawa et al. (2017)  
(16b) Atlantic Ocean deep seawater (>1500 m): van de Fliert et al. (2016), Tachikawa et al. (2017), Stichel et al. (2018)  
(17) Scrivner et al. (2004): East Mediterranean shallow water: 0–200 m  
(18) Tachikawa et al. (2004): East Mediterranean deep water: average of 11 samples from 857–2257 m  
(19) Blanc (1987): modern Red Sea seawater  
(20) Pilson (2013, chapter 4): normal seawater  
(21) de Villiers (1999): normal seawater, various oceans and depths  
(22) Zierenberg and Shanks (1986, 1988): Red Sea: Upper Miocene evaporites (proxy for paleo-seawater)  
(23) Bridgestock et al. (2018): Central Atlantic seawater  
(24) Inferred from average deep-sea Mn nodules in Pacific Ocean (Reynolds and Dasch, 1971)  
(25) Ambient seawater, southern Juan de Fuca ridge (Chen, 1987)  
(26) Dupré et al. (1988): Atlantis II Deep: two samples of carbonate sediment (seawater proxy) from core 684, 11.6 m and 13.7 m

Deep-sea detritus in Red Sea

- (27) Laurila et al. (2014b): Atlantis II Deep: aluminosilicate component of sediment (avg. Al-rich sediment minus avg. non-detrital component)  
(28) Cocherie et al. (1994): Shaban Deep: core KS-01, upper 5 m of biotrital sediment  
(29) Palchan et al. (2013): siliciclastic dust, northern Red Sea, deepwater core KL23: average of 20 samples (age = 5.5 to 20.5 ka)  
(30) Stein et al. (2007): Red Sea: loess dust in seafloor sediments over last 80 ka  
(31) Dupré et al. (1988): 2 samples of Recent detrital sediment, ca. 50 km N of Atlantis II Deep; 1 sample of Miocene shale, DSDP Leg 23, hole 227 (4 km E of Atlantis II Deep)

Brines and sediments in Red Sea closed basins

- (32) Cocherie et al. (1994): Shaban Deep in northern Red Sea: core KS-01, brine sample  
(33) Pierret et al. (2001): Atlantis II Deep, lower brine layer  
(34) Anschutz et al. (1995): Atlantis II Deep: core 684, upper 12 m of sediments: interstitial brine and metalliferous solids (measured separately)  
(35) Blanc et al. (1995): Atlantis II Deep, lower brine layer  
(36) Pierret et al. (2010): Atlantis II Deep: metalliferous sediment from core 1028: 5 samples at depths of 0.2 to 22.2 m  
(37) Brooks et al. (1969): brines of Atlantis II Deep (37a) and nearby Discovery Deep (37b)  
(38) Delevaux and Doe (1974): Atlantis II Deep: pore-water of metalliferous sediment at 4.5 m depth, hole 226, DSDP Leg 23  
(39) Atlantis II Deep, lower brine layer, 2 samples from Southwest and West basins (Anschutz et al., 2000)  
(40) Delevaux et al. (1967): Atlantis II Deep brine  
(41) Laurila et al. (2014a): Atlantis II Deep: metalliferous sediment samples from 9 cores, salt-free basis (excludes lowest DOP facies)  
(42a) Cocherie et al. (1994): Atlantis II Deep: Southwest Basin, core 268, upper 11 m: 5 samples for Nd isotopes and 13 samples for Sr isotopes  
(42b) Cocherie et al. (1994): Shaban Deep, northern Red Sea: core KS-01, upper 5 m: average of 5 samples of biotrital sediment (seawater proxy)  
(43) Dupré et al. (1988): Atlantis II Deep: cores 683 & 684: 11 samples of metalliferous sediment at depths of 1–16 m

Metalliferous sediments - Eastern Pacific Ocean

- (44) Barrett et al. (1986): Eastern Pacific: DSDP Leg 92 metalliferous sediments: holes 598–601, carbonate-free fraction  
(45) Halliday et al. (1992): Eastern Pacific: DSDP Leg 92, hole 598 (bulk sediments)  
(46) Sun et al. (2018): Juan de Fuca Ridge: Fe-Mn oxyhydroxides on ridge flank

Barrett et al 2021 EarthSciRev SUPPLEMENTARY DATA TABLE 1

Supplementary Data Table 1. Chemical analyses of metalliferous sediments from the Atlantis II Deep, Red Sea																																	
Sample no. <sup>(1)</sup>	Depth in core	Lab no.	SiO <sub>2</sub>	TiO <sub>2</sub>	Al <sub>2</sub> O <sub>3</sub>	Fe <sub>2</sub> O <sub>3</sub> (t)	MnO	MgO	CaO	K <sub>2</sub> O	LOI	Total <sup>(2)</sup>	CO <sub>2</sub> (t)	C	S (t)	Na	Cl	Ba	Cu	Zn	Pb	Au	Ag	As	Sb	Bi	Cd	In	Tl	Br	Rb	Cs	
	cm		wt%	wt%	wt%	wt%	wt%	wt%	wt%	wt%	wt%	wt%	wt%	wt%	wt%	ppm	ppm	ppm	ppm	ppm	ppm	ppm	ppm	ppm	ppm	ppm	ppm	ppm	ppm	ppm	ppm	ppm	ppm
			ICP-ES	ICP-ES	ICP-ES	ICP-ES	ICP-ES	ICP-ES	ICP-ES	ICP-ES	ICP-ES				LECO	INAA	calculated	INAA	ppm	ICP-ES	INAA	AA	ICP-MS	INAA	INAA	INAA	ICP-MS	ICP-MS	ICP-MS	ICP-MS	INAA	ICP-MS	ICP-MS
274-1	ca. 100	RS-1														11400	17579	570	470	5800	130	0.35	5.2	220	29	<0.5	12	0.11	3.3	24	52	4.4	
274-4	ca. 390	RS-2*	15.4	0.06	1.2	8.8	0.47	0.34	14.90	0.18	21.8	63.2				4150	6399	61000		48000		3.73	120	520	95	1.8	280	0.17	27	9	9.1	0.8	
274-8	ca. 730	RS-3	9.1	0.02	0.3	78.7	0.21	0.09	0.10	0.05	10.7	99.3				916	1412	1000		670		0.62	1.8	170	11	0.6	4.2	0.08	1.0	3.3	5.7	0.2	
274-12	ca. 950	RS-4														4370	6738	7900	14000	27000	860	3.27	78	190	60	0.7	120	0.35	23	4.8	11	0.7	
274-13	ca. 1000	RS-5														2090	3223	470	3800	1400	71	0.58	9.7	160	16	0.7	2.2	1.20	2.0	6.6	1.5	0.1	
274-15	ca. 1080	RS-6														8770	13523	790	4900	28000	490	1.57	46	170	33	<0.5	72	0.21	6.0	15	39	3.0	
48-1	111-114	RS-7	17.3	0.04	1.0	56.4	0.10	0.47	0.62	0.23	15.8	92.0	<0.1	0.4	3.2	10700	16499	360	7600	7200	890	2.24	52	440	30	<0.5	14	0.29	25	13	8.9	0.7	
48-2	484-487	RS-8	19.5	0.05	1.3	51.2	0.06	8.59	0.83	0.13	8.3	90.0	<0.1	0.4	3.0	21900	33769	<79	8700	510	250	2.78		350	14								
54-1	151-154	RS-9	22.5	0.07	1.4	38.3	0.13	0.93	1.38	0.41	18.5	83.6				19600	30223	360	9000	72000	850	2.83	75	340	43	<0.5	230	0.48	4.5	23	17	2.2	
54-2	394-398	RS-10	24.4	0.07	1.6	50.5	0.17	4.51	1.73	0.25	10.4	93.6	0.1	0.6	2.0	10400	16037	660	4300	11000	600	1.99	46	470	33	<0.5	24	0.13	5.8	7.1	12	1.2	
64-1	148-152	RS-11	16.3	0.04	1.5	44.1	0.10	1.08	0.78	0.18	23.5	87.6	<0.1	0.3	6.7	10200	15728	980	14000	65000	1100	3.94	110	310	45	0.6	260	0.20	46	9.5	7	0.6	
64-3	567-569	RS-12*	19.9	0.10	2.0	30.4	0.41	1.66	0.69	0.40	16.8	80.4	1.1	0.6	7.6	5920	9128	3500	14000	29000	770	3.29	89	170	38	<0.5	99	0.20	13	9.9	19	1.3	
71-1	190-194	RS-13	15.7	0.05	1.5	38.1	0.05	1.07	0.75	0.24	23.9	81.4	0.3	0.3	7.1	8670	13369	930	15000	110000	1200	5.03	130	400	54	0.6	400	0.15	40	10	7.9	0.7	
71-2	492-497	RS-14	18.0	0.08	2.0	51.9	0.04	5.26	1.24	0.07	12.0	90.6	<0.1	0.4	7.2	6600	10177	350	14000	24000	430	4.00	110	500	60	0.5	160	0.28	15	10	3.2	0.4	
71-3	967-970	RS-15	18.4	0.04	1.1	65.9	0.11	0.78	1.18	0.10	4.2	92.8				10600	16345	<85	9300	8200	230	2.36	48	130	14	0.6	47	0.06	7.0	9.2	4.6	0.3	
98-1	113-116	RS-16	17.3	0.04	1.1	37.0	0.18	0.62	1.41	0.46	19.5	77.6				37100	57207	590	8100	80000	790	2.97	89	320	44	<0.5	250	0.37	6.9	32	13	1.2	
98-2	224-227	RS-17	15.4	0.07	1.7	60.2	0.12	0.83	2.23	0.49	12.5	94.9				4330	6677	1100	9500	12000	440	2.36	82	290	38	0.7	63	0.08	5.0	6.1	46	1.1	
98-3	508-511	RS-18	17.6	0.05	1.9	31.9	0.15	0.88	2.44	0.38	23.3	78.6	0.4			7450	11488	<120	12000	150000	1300	4.40	140	300	69	0.5	480	0.13	17	7.3	22	0.9	
345-1	182-186	RS-19	18.7	0.04	0.8	53.3	0.97	0.66	1.27	0.56	15.8	92.1	1.9			20500	31610	<79	3700	7600	770	1.70	24	830	20	<0.5	23	0.26	5.1	24	18	1.2	
345-2	369-372	RS-20	28.7	0.07	2.5	25.9	0.25	2.37	0.89	0.38	28.3	89.4				15500	23901	490	14000	63000	1500	3.90	170	520	47	0.7	130	0.26	5.1	21	13	1.0	
345-3	451-453	RS-21	9.5	0.01	0.3	82.0	0.69	0.10	0.14	0.18	11.5	104.4				6370	9822	1500	880	3500	61	0.20	1.2	79	6.5	<0.5	3.1	<0.05	0.5	6.8	3.3	0.2	
345-4	507-510	RS-22														8910	13739	<100	1500	2600	160	0.29	0.8	370	7.3	<0.5	1.4	0.06	0.4	7.1	5.1	0.4	
345-5	570-574	RS-23	21.2	0.02	0.4	43.8	4.14	0.90	1.67	0.41	20.0	92.5	12.4	<0.2	0.2	22700	35003	7400	3200	1700	140	0.55	2.0	200	16	<0.5	0.7	0.52	0.6	16	12	2.0	
361-1	169-163	RS-24	25.7	0.09	1.8	43.5	0.09	1.34	1.69	0.44	13.8	88.5	<0.1	0.7	3.4	13900	21433	440	12000	40000	850	3.42	94	270	44	<0.5	110	0.13	11	21	17	1.7	
367-1	24-26	RS-25	26.9	0.11	2.0	25.7	0.19	2.64	3.96	0.38	20.5	82.4				19500	30069	<100	8400	76000	690	2.87	100	100	48	0.5	200	0.20	15	31	12	0.9	
367-2	117-121	RS-26	46.0	0.12	1.9	26.4	0.10	3.62	1.68	0.40	22.7	102.9				13800	21279	<100	12000	75000	640	3.77	150	63	92	0.6	250	0.18	13	19	11	0.8	
367-3	187-190	RS-27	31.2	0.06	1.1	38.0	0.04	9.21	0.99	0.72	13.3	94.6				49900	76945	620	4600	12000	130	1.49	13	200	13	<0.5	19	1.10	1.5	27	7.8	0.8	
367-4	459-463	RS-28														23200	35774	8100		120000		3.08	87	680	57	1.1	230	0.19	28	10	15	1.1	
369-1	134-137	RS-29	18.8	0.05	1.0	55.5	0.47	0.55	0.65	0.35	15.5	92.9	0.4	0.4	2.1	12900	19891	<64	3700	6400	680	1.33	51	360	18	<0.5	11	0.13	21	15	15	1.1	
369-2	413-414	RS-30	30.7	0.07	1.8	35.0	0.90	1.37	1.51	0.52	20.5	92.4				20200	31148	1500	5700	21000	1100	1.68	99	210	36	<0.5	4.5	0.06	33	16	22	2.0	
369-3	476-485	RS-31**	5.2	0.01	0.1	0.1	bd	bd	36.60	0.07	8.8	50.9				818	1261	6900	<100	170	8	0.04	0.5	4.7	0.4	<0.5	0.7	0.49	1.5	<0.5	0.3	0.0	
397-1	71-74	RS-32	22.7	0.09	1.9	36.0	0.11	1.13	1.35	0.67	18.5	82.5	<0.1	0.6	4.4	38300	59058	1000	14000	32000	740	3.15	270	280	41	<0.5	87	0.11	21	43	18	1.4	
397-2	244-247	RS-33	23.4	0.05	1.0	48.4	0.05	0.83	0.93	0.51	13.8	89.0				26000	40091	260	6800	14000	660	2.29	38	310	27	0.6	24	1.20	11	22	16	1.4	
397-3	550-553	RS-34	39.4	0.03	1.2	32.3	0.09	1.21	1.14	0.58	15.2	91.2				19900	30685	<76	8300	11000	750	2.19	38	230	42	<0.5	12	0.08	23	17	25	1.3	
397-4	583-585	RS-35	17.4	0.27	3.9	54.5	3.74	1.20	1.21	0.72	13.0	95.9				4180	6445	3200	1500	6100	180	0.24	3.5	750	16	<0.5	15	0.17	3.1	<0.5	29	2.4	
409-1	146-149	RS-36	24.5	0.07	1.5	36.3	0.06	1.12	1.24	0.32	21.3	86.4				21100	32536	510	7100	41000	830	2.14	40	240	31	0.6	110	0.24	20	19	10	0.8	
409-2	317-321	RS-37	17.4	0.04	1.2	46.2	0.05	0.66	0.65	0.25	23.7	90.2	0.2			9530	14695	<76															

Supplementary Data Table 1.																	
Sample no. <sup>(1)</sup>	Depth in core	Lab no.	Cr	Ni	Co	Sc	Sn	W	Mo	Ga	U	Hf	Ta	Th	Nb	Y	Zr
	cm		ppm	ppm	ppm	ppm	ppm	ppm	ppm	ppm	ppm	ppm	ppm	ppm	ppm	ppm	ppm
			INAA	ICP-ES	INAA	INAA	ICP-MS	INAA	INAA	ICP-MS							
274-1	ca. 100	RS-1	110	92	44	15	2.4	<1	67	16	7.2	2.30	1.3	4.80	13.0	25.0	93
274-4	ca. 390	RS-2*	31		350	2.0	0.7	29	240	28	5.4	0.29	0.4	0.53	1.6	2.5	13
274-8	ca. 730	RS-3	26		6	0.8	0.5	9	350	6.4	24	0.08	0.3	0.23	0.9	1.2	5.9
274-12	ca. 950	RS-4	35	120	210	2.8	0.8	21	220	35	7.2	0.34	0.2	0.61	2.2	3.3	13
274-13	ca. 1000	RS-5	10	29	22	0.9	4.5	6	400	7.6	23	0.07	<0.2	0.16	1.1	1.6	5.8
274-15	ca. 1080	RS-6	27	46	140	2.4	1.1	66	85	15	7.4	0.55	0.2	0.53	2.2	3.3	23
48-1	111-114	RS-7	22	40	220	1.2	3.8	13	360	14	12	0.31	<0.2	0.21	0.7	1.6	15
48-2	484-487	RS-8	27	59	130	1.5		19	160								
54-1	151-154	RS-9	20	63	110	1.7	17	20	150	21	8.4	0.29	<0.2	0.41	1.3	2.8	16
54-2	394-398	RS-10	27	53	250	2.1	<0.5	43	170	18	9.6	0.41	<0.2	0.48	1.5	3.0	21
64-1	148-152	RS-11	32	61	340	1.3	1.2	17	280	23	16	0.21	<0.2	0.25	0.8	1.8	11
64-3	567-569	RS-12*	29	56	280	2.5	1.5	23	70	18	5.6	0.56	<0.2	0.60	1.9	3.9	25
71-1	190-194	RS-13	33	66	250	1.7	0.6	<1	220	26	12	0.34	<0.2	0.38	1.2	2.2	16
71-2	492-497	RS-14	28	77	280	2.3	0.9	28	290	27	17	0.44	<0.2	0.54	1.7	3.2	22
71-3	967-970	RS-15	30	46	140	1.0	<0.5	15	220	16	14	0.13	0.2	0.23	0.9	1.8	7.3
98-1	113-116	RS-16	10	78	180	1.0	1.0	19	140	20	8.4	0.27	<0.2	0.25	0.8	1.9	13
98-2	224-227	RS-17	41	48	77	1.6	<0.5	20	230	20	20	0.23	0.2	0.42	1.3	2.5	12
98-3	508-511	RS-18	34	67	280	1.2	0.5	19	220	37	8.7	0.22	<0.2	0.27	1.0	1.8	13
345-1	182-186	RS-19	18	32	75	1.3	10	<1	400	11	8.7	0.24	<0.2	0.28	0.8	2.0	14
345-2	369-372	RS-20	28	74	280	2.0	1.6	28	170	36	4.4	0.39	0.2	0.40	1.3	2.5	19
345-3	451-453	RS-21	21	36	28	1.4	<0.5	<1	300	1.9	23	0.10	0.2	0.17	1.0	1.3	6.3
345-4	507-510	RS-22	10	15	16	1.4	<0.5	<1	320	6.7	20	0.08	<0.2	0.15	1.1	1.4	6.4
345-5	570-574	RS-23	13	<15	21	0.9	1.5	<1	140	8.6	6.1	0.16	<0.2	0.14	0.6	1.9	8.1
361-1	169-163	RS-24	27	35	220	2.0	0.5	19	140	21	11	0.40	<0.2	0.47	1.7	3.2	21
367-1	24-26	RS-25	23	35	390	2.7	0.7	19	100	25	7.7	0.59	<0.2	0.53	1.8	3.7	29
367-2	117-121	RS-26	29	35	210	2.1	0.8	53	82	28	8.4	0.48	0.4	0.51	1.7	5.3	23
367-3	187-190	RS-27	17	14	99	1.7	2.5	80	170	12	14	0.28	<0.2	0.42	1.2	3.1	16
367-4	459-463	RS-28	10		130	2.0	1.2	23	290	33	1.8	0.73	0.5	0.44	1.5	2.0	31
369-1	134-137	RS-29	20	19	210	1.3	1.0	11	240	13	11	0.25	<0.2	0.36	1.0	1.8	14
369-2	413-414	RS-30	24	39	300	1.9	3.5	26	130	28	7.4	0.26	0.3	0.41	1.4	2.4	12
369-3	476-485	RS-31**	<5	<15	2	0.2	0.6	<1	<2	0.7	0.3	0.07	<0.2	<0.02	0.1	0.3	3.3
397-1	71-74	RS-32	21	31	360	1.9	<0.5	26	170	22	8.5	0.46	0.2	0.95	1.8	3.4	20
397-2	244-247	RS-33	16	26	180	1.4	6.7	<1	130	16	9.6	0.39	<0.2	0.30	1.0	2.1	18
397-3	550-553	RS-34	20	18	81	0.9	2.1	66	190	28	9.5	0.09	0.7	0.14	0.6	1.8	6.6
397-4	583-585	RS-35	46	19	23	5.4	0.7	<1	490	10	17	1.30	0.4	1.90	5.1	9.0	57
409-1	146-149	RS-36	18	22	240	1.4	0.7	26	170	20	7.9	0.31	0.3	0.42	1.4	2.6	17
409-2	317-321	RS-37	18	32	270	1.1	0.5	19	290	21	10	0.22	0.4	0.20	0.7	1.5	11
409-3	572-576	RS-38	24	18	180	1.3	0.5	16	200	19	12	0.31	0.2	0.29	1.0	2.5	16
416-1	112-116	RS-39	32	48	300	1.8	1.5	18	140	27	10	0.48	0.3	0.53	1.7	3.4	22
416-2	341-345	RS-40	23	21	97	1.4	<0.5	26	120	17	10	0.32	0.4	0.34	1.2	2.7	16
416-3	553-556	RS-41	27	100	330	2.2	1.5	15	250	51	7.5	0.57	0.7	2.20	9.2	5.8	24
419-1	149-153	RS-42	10	29	260	1.0	0.6	15	240	22	12	0.21	0.4	0.23	0.8	1.7	11
419-2	288-292	RS-43	7	<15	7	0.4	2.6	30	70	5.4	5.0	0.05	<0.2	0.06	0.3	1.5	4.1
436-1	216-219	RS-44	30	18	220	2.5	0.7	17	140	18	10	0.53	0.2	0.82	2.1	4.2	26
436-2	359-362	RS-45	18	8	110	0.9	0.9	14	290	11	9.7	0.18	0.2	0.18	0.6	1.4	9.5
436-3	671-674	RS-46	20	33	99	1.4	<0.5	16	110	34	2.6	0.18	0.2	0.30	0.7	2.0	8.7
436-5	950-953	RS-47	<5	29	24	0.8	<0.5	31	33	4.1	2.5	0.08	0.3	0.12	0.4	1.7	4.2
436-6	962-966	RS-48	36	16	14	1.9	0.5	<1	350	1.9	6.0	0.54	0.2	0.50	1.3	2.5	26
436-7	973-975	RS-49	28	<15	150	3.2		<1	290								
436-8	994-997	RS-50	<5	<15	8	1.5	0.6	<1	300	1.2	25	0.14	<0.2	0.15	0.7	1.2	8.4
443-1	135-138	RS-51	17	17	360	1.6	<0.5	70	330	5	3.8	0.05	<0.2	0.07	0.3	0.4	2.7
443-2	261-264	RS-52	10	28	150	1.9	1.0	22	450	18	17	0.22	0.3	0.38	1.4	2.3	14
443-3	472-475	RS-53	25	46	190	1.8	0.6	18	370	37	11	0.27	<0.2	0.21	0.7	2.4	14

<sup>(1)</sup> First part of sample number refers to the core ID, the second part refers to the depth in cm.

<sup>(2)</sup> Totals are the sum of the major elements.

Analytical methods are given in the third row.

Note: Se <3 ppm (DL) in all samples.

Note: Hg <2 ppm (DL) in all samples except R.

\*Anhydrite-bearing sample

\*\*Massive anhydrite

Supplementary Data Table 2. Chemical analyses of metalliferous sediments from the East Pacific Rise transect (DSDP Leg 92) on a carbonate-free basis																																
Lab no.	DSDP no.*	Depth** (cm)	Depth BSF*** (m)	SiO <sub>2</sub>	TiO <sub>2</sub>	Al <sub>2</sub> O <sub>3</sub>	Fe <sub>2</sub> O <sub>3</sub> (t)	MnO	MgO	CaO	Na <sub>2</sub> O	K <sub>2</sub> O	P <sub>2</sub> O <sub>5</sub>	LOI	Trace elements	Total using Fe <sub>2</sub> O <sub>3</sub> measured by ICP	Total using Fe <sub>2</sub> O <sub>3</sub> calculated from Fe measured by INAA	Fe	Ba	Cu	Pb	Zn	Au	Ag	As	Sb	Bi	Cd	Tl	In	V	
				wt%	wt%	wt%	wt%	wt%	wt%	wt%	wt%	wt%	wt%	wt%	wt%	wt%	wt%	ppm	ppm	ppm	ppm	ppm	ppm	ppm	ppm	ppm	ppm	ppm	ppm	ppm	ppm	ppm
				ICP-ES	ICP-ES	ICP-ES	ICP-ES	ICP-ES	ICP-ES	ICP-ES	ICP-ES	ICP-ES	ICP-ES				INAA	INAA	ICP-ES	ICP-ES	INAA	INAA	ICP-MS	INAA	INAA	ICP-MS	ICP-MS	ICP-MS	ICP-MS	ICP-MS	ICP-ES	
DS-1	597-2-1	76-78	5.37															37.2	2200			1300	9		436	20						
DS-2	597-2-3	75-77	8.36															40.5	2200			1400	5		425	14						
DS-3	597-2-6	68-79	12.84															38.0	2500			1400	4		377	11						
DS-4	597-3-2	78-90	16.54															38.5	4100			1700	45		373	11						
DS-5	597-3-5	76-78	20.97															37.6	2200			1200	32		357	10						
DS-6	597-4-1	69-71	24.50															34.6	2400			1000	7		327	7.7						
DS-7	597-4-3	74-76	27.55															35.1	2600			1100	20		317	7.6						
DS-8	597-4-6	74-76	32.05															33.6	2600			1000	46		356	7.3						
DS-9	597A-5-1	74-76	34.15															33.4	1500			810	60		344	6.6						
DS-10	597A-5-3	75-77	37.16															29.2	1400			1000	<3		310	5.6						
DS-17	597-6-1	75-77	43.76	9.5	0.27	2.97	44.0	15.5	1.15	1.91	0.17	0.39	1.57	20.1	0.680	98.2	100.1	32.1	1300	1200	150	930	7	6.9	369	6.5		3.9	10	0.15	1300	
DS-18	597-6-3	74-76	46.75	10.7	0.39	3.44	41.2	15.3	1.06	2.98	0.27	0.46	1.90	19.6	0.696	98.0	100.3	30.4	1500	1300	88	1000	4	21.0	372	8.5		4.6	13	0.16	1200	
DS-19	597-6-4	74-76	48.25	14.2	0.48	3.55	41.9	13.7	1.14	1.66	0.20	0.57	1.23	19.0	0.663	98.3	103.0	32.6	1400	1200	56	1200	29	5.2	389	17	1.3	4.5	11	0.12	1200	
DS-20	597-6-5	74-76	49.75	12.1	0.47	3.91	39.6	15.2	1.11	2.52	1.63	0.63		19.4	0.150	96.7	98.4	28.9	1400			790	18		366	17						
DS-21	597-6-6	74-76	51.25	9.0	0.44	3.18	44.6	13.9	1.30	1.79	2.12	0.37		19.8	0.177	96.7	99.0	32.8	1500			1100	3		389	18						
DS-22	598-1-1	71-73	0.72	22.6	0.65	7.41	34.9	7.5	1.51	3.20	0.38	0.87	2.98	17.2	1.457	100.6	101.2	24.8	8100	1800	160	820	3	2.0	358	21	2.2	1.3	5.9	0.26	540	
DS-23	598-1-2	71-73	2.22	16.5	0.47	6.38	43.1	6.8	1.61	2.50	0.26	0.73	3.02	17.5	1.046	99.9	100.7	30.7	3100	2200	140	1000	10	5.8	440	21	1.9	1.3	6.1	0.31	690	
DS-24	598-1-4	71-75	5.23	12.4	0.26	4.68	47.3	6.3	1.54	3.20	0.26	0.39	3.15	18.0	1.368	98.8	101.7	35.1	8300	2000	160	990	16	12	411	20	2.6	1.6	5.3	0.16	680	
DS-11	598-2-2	72-76	8.44															34.0	7100			1000	40		304	13						
DS-12	598-2-3	72-76	9.94															39.2	6100			1200	9		365	15						
DS-13	598-2-5	79-83	13.01															39.2	3500			1000	16		392	15						
DS-25	598-3-1	67-69	16.48	7.5	0.17	2.00	58.4	8.6	1.27	0.79	0.10	0.14	1.74	18.8	0.764	100.3	101.5	41.7	2500	1700	140	1100	17	60	414	15	0.6	1.3	5.8	0.24	1000	
DS-14	598-3-2	73-77	18.05															40.6	2800			1100	25		414	14						
DS-15	598-3-3	71-75	19.53															39.4	2200			1100	30		423	11						
DS-26	598-3-4	70-74	21.02	6.0	0.11	1.05	51.4	14.5	0.94	1.29	0.06	0.07	1.73	20.2	0.732	98.1	100.6	37.7	2600	1400	120	990	<4	36	409	9.3	1.1	2.2	7.9	0.23	1000	
DS-27	598-4-1	15-17	25.56	5.3	0.10	0.95	27.7	17.1	0.90	1.02	0.03	0.03	0.89	20.6	0.509	75.1	99.5	36.4	2100	820	80	1000	5	13	423	9.5	0.8	2.3	12	0.20	620	
DS-28	598-4-3	25-27	28.66	5.3	0.10	0.96	45.8	16.2	0.94	1.27	0.04	0.06	1.31	20.8	0.719	93.5	99.2	36.0	1800	1500	140	1000	9	3.1	439	8.8	1.9	1.3	13	0.22	1000	
DS-29	598-4-5	26-28	31.67	4.6	0.10	0.93	51.8	17.2	0.97	0.78	3.76	0.07		20.5	0.228	100.9	101.5	36.6	2100			920	10		464	9.2						
DS-30	598-5-1	81-83	35.82	5.3	0.09	0.88	50.8	17.7	0.94	0.85	1.71	0.08		20.4	0.247	99.0	99.8	36.1	2300			960	4		444	8.8						
DS-31	598-5-2	72-74	37.23	4.6	0.06	0.67	51.9	16.2	0.92	0.84	<0.03	0.03	1.27	20.4	0.728	97.6	97.5	36.2	2100	1500	130	1000	4	3.3	439	8.6	2.0	10	0.25	1200		
DS-32	598-5-4	80-82	40.31	5.7	0.07	0.69	50.0	15.3	0.90	1.19	<0.03	0.05	1.57	19.9	0.719	96.1	100.0	37.7	2700	1400	130	1100	9	2.6	459	8.2	2.4	10	0.32	1100		
DS-16	598-5-5	71-73	41.72															36.5	2500			1100	4		434	7.8						
DS-33	598-5-6	71-73	43.22	7.4	0.14	1.58	46.7	14.5	1.29	2.22	1.28	0.10		19.5	0.250	95.0	100.2	36.3	2100			750	11		471	7.5						
DS-34	599-1-1	71-75	0.73	17.9	0.41	7.10	36.7	6.0	1.40	4.08	2.40	0.71		18.0	1.147	95.8	101.5	29.6	14000			1000	20		428	20						
DS-35	599-1-5	72-76	6.74	8.4	0.13	1.79	54.1	10.3	1.11	0.41	3.33	0.13		19.9	0.316	99.9	106.4	42.4	3500			860	50		437	15						
DS-36	599-2-2	70-74	10.12	6.6	0.05	0.38	48.0	14.8	0.76	3.89	0.04	0.03	2.99	20.5	0.709	98.7	97.5	32.7	2500	1500	110	890	9	1.8	416	6.1	1.7	11	0.27	1100		
DS-37	599-2-3	70-74	11.62	7.0	0.06	0.55	51.1	14.7	0.83	1.03	<0.03	0.03	1.93	20.4	0.779	98.4	97.2	34.9	2800	1500	130	930	6	2.7	443	6.3	1.7	12	0.25	1100		
DS-38	599-2-5	70-73	14.62	7.8	0.06	0.59	48.0	14.7	0.81	0.78	0.03	0.03	1.69	20.3	0.714	95.5	96.4	34.2	2300	1400	120	860	7	3.4	414	7.0	1.6	12	0.26	980		
DS-39	599-3-1	70-74	18.22	12.5	0.06	0.53	46.3	13.5	0.77	2.18	0.03	0.03	1.90	20.1	0.733	98.6	98.1	32.0	3100	1400	130	870	9	3.9	437	5.6	2.2	13	0.24	990		
DS-40	599-3-2	70-74	19.72	8.2	0.05	0.31	49.3	14.7	0.74	0.93	<0.03	0.03	1.52	20.0	0.688	96.5	95.8	34.0	2400	1400	120	840	13	12	452	5.8	1.7	15	0.27	1100		
DS-41	599-3-5	70-74	24.22	7.5	0.04	0.32	47.8	14.8	0.70	3.44	0.04	0.03	2.94	20.2	0.717	98.5	97.3	32.6	2100	1500	290	810	9	1.1	437	5.4	2.0	13	0.25	1100		
DS-42	599-4-1	71-73	27.82	7.2	0.06	0.32	29.9	16.6	0.67	0.50	<0.03	0.03	1.35	21.1	0.491	78.2	96.8	33.9	2100	840	85	720	15	1.5	433	6.5	1.1	8.9	0.13	640		
DS-43	599-4-3	71-73	30.82	9.8	0.06	0.79	48.4	14.0	0.89	0.38	0.03	0.05	1.19	20.3	0.723	96.6	97.5	34.5	2500	1500	140	920	10	7.4	447	6.8	2.1	12	0.31	1000		
DS-44	599-4-4	72-74	32.33	7.1	0.05	0.35	42.1	15.8	0.70	2.29	<0.03	0.03	2.03	20.9	0.651	92.0	95.7	32.0	2400	1300	110	780	24	2.7	430	5.4	1.8	13	0.20	960		
DS-45	599-4-5	72-74	33.82	7.0	0.05	0.39	34.9	14.9	0.75	1.90	<0.03	0.03	1.57	20.6	0.596	82.7	96.1	33.8	2200	1100	94	830	40	5.5	481	5.8	1.7	9.9	0.20	810		
DS-46	599B-2-3	70-74	36.02	8.6	0.08	1.02	50.1	10.9	0.92	1.37	<0.03	0.03	0.54	19.8	0.465	93.8	96.3	36.8	3200	490	53	800	28	3.8	478	7.0	0.6	2.8	0.15			

Supplementary Data Table 2. Chemical analysis																								
Lab no.	DSDP no.*	Depth** (cm)	Depth BSF*** (m)	Cr ppm INAA	Ni ppm ICP-ES	Co ppm INAA	Sc ppm INAA	Sn ppm ICP-MS	Mo ppm INAA	W ppm INAA	Ga ppm ICP-MS	Be ppm ICP-ES	Rb ppm ICP-MS	Sr ppm ICP-ES	Cs ppm ICP-MS	U ppm ICP-MS	Hf ppm ICP-MS	Th ppm ICP-MS	Nb ppm ICP-MS	Y ppm ICP-MS	Zr ppm ICP-ES	Zr ppm ICP-MS	La ppm ICP-MS	
DS-1	597-2-1	76-78	5.37	18		130	13		310	18														
DS-2	597-2-3	75-77	8.36	27		130	6.6		350	21														
DS-3	597-2-6	68-79	12.84	29		120	11		93	11														
DS-4	597-3-2	78-90	16.54	34		120	11		110	9														
DS-5	597-3-5	76-78	20.97	33		120	9.1		92	3														
DS-6	597-4-1	69-71	24.50	19		110	5.8		88	8														
DS-7	597-4-3	74-76	27.55	12		120	5.9		95	13														
DS-8	597-4-6	74-76	32.05	24		110	6.9		83	3														
DS-9	597A-5-1	74-76	34.15	13		120	6.3		64	14														
DS-10	597A-5-3	75-77	37.16	27		100	9.1		71	12														
DS-17	597-6-1	75-77	43.76	37	790	110	7.6	27	230	9	23	3.1	7.4	320	0.26	1.9	1.20	0.65	5.4	95	86	95	91	79
DS-18	597-6-3	74-76	46.75	<5	770	120	11	31	510	11	18	2.3	7.5	350	0.20	2.2	0.95	0.50	5.5		110	67	64	85
DS-19	597-6-4	74-76	48.25	<5	710	110	11	16	610	17	16	2.6	11.0	210	0.21	1.8	1.10	0.51	6.7	73	62		160	56
DS-20	597-6-5	74-76	49.75	18		100	9.1		610	18														
DS-21	597-6-6	74-76	51.25	<5		98	8.7		530	63														
DS-22	598-1-1	71-73	0.72	<5	1200	410	41	5.4	170	26	16	2.4	27	240	1.80	2.6	7.90	6.5	32		640		450	
DS-23	598-1-2	71-73	2.22	<5	1200	300	35	9.8	190	22	14	3.0	21	200	1.20	4.0	7.20	3.2	27		600		470	
DS-24	598-1-4	71-75	5.23	<5	670	250	21	31	220	15	16	4.4	11	200	0.74	2.9	3.30	1.9	16		480		250	
DS-11	598-2-2	72-76	8.44	11		140	12		200	23														
DS-12	598-2-3	72-76	9.94	<5		150	13		200	12														
DS-13	598-2-5	79-83	13.01	<5		130	12		180	11														
DS-25	598-3-1	67-69	16.48	<5	510	110	9.7	15	200	5	8.1	3.2	4.1	99	0.34	2.7	2.00	0.87	6.1		140		180	100
DS-14	598-3-2	73-77	18.05	<5		120	9.6		170	19														
DS-15	598-3-3	71-75	19.53	<5		130	5.9		230	9														
DS-26	598-3-4	70-74	21.02	31	650	120	4.8	17	210	12	12	2.7	2.2	150	0.15	2.2	1.00	0.45	5.3		120	99	89	90
DS-27	598-4-1	15-17	25.56	47	450	130	5.4	22	170	10	14	1.6	2.3	79	0.19	2.0	0.97	0.69	4.6		51	98	50	93
DS-28	598-4-3	25-27	28.66	27	840	130	5.6	6.7	130	11	8.5	2.3	2.1	190	0.14	2.1	0.48	0.53	3.7		120	49	43	
DS-29	598-4-5	26-28	31.67	<5		140	5.4		150	5														
DS-30	598-5-1	81-83	35.82	25		120	5.5		150	19														
DS-31	598-5-2	72-74	37.23	11	900	130	4.9	4.0	130	16	7.1	2.0	1.3	120	0.09	1.9	0.91	0.27	3.3	72	68	89	89	67
DS-32	598-5-4	80-82	40.31	<5	840	130	4.8	16.0	130	16	8.6	2.2	2.0	140	0.12	2.2	0.43	0.29	3.0	100	87	42		76
DS-16	598-5-5	71-73	41.72	28		130	6.6		110	15														
DS-33	598-5-6	71-73	43.22	18		120	5.9		120	16														
DS-34	599-1-1	71-75	0.73	<5		310	29		180	23														
DS-35	599-1-5	72-76	6.74	26		140	8.1		260	3														
DS-36	599-2-2	70-74	10.12	<5	560	85	2.4	3.6	110	18	6.8	0.9	1.0	280	0.05	3.4	0.45	0.17	2.2	100	86	52	48	50
DS-37	599-2-3	70-74	11.62	<5	670	93	3.1	5.7	110	14	6.9	1.3	1.2	130	0.07	3.7	0.65	0.25	2.7		110	68	66	63
DS-38	599-2-5	70-73	14.62	<5	570	90	3.5	13	68	18	8.2	1.6	1.4	130	0.09	3.0	0.51	0.23	2.7		110	50	44	68
DS-39	599-3-1	70-74	18.22	<5	550	87	3.5	5.6	56	<1	7.2	1.3	1.4	210	0.07	3.4	0.70	0.23	2.7		110	71	66	66
DS-40	599-3-2	70-74	19.72	16	550	85	2.8	4.0	67	13	7.1	1.0	1.1	170	0.04	3.2	0.54	0.16	2.2	100	86	58	55	51
DS-41	599-3-5	70-74	24.22	<5	530	88	2.8	2.0	65	9	7.1	1.1	1.0	260	0.05	3.8	0.46	0.24	2.1	96	81	52	50	56
DS-42	599-4-1	71-73	27.82	13	320	94	3.2	1.4	67	5	5.9	0.6	0.7	81	0.04	2.9	0.36	0.20	1.4	75	67	36		38
DS-43	599-4-3	71-73	30.82	<5	520	90	4.4	6.6	58	14	6.0	1.9	1.4	70	0.11	2.4	0.45	0.33	3.0		130	44	42	80
DS-44	599-4-4	72-74	32.33	7	550	96	2.5	11	78	13	5.6	0.9	0.9	210	0.04	3.2	0.43	0.15	1.9	81	71	46	43	47
DS-45	599-4-5	72-74	33.82	10	430	92	2.8	2.7	83	9	6.0	1.1	0.8	140	0.04	2.5	0.44	0.15	1.9	76	61	48	41	42
DS-46	599B-2-3	70-74	36.02	20	170	94	3.7	6.2	83	12	4.6	1.1	0.7	54	0.05	1.0	0.43	0.12	1.7	65	53	44		29
DS-47	599B-2-4	70-73	37.52	<5	580	98	3.8	5.1	160	14	6.5	1.0	1.1	190	0.05	3.3	0.60	0.17	2.3	100	84	61	57	59
DS-48	599B-2-5	74-77	39.06	<5	540	81	7.0	3.0	330	15	8.8	0.9	9.1	250	0.16	3.5	0.78	0.18	2.1	94	81	65	60	52
DS-49	599B-2-6	71-74	40.53	<5	620	79	9.1	5.2	360	13	11	0.9	17	230	0.29	4.1	0.90	0.17	2.1		97	64	62	51
DS-52	600C-1-2	94-99	2.47	<5		170	19		250	<2														
DS-53	600C-1-4	99-104	5.52	21	400	120	9.3	1.5	160	5	6.0	1.3	1.5	68	0.15	2.3	1.10	0.54	3.3		120	99	100	70
DS-54	600C-1-6	99-104	8.52	<5	370	79	5.2	2.2	120	11	5.9	0.6	0.7	150	0.04	3.0	0.60	0.18	1.7	100	94	48	47	48
DS-55 #	600C-2-2	91-96	11.84	<5	340	64	18	1.8	140	16	9.6	0.6	1.2	32	0.11	0.4	0.56	0.24	0.8	25	20	42		7
DS-50	601B-1-2	76-81	16.69	<5	610	83	4.5	3.5	280	16	7.7	0.9	1.2	110	0.07	3.3	0.70	0.25	2.2		110	65	62	65
DS-51	601B-1-3	74-79	18.17	<5	480	79	4.6	2.6	340	14	6.7	0.8	0.8	320	0.05	5.8	0.63	0.16	1.9		100	52	50	52

\* Sample number indicates hole-core-section  
\*\* Depth in section  
\*\*\* BSF = below sea floor  
# Contains basaltic material  
Note: 4 samples from Sites 599 and 600 yielded CO<sub>2</sub>(t), Ca  
Hg <1 ppm (INAA detection limit) in all samples except DS-1  
Se <3 ppm (INAA detection limit) in all samples.  
Br <1 ppm (INAA detection limit) in all samples except DS-5  
Cs <1 ppm (INAA detection limit) in all samples except DS-2  
Ta <1 ppm (INAA detection limit) in all samples except DS-4

Supplementary Data Table 2. Chemical analysis																			
Lab no.	DSDP no.*	Depth**	Depth BSF***	La	Ce	Pr	Nd	Sm	Eu	Gd	Tb	Dy	Ho	Er	Tm	Yb	Lu	ΣREE	
		(cm)	(m)	ppm															
				ICP-ES	ICP-MS														
DS-1	597-2-1	76-78	5.37																
DS-2	597-2-3	75-77	8.36																
DS-3	597-2-6	68-79	12.84																
DS-4	597-3-2	78-90	16.54																
DS-5	597-3-5	76-78	20.97																
DS-6	597-4-1	69-71	24.50																
DS-7	597-4-3	74-76	27.55																
DS-8	597-4-6	74-76	32.05																
DS-9	597A-5-1	74-76	34.15																
DS-10	597A-5-3	75-77	37.16																
DS-17	597-6-1	75-77	43.76	80	26	13	55	10	1.4	13	2.0	12.0	2.8	7.8	1.2	7.1	1.0	232	
DS-18	597-6-3	74-76	46.75	85	21	15	62	12	3.5	15	2.4	16.0	3.6	9.9	1.4	8.9	1.3	257	
DS-19	597-6-4	74-76	48.25	55	18	12	45	9.4	2.4	10	1.8	11.0	2.4	6.6	1.0	6.1	0.9	182	
DS-20	597-6-5	74-76	49.75																
DS-21	597-6-6	74-76	51.25																
DS-22	598-1-1	71-73	0.72	340	180	69	300	64	15	80	13.0	79.0	18.0	51.0	7.5	49.0	7.5	1273	
DS-23	598-1-2	71-73	2.22	320	110	63	270	54	15	69	11.0	74.0	17.0	47.0	7.0	44.0	6.7	1108	
DS-24	598-1-4	71-75	5.23	250	81	43	200	40	8.8	53	8.3	54.0	13.0	36.0	5.2	33.0	5.1	830	
DS-11	598-2-2	72-76	8.44																
DS-12	598-2-3	72-76	9.94																
DS-13	598-2-5	79-83	13.01																
DS-25	598-3-1	67-69	16.48	100	43	17	73	15	3.4	19	3.0	20.0	4.6	13.0	1.9	12.0	1.8	327	
DS-14	598-3-2	73-77	18.05																
DS-15	598-3-3	71-75	19.53																
DS-26	598-3-4	70-74	21.02	85	31	14	61	12	2.8	16	2.5	17.0	4.1	11.0	1.7	10.0	1.6	270	
DS-27	598-4-1	15-17	25.56	50	30	14	61	11	2.6	14	2.2	15.0	3.3	9.3	1.4	9.3	1.4	225	
DS-28	598-4-3	25-27	28.66	99	28	17	77	14	3.6	19	2.9	18.0	4.1	11.0	1.7	10.0	1.6	307	
DS-29	598-4-5	26-28	31.67																
DS-30	598-5-1	81-83	35.82																
DS-31	598-5-2	72-74	37.23	69	20	12	49	9.0	2.1	11	1.8	11.0	2.5	7.2	1.1	7.4	1.1	204	
DS-32	598-5-4	80-82	40.31	72	20	12	55	10	2.3	13	2.0	13.0	3.0	8.5	1.3	8.4	1.3	222	
DS-16	598-5-5	71-73	41.72																
DS-33	598-5-6	71-73	43.22																
DS-34	599-1-1	71-75	0.73																
DS-35	599-1-5	72-76	6.74																
DS-36	599-2-2	70-74	10.12	47	12	7.4	34	6.4	1.5	9.3	1.4	10.0	2.6	7.7	1.2	7.5	1.2	149	
DS-37	599-2-3	70-74	11.62	61	15	9.5	43	8.0	1.8	12	1.9	13.0	3.2	9.5	1.5	9.1	1.5	190	
DS-38	599-2-5	70-73	14.62	59	16	9.6	42	8.0	1.9	12	1.9	13.0	3.2	10.0	1.6	9.6	1.5	189	
DS-39	599-3-1	70-74	18.22	61	16	9.6	45	8.3	1.7	13	1.9	13.0	3.3	10.0	1.5	9.5	1.4	195	
DS-40	599-3-2	70-74	19.72	48	12	7.9	35	6.5	1.8	9.7	1.6	11.0	2.7	7.8	1.3	7.7	1.2	154	
DS-41	599-3-5	70-74	24.22	54	12	7.5	34	6.2	1.3	8.8	1.4	9.8	2.5	7.5	1.2	7.7	1.2	155	
DS-42	599-4-1	71-73	27.82	36	8.0	5.6	26	4.7	1.2	7.1	1.1	7.5	1.9	5.7	0.9	5.5	0.8	112	
DS-43	599-4-3	71-73	30.82	76	20	11	52	9.5	2.2	14	2.1	14.0	3.8	11.0	1.8	11.0	1.7	230	
DS-44	599-4-4	72-74	32.33	45	11	7.0	31	5.9	1.2	8.2	1.3	9.2	2.3	6.8	1.1	6.9	1.1	138	
DS-45	599-4-5	72-74	33.82	38	10	6.2	27	5.3	1.1	7.0	1.2	8.1	2.1	6.1	1.0	6.1	1.0	120	
DS-46	599B-2-3	70-74	36.02	27	8.7	4.2	20	3.7	0.77	5.3	0.8	5.7	1.5	4.2	0.7	3.8	0.6	87	
DS-47	599B-2-4	70-73	37.52	56	14	8.7	38	7.1	1.5	9.5	1.5	10.0	2.6	7.7	1.2	7.8	1.2	167	
DS-48	599B-2-5	74-77	39.06	49	13	7.5	34	6.7	1.9	9.3	1.5	10.0	2.6	7.6	1.2	7.7	1.2	153	
DS-49	599B-2-6	71-74	40.53	50	13	7.2	34	6.8	2.0	9.8	1.6	11.0	2.9	8.5	1.4	8.3	1.3	158	
DS-52	600C-1-2	94-99	2.47																
DS-53	600C-1-4	99-104	5.52	71	19	12	52	10	<0.02	14	2.3	15.0	3.8	11.0	1.6	9.9	1.6	223	
DS-54	600C-1-6	99-104	8.52	48	10	7.0	33	6.4	1.8	9.7	1.5	10.0	2.6	7.8	1.2	7.7	1.2	148	
DS-55 #	600C-2-2	91-96	11.84	<10	3.9	1.2	6.2	1.3	0.42	2.1	0.4	2.4	0.6	2.0	0.3	2.0	0.3	23	
DS-50	601B-1-2	76-81	16.69	63	14	9.3	43	8.2	2.1	12	2.0	13.0	3.3	9.8	1.6	9.6	1.6	193	
DS-51	601B-1-3	74-79	18.17	50	9.7	7.0	33	6.7	1.9	10	1.7	12.0	2.9	8.8	1.4	8.9	1.4	155	
* Sample number indicates hole-core-section																			
** Depth in section																			
*** BSF = below sea floor																			
# Contains basaltic material																			
Note: 4 samples from Sites 599 and 600 yielded CO <sub>2</sub> (t), C ai																			
Hg <1 ppm (INAA detection limit) in all samples except DS-1																			
Se <3 ppm (INAA detection limit) in all samples.																			
Br <1 ppm (INAA detection limit) in all samples except DS-5																			
Cs <1 ppm (INAA detection limit) in all samples except DS-2																			
Ta <1 ppm (INAA detection limit) in all samples except DS-4																			